ROLE OF PLASMA IN THE GROWTH AND FIELD EMISSION PROPERTIES OF 2D GRAPHENE NANOMATERIAL

THESIS SUBMITTED TO
DELHI TECHNOLOGICAL UNIVERSITY
FOR THE AWARD OF THE DEGREE OF

DOCTOR OF PHILOSOPHY

By

Ms. NEHA GUPTA
(2K14/PhD/AP/03)

Under the supervision of
PROF. (DR.) SURESH C. SHARMA

DEPARTMENT OF APPLIED PHYSICS
DELHI TECHNOLOGICAL UNIVERSITY
SHAHBAD DAULATPUR, MAIN BAWANA ROAD,
DELHI-110042, INDIA

JUNE, 2018

Dedicated

To

My Family

Delhi Technological University

(Govt. of National Capital Territory of Delhi)
Shahbad Daulatpur, Bawana Road, Delhi-110042

CERTIFICATE

This is to certify that the thesis entitled ***"Role of Plasma in the Growth and Field Emission Properties of 2D Graphene Nanomaterial"*** submitted by **Ms. Neha Gupta (2K14/PhD/AP/03)** to Delhi Technological University (DTU), Delhi, India for the degree of Doctor of Philosophy, is a bonafide record of the research work carried out by her under my supervision and guidance. The work embodied in this thesis has been carried out in the Plasma & Nano Simulation Lab, Department of Applied Physics, Delhi Technological University (DTU), Delhi, India. The work of this thesis is original and has not been submitted in parts or fully to any other Institute or University for the award of any other degree or diploma.

_____

Prof. (Dr.) Suresh C. Sharma
Supervisor
Head, Department of Applied Physics
Delhi Technological University
Shahbad Daulatpur, Bawana Road
Delhi-110042, India

Delhi Technological University
(Govt. of National Capital Territory of Delhi)
Shahbad Daulatpur, Bawana Road, Delhi-110042

CANDIDATE'S DECLARATION

I, herby certify that the thesis titled ***"Role of Plasma in the Growth and Field Emission Properties of 2D Graphene Nanomaterial"*** submitted in the fulfilment of the requirements for the award of the degree of Doctor of Philosophy is an authentic record of my research work carried out under the supervision of **Prof. (Dr.) Suresh C. Sharma**. Any material borrowed or referred to is duly acknowledged.

_____

Neha Gupta
(2K14/PhD/AP/03)
Delhi Technological University
Shahbad Daulatpur, Bawana Road
Delhi-110042, India

ACKNOWLEDGEMENTS

The completion of this thesis required a lot of guidance, assistance and encouragement from numerous people including my university, supervisor, well wishers, colleagues, and my friends. I am extremely privileged to thank all who in one way or another made this thesis possible and made it an unforgettable experience for me.

Foremost, it is a genuine pleasure to express my deep sense of thanks and gratitude to my *Ph.D supervisor*, ***Prof. Suresh C. Sharma***, Head of Department, Applied Physics, Delhi Technological University, Delhi, India for his valuable guidance, scholarly inputs, and consistent encouragement I received throughout my Ph.D study and research. His dedication, timely advice, and meticulous scrutiny have enabled me to accomplish my Ph.D thesis on time. I owe him special thanks for enabling me to enter into the art of research under his guidance and to learn from him research expertise.

My sincere thanks also goes to ***Hon'ble Prof. Yogesh Sharma***, Vice Chancellor, DTU and officials of DTU for their precious support and providing ample research facilities to conduct this research. I would also like to acknowledge their financial support to attend the 44th European Physical Society Conference on Plasma Physics held at Queen's University, Belfast, Northern Ireland (June 2017).

I would also thank profusely ***Prof. Rinku Sharma*** and all other faculty and staff members of Department of Applied Physics, DTU for their help and cooperation throughout my study period.

I express my heart-felt gratitude to ***Mr. Ravi Gupta*** (*Research Fellow*) for his constant motivation and support during the course of my thesis. His scientific inputs, personal helps, moral support and encouragement have always made me feel at ease and enhance the quality of my research. I would also like to express huge and warm thanks to my other fellow lab mates in Plasma & Nano

Simulation Research Laboratory: ***Ms. Aarti Tewari, Ms. Pratibha Malik, Ms. Jyotsna Panwar, Ms. Umang Sharma, Ms. Monika Yadav, Ms. Kavita Rani, Ms. Ruchi Sharma, Ms. Renu Kumari, Ms. Anshu Dahiya, and Ms. Suman Dahiya*** for the stimulating discussions, selfless support, and for all the fun we have had in the last four years. I also explicitly thank my colleagues ***Mr. Ajay Kumar, Ms. Nisha Deopa, Ms. Sumandeep Kaur, Mr. Aman Prasad,*** and ***Mr. Abhishek Bhardwaj*** for all their selfless support.

I am indebted to some of my dear friends ***Ms. Aakriti Sharma*** and ***Ms. Urvashi Tripathi*** for influencing me in a positive way and for their moral support and motivation, which drives me to give my best.

I would like to acknowledge all the teachers I learnt from since my childhood, I would not have been here without their guidance, blessings and support.

I would also like to thank ***Science and Engineering Research Board (SERB)–Department of Science and Technology (DST)***, ***Government of India*** for providing me with the necessary funding and fellowship to pursue research at DTU and attend the 18^{th} International Conference on the Physics of Highly Charged Ions held at Kielce, Poland (September 2016).

Last but not the least, I would like to pay high regards to my father ***(Mr. Raj Kumar Gupta)***, to my mother ***(Mrs. Sadhna Gupta)***, brother ***(Rohit Gupta)***, sisters ***(Shalini Gupta and Vaishali Gupta)***, sister-in-law ***(Nikita Gupta)***, brother-in-law ***(Anshul Gupta)***, niece ***(Inaya Gupta)*** and nephews ***(Vansh Gupta and Darsh Gupta)*** for supporting me spiritually throughout writing this thesis and my life in general. Their cooperation, understanding, and sincere encouragement were the sustaining factors in accomplishing this thesis successfully.

Above all, I thank the Almighty and Guruji for giving me the strength and patience to work through all these years so that today I can stand proudly with my head held high.

(Neha Gupta)

ABSTRACT

Graphene is the two dimensional monolayer of densely packed carbon atoms arranged hexagonally in the lattice in two dimensions. Vertically aligned graphene sheets are the potential candidate in the applications of the field emission devices, electronic sensors, and electron emission displays etc. There are various techniques available through which graphene can be synthesized, however, plasma based techniques e.g. plasma enhanced chemical vapour deposition (PECVD) are exclusively used to synthesize vertically oriented graphene sheets at low temperatures. The present thesis aims to elucidate the deep insights of the growth mechanism of the graphene sheet in the reactive plasma environment and consequent field emission characteristics from them.

In the present work, the multiscale analytical models describing the growth mechanism of the graphene sheet without catalyst and on the catalyst-substrate surface have been developed separately. The model dealing with the growth of graphene in the plasma without catalyst incorporates the charging of the graphene sheet in the plasma, particle and energy balance of the plasma species (charged and neutral species), and energy balance of the graphene sheet. The simultaneously coupled model equations have been solved for typical glow discharge plasma parameters. It is found that plasma parameters (number densities and temperatures of electrons and ions), presence of dopant species (nitrogen species), and presence of negatively charged species significantly affect the growth characteristics of the graphene sheet, and consequently affects the field emission properties of the graphene sheet.

The multistage model dealing with the plasma-assisted catalyzed growth of graphene sheet mainly incorporates two sub-analytical models. One is the plasma sheath model that accounts the excitation of the gaseous sources due to applied plasma power and kinetics of the plasma species and the other one is the surface deposition model that incorporates the adsorption and dissociation of carbon bearing species over the catalyst nanoislands active surface (free surface available for the adsorption of the plasma species) to generates building species

(carbon species) via various surface processes, diffusion of building species over the catalyst nanoislands surface, formation of carbon clusters, nucleation and growth of graphene island, and vertical growth of graphene sheet. The solutions of the model equations have been carried out for experimentally determined initial conditions. It is found that the plasma parameters, doping elements (nitrogen and boron), type of gaseous sources, and plasma operating parameters have great influence on the growth characteristics of the graphene sheet and thus, affect the field emission properties of the graphene sheet. In addition, the growth of graphene sheet over the CNT template is also studied. It is considered that graphene sheet growth over the CNT surface is defect guided and density profiles of the defects created over the CNT surface can be controlled by suitably varying the plasma operating conditions and henceforth affect the growth characteristics (i.e., number density and dimensions) of the graphene sheets grown over the CNT surface. A good comparison of the obtained theoretical results with the available experimental observations confirms the adequacy of the present model.

The present work of the thesis can be extended to fabricate the thin and long vertically oriented graphene sheets for their potential applications in the field emitters as the field emission characteristics of the graphene sheet depend on its geometrical characteristics, i.e., height and thickness. Moreover, the present work can also be extended to investigate the growth of other carbon based nanostructures.

LIST OF PUBLICATIONS

International Journals

1. Ravi Gupta, **Neha Gupta**, and Suresh C. Sharma, Modeling to study the role of catalyst in the formation of graphitic shells during carbon nanofiber growth subjected to reactive plasma, ***Phys. Plasmas* 25, 043504 (2018)**.

2. **Neha Gupta** and Suresh C. Sharma, Effect of gas composition on morphological properties of graphene nanosheets, ***Phys. Plasmas* 24, 073510 (2017).**

3. **Neha Gupta**, Suresh C. Sharma, and Rinku Sharma, Modeling the effect of doping on the catalyst assisted growth and field emission properties of plasma grown graphene sheet, ***Phys. Plasmas* 23, 083509 (2016).**

4. Suresh C. Sharma and **Neha Gupta**, Theoretical modeling of the plasma-assisted catalytic growth and field emission properties of graphene sheet, ***Phys. Plasmas* 22, 123517 (2015).**

5. **Neha Gupta**, Aarti Tewari, and Suresh C. Sharma, Role of plasma parameters on the growth and field emission properties of 2D graphene sheet, ***Journal of Atomic, Molecular, Condensate & Nano Physics* 2, 215 (2015).**

International peer reviewed proceedings

6. **Neha Gupta**, Suresh C. Sharma, and Ravi Gupta, Oxygen assisted growth of graphene sheet by PECVD process (**accepted** in Indian Journal of Pure and Applied Physics).

7. Ravi Gupta, Suresh C. Sharma, and **Neha Gupta**, Role of carrier gas on the morphology of plasma grown carbon nanofibers (**accepted** in Indian Journal of Engineering and Material Sciences).

8. Ravi Gupta, Suresh C. Sharma, and **Neha Gupta**, Role of different etchants on the growth of catalyst nanoparticles during the plasma processing of the metal catalyst thin film, ***Materials Today: Proceedings 5, 15416 (2018).***

9. **Neha Gupta**, Suresh C. Sharma, and Ravi Gupta, Formalism to study the effect of hydrogen on the plasma-assisted growth and field emission properties of the graphene sheet, ***44th EPS Conference on Plasma Physics, (2017) P1.309.***

10. **Neha Gupta**, Suresh C. Sharma, and Ravi Gupta, Modelling graphene sheet growth subjected to plasma containing negatively charged ions, ***44th EPS Conference on Plasma Physics, (2017) P4.418.***

11. Ravi Gupta, Suresh C. Sharma, and **Neha Gupta**, Role of etchant on the morphology of plasma grown carbon nanofibers: theoretical modeling, ***44th EPS Conference on Plasma Physics, (2017) P2.304.***

12. Umang Sharma, Suresh C. Sharma, Ravi Gupta, and **Neha Gupta**, Theoretical investigations to study the effect of C_2H_2/H_2 gas ratio on the multi-walled carbon nanotubes growth, ***44th EPS Conference on Plasma Physics, (2017) P2.309***.

13. **Neha Gupta**, Suresh C. Sharma, and Ravi Gupta, Theoretical investigation on the effect of nitrogen doping on the growth and field emission properties of the plasma-grown graphene sheet, ***IOP Conf. Series: Journal of Physics: Conf. Series 836, 012010 (2017).***

14. Ravi Gupta, Suresh C. Sharma, and **Neha Gupta**, Theoretical study to investigate the impact of plasma parameters on the catalyst nanoparticle growth, ***IOP Conf. Series: Journal of Physics: Conf. Series 836, 012024 (2017).***

15. Umang Sharma, **Neha Gupta**, Ravi Gupta, and Suresh C. Sharma, Analytical modeling to study the effect of hydrogen plasma on the growth of multi-walled carbon nanotubes, ***IOP Conf. Series: Journal of Physics: Conf. Series 836, 012017 (2017).***

CONTENTS

List of Figures

Chapter: 3

LIST OF TABLES

1 Introduction

1.1 Background

Nanostructures, cornerstones of nanotechnology, are the interdisciplinary area of development activity and research which is growing explosively across the globe. Nanostructures have ability to bring revolution in the area of material sciences. Nanomaterials are of huge interest because of their unique scale in which atleast one of the dimension is of the order of nanometer scale (10^{-9} nm) and at this scale materials show unique optical, electronic, mechanical, and thermal properties. The surface atoms on nanomaterials are responsible for their miraculous properties. The scientific history of nanostructures began when Michael Faraday synthesized colloidal gold nanoparticles [1] but researchers took interest in graphitic carbon nanostructures after the discovery of one dimensional carbon nanotubes (CNTs) by Iijima [2]. We are familiar with graphite which is used in day to day life in the pencil. The two dimensional graphitic nanostructures like graphene, carbon nanowalls (consisting few layers of graphene sheets), and nanoflakes etc. gathered the huge research interest as a consequence of their distinctive properties compared to other 0D, 1D, and 3D carbon based nanostructures. The 2D graphene sheet is elected as the potential candidate for the application in electronics due to their high mobility and high ballistic transport [3].

1.2 Structure of Graphene

Graphene is the monolayer of densely packed carbon atoms arranged hexagonally in the lattice in two dimensions. All other forms of carbon nanostructures with different dimensions can be obtained using this basic structure of graphene. Rolled graphene sheets results in the one dimensional

carbon nanotubes, stacked graphene sheets results in the three dimensional graphite, and wrapped graphene sheets can be transformed into zero dimensional fullerenes as shown in Fig 1.1.

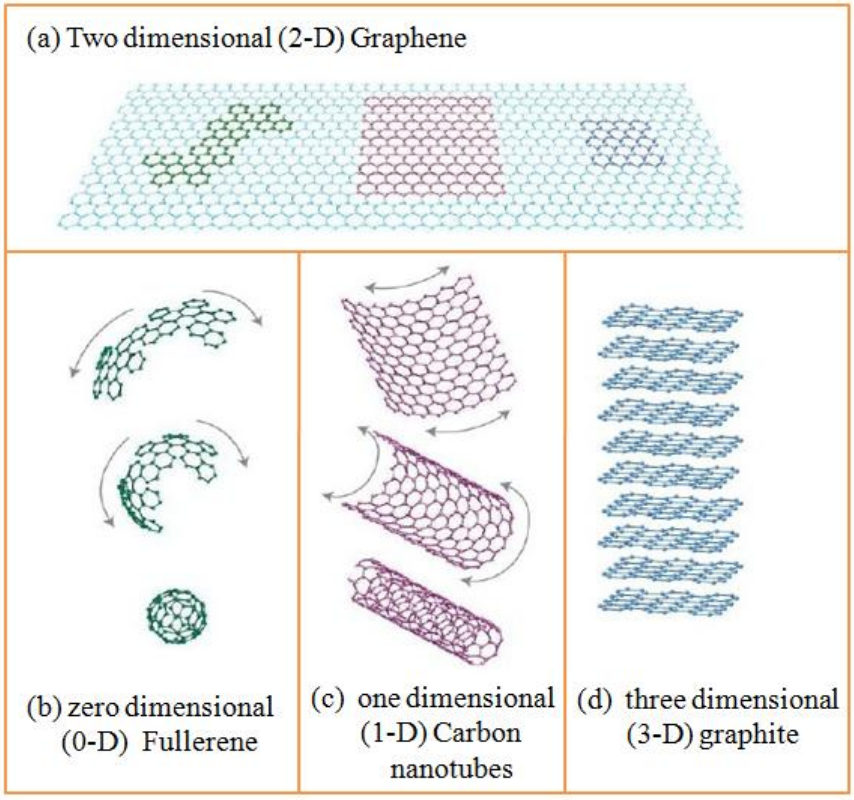

Fig.1.1. Transformation of two dimensional graphene into different dimensional carbon nanostructures [4].

Prior to the discovery of graphene, it was believed that two dimensional (numerical values of third dimension is extremely small compared to the numerical value of other two dimensions) stable structure cannot exist. However, after careful study of the structure of graphene, scientists proposed that distortions in the graphene sheet make the graphene stable [5]. This reveals that graphene is not perfectly flat and has ripples (out of plane distortions) on its surface. Mayer *et al.* [6] observed the ripples inside the graphene membrane [6].

Atomic structure of graphene can be understood on the basis of the orbital theory. Atomic number of carbon is 6 and thus, electronic configuration of carbon is $1s^2 2s^2 2p^2$ which clearly shows that carbon has four valence electrons. Generally, two valence electrons occupy 2s orbital and other two

electrons occupy $2p_x$ and $2p_y$ planar orbitals whereas, $2p_z$ orbital remain vacant. Depending upon the occupancy of valence electrons in the respective orbitals, two hybridizations are possible in the solid allotropes of carbon. One of the precious allotrope of carbon is diamond in which carbon atoms form sp^3 hybridization and other allotrope is graphene in which carbon atoms form sp^2 hybridization (see Fig.1.2). In sp^3 hybridization, out of four valence electrons each occupy 2s, $2p_x$, $2p_y$, and $2p_z$ orbitals, respectively, and all four electrons make four strong covalent σ bonds with neighbouring atoms constructing the tetragonal shape. However, in sp^2 hybridization, only three valence electrons take part in forming three planar covalent σ bonds with neighbouring carbon atoms and the remaining electron form out of plane weak-π bond. These σ bonds in sp^2 and sp^3 hybridization are responsible for high mechanical strength of diamond and graphene, and the π bonded electrons in graphene are responsible for high conductivity and also contribute in the interaction between the stacked graphene sheets [6-8].

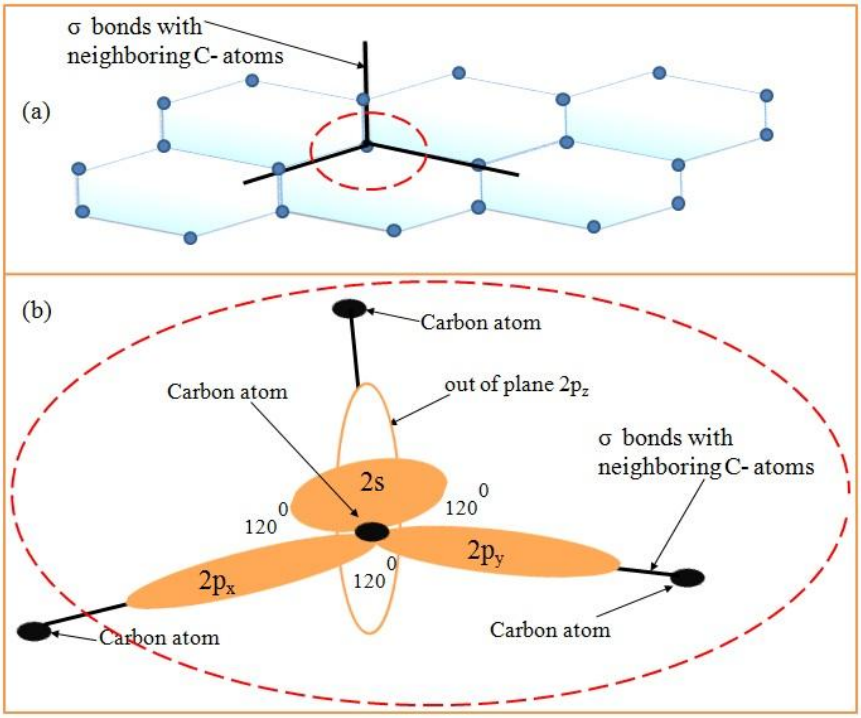

Fig.1.2. (a) Formation of planar σ bonding with neighbouring carbon atoms and (b) detailed representation of orbitals of carbon atoms and formation of sp^2 hybridization in graphene.

1.3 Properties of graphene

Graphene, ultra thin (10^5 order thinner than human hair) possible material composed of single layer of carbon atoms in the form of hexagonal rings. Owing to the outstanding mechanical, electronic, chemical, thermal, and optical properties, graphene gained the huge research attention in the field of physics and chemistry.

1.3.1 Mechanical properties

The parametric scales to measure the mechanical strength of any material and their corresponding numerical value for the graphene are listed in Table 1.1 which clearly states that graphene is the strongest imaginable material ever discovered because of the presence of strongest C-C bonds in sp^2 hybridization. It is much harder than diamond, lighter than feather and about 300 times harder than steel. Owing to high mechanical stability, graphene can be seen as the display screens in the near future.

Table 1.1. Parameters defining the mechanical strength of the graphene [9,10].

Parametric scale	Numerical value for graphene
Young's modulus	1 Tpa (tera pascal)
Elastic stiffness	33 N m^2
Tensile strength	130 giga pascal
Thickness	0.35-1 nm

1.3.2 Electronic properties

With the zero band gap, graphene is regarded as the semimetal that consist both holes and electrons as the charge carriers and offers resistivity (10^{-6} Ω cm) lower than the silver. In the two dimensional structure of the hexagonal rings in graphene, three of the four valence electrons of each C- atom are occupied in making C-C bond with other three C-atoms leaving fourth electron free for electrical conduction in third dimension. In graphene, mobility of holes is same as of electrons which is about 15×10^3 cm^2 V^{-1} S^{-1}

[11]. Moreover, single layer graphene also show Quantum Hall Effect (QHE) at the half integral multiple of $4e^2/h$ [12].

1.3.3 Chemical properties

Graphene offers the huge binding sites to other atoms and molecules for the adsorption or desorption to/from its surface. Most of the adsorbents have tendency to donate the electrons to the graphene, thereby, increasing the carrier concentration in it and thus, making it highly conductive [13]. This inherent property makes graphene to be the promising candidate for the gas sensors. Moreover, single layer graphene is much more reactive than multilayer graphene. At normal conditions, graphene show inert behaviour. However, it shows reactive nature when exposed to the crucial reactive environment.

1.3.4 Thermal properties

Hexagonally arranged carbon atoms in graphene provide good path for heat transfer via lattice vibrations. Graphene is considered as the good thermal conductor. The thermal properties of any material can be measured on the basis of its specific heat and thermal conductivity. The thermal constant of the material determines how fast a material can cool down or heat up. Thermal constant for the single layered graphene is about 0.1 ns [14]. At room temperature, the thermal conductivity of the graphene is exceptionally large (2000 $W\ m^{-1}\ K^{-1}$).

1.3.5 Optical properties

Although, having the thickness of the nanometer regime, graphene can be seen through naked eyes and absorb significant incident light in the infrared-to-visible range. Adding a layer to monolayer graphene decreases the transmittance by 2.8% at 550 nm wavelength [15]. It is hard to identify single layer graphene due to such high transparency; however, the visibility of graphene can be enhanced when it is deposited on the silicon oxide or silicon wafer or on the combination of both.

1.3.6 Magnetic properties

The magnetism in pristine graphene sheet is weak and can be induced by doping it with magnetic impurities. However, these impurities tend to interfere with the electronic properties of graphene. Wang *et al.*[16] coupled the graphene sheet with the magnetic insulator (yttrium iron garnet) to induce ferromagnetism in graphene while maintaining its exceptional electronic properties.

1.4 Applications of 2-D graphene nanosheet

The vertically oriented graphene sheets are promising material for the electrical energy applications such as in batteries, cells, field emission devices etc.

1.4.1 Applications in electron emission devices

Field emission is the property of the material to eject the electron from its surface under the influence of external electric field. The high electrical conductivity, atomic thickness, high aspect ratio, and high specific area of vertical graphene, render them to be the superior field emission candidates. Experimentally, field emission properties of any solid material are calculated by measuring the emission current density at turn on voltage. However, field enhancement factor is the physical quantity that characterizes the field emission property of the material.

Soin *et al.* [17] have calculated the field enhancement factor using Fowler-Nordheim (FN) equation; $J = A(\beta^2 E^2 / \varphi)\exp(-B\varphi^{3/2} / \beta E)$, where constant A is 1.54×10^{-10} AV^{-2} eV and constant B is 6.83×10^{-10} $Vm^{-1}eV^{-3/2}$. The work function φ of few layer graphene (FLG) is assumed to be same as that of graphite at 5eV. The value of the field enhancement factor β is calculated from the slope of the high- field and low- field regions of the FN plot using the following equation;

$$\beta = -(B\varphi^{3/2}) / slope$$

For pristine FLGs, the field enhancement factors calculated are 815 and 4710 for the low field and high field regions, respectively. Upon nitrogen doping, the field enhancement factor increases to approximately 3120 and 17350 for the low field and high field regions, respectively.

1.4.1.1 Graphene-based Field Effect Transistor (Graphene-FET)

Graphene in the form of nanoribbons with controlled width, termination, and edge structure are predicted to be used for FET applications. Chen *et al.*[18] have fabricated graphene nanoribbon (GNR) FET devices with GNRs as channels of FETs. They have observed that the resistivity of a GNR increases as their width decreases which could be the consequence of edge states. In addition, they found that dominant electrical noise of GNR at low frequencies to be dominated by 1/*f* noise.

1.4.1.2 Graphene-based electron emission display

Lei *et al.* [19] fabricated the 21 cm long graphene based (CNT-graphene hybrid) electron emission display panel using the screen printed triode edge emission geometry shown in Fig. 1.3. The aim of using CNT-graphene hybrid is to minimize the electrostatic shielding induced by the proximal bulk substrate and obtained the high emission efficiency (greater than 90%) at low driving voltages (less than 60 V), much fast emission response (less than 1ms), and extraordinary stable lifetimes (less than 3% variation in 10 hour).

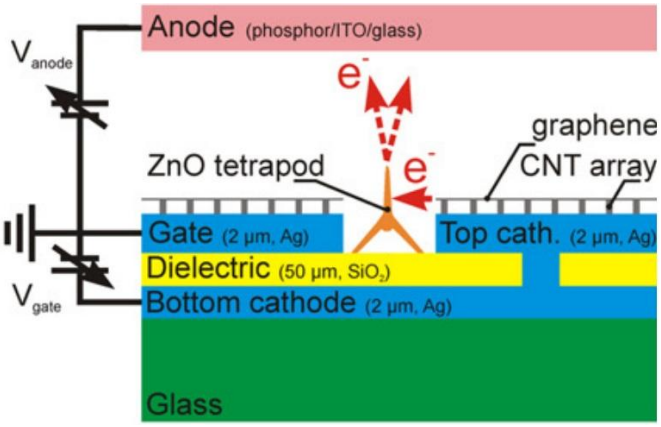

Fig. 1.3. Graphene based screen-printed triode edge electron emission geometry [19].

1.4.1.3 Graphene-based X-ray tubes

Among several carbon based nanostructures, graphene is considered to be the superior candidate for electron emission applications compared to other carbon based electron emitters because of its ability of stable field emission in high residual pressure region (10^{-4} Pa). The high current density and stable field emission properties of graphene make them promising candidates for X-rays, electron microscopes, and microwave generators. Matsumoto *et al.* [20] fabricated the X-ray tube using graphene nanosheet as the cathode material (grounded) and Beryllium (Be) as the anode (positively biased) and found the drastically high emission current at 5KV voltage supply and at 8.5 KV emission current exceeds the 1mA.

1.4.2 Application in fuel cells

Fuel cells are the devices that convert chemical energy of the fuel into electrical energy via numerous chemical reactions occurring at the interface of the anode which is employed with the catalyst to assist the oxidation of the chemical species. The non agglomerated morphology of the vertical oriented graphene sheets enhance the deposition of catalyst [21] and also provide the fast electron transport between the collector and reactions sites [22].

1.4.3 Application in biosensors

Vertically oriented graphene sheets are believed to be the suitable candidate for biosensors applications due to their open structure, high carrier mobility, high surface to volume ratio, and long exposed edges which augment the accessible area to analytes. The graphene based sensors are highly performing sensing material because they show high sensitivity (2 ng ml^{-1}) and much fast response (order of seconds) [22]. The schematic of the graphene based electronic sensor is shown in Fig.1.4.

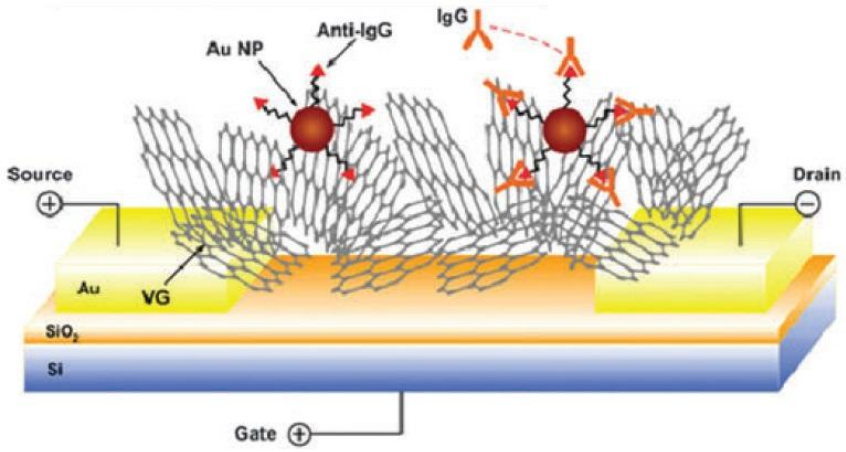

Fig. 1.4. Schematic of graphene based FET bio sensor [22].

1.4.4 Application in rechargeable batteries

The vertically aligned graphene sheets are considered to be promising material as anode in the Lithium ion batteries as shown in Fig.1.5. Vertical graphene sheet provides the numerous collecting sites to capture Lithium ions (Li^+). Moreover, better electrical connection and minimum contact between vertical graphene sheet and substrate surface provide minimum transport resistance for Lithium ions. Thus, vertical graphene sheet as the anode of the Lithium ion battery provide the high cycling stability and reversible capacity [23, 24]. It has been reported that the sandwich of vertical graphene and lithium alloying material i.e., GeO_x increases the lithium capturing capacity [25].

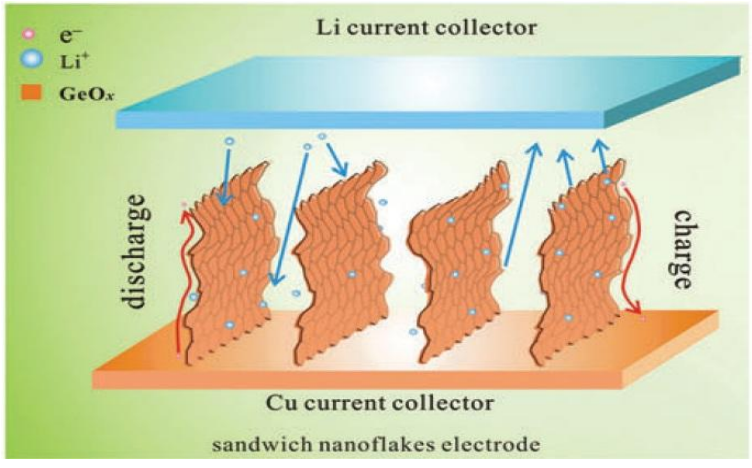

Fig. 1.5. Schematic of the Li ion diffusion mechanism in the VG@GeO_x sandwich nanoflakes-based electrode [25].

1.4.5 Application in gas sensors

Gas sensors detect the air pollutants such as carbon monoxides, sulphur oxides, nitrogen oxides, ammonia etc. Graphene based electronic sensors are preferred because graphene offers the high adsorbing sites for the atomic impurities. When gas molecules are adsorbed over the graphene surface, they change the carrier concentration of the graphene (either in magnitude or sign) which in turn changes the conductivity in graphene (either in magnitude or sign). The change in sign depends on the electronic property of the gas i.e., whether the gas is electron donor (NH_3) or electron acceptor (NO_2) [22].

1.5 Synthesis techniques of 2-D graphene nanosheet

Since graphene discovered by A. Geim and K. Novoselov in 2004 by exfoliation of graphite into graphene using adhesive tape, several other approaches have been reported for the efficient synthesis of graphene at large scale. All of these methods are suitable for the synthesis of graphene with different characteristics and have their own advantages and disadvantages. These synthesis methods can be broadly classified into two categories:

1. Top-down category

2. Bottom-up category

1.5.1 Top-down category

The top-down category involves the subtractive approach in which bulk graphite sources are exfoliated /cleaved to obtain graphene sheets. This approach has been experimentally realized by mechanical and chemical routes.

1.5.1.1 Micromechanical exfoliation

In the micromechanical exfoliation, the graphene sheets of different thicknesses are obtained by repeated peeling off the weakly bonded graphene layers from graphitic materials such as single crystal graphite flakes (Kish graphite), highly pyrolytic graphite (HOPG), and natural graphite [26,27]. The external force of ~ 300 $nN/\mu m^2$ is needed to separate a

monolayer of graphene from graphite [28]. Novoselov *et al.* [29] prepared graphene films by repeated peeling off layers of graphene from small mesas of HOPG via scotch tape. The films were then transferred onto the silicon substrate (see Fig.1.6). This method is simple and easy for the production of pure and high quality graphene samples but has the limitation of the large scale production for industrial applications.

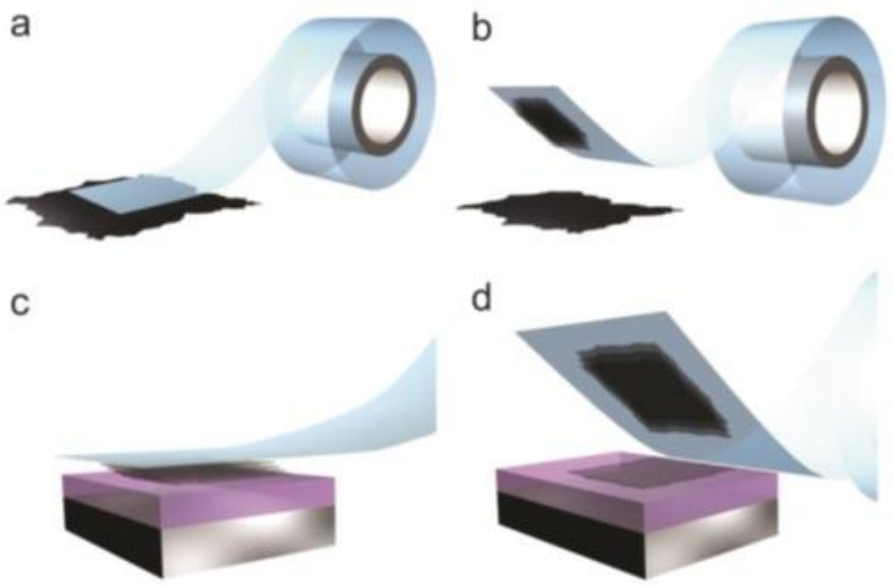

Fig. 1.6. Steps involved in mechanical exfoliation method: (a) adhesive tape is pressed against a HOPG surface so that the top few layers are attached to the tape (b), (c) the tape with crystals of layered material is pressed against a surface of choice, and (d) upon peeling off, the bottom layer is left on the substrate [30].

1.5.1.2 Chemical exfoliation

In a little altered way of exfoliation by mechanical route, another approach to obtain graphene by exfoliation is via chemical route i.e., by chemical exfoliation of bulk graphite. In this process, reactant (surfactant) is intercalated with graphite to break the van der waals interactions among the graphene sheets in graphite bulk, which is then followed by ultrasonication. The accomplishment of this technique is directed by the fact that the solvent must have comparative surface energy as that of the graphene [31].

1.5.1.3 Chemical Synthesis

This method is used to obtain graphene films from graphite via chemical route but without exfoliation. This method was firstly adopted by Horiuchi *et al.* [32]. The natural graphite is first oxidized to weaken the interlayer bonding among the graphene layers in graphite followed by dispersion in methanol and several centrifugation steps to obtain thin films of graphene (see Fig.1.7). In an another chemical method, sulphuric acid, nitric acid, and potassium permanganate are intercalated between the layers of graphite followed by heating at high temperatures to obtain thin graphene films by the evaporation of acid molecules. The chemical synthesis routes holds the promise for the large scale production of graphene and also offers the advantage to manipulate but this route has the disadvantage of producing graphene with poor electronic properties due lots of defects and generation on account of several chemical steps involved in the synthesis process.

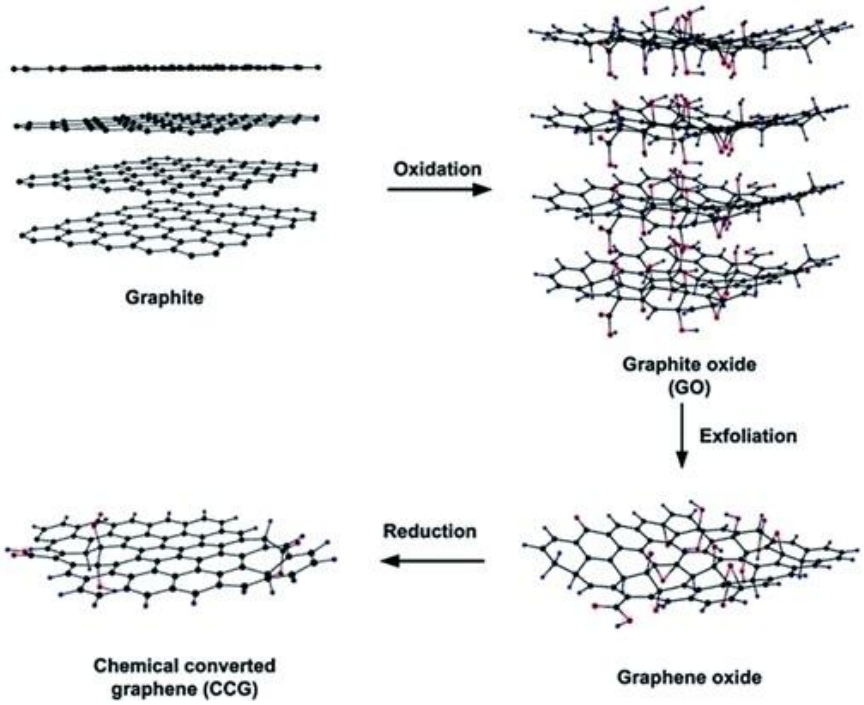

Fig. 1.7. Preparation of chemically converted graphene by reduction of graphene oxide **[33]**

1.5.2 Bottom-up category

1.5.2.1 Thermal decomposition of SiC

This is a popular growth technique to synthesize graphene epitaxially on a substrate. In this technique, graphene sheets are formed when crystalline silicon carbide wafers are heated at high temperatures for a short time in a controlled atmosphere of argon (or vacuum) to sublimate the silicon atoms of the SiC surface [34]. The numbers of layers of the graphene are dependent on the deposition temperature. Bommel *et al.*[35] were the first to fabricate graphene films on both the 6H-SiC surface by the heat treatment in the range of 1000-1500 ^{0}C. In a similar process, de Heer's [36] group have produced ultrathin graphene films of 1-3 monoatomic graphene layers on 6H-SiC surface and investigated their electronic characteristics. This technique is considered to be deployable for semiconductor industries but thickness control of the graphene sheet and large scale production restrict this technique to be employed at an industrial scale.

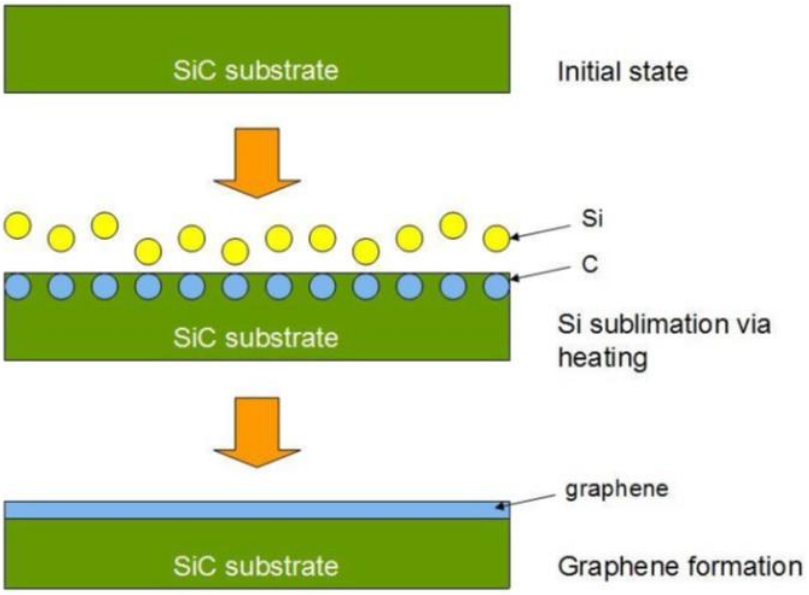

Fig. 1.8. Illustration of an epitaxial growth on a SiC substrate. After the sublimation of silicon, carbon remains on the surface where it would became graphene later [34].

1.5.2.2 Chemical Vapor Deposition (CVD)

CVD is the parent of the group of many synthesis methods because of the high versatility shown by it. In this process, gaseous sources (precursors) are introduced in the chamber. The energy required to activate gaseous reactants is supplied with the aid of heat, thus, it is generally known as thermal CVD. The typical CVD process generally includes two types of reactions: (i) the homogeneous gas phase reactions between various gaseous species which results in the generation of highly energetic radials, ions and neutral species and (ii) reactions occur on the heated substrate surface (heterogeneous surface reactions) which results in the generation of building units of the material (carbon in the case of carbon nanostructures) and other solid phase radicals. The heated surfaces act as the fuel for the decomposition of the precursors on the surface. Fig.1.9 shows the schematic of the CVD system. The main stages of the deposition processes re illustrated below:

(i) Transportation of the gaseous species towards the substrate surface via gas diffusion mechanism,

(ii) Adsorption and dissociation of the gaseous sources on the substrate surface via various complex processes and desorption of by-products formed on the surface,

(iii) Diffusion and dissolution of the species (building units) which ultimately leads to the growth of the graphene.

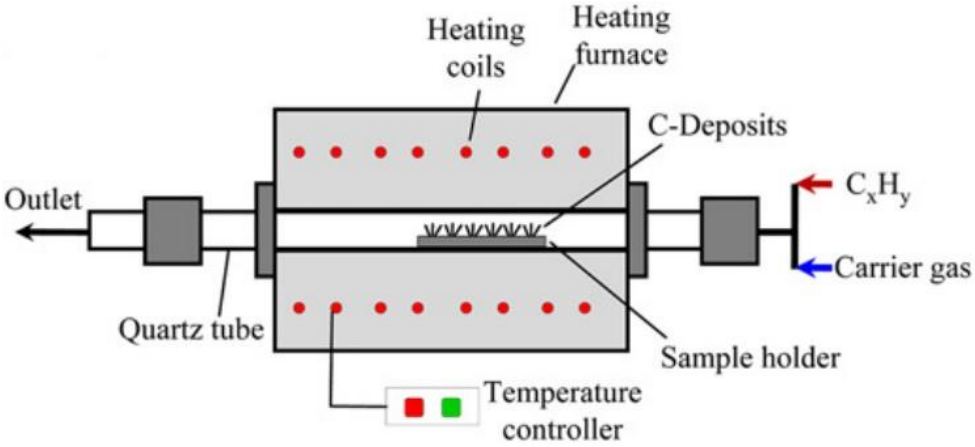

Fig. 1.9. Schematic of the chemical vapor deposition system [37].

The gases and the substrate surface (catalyst-substrate surface) are heated to sufficient pre-process temperature. The temperature and gas atmosphere are necessary to maintain during the experiment. After the growth of the graphene it is required to cool down the reactor.

1.5.2.3 Plasma Enhanced Chemical Vapor Deposition (PECVD)

The branch of the CVD process in which chemical processes are preceded with the plasma, is known as PECVD. In PECVD process, the gaseous reactants are activated by electron impact processes in the plasma and consequently, plethora of ions, radicals and neutral species are generated. In place of high temperature growth in CVD, PECVD employs energetic reactions at low temperatures due to the formation of cold plasma by electrical ionization. The energy from the electrons is utilized to dissociate the reactive gaseous sources (source gas molecules) leading to the generation of the highly-energetic ions, and subsequently reactions between these highly-energetic ions and gaseous sources begins to proceed in the plasma. In place of neutral gas chemistry involved in CVD, the growth of vertical graphene is more complex process as the gas phase and surface reactions are influenced by the plasma source and plasma operational properties, which subsequently affect the morphology and structure of as-grown vertical graphene. Moreover, this method offers the advantage of low-temperature processing and higher growth selectivity. To sustain the plasma inside the reactor, gas pressure is kept low and source power is kept high. In the PECVD growth process, proper knowledge of the source of plasma excitation is crucially important. The various plasma sources namely, microwave (MW) plasma, radiofrequency (RF) plasma, direct current (DC) plasma, and combinations of them are used to ignite the plasma. The process operating conditions with various sources gases used in the different PECVD techniques are listed in Table 1.2.

1.5.2.3.1 DC-PECVD

DC glow discharge plasma is the simple and widely used plasma source. The earliest report on the synthesis of so called graphite like nanostructured

Table 1.2. Overview of operating parameters used in the different PECVD systems

Source of plasma excitation	Gaseous sources	Operating pressure (Pa)	Substrate temperature (^{0}C)	Flow rate (sccm)	Gas ratio	Ref.
Microwave (MW)	CH_4/Ar	17.33	450-500	-	1:8	[42]
(MW)	CH_4/N_2	5.32×10^3	1250	-	-	[43]
(MW)	CH_4/N_2	5.32×10^3	>1000	-	-	[44]
(MW)	C_2H_2/N_2/Ar	1.33×10^4	650-1050	200	0.5% of C_2H_2	[45]
(MW)	CH_4/N_2/Ar	1.33×10^4	650-1050	200	4% of C_2H_2	[45]
(MW)	CH_4/H_2	133	650-700	50	1:4	[46]
(MW)	CH_4/H_2	220	550	-	1:20	[47]
(MW)	CO/H_2	250	700	50	23:2	[48]
(MW)	CH_4/H_2	5.32×10^3	700	200	1:8	[49]
(MW)	CH_4/H_2/Ar	1.33×10^4	650	44	1:1:20	[50]
(MW)	C_2H_2/NH_3	1.33×10^3	-	-	>1:1	[51]
Inductively coupled plasma (ICP)	CH_4	12	630-830	10	-	[52]
(ICP)	CH_4/Ar	0.3	400	30.4	16.4:14	[53]
(ICP)	CH_4/H_2	12	630-830	10	>1:9	[52]
(ICP)	CH_4/H_2	2.66-53.2	600-950	-	>1:19	[54]
(ICP)	CH_4/H_2	13.33	700	10	2:3	[55]
(ICP)	C_2H_2/H_2	4-5.33	550-600	5	4:1	[55]
CCP+ICP	CH_4/H_2, CH_4/H_2, CHF_3/H_2, C_2F_6/H_2,	13.3	500	45	1:2	[56]
Direct current (DC) glow	CH_4/H_2	1×10^4	1000	-	1:9	[57]
DC glow	CH_4/H_2	9975	1000	-	8:92	[58]
DC glow	CH_4/H_2	2.66×10^4	900-1000	50	3.8% of CH_4	[59]
DC glow	CH_4/H_2/Ar	1.3	550-800	87	1:1.25:5	[60]
DC glow	CH_4/H_2O/Ar	1.05×10^5	700	1500	10% of CH_4 with 40% relative humidity	[61]

carbon by parallel plate dc glow PECVD was published by Obraztsov *et al.* [38]. DC glow PECVD synthesis of vertical graphene has been realized on two geometric setups: parallel plate and pin to plate [see Fig.1.10 & Fig.1.11)]. In parallel plate DC glow discharge method, a dc voltage is applied between planar cathode and anode across a space filled with low pressure gas for breakdown to occur. The breakdown voltage or gaseous ionization depends on the particular gas composition, pressure, and electrode distance which are described by the Paschen's law [39]. The substrate is usually placed at the cathode or serves the cathode directly. The glow discharge that is initiated can be divided into eight regions, and is arranged from cathode to anode: Aston dark space, cathode glow, cathode dark space (cathode sheath), negative glow, Faraday space, positive column, anode glow, and anode dark space [40,41]. The electric field within the cathode sheath and ions accelerated by the applied voltage are responsible for the growth and alignment of graphene sheet in the vertical direction. However, the pin to plate dc glow method is a non-uniform plasma source in which asymmetric electrodes i.e., tungsten tip and a planar substrate are used. This method results in the non-uniformity in the morphology and structure of as-grown vertical graphene sheets on the substrate [40]. The limitation of this technique is the necessity of a conductive substrate in order to maintain glow discharge.

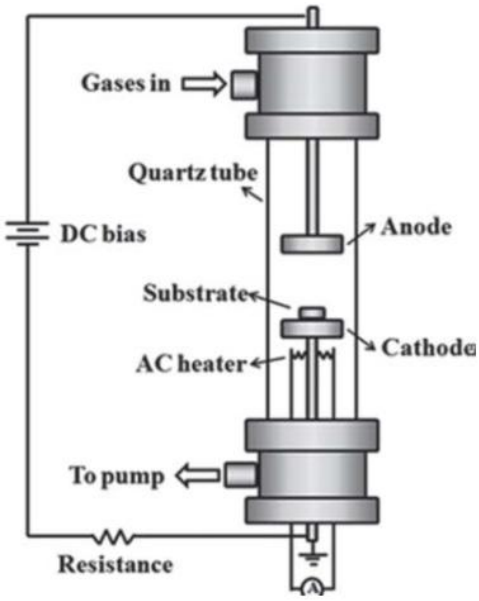

Fig. 1.10. Schematic of the parallel plate DC-PECVD system [40]

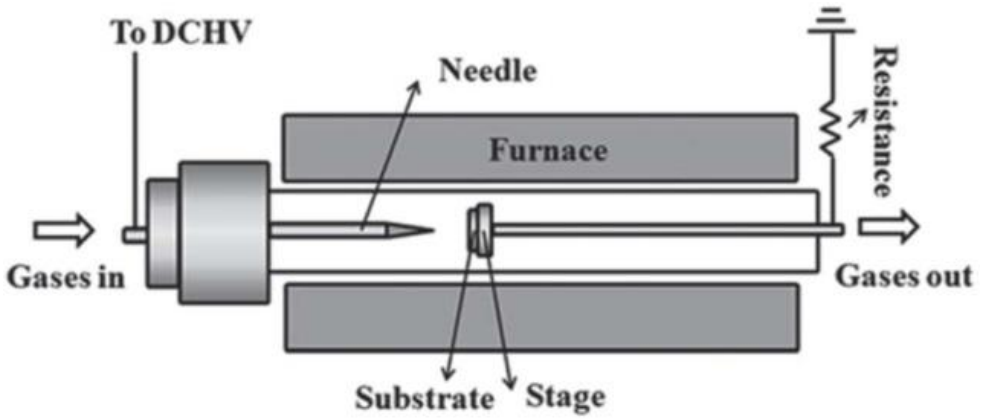

Fig. 1.11. Schematic of the pin to plate DC-PECVD system [40]

1.5.2.3.2 RF-PECVD

This is another popular source for vertical graphene synthesis which operates in the MHz frequency domain. The electron density in the RF-PECVD is much higher than the former case (DC-PECVD) and thus results in more effective ionization of the gas molecules. Generally, the energy from the RF generator is coupled to the plasma in three main modes: the evanescent electromagnetic (H) mode, the propagating wave (W) mode, and the electrostatic (E) mode [40].

In the H mode inductively coupled plasma (ICP), the energy from the RF power is coupled by an inductive coil antenna through a quartz window. The inductive circuit element can be of planar or cylindrical (helical) geometry (see Fig.1.12). The time varying electric field is passed through the RF coil antenna, as a result of which a time-varying magnetic field is generated around the coil which in turn induces azimuthal electric current inside the gas chamber and results in the breakdown of the gases and production of high density plasma.

In W mode, a propagating static magnetic field is introduced to a plasma excited by ICP with helical circuit element. This results in the generation of plasma of larger volume and high energy density.

In E mode capacitively coupled plasma (CCP), RF voltage source is connected to one of the circular electrode and the other electrode is grounded. Both the electrodes are separated by a distance of 5cm. CCP

cannot be used as an independent plasma source for the vertical graphene growth due to relatively low electron energy and density.

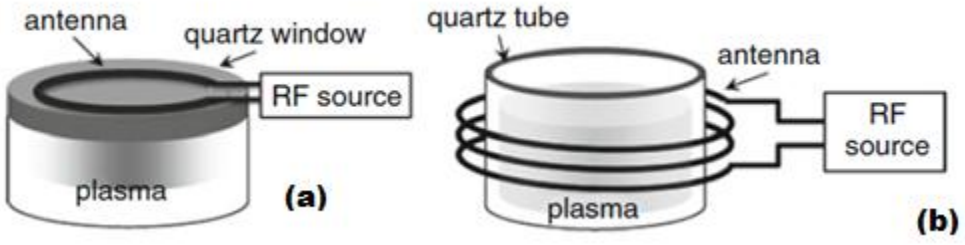

Fig. 1.12. Schematic of inductively coupled plasma with (a) planar spiral antenna and (b) helical antenna [62]

1.5.2.3.3 MW-PECVD

MW-PECVD method employs electromagnetic radiation of high frequency (2.54 GHz) to dissociate the gas molecules via high density of energetic electrons. The technique is capable of activating the electrode less gas discharges. Wu *et al.* [63] at first, reported the growth of 2D vertically aligned carbon nanostructures (carbon nanowalls) during the growth of carbon nanotubes and later synthesized carbon nanowalls on various substrates using MW-PECVD [64,65]. The Fig.1.13 shows the schematic of the MW-PECVD system used by Wu *et al.*[63]. The system is equipped with a 500 W microwave power source which is coupled to a rectangular quartz tube via traverse rectangular cavity to generate the plasma. The dc bias is applied through two parallel electrodes positioned in the longitudinal direction inside the quartz tube. No external substrate heating is provided in this system; the substrate is heated by the plasma and is determined by the power of the microwave source. Various other reports on the growth of 2D vertical graphene sheets using MPECVD are summarized in Table 1.2.

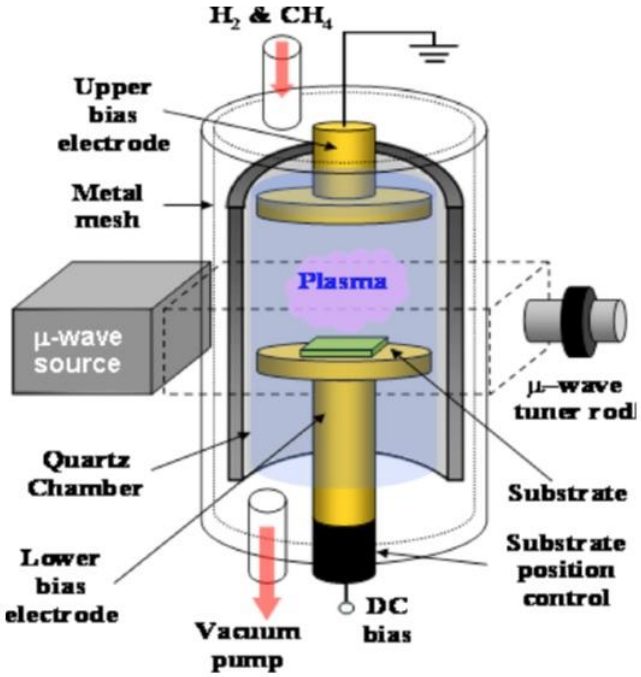

Fig. 1.13. Schematic of the MPECVD system used by Wu *et al.* [63-65].

1.6 Growth mechanism of the graphene on the catalyst-substrate surface in the reactive plasma environment

The nucleation and growth of graphene sheet in the reactive plasma environment is a complex process. The schematic Fig. 1.14 illustrates the two elementary stages during the plasma assisted catalyzed growth of graphene sheet: (a) all complex processes in the reactive plasma (plasma bulk) which has already been discussed in the Sec. 1.5.2.3 and (b) all elementary surface mechanism during deposition processes which includes following elementary stages;

(i) Transportation of the highly reactive species to the catalyst-substrate surface through plasma sheath.

(ii) Fragmentation of the predeposited metal catalyst thin film into many catalyst nanoislands [66],

(iii) Surface reactions: adsorption and dissociation of highly reactive plasma species onto the catalyst nanoislands active surface to generate building units (carbon species) and atomic radicals via various surface processes [67-75].

(iv) Nucleation stage: Diffusion of carbon species through catalyst nanoislands and formation of graphene nuclei via various intermediate processes [76].

(v) Growth stage: lateral growth of graphene which eventually turns into vertical growth under the influence of electric field induced in the plasma sheath and other intermediate forces [77].

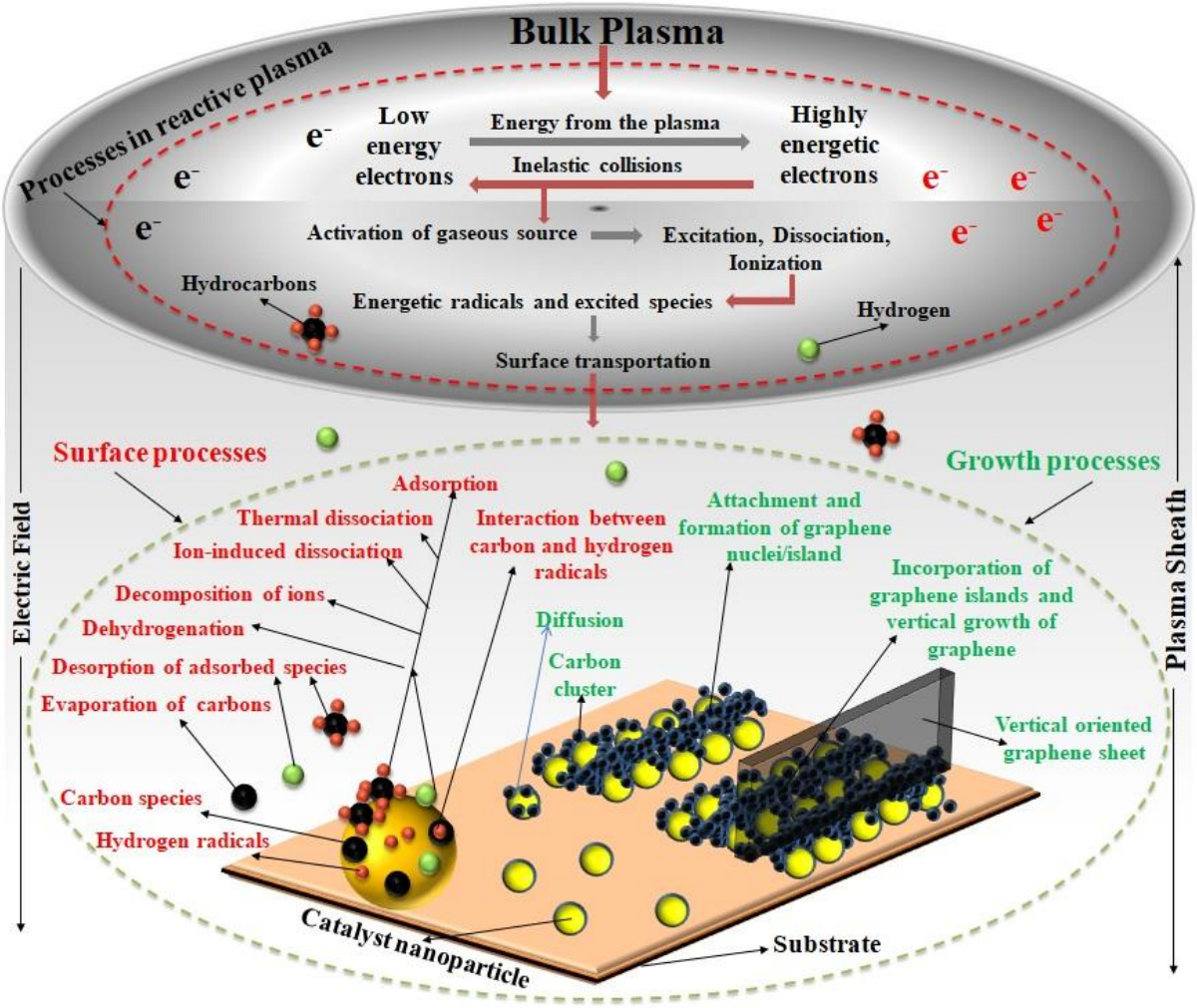

Fig. 1.14. Schematic of the nucleation and growth mechanism of the vertically oriented graphene sheet in the reactive plasma environment. The top most dark space shows the bulk plasma region and the red dotted elliptical circle shows the main elementary step wise processes (written in black) responsible plasma ignition and activation of gaseous sources in the bulk plasma region. The grey coloured region between bulk plasma and the substrate surface represents the plasma sheath region through which reactive plasma species travel under the influence of strong sheath electric field and reach to the substrate surface. The processes under the grey dotted elliptical circle includes the all surface processes over the catalyst nanoislands active surface (written in red colour) to generate building units and all growth processes (written in green colour) responsible for the growth of vertically oriented graphene sheet.

1.6.1 Formation of plasma sheath

In the plasma assisted growth of graphene sheet, the entire region of the plasma reactor can be divided into three regions namely, plasma bulk, plasma sheath and, substrate surface. Usually, bulk plasma region is highly dense that comprises the large number of electrons and positively charged species by maintaining the quasi-charge-neutrality condition i.e. number density of electrons and positively charged species are equal in magnitude. The plasma sheath region generally forms between the bulk plasma and interaction boundaries or walls of the reactor. In the graphene growth mechanism, the catalyst-substrate-surface interacts with the bulk plasma as the reactor boundary and thus plasma sheath is formed between these two regions as shown in Fig 1.15.

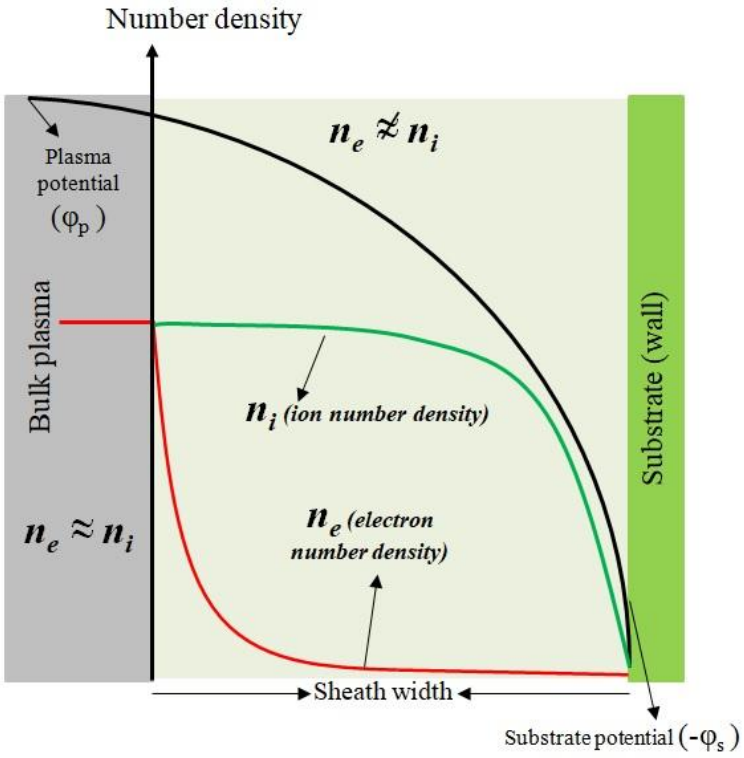

Fig. 1.15. Mechanism of the plasma sheath formation between bulk plasma region and substrate surface. The red curve shows the rapid decay of the electron density in the sheath region. The green curve shows that the sheath region mainly comprises the positively charged ions. The black curve shows that bulk plasma has almost constant potential and substrate or wall attain negative potential due to the loss of electrons near the walls.

Since electrons have much higher thermal velocity $\left(\frac{T_e}{m_e}\right)^{\frac{1}{2}}$ than ions $\left(\frac{T_i}{m_i}\right)^{\frac{1}{2}}$ (because, $m_e \ll m_i$ and $T_e \geq T_i$), thus the electrons tend to move faster than ions towards the deposition substrate which in turn develop the negative potential at the deposition substrate surface after a very short time scale, leaving the bulk plasma with the positively charged species due to which bulk plasma acquire the net positive potential. As a result, a strong electric field is set up in the region between bulk plasma region and substrate surface region which reflects electrons back into the plasma and conversely, accelerate the ions towards the deposition substrate. This non-neutral region between the plasma bulk and deposition substrate is called plasma sheath. Generally, external negative potential is also applied to the catalyst-substrate surface to induce strong electric field in the plasma sheath region.

1.6.2 Surface deposition of reactive species

Prior to the deposition of reactive plasma species, the predeposited metal catalyst thin film is pre-treated with hydrogen plasma at low temperature and low pressure. The heavy bombardment of the plasma species segregates the catalyst film into many catalyst nanoislands. The reactive plasma species (positively charged and neutral species of carbon source gas and etching gas) from the bulk plasma are accelerated towards the substrate surface through plasma sheath region and gets adsorbed on the catalyst nanoislands active surface (free surface available for the adsorption). The adsorbed species dissociate to generate building units (carbon species) and etching species (generally hydrogen radicals) via various surface processes [67-76] such as; thermal dissociation of hydrocarbons, ion induced dissociation of hydrocarbons, direct carbon flux towards the catalyst surface, loss of carbon due to interaction of neutral hydrocarbons with neutral hydrogen, carbon evaporation and ion–ion recombination i.e. hydrocarbon ion and hydrogen ion recombination as shown in Fig. 1.14.

1.6.3 Formation of graphene nuclei and growth of vertical graphene sheet

The carbon species generated on the catalyst surface diffuse and attach each other to form carbon clusters, which in turn diffuse and collide with each other to form graphene nuclei. These graphene nuclei diffuse and coalesce (or stitch) together to form large graphene islands which can also be regarded as the planar growth of the graphene sheet [77].

Once the growth of planar graphitic layers is initiated, internal stress or tensile stress is developed at the graphene island boundaries. These internal stresses may cause defects within the initial planar graphitic layer, which trigger the growth of graphene in the upward direction. Under the influence of inbuilt electric field associated with the plasma, the graphene sheet grows vertically due to continuous supply of carbon species, Moreover, the diffusion and attachment of carbon atoms at the peripherals of the growing graphitic platelets additionally contribute to the vertical graphene sheet growth as shown in Fig.1.14.

1.7 Factors influencing the morphology and growth of graphene sheet

The plasma assisted catalyzed growth mechanism of the graphene sheet includes many critical parameters that influence the resulting structure, morphology, and growth of graphene sheet. Some of them are discussed in detail below:

1.7.1 Effect of source precursors

Many extensive studies report the influence of the feedstock gas (source precursor) on the structure, morphology, and growth of graphene sheet [43,45, 47, 48, 51, 56, 78-80]. The general carbon source gases with their corresponding operating parameters and source of plasma ignition are listed in Table 1.2. Generally, three different gases carbon source gas, etching gas and carrier gas are used in the PECVD growth process. Each type of gas has different impact on the graphene sheet growth.

1.7.1.1 Impact of carbon source precursors

Most of the PECVD systems adopt the C_2H_2 and CH_4 gases (hydrocarbon gases) as the carbon source gas. Moreover, CF_4, CHF_3, and C_2F_6 (fluorocarbon gases) are some other popular carbon source gases. Some experimental reports also adopted CO_2 and CO gases as the carbon source precursors [81]. Shiji *et al.* [56] performed the comparative study for the CH_4, CF_4, CHF_3, and C_2F_6 gases diluted with hydrogen and found that graphene sheet growth rate is highest in the case of C_2F_6 followed by CHF_3, CH_4, and CF_4, respectively, and interlayer spacing is found minimum for CH_4 followed by C_2F_6, CHF_3, and CF_4, respectively. Zhu *et al.* [55] synthesized the graphene sheet with two different gas mixtures i.e. C_2H_2/H_2 and CH_4/H_2. It is found that the vertical graphene sheet grown in the C_2H_2/H_2 plasma shows the higher growth rate, more vertical orientation, and uniform height distribution as compared to CH_4/H_2 plasma. However, thickness of the CH_4/H2 grown graphene sheet is found to be less than the CH_4/H_2 grown graphene sheets.

1.7.1.2 Impact of etching gas

During the graphene sheet growth, the removal of amorphous carbon is inevitable and crucial process for the high quality growth. Hydrogen radicals (atomic hydrogen), oxygen radicals (atomic oxygen), highly excited nitrogen species and atomic fluorine are the most commonly found etchants in the growth atmosphere [44-46, 47-52, 57, 60, 82, 83]. It is reported that the NH_3 is considered as the most effective source of atomic hydrogen rather and H_2. Kondo *et al.* [80] introduced the small amount of O_2 in the C_2F_6/H_2 plasma and found the much enhanced growth of vertical graphene sheet due to the more effective control over the growth of amorphous carbon layer.

Shang *et al.* [44] synthesized the vertically oriented graphene sheets using CH_4/N_2 plasma and CH_4/H_2 plasma, and suggested that the nitrogen is better etching agent than the hydrogen for the removal of unwanted amorphous carbon. Meanwhile, insertion of nitrogen in the growth

atmosphere leads to the incorporation of nitrogen species into the growing graphene lattice which in turn affects the morphology, structure, and properties of the resulting graphene sheet (nitrogen doped graphene sheet) [84].

1.7.1.3 Role of carrier gas

In the PECVD process, the gaseous sources are activated by the electron impact reactions between electrons and gaseous reactants. Thus, it is necessary to preserve the electron energy for the production of the stable plasma. One way to retain the electron energy is to minimize the inelastic collisions responsible for the electron energy loss. The Argon (Ar) has high excitation and ionization potential [85]. These features of Ar gas make it to interact with electron via elastic collisions and make electrons capable to increase the ionization rate of the system. Moreover, the chemical reactions between Ar atoms and hydrocarbon species lead to the formation of carbon dimmers (C_2) [45] which increase the number of building units on the catalyst nanoislands surface, consequently increases the degree of graphitization.

1.7.2 Effect of gas proportion

The gas ratio or flow rate of the sources gases is the preliminary parameter to control the growth, structure, and morphology of the vertically oriented graphene sheet. It was reported by Wu *et al.* [46] that by suitably increasing the hydrogen gas ratio in CH_4/H_2, different nanostructures deposits are obtained. Wang *et al.* [52] studied the effect of CH_4 flow rate on the size and density of the vertical graphene sheet and found the reduction in lateral size and increase in number density of the vertical graphene sheet when CH_4 flow rates is raised in the plasma. It is important to note that the optimum gas ratio to control the growth characteristics of the graphene or any other carbon based nanostructure strictly depend on the many PECVD conditions. Thus it is not justified to mention the exact range for the quality growth of the nanostructure.

1.7.3 Effect of temperature

As already discussed above, the PECVD growth of nanostructure is low temperature process because thermal energy required in dissociating the source species to generate building species is provided by the plasma that contains highly energetic electrons and other activated positively charged and neutral species (molecules and radicals). The substrate temperature is one of the most important parameter in the PECVD technique as it directly affects the surface processes (surface reactions over the catalyst nanoislands active surface) to generate building species [86]. Generally, external heating is required in most of the PECVD techniques to provide the sufficient energy to the reactive species for their surface dissociation. However, MW-PECVD technique does not require any external substrate heating. As name suggested, microwaves have primary heating property which leads to the substrate heating. Moreover, RF-PECVD technique also has ability to generate high energy and high density plasma which also leads to substrate heating, whereas, DC-PECVD technique rely on the external heating due to the limited input energy for glow discharge. The substrate temperature not only affects the surface dissociation rate of the reactive radicals but also influence the relative etching of the substrate surface and nanostructure [59]. It is reported that the high substrate heating leads to the higher growth of the graphene sheet and increase in the number density of graphene nuclei. However, it is also believed that the defects densities over the graphene sheet increases with increase in substrate heating [52, 55, 87].

1.7.4 Effect of substrate

Many experimental studies report the plasma assisted growth of vertical graphene over the catalyst free and catalyst coated substrate surface (planar substrate). When catalyst free substrate is subjected to reactive plasma, the defects are produced over the substrate surface as a result of substrate etching via highly energetic ion bombardment. These defects provide the nucleation sites for dissociation of the reactive species and generation of building units, and also provide the grain boundaries for the vertical growth of the graphene sheets. However, catalyst coated substrate require plasma pre-treatment for the

segregation on catalyst film into catalyst nanoislands and the vertical growth of graphene sheets over these nanoislands is more pronounced as compared to the former case discussed above. Moreover, growth of graphene over the CNT substrate surface leads to the utilization of the field emission sites as compared to the growth over the planar substrate.

1.7.5 Effect of pressure

Pressure is the one of the most essential PECVD process parameter which affects the plasma characteristics and consequently, affects the PECVD growth processes. The gas pressure affects the mean free path of the electrons (i.e., mean free path is inversely proportional to the gas pressure) which directly influence the temperature, energy and density of electrons in the bulk plasma. The gas pressure of the plasma reactor must be kept in the optimum range. At very low pressure, mean free path of the electron can exceed the dimension of the plasmas system which leads to the sufficient loss of density and energy of electrons However, at high pressure, mean free path becomes smaller which increases the collisions in the plasma and ultimately leads to the loss of energetic electrons. Thus, high energy is required to stabilize the plasma at very low or high gas pressures. It is reported that the growth of graphene sheet is high at reduced gas pressures [88, 89].

1.7.6 Effect of input plasma power

Apart from above discussed operating parameters, input plasma power is also one of the most important PECVD process parameter. The stability and density of the plasma strongly depend on the input power. The sufficient energy to activate the gaseous sources via electron impact reactions is provided by the input power. Collison *et al.* [90] experimental found the effect of input plasma power on the electron density and electron temperature which are the primary scale for the measurement of the stability and strength of the plasma. It is observed that when input plasma power is raised, the electron density and electron temperature in the plasma increases. Srivastava *et al.*[91], Cho *et al.* [89], Nang and Kim [92], and Ghosh *et al.* [93] found that the input plasma

power greatly influence the growth characteristics of the vertical graphene sheet in the reactive plasma environment.

1.8 Objectives and organization of the thesis

In view of the literature and studies on the growth of graphene sheet in plasma and field emission from them, the proposed thesis aims to study the effect of plasma parameters on growth and field emission characteristics of the graphene sheet. The effect of plasma parameters such as number densities and temperatures of ions and electrons on the growth of graphene sheet (without catalyst) in plasma environment is studied in the present thesis. In addition, the catalyst-assisted growth mechanism of the two-dimensional vertical graphene sheet in plasma medium is discussed in detail and the effect of plasma parameters, process parameters namely, input power and total gas pressure, different gas mixtures, and doping on the growth and field emission characteristics of the vertical graphene sheet is investigated in the present thesis. The plasma-assisted growth of graphene sheet on CNT as a substrate is also studied in the present thesis. The entire work in the present thesis is divided into eight chapters.

- **Chapter 2** describes the growth of the graphene sheet (without catalyst) in the plasma environment through condensation process. A theoretical model comprising the charge neutrality, the particle and energy balance of all the plasma species i.e., charged and neutral species is developed to study how the growth (or thickness) of graphene sheet is affected by changing the plasma characteristics, i.e., by tuning the plasma parameters (electron density and temperature, ion density and temperature), parameters related with the different type of plasma species i.e., negative ions, and by introduction of nitrogen doping element in the plasma. By obtaining the variation of the thickness of the graphene sheet with plasma parameters, nitrogen doping and relative number density of negative ions, the consequent variations in the field enhancement factor of the graphene sheet is estimated.

- **Chapter 3** includes the modeling for the catalyst-assisted growth of graphene sheet in the presence of plasma. The model developed accounts for the charging rate of the graphene sheet; number density of electrons, ions,

and neutral atoms; various elementary processes on the surface of the catalyst nanoparticle; surface diffusion and accretion of ions; and formation of carbon-clusters and large graphene islands. The effect of various plasma parameters and rf power on dimensions i.e., height and thickness and further their repercussions on the field enhancement factor of the graphene sheet is examined.

- **Chapter 4** presents a theoretical model to understand the growth and field emission characteristics of the graphene sheet on account of effect of doping of heteroatoms such as nitrogen and boron in a PECVD process. The charging rate of the graphene sheet, kinetics of the electrons, ions, and neutrals; adsorption, surface diffusion, and accretion of carbon species via several processes on the catalyst surface; formation of clusters and graphene islands; vertical growth of graphene sheet in the presence of doping species are incorporated in the model to study the effect of nitrogen and boron doping on the dimensions, i.e., thickness and height of the graphene sheet and further the field emission properties of the graphene sheet are proposed on the basis of the results obtained.

- **Chapter 5** presents a multiscale theoretical model to study the effect of different gas mixtures on the nucleation and growth kinetics of a graphene nanosheet in the reactive low-temperature plasma environment. The present model describes the key processes involved in the catalyst-aided growth of vertical graphene sheet in its entirety, from formation of carbon clusters, nucleation and growth of graphene islands and growth of vertical graphene sheet in the presence of different gas mixtures. In addition, the present model considers the kinetics of various plasma species, i.e., electrons, ions, and neutrals, charging rate of the graphene sheet, number density profiles of carbon clusters and graphene islands, growth rate equation of graphene islands, and vertical graphene sheet. The numerical solutions of the model are used to investigate the consequence of different carbon feedstock gases, i.e., C_2H_2, CH_4, and CF_4 on the graphene sheet growth parameters (e.g., graphene sheet dimensions, i.e., height and thickness, growth rate of carbon species and etchant species on the catalyst surface, and graphene sheet

nucleation density) with time and further its repercussions on the field enhancement factor of the graphene sheet.

- **Chapter 6** describes the multistage numerical model comprising the plasma kinetics and surface deposition sub-models to study the influence of PECVD process parameters on the plasma composition and characteristics and to understand the insights of the evolution of growth characteristics of vertically oriented graphene sheets (VOGS) grown in the $Ar+H_2+C_2H_2$ reactive plasma environment. The spatial distributions of temperature and densities of electrons, positively charged, and neutral species in the plasma reactor are examined using inductively coupled plasma module (ICP) of COMSOL Multiphysics 5.2 modeling suite. The numerical data from the computational plasma model are fed as the input parameters for the surface deposition model to control the growth characteristics of the plasma grown VOGS over the catalyst-substrate surface.

- **Chapter 7** presents the theoretical model to describe the plasma-assisted nucleation and growth kinetics of vertical graphene (VG) sheet on the CNT surface. The model accounts the formalization of charge separation region i.e., plasma sheath between the bulk plasma and substrate surface in one-dimension along with the kinetics of all the plasma species (neutrals, positively charged species, and electrons), rate of charge accumulation on the graphene sheet surface, and growth of VG sheet on the CNT surface owing to defects generation and various processes on the CNT surface. Using the model, we demonstrated that variations in the plasma enhanced chemical vapor deposition (PECVD) process control parameters such as the total gas pressure, input power, and substrate bias can be used for significant variation in the plasma composition and characteristics that in turn control the ion bombardment and generation of carbon species on the CNT surface, and consequently tune the VG sheet growth characteristics such as, height, thickness and number density profiles of VG sheet on the CNT surface.

- **Chapter 8** summarizes the conclusion and future scope of the present work. Moreover, the conclusions made in the present study are not only valid for 2D graphitic nanostructures but can also be extended to investigate the

growth characteristics of the other graphitic nanostructures in the reactive plasma environment.

References

[1] A. Alagarasi, Chapter-Introduction to nanomaterials (2011).

[2] S. Iijima, Nature **354**, 56 (1991).

[3] A. H. Castro Neto, F. Guinea, N. M. R. Peres, K. S. Novoselov, and A. K. Geim, Rev.of Mod. Phys. **81**, 109 (2009).

[4] J. Liu, L. Cui, D. Losic, Acta Biomater. **9,** 9243 (2013).

[5] J. H. Warner, Y. Fan, A. W. Robertson, K. He, E. Yoon, and G. D. Lee, Nano Letters **13**, 4937 (2013).

[6] J. C. Meyer, A. K. Geim, M. I. Katsnelson, K. S. Novoselov, T. J. Booth, and S. Roth, Nature **446**, 60 (2007).

[7] J. C. Meyer, A. K. Geim, M. I. Katsnelson, K. S. Novoselov, D. Obergfell, S. Roth, C. Girit, and A. Zettl, Solid State Commun. **143**, 101 (2007).

[8] R. R. Haering, Can. J. Phys. **36**, 352 (1958).

[9] I. W. Frank, D. M. Tanenbaum, A. M. Van der Zande, and P. L. McEuen, J. Vac. Sci. Technol. B **25**, 2558 (2007).

[10] R. Ansari, B. Motevalli, A. Montazeri, and S. Ajori, Solid State Commun. **151**, 1141 (2011).

[11] A. K. Geim, K. S, Novoselov, Nature Materials. **6**, 183 (2007).

[12] P. M. Ostrovsky, I. V. Gornyi, and A. D. Mirlin, Phys. Rev. B **77**, 195430 (2008)

[13] H. Y. Mao, Y. H. Lu, J. D. Lin, S. Zhong, A. T. S. Wee, and W. Chen, Prog. Surf. Sci. **88**, 132 (2013).

[14] Z.-Y. Ong, E. Pop , J. Appl. Phys. **108** , 103502 (2010).

[15] Z. Sun , Z. Yan, J. Yao , E. Beitler, Y. Zhu, and J. M. Tour, Nature **468**, 549 (2010).

[16] Z. Wang, C. Tang, R. Sachs, Y. Barlas, and J. Shi, Phys. Rev. Lett. **114**, 016603 (2015).

[17] N. Soin, S. S. Roy, S. Roy, K. S. Hazra, D. S. Misra, T. H. Lim, C. J. Hetherington, and J. A. McLaughlin, J. Phys. Chem C **115,** 5366 (2011).

[18] Z. Chen, Y.-M. Lin, M. J. Rooks, P. Avouris, Physica E **40** 228 (2007).

[19] W. Lei, C. Li, M. T. Cole, K. Qu, S. Ding, Y. Zhang, J. H. Warner, X. Zhang, B. Wang, and W. I. Milne, Carbon **56,** 255 (2013).

[20] T. Matsumoto, T. Nakamura, Y. Neo, H. Mimura, and M. Tomita, *Field Emission from Graphene Nanosheets*, In Graphene Simulation. InTech (2011).

[21] Z. Bo, D. Hu, J. Kong, J. Yan and K. Cen, J. Power Sources **273**, 530 (2015).

[22] Z. Bo, S. Mao, Z. J. Han, K. Cen, J. Chen, and K. Ostrikov, Chem. Soc. Rev**. 44,** 2108 **(**2015).

[23] X. Xiao, P. Liu, J. S. Wang, M. W. Verbrugge, and M. P. Balogh, Electrochem. Commun. **13**, 209 (2011).

[24] H. Kim, Z. Wen, K. Yu, O. Mao, and J. Chen, J. Mater. Chem. **22,** 15514 (2012).

[25] S. Jin, N. Li, H. Cui, and C. Wang, Nano Energy **2**, 1128 (2013).

[26] Y. H. Wu, T. Yu, and Z. X. Shen, J. Appl. Phys. **108**, 071301 (2010).

[27] Md. S. A. Bhuyan, Md. N. Uddin, Md. M. Islam, F. A. Bipasha, S. S. Hossain, Int Nano Lett **6**, 65 (2016).

[28] Y.B. Zhang, J.P. Small, W.V. Pontius, and P. Kim, Appl. Phys. Lett. **86**, 073104 (2005).

[29] K. S. Novoselov, A. K. Geim, S. V. Morozov, D. Jiang, Y. Zhang, S. V. Dubonos, I. V. Grigorieva, and A. A. Firsov, Science **306**, 666 (2004).

[30] K. S. Novoselov and A. H. Castro Neto, Phys. Scr. **T146,** 014006 (2012).

[31] W. Choi, I. Lahiri, R. Seelaboyina, and Y. S. Kang, Crit. Rev. Solid State Mater. Sci. **35**, 52 (2010).

[32] S. Horiuchi, T. Gotou, M. Fujiwara, T. Asaka, T. Yokosawa, and Y. Matsui, Appl. Phys. Lett. **84**, 2403 (2004).

[33] H. Bai, C. Li , and G. Shi, Adv. Mater. **23**, 1089 (2011).

[34] See graphenewiki.org/graphene/graphene-platform-supplies-the-worlds-largest-single-layer-single-crystal-graphene-samples

[35] A. J. Van Bommel, J.E. Crombeen, and A. Van Tooren, Surf. Sci. **48**, 463 (1975).

[36] W. De Heer, *The development of epitaxial graphene for 21st century electronics*; ar Xiv: 1012. 1644v1

[37] W. M. Merchan, A. V. Saveliev, L. Kennedy , and W. C. Jimenez, Progress in Energy and Combustion Science **36,** 696 (2010).

[38] A. N. Obraztsov, A. P. Volkov, K. S. Nagovitsyn, K. Nishimura, K. Morisawa, Y. Nakano and A. Hiraki, J. Phys. D: Appl. Phys. **35**, 357 (2002).

[39] F. Paschen, Ann. Phys. Chem. **273**, 69 (1889).

[40] Z. Bo, Y. Yang, J. Chen, K. Yu, J. Yan and K. Cen, Nanoscale **5**, 5180 (2013).

[41] M. Lieberman and A. Lichtenberg, *Principles of Plasma Discharges and Materials Processing* (John Wiley & Sons, Inc., New Jersey, 2005).

[42] Z. P. Wang, M. Shoji and H. Ogata, Appl. Surf. Sci. 257, 9082 (2011).

[43] N. Soin, S. S. Roy, T. H. Lim and J. A. D. McLaughlin, Mater. Chem. Phys. **129**, 1051 (2011).

[44] [N. G. Shang, P. Papakonstantinou, M. McMullan, M. Chu, A. Stamboulis, A. Potenza, S. S. Dhesi and H. Marchetto, Adv. Funct. Mater. **18**, 3506 (2008).

[45] K. Teii, S. Shimada, M. Nakashima and A. T. H. Chuang, J. Appl. Phys. **106**, 084303 (2009).

[46] Y. H. Wu, P. W. Qiao, T. C. Chong and Z. X. Shen, Adv. Mater. **114**, 64 (2002).

[47] Y. Zhang, J. Du, S. Tang, P. Liu, S. Deng, J. Chen and N. Xu, Nanotechnology **23**, 015202 (2012).

[48] T. Mori, M. Hiramatsu, K. Yamakawa, K. Takeda and M. Hori, Diamond Relat. Mater.**17**, 1513 (2008).

[49] A. Malesevic, R. Vitchev, K. Schouteden, A. Volodin, L. Zhang, G. Van Tendeloo, A. Vanhulsel and C. Van Haesendonck, Nanotechnology **19**, 305604 (2008).

[50] L. Y. Zeng, D. Lei, W. B. Wang, J. Q. Liang, Z. Q. Wang, N. Yao and B. L. Zhang, Appl. Surf. Sci. **254**, 1700 (2008).

[51] A. T. H. Chuang, B. O. Boskovic and J. Robertson, Diamond Relat. Mater. **15**, 1103 (2006).

[52] J. J. Wang, M. Y. Zhu, R. A. Outlaw, X. Zhao, D. M. Manos, and B. C. Holloway, Carbon **42**, 2867 (2004)

[53] M. Hiramatsu, K. Shiji, H. Amano and M. Hori, Appl. Phys. Lett. **84**, 4708 (2004).

[54] M. Zhu, J. Wang, B. C. Holloway, RA. Outlaw, X. Zhao, K. Hou, V. Shutthanandan, and D. M. Manos, Carbon **45**, 2229 (2007).

[55] M. Y. Zhu, R. A. Outlaw, M. Bagge-Hansen, H. J. Chen, and D. M. Manos, Carbon **49,** 2526 (2011).

[56] K. Shiji, M. Hiramatsu, A. Enomoto, M. Nakamura, H. Amano, and M. Hori, Diamond Relat. Mater. **14**, 831 (2005).

[57] A. N. Obraztsov, A. A. Zolotukhin, A. O. Ustinov, A. P. Volkov, Y. Svirko and K. Jefimovs, Diamond Relat. Mater. **12**, 917 (2003).

[58] N. Jiang, H. X. Wang, H. Zhang, H. Sasaoka, and K. Nishimura, J. Mater. Chem. **20**, 5070 (2010).

[59] V. A. Krivchenko, V. V. Dvorkin, N. N. Dzbanovsky, M. A. Timofeyev, A. S. Stepanov, A. T. Rakhimov, N. V. Suetin, O. Y. Vilkov, and L. V. Yashina, Carbon **50**, 1477 (2012).

[60] S. Kurita, A. Yoshimura, H. Kawamoto, T. Uchida, K. Kojima, M. Tachibana, P. Molina-Morales, and H. Nakai, J. Appl. Phys. **97**, 104320 (2005).

[61] Z. Bo, K. H. Yu, G. H. Lu, P. X. Wang, S. Mao and J. H. Chen, Carbon **49**, 1849 (2011).

[62] M. Hiramatsu, M. Hori, *Carbon Nanowalls* (Springer, Vienna, 2010)

[63] Y. Wu, P. Qiao, T. Chong, and Z. Shen, Adv. Mater. **14**, 64, (2002).

[64] Y. H. Wu, B. J. Yang, B. Y. Zong, H. Sun, Z. X. Shen, and Y. P. Feng, J. Mater. Chem. **14**, 469 (2004).

[65] Y. H. Wu and B. J. Yang, Nano Lett. **2**, 355 (2002).

[66] K.Ostrikov, *Plasma Nanoscience* (John Wiley & Sons, 2008).

[67] I. B. Denysenko, S. Xu, J. D. Long, P. P. Rutkevych, N. A. Azarenkov, and K. Ostrikov, J. Appl. Phys. **95**, 2713 (2004).

[68] Ch. Deschenaux, A. Affolter, D. Magni, Ch. Hollenstein and P. Fayet, J. Phys. D: Appl. Phys. **32**, 1876 (1999).

[69] H. Mehdipour, K. Ostrikov, and A.E. Rider, Nanotechnology **21**, 455605 (2010).

[70] R. Gupta, S.C. Sharma, and R. Sharma, Plasma Sources Sci. Technol. **26**, 024006 (2017).

[71] Z. Marvi, S. Xu, G. Foroutan, and K. Ostrikov, Phys. Plasmas **22**, 013504 (2015).

[72] N.V. Mantzaris, E. Gogolides, A.G. Boudouvis, A. Rhallabi, and G. Turban, J. Appl. Phys. **79**, 3718 (1996).

[73] B. B. Wang, K. Ostrikov, T. van der Laan, K. Zheng, J. J. Wang, Y. P. Yan and X. J. Quan, J. Mater. Chem. C **1**, 7703 (2013).

[74] O. A. Louchev, C. Dussarat, and Y. Sato, J. Appl. Phys. **86**, 1736 (1999).

[75] I. Denysenko and N.A. Azarenkov, J. Phys. D: Appl. Phys. **44**, 174031 (2011).

[76] H. Mehdipour and K. Ostrikov, ACS Nano **6**, 10276 (2012).

[77] S. Ghosh, K. Ganesan, S.R. Polaki, T. Mathews, S. Dhara, M. Kamruddin, A.K. Tyagi, Appl. Surf. Sci.**349,** 576 (2015).

[78] G. Sato, T. Morio, T. Kato and R. Hatakeyama, Jpn. J. Appl. Phys. **45**, 5210 (2006).

[79] M. Cai, R. A. Outlaw, R. A. Quinlan, D. Premathilake, S. M. Butler, and J. R. Miller, ACS Nano **8**, 5873 (2014).

[80] S. Kondo, S. Kawai, W. Takeuchi, K. Yamakawa, S. Den, H. Kano, M. Hiramatsu, and M. Hori, J. Appl. Phys. 106, 094302 (2009).

[81] S. Mori, T. Ueno and M. Suzuki, Diamond Relat. Mater. **20**, 1129 (2011).

[82] S. Kondo, M. Hori, K. Yamakawa, S. Den, H. Kano, and M. Hiramatsu, J. Vac. Sci. Technol. B Microelectron. Nanometer Struct. Process. Meas. Phenom. **26**, 1294 (2008).

[83] A. Stamboulis, A. Potenza, S. S. Dhesi, and H. Marchetto, Adv. Funct. Mater.**18**, 3506 (2008).

[84] W. Takeuchi, M. Ura, M. Hiramatsu, Y. Tokuda, H. Kano, and M. Hori, Appl. Phys. Lett. **92**, 213103 (2008).

[85] C. Yamabe, S. J. Buckman, and A. V. Phelps, Phys. Rev. A: At.,Mol., Opt. Phys. **27**, 1345 (1983).

[86] V. Krivchenko, P. Shevnin, A. Pilevsky, A. Egorov, N. Suetin, V. Sen, S. Evlashin and A. Rakhimov, J. Mater. Chem. **22**, 16458 (2012).

[87] [87] B. P. C. Rao, R. Maheswaran, S. Ramaswamy, O. Mahapatra, C. Gopalakrishanan, and D. J. Thiruvadigal, Full. Nano. Carb. Nano. **17**, 625 (2009).

[88] W. Takeuchi, H. Sasaki, S. Kato, S. Takashima, M. Hiramatsu, and M. Hori, J. Appl. Phys. **105**, 113305 (2009)].

[89] H. J. Cho, H. Kondo, K. Ishikawa, M. Sekine, M. Hiramatsu, and M. Hori, Carbon **68**, 380 (2014).

[90] W. Z. Collison, T. Q. Ni, and M. S. Barnes, J. Vac. Sci. Technol. A **16**,100 (1998).

[91] S. K. Srivastava, A.K. Shukla, V.D. Vankar, V. Kumar, Thin Solid Films **492**, 124 (2005).

[92] L. V. Nang and E.-T. Kim, J. Electrochem. Soc. **159**, K93 (2012).

[93] S. Ghosh, S. R. Polaki, N. Kumar, S. Amirthapandian, M. Kamruddin, and K. Ostrikov, Beilstein J. Nanotechnol. **8**, 1658 (2017).

2

Impact of plasma on the thinning of graphene sheet

2.1 Brief outline of the chapter

The present chapter describes the growth of graphene sheet (without catalyst) in the plasma environment through condensation process. A theoretical model comprising the charge neutrality, particle and energy balance equations of all the plasma species i.e., charged and neutral species is developed to study the influence of plasma parameters (number density and temperature of electrons and ions), nitrogen doping, and negative charged ions in plasma on the growth of embryonic graphene sheet in plasma environment is developed.

2.2 Introduction

The growth of graphene nanosheets in the presence of plasma atmosphere has gained a heightened interest in recent years. Subsequently, extensive studies have been carried out to control the morphology, growth rate, dimensions, and structure of graphene by effectively tuning the plasma parameters [1,2], growth time [3], input power [4], substrate temperature [5,6], and plasma composition [6-8].

Yu *et al*. [1] have reported a patterned synthesis of vertical graphene nanosheets using plasma-enhanced chemical vapor deposition (PECVD) and suggested that the electric field distribution above the substrate material plays a key role in the graphene coverage. Malesevic *et al*. [2] have presented a possible route for the mass production of freestanding few layer graphene (FLG) by means of microwave PECVD. In this experiment, the average thickness of the FLG flakes grown by above method was between 4 and 6 atomic layers. This technique is most promising since it does not rely on the use of catalyst which

implies that any material that can withstand elevated temperature can be used as substrates. It was also observed that growth process slows down and the average dimensions of the flakes decrease as the hydrogen gas flow increases relative to methane flow, keeping all the other parameters constant.

Soin *et al.* [3] have grown vertically aligned few layered graphene (FLG) nanoflakes on Si (100) substrate by microwave PECVD method. They suggested that the growth of FLGs proceeds via the nucleation of highly stressed nanocrystalline graphite layers. They also studied the time dependent growth of FLG nanoflakes.

Kim *et al.* [4] have synthesized single-layer graphene on Cu foil in the absence of H_2 flow by PECVD. In this case, they have observed that the average grain size is ~0.4 μm when the plasma power is 10 W, but it sharply increases to ~3 μm when the plasma power is increased to 50 W. It also sharply decreased to ~0.8 μm at a plasma power of 170 W. This result is due to the increased amount of hydrogen species at higher plasma power. They have experimentally demonstrated that as plasma power increases there is reduction in the graphene thickness (cf. Fig. 2a to 2c of Kim *et al.* [4]). It is found that the plasma plays an important role in the graphene growth by generating hydrogen species during the decomposition process of methane into active species. The amount of hydrogen species increases with the plasma power, resulting in a drastic change of grain size. When the plasma power is high enough, good-quality graphene with the carrier mobility of ~3,200 $cm^2V^{-1}s^{-1}$ can be produced at 830 °C by using methane as both carbon and hydrogen sources.

French *et al.* [5] have prepared carbon nanosheets using radio frequency PECVD and studied the structure of graphene sheets at different substrate temperatures. Their results suggest that the average number of graphene layers reduces significantly with increase of temperature. Wang *et al.* [6] have used microwave plasma to synthesize single- or double-layer graphene sheets on copper foils using a solid carbon source, polymethylmetacrylate. They have studied the effect of substrate temperature on graphene quality and observed the reduction of defects at elevated temperature. In addition, they also synthesised

nitrogen doped graphene sheets by treating graphene sheets in nitrogen/hydrogen plasma treatment.

Shen *et al.*[7] have studied structural changes of few-layer graphene sheets induced by CF_4 plasma treatment optical microscopy and Raman spectroscopy. Their experimental results suggest a thickness reduction of few-layer graphene sheets subjected to prolonged CF_4 plasma treatment while plasma treatment with short time only leads to fluorine functionalization on the surface layer by formation of covalent bonds. Seo *et al.*[8] have reported that the thickness of the graphene sheet reduces upon addition of nitrogen to the $CH_4/Ar/H_2$ gas mixture.

Sodha *et al.* [9] in their theoretical model have investigated the growth of embryonic dust particles in complex plasma and found that the radius of the embryonic dust grains decreases with the number density of dust particles.

Graphene sheets grown via PECVD are reported to exhibit excellent field emission characteristics. Malesevic *et al.* [10] experimentally studied the field emission from vertically aligned FLG and found that the graphene can be characterized by turn on fields as low as 1V/ μm and the field amplification factor up to several thousand has been reported.

Soin *et al.* [11] have also synthesized vertically aligned FLG on bare Si-substrates by MWPECVD method and showed significant improvement in field emission characteristics of FLG by nitrogen plasma treatment. They reported field enhancement factors for pristine FLGs to be 815 and 4710 for the low field and high field regions, respectively and for N-doped graphene, the field enhancement factor increases to approximately 3120 and 17350 for the low field and high field regions, respectively.

Palnitkar *et al.* [12] have studied the field emission of undoped graphene films and of those doped with nitrogen and boron doped films. The N-doped graphene shows the lowest turn-on field of 0.6 V/μm, corresponding to emission current density of 10 $\mu A/cm^2$.

2.3 Model

We consider plasma containing electrons, positively charged ions and neutrals of carbon, hydrogen, and nitrogen denoted as species of type A, B, and C respectively, negatively charged ions (SF_6^-) and graphene sheet is grown in the presence of plasma. The positively charged ions are assumed to be singly ionized. The growth of graphene sheet in plasma environment without catalyst can occur by many ways, namely, cluster formation, nucleation, coagulation, and growth of embryonic graphene sheet by condensation. However, in the present investigation, we consider the embryonic growth of graphene sheet by condensation in the plasma and the present model does not involve the kinetics for the formation of embryonic graphene sheet (i.e., pre-grown graphene sheet) as we aim to explore how the growth (or thickness) of graphene sheet is affected by changing the plasma characteristics, i.e., by tuning the plasma parameters (electron density and temperature, ion density and temperature), parameters related with the different type of plasma species i.e., negative ions, and by introduction of nitrogen doping element in the plasma.

The present model accounts the charge neutrality equation, particle balance and energy balance equations all the plasma species that incorporates the various processes i.e., (i) ionization of neutral atoms, (ii) electron-ion recombination, (iii) accumulation of plasma species on the graphene sheet surface, and (iv) elastic collision among plasma species (collision between ionic species is neglected) and with the graphene sheet surface

Following Sodha *et al.*[9], the surface potential V_s on the surface of graphene sheet can be estimated by equating the number of electrons and number of ions striking on the graphene surface.

$$n_e\left(\frac{T_e}{m_e}\right)^{\frac{1}{2}}\exp\left(-\frac{eV_s}{k_BT_e}\right)+X=\left(1+\frac{eV_s}{k_BT_i}\right)\left[n_{iA}\left(\frac{T_i}{m_{iA}}\right)^{\frac{1}{2}}+n_{iB}\left(\frac{T_i}{m_{iB}}\right)^{\frac{1}{2}}\right], \quad (2.1)$$

where n_e, T_e are the number density and temperature of electron, k_B is the Boltzmann's constant, e is the electronic charge, T_i is the ion temperature, n_{ij}

Neha Gupta
Delhi Technological University, Delhi, India

and m_{ij} are the number density and mass of ion *j* (where *j* refers to A and B type of species considered in the model). $X\left(=n_{-}\left(\frac{T_e}{m_{-}}\right)^{\frac{1}{2}}\right)$ is accounted when negatively charged species are considered in the plasma; where $n_{-}\left(=\varepsilon_r n_p\right)$ is the number density of negatively charged ions, ε_r is the relative density of negatively charged ions, $n_p=(n_{iA}+n_{iB})$, and m_{-} is the mass of negatively charged ion.

2.3.1 Charge neutrality equation

$$Zn_{gn}+\sum_{j}^{A,B,C} n_{ij}=n_e+n_{-}, \tag{2.2}$$

where Z is the charge on graphene sheet surface, n_{gn} is the number density of graphene sheet, and *j* refers to A, B, and C type of ions considered in the model. Ions of type C and the term n_{-} are taken into account when doping species and negatively charged species are considered in the plasma, respectively.

2.3.2 Charging of graphene

This equation describes the charge developed on the graphene sheet due to accretion of electrons and positively charged ions on the surface of graphene.

$$\frac{dZ}{d\tau}=\sum_{j}^{A,B,C} n_{ijgn}-\gamma_e n_{egn}, \tag{2.3}$$

where $n_{egn}=(lt+ht+lh)\left(\frac{2\pi k_B T_e}{m_e}\right)^{\frac{1}{2}} n_e \exp\left[-\frac{eV_s}{k_B T_e}\right]$ is the electron collection current at the graphene sheet surface and γ_e is the sticking coefficient of electron; *l*, *t*, and *h* are the length, thickness, and height of the graphene sheet, respectively. n_{ijgn} is the ion collection current at the graphene

sheet surface and j refers to either A, B or C type of positively charged ion considered in the model. Ions of type C are taken into account when doping species are considered in the plasma.

$$n_{ijgn} = (lt + ht + lh)\left(\frac{2\pi k_B T_i}{m_j}\right)^{\frac{1}{2}} n_{ij}\left\{\frac{2}{\sqrt{\pi}}\left(\frac{eV_s}{k_B T_i}\right)^{\frac{1}{2}} + \exp\left(\frac{eV_s}{k_B T_i}\right) erfc\left[\left(\frac{eV_s}{k_B T_i}\right)^{\frac{1}{2}}\right]\right\}.$$

2.3.3 Growth rate equation of electron density

The equation describes the growth rate of electron density in the plasma

$$\frac{dn_e}{d\tau} = \sum_{j}^{A,B,C} \beta_j n_j - \sum_{j}^{A,B,C} \alpha_j n_e n_{ij} - \gamma_e n_{gn} n_{egn}, \qquad (2.4)$$

where β_j is the coefficient of ionization of the constituent neutral atoms due to external agency, $\alpha_j(T_e) = \alpha_{j0}\left(\frac{300}{T_e}\right)^k$ cm^3/sec is the coefficient of recombination of electrons and positively charged ions, and $n_e = (1-\varepsilon_r)n_p$ when negatively charged ions are considered in the model. The first term in Eq. (2.4) is the rate of gain in electron density per unit time on account of ionization of neutral atoms and second term is the decaying rate of the electron density due to electron–ion recombination and the third term is the electron collection current at the surface of graphene. Species of type C are taken into account when doping species are considered in the plasma.

2.3.4 Growth rate equation of positively charged ions

The equation describes the growth rate of j^{th} positively charged ion in plasma.

$$\frac{dn_{ij}}{d\tau} = \beta_j n_j - \alpha_j n_e n_{ij} - n_{gn} n_{ijgn}, \qquad (2.5)$$

Neha Gupta
Delhi Technological University, Delhi, India

The first term in Eq. (2.5) is the gain in ion density per unit time on account of ionization of neutral atoms, second term is the electron-ion recombination and third term is the ion collection current to the surface of graphene sheet.

2.3.5 Growth rate equation of negatively charged ions

The equation describes the growth of negatively charged ion density in plasma.

$$\frac{dn_{-}}{d\tau} = \varepsilon_r \frac{dn_p}{d\tau} = \sum_{j}^{A,B} \beta_j n_j - \sum_{j}^{A,B} \alpha_j n_e n_{ij} - \gamma_e n_{gn} n_{egn}. \qquad (2.6)$$

The explanations of all the terms incorporated in Eq. (2.6) are same as of Eq. (2.4).

2.3.6 Growth rate equation of neutral atoms

The equations describe the growth rate of neutral atoms in plasma.

$$\frac{dn_A}{d\tau} = \alpha_A n_e n_{iA} - \beta_A n_A + n_{gn}\left(1-\gamma_{iA}\right) n_{iAgn} - n_{gn}\gamma_A n_{Agn}, \qquad (2.7)$$

$$\frac{dn_B}{d\tau} = \alpha_B n_e n_{iB} - \beta_B n_B + n_{gn} n_{iBgn} - n_{gn} n_{Bgn}, \qquad (2.8)$$

$$\frac{dn_C}{d\tau} = \alpha_C n_e n_{iC} - \beta_C n_C + n_{gn}\left(1-\gamma_{iC}\right) n_{iCgn} - n_{gn}\gamma_C n_{Cgn}, \qquad (2.9)$$

where $n_{jgn} = (lt + ht + lh)\left(\frac{2\pi k_B T_n}{m_j}\right)^{\frac{1}{2}} n_j$ is the neutral collection current at the surface of graphene sheet. The first term in Eqs. (2.7)-(2.9) is the gain in neutral atom density per unit time due to electron–ion recombination, second term corresponds to the decrease in neutral density due to ionization, third term corresponds to the gain in neutral density due to neutralization of the atoms collected at the surface of graphene, and the last term in Eqs. (2.7) and (2.9) is the accretion of neutral atoms of species A and C, respectively on the surface of graphene.

2.3.7 Growth rate equation of graphene sheet

$$\frac{dm_{gn}}{d\tau} = m_A\gamma_A n_{Agn} + m_{iA}\gamma_{iA} n_{iAgn} + m_C\gamma_C n_{Cgn} + m_{iC}\gamma_{iC} n_{iCgn}, \quad (2.10)$$

$$[h(\tau)+l(\tau)]\frac{dt}{d\tau} = m_B n_{Bgn} + m_{iB} n_{iBgn} + m_C\gamma_C n_{Cgn} + m_{iC}\gamma_{iC} n_{iCgn}, \quad (2.11)$$

where $m_{gn}= (l\times h\times t)\rho_{gn}$ is the mass of the graphene sheet, ρ_{gn} is the density of graphene. The Eq. (2.10) describes the gain in mass density of graphene sheet due to collection of atomic and ionic species of type A and C. The Eq. (2.11) represents the change in thickness of the graphene sheet due to collection current of atomic and ionic species of type B and C. Species of type C are taken into account when doping species are considered in the plasma.

2.3.8 Energy balance for electrons

$$\begin{aligned}\frac{d}{d\tau}\left(\frac{3}{2}n_e k_B T_e\right) &= \left(\begin{matrix}\beta_A n_A \varepsilon_A + \beta_B n_B \varepsilon_B \\ + \beta_C n_C \varepsilon_C\end{matrix}\right) \\ &\quad -\left(\frac{3}{2}k_B\right)\left(\begin{matrix}\alpha_A n_e n_{iA} + \alpha_B n_e n_{iB} \\ + \alpha_C n_e n_{iC}\end{matrix}\right)T_e \\ -n_{gn}n_{egn}&\left\{\gamma_e\varepsilon_{egn}^{lh} + \delta_{egn}(1-\gamma_e)\left[\varepsilon_{egn}^{s} - \left(\frac{3}{2}k_B\right)T_{gn}\right]\right\} \\ &\quad -\left(\frac{3}{2}k_B\right)\left[\begin{matrix}f_{eA}\delta_{eA} + f_{eB}\delta_{eB} \\ + f_{eC}\delta_{eC}\end{matrix}\right](T_e - T_n)n_e \\ &\quad -\left(\frac{3}{2}k_B\right)\left(\begin{matrix}f_{eAi}\delta_{eAi} + f_{eBi}\delta_{eBi} \\ + f_{eCi}\delta_{eCi}\end{matrix}\right)(T_e - T_i)n_e, \quad (2.12)\end{aligned}$$

where T_n is the temperature of neutral atoms, T_{gn} is the temperature of graphene sheet, ε_j is the mean energy of electrons due to ionization of neutral atoms, $\varepsilon_{egn}^{lh}(Z)\left(=\varepsilon_{egn}^{s}(Z)-eV_s\right)$ is the mean energy of electrons (at a large distance from the surface of graphene sheet) collected by graphene sheet, $\varepsilon_{egn}^{s}(Z)=2k_BT_e$ is the mean energy of electrons collected by graphene,

Neha Gupta
Delhi Technological University, Delhi, India

$f_{ej}\left(=f_{ej0}\left(\frac{n_j}{n_{j0}}\right)\left(\frac{T_e}{T_{e0}}\right)^{\frac{1}{2}}\right)$ is the electron collision frequency due to elastic collisions with neutral atom; $f_{ej0}\left(=(8.3\times10^5)\pi r_j{}^2 n_{j0}T_{e0}{}^{\frac{1}{2}}\right)$ is the electron collision frequency due to collision with atom j in the absence of graphene, r_j is the mean radii of atomic species, T_{e0} is the temperature of electrons in the absence of graphene, $f_{eji}=f_{eji0}\left(\frac{n_{ij}}{n_{ij0}}\right)\left(\frac{T_e}{T_{e0}}\right)^{-\frac{3}{2}}$ is the electron collision frequency due to elastic collisions with positively charged ions and $f_{eji0}\left(=\left(5.5\frac{n_{i0}}{T_{e0}{}^{\frac{3}{2}}}\right)\ln\left(\frac{220T_{e0}}{n_{i0}{}^{\frac{1}{3}}}\right)\right)$ is the electron collision frequency due to collisions with ion j in the absence of graphene, $\delta_{ej}\left[\approx 2\frac{m_e}{m_j}\right]$ is the fraction of excess energy of electron lost in a collision with the neutral atom j, $\delta_{eji}\left[\approx 2\frac{m_e}{m_{ij}}\right]$ is the fraction of excess energy of electron lost in a collision with positively charged ion j, $\delta_{egn}\left[\approx 2\frac{m_e}{m_{gn}}\right]$ is the fraction of excess energy of electron lost in a collision with graphene, m_j is the mass of neutral atom, , n_j is the number density of neutral atom j , n_{j0} is the initial number density of neutral atom of type j, and $n_{e0}=(1-\varepsilon_r)n_{p0}$ is the initial number density of electrons when negatively charged ions are considered in the plasma.

The first term on the right hand side in Eq. (2.12) is the power gained per unit volume by electrons due to ionization of neutral atoms and last four terms refer to the energy loss by electrons per unit volume per unit time due to recombination with positively charged ions in plasma, the sticking

accretion and elastic collisions of electron at the surface of graphene, elastic electron-atom collision, and elastic electron-ion collision, respectively. Species of type C are taken into account when doping species are considered in the plasma.

Substituting the value of $\frac{dn_e}{d\tau}$ from Eq. (2.4) in Eq. (2.12), we get

$$\begin{aligned}\left(\frac{3}{2}k_B\right)n_e\left(\frac{dT_e}{d\tau}\right)=&\left[\begin{matrix}\left(\beta_A n_A\varepsilon_A+\beta_B n_B\varepsilon_B+\beta_C n_C\varepsilon_C\right)-\\ \left(\frac{3}{2}k_B\right)\left(\beta_A n_A+\beta_B n_B+\beta_C n_C\right)T_e\end{matrix}\right]\\ &-n_{gn}n_{egn}\left\{\gamma_e\left[\varepsilon^l_{egn}-\left(\frac{3}{2}k_B\right)T_e\right]\right.\\ &\left.+\delta_{egn}\left(1-\gamma_e\right)\left[\varepsilon^s_{egn}-\left(\frac{3}{2}k_B\right)T_{gn}\right]\right\}\\ &-\left(\frac{3}{2}k_B\right)\left[\begin{matrix}f_{eA}\delta_{eA}+f_{eB}\delta_{eB}\\ +f_{eC}\delta_{eC}\end{matrix}\right]\left(T_e-T_n\right)n_e\\ &-\left(\frac{3}{2}k_B\right)\left[\begin{matrix}f_{eAi}\delta_{eAi}+f_{eBi}\delta_{eBi}\\ +f_{eCi}\delta_{eCi}\end{matrix}\right]\left(T_e-T_i\right)n_e. \qquad (2.13)\end{aligned}$$

2.3.9 Energy balance of positively charged ions

$$\begin{aligned}\frac{d}{d\tau}\left[\frac{3}{2}\left(n_{iA}+n_{iB}+n_{iC}\right)k_BT_i\right]=&\left(\beta_A n_A\varepsilon_{iA}+\beta_B n_B\varepsilon_{iB}+\beta_C n_C\varepsilon_{iC}\right)\\ &+\left(\frac{3}{2}k_B\right)n_e\left[\begin{matrix}f_{eAi}\delta_{eAi}+f_{eBi}\delta_{eBi}\\ +f_{eCi}\delta_{eCi}\end{matrix}\right]\left(T_e-T_i\right)\\ &-\left(\frac{3}{2}k_B\right)\left(\alpha_A n_e n_{iA}+\alpha_B n_e n_{iB}+\alpha_C n_e n_{iC}\right)T_i\\ &-n_{gn}\left[\begin{matrix}n_{iAgn}\varepsilon^l_{iAgn}+n_{iBgn}\varepsilon^l_{iBgn}\\ +n_{iCgn}\varepsilon^l_{iCgn}\end{matrix}\right]\\ -\left(\frac{3}{2}k_B\right)&\left[\begin{matrix}\left(f_{iAA}\delta_{iAA}+f_{iAB}\delta_{iAB}+f_{iAC}\delta_{iAC}\right)n_{iA}\\ +\left(f_{iBA}\delta_{iBA}+f_{iBB}\delta_{iBB}+f_{iBC}\delta_{iBC}\right)n_{iB}\\ +\left(f_{iCC}\delta_{iCC}+f_{iCA}\delta_{iCA}+f_{iCB}\delta_{iCB}\right)n_{iC}\end{matrix}\right]\left(T_i-T_n\right), \qquad (2.14)\end{aligned}$$

where $\varepsilon^l_{ijgn}(Z)\left(=\left(2-\frac{eV_s}{k_BT_i}\right)k_BT_i\right)$ is the mean energy of positively charged

Neha Gupta
Delhi Technological University, Delhi, India

ions (at large distance from the surface of graphene sheet) collected by graphene sheet, ε_{ij} is the mean energy of positively charged ions produced by the ionization of neutral atoms, $f_{ijj'}\left(= f_{ijj'0}\left(\frac{n_{j'}}{n_{j'0}}\right)\left(\frac{m_{j'}T_i + m_{ij}T_n}{\left(m_{j'}T_{i0} + m_{ij}T_{n0}\right)}\right)^{\frac{1}{2}}\right)$ is the collision frequency of a j^{th} type of ion with j'^{th} ion of neutral atom , $\delta_{ijj'} = \left[\frac{2m_{ij}}{(m_{j'} + m_{ij})}\right]$ is the fraction of excess energy of a j^{th} type positively charged ion lost in a collision with neutral j' kind of neutral atom. $f_{ijj'0} = \left(\frac{8}{3}\right)(2\pi k_B)^{1/2}(r_{ij} + r_{j'})^2\left(\frac{n_{j'0}m_{j'}}{\left(m_{ij} + m_{j'}\right)}\right)\left[\left(\frac{T_{i0}}{m_{ij}}\right) + \left(\frac{T_{n0}}{m_{j'}}\right)\right]^{\frac{1}{2}}$, T_{i0} and T_{n0} are the initial temperatures of positively charged ions and neutrals, respectively. Species of type C are taken into account when doping species are considered in the plasma.

The first and second terms on the right hand side in Eq. (2.14) are the energy gained per unit volume per unit time by the positively charged ions due to ionization of neutral atoms, elastic collision of ions with electrons, respectively and last three terms are the energy loss per unit volume per unit time due to electron–ion recombination, sticking accretion of ions at the surface of graphene, and elastic collision with neutral species, respectively. Since both species of ions are assumed to be at the same temperature, the ion–ion collisions do not contribute to the energy balance.

Substituting the value of $\frac{dn_{ij}}{d\tau}$ from Eq .(2.5) in Eq.(2.14), we get

$$\left(\frac{3}{2}k_B\right)\left(n_{iA} + n_{iB} + n_{iC}\right)\left(\frac{dT_i}{d\tau}\right) = \begin{bmatrix}\left(\beta_A n_A \varepsilon_{iA} + \beta_B n_B \varepsilon_{iB} + \beta_C n_C \varepsilon_{iC}\right) \\ -\frac{3}{2}k_B\left(\beta_A n_A + \beta_B n_B + \beta_C n_C\right)T_i\end{bmatrix} + \frac{3}{2}k_B n_e\left[f_{eAi}\delta_{eAi} + f_{eBi}\delta_{eBi} + f_{eCi}\delta_{eCi}\right](T_e - T_i)$$

$$-n_{gn}\left[\begin{array}{c} n_{iAgn}\left(\varepsilon^{l}_{iAgn}-\frac{3}{2}k_BT_i\right)+n_{iBgn}\left(\varepsilon^{l}_{iBgn}-\frac{3}{2}k_BT\right) \\ +n_{iCgn}\left(\varepsilon^{l}_{iCgn}-\frac{3}{2}k_BT_i\right) \end{array}\right]$$

$$-\frac{3}{2}k_B\left[\begin{array}{l} \left(\begin{array}{c} f_{iAA}\delta_{iAA}+f_{iAB}\delta_{iAB}+ \\ f_{iAC}\delta_{iAC} \end{array}\right)n_{iA} \\ +\left(\begin{array}{c} f_{iBA}\delta_{iBA}+f_{iBB}\delta_{iBB}+ \\ f_{iBC}\delta_{iBC} \end{array}\right)n_{iB} \\ +\left(\begin{array}{c} f_{iCC}\delta_{iCC}+f_{iCA}\delta_{iCA} \\ +f_{iCB}\delta_{iCB} \end{array}\right)n_{iC} \end{array}\right](T_i-T_n). \quad (2.15)$$

2.3.10 Energy balance of negatively charged ions

$$\frac{d}{d\tau}\left(\frac{3}{2}n\_k_BT_e\right)=(\beta_An_A\varepsilon_A+\beta_Bn_B\varepsilon_B)$$
$$-\frac{3}{2}k_B(\alpha_An\_n_{iA}+\alpha_Bn\_n_{iB})T_e$$
$$-n_{gn}n_{egn}\left\{\gamma_e\varepsilon^{lh}_{egn}+\delta_{egn}(1-\gamma_e)\left[\varepsilon^{s}_{egn}-\left(\frac{3}{2}k_B\right)T_{gn}\right]\right\}$$
$$-\left(\frac{3}{2}k_B\right)[f_{eA}\delta_{eA}+f_{eB}\delta_{eB}](T_e-T_n)n\_$$
$$-\left(\frac{3}{2}k_B\right)(f_{eAi}\delta_{eAi}+f_{eBi}\delta_{eBi})(T_e-T_i)n\_. \quad (2.16)$$

The explanations of all the terms used in Eq. (2.16) are same as in Eq. (2.12), and this equation is considered when negatively charged ions are taken into account in the plasma.

2.3.11 Energy balance of neutral atoms

$$\frac{d}{d\tau}\left[\frac{3}{2}(n_A+n_B+n_C)k_BT_n\right]=\left[\left(\frac{3}{2}k_B\left(\begin{array}{c}\alpha_An_en_{iA}+\alpha_Bn_en_{iB}\\+\alpha_Cn_en_{iC}\end{array}\right)(T_e+T_i)\right)\right.$$
$$\left.+\left(\alpha_An_en_{iA}I_{pA}+\alpha_Bn_en_{iB}I_{pB}+\alpha_Cn_en_{iC}I_{pC}\right)\right]$$
$$+\frac{3}{2}k_B\left[n_e\left(\begin{array}{c}f_{eA}\delta_{eA}+f_{eB}\delta_{eB}\\+f_{eC}\delta_{eC}\end{array}\right)(T_e-T_n)+\right.$$

Neha Gupta
Delhi Technological University, Delhi, India

$$\left[\begin{bmatrix}\left(f_{iAA}\delta_{iAA}+f_{iAB}\delta_{iAB}++f_{iAC}\delta_{iAC}\right)n_{iA}\\+\left(f_{iBA}\delta_{iBA}+f_{iBB}\delta_{iBB}+f_{iBC}\delta_{iBC}\right)n_{iB}\\+\left(f_{iCC}\delta_{iCC}+f_{iCA}\delta_{iCA}+f_{iCB}\delta_{iCB}\right)n_{iB}\end{bmatrix}\left(T_i-T_n\right)\right]$$

$$+\left(\frac{3}{2}k_B\right)n_{gn}\begin{bmatrix}\left(1-\gamma_{iA}\right)n_{iAgn}+n_{iBgn}\\+\left(1-\gamma_{iC}\right)n_{iCgn}\end{bmatrix}\left(T_{gn}-T_n\right.$$

$$-\left(\frac{3}{2}k_B\right)n_{gn}\begin{bmatrix}n_{Agn}\left[\gamma_A T_n+\delta_{Agn}\left(1-\gamma_A\right)\right]+n_{Bgn}\delta_{Bgn}\\+n_{Cgn}\left[\gamma_C T_n+\delta_{Cgn}\left(1-\gamma_C\right)\right]\end{bmatrix}\left(T_n-T_{gn}\right)$$

$$-\left(\frac{3}{2}k_B\right)\left(\beta_A n_A+\beta_B n_B+\beta_C n_C\right)T_n-E_{diss}, \quad (2.17)$$

where I_{pj} is the ionization energy of the constituent atomic species, $E_{diss}=\left(E_{A,diss}+E_{B,diss}+E_{C,diss}\right)$, $E_{j,diss}$ is the energy dissipated per unit volume per unit time by neutral atoms to the surrounding atmosphere, $\delta_{jgn}\left(=\left[\frac{2m_j}{\left(m_j+m_{gn}\right)}\right]\right)$ is the fraction of excess energy of an atom lost in a collision with the graphene, T_a is the ambient temperature. The dissipation energy, $E_{j,diss}\left(=E_{j,diss0}\left[\frac{\left(T_n-T_a\right)}{\left(T_{n0}-T_a\right)}\right]\right)$ may be assumed to be proportional to the difference between the temperatures of the neutral atomic species T_n and the ambient temperature T_a. The constant $E_{j,diss0}$ is easily obtained by imposing the ambient condition of the complex plasma system in Eq. (2.17) for the constituent neutral species.

The first term on the right hand side of Eq. (2.17) is the power gained per unit volume by the neutral species due to recombination of electrons and positively charged ions, second and third terms are the rate of power gained per unit volume by neutral atoms in elastic collision with electrons and positively charged ions, respectively, fourth term is the energy gained per unit volume per unit time due to formation of neutrals at the surface of the graphene on account of ion collection currents. The fifth term refers to the power loss per unit volume due to sticking accretion and elastic collisions with graphene. The next term refers to the thermal energy loss per unit

volume per unit time by neutral atoms due to ionization. The last term is the energy dissipation rate per unit volume by neutral atoms to the surroundings. Substituting the value of $\frac{d\left(n_A+n_B+n_C\right)}{d\tau}$ from Eqs. (2.7)–(2.9) in Eq. (2.17), we get,

$$\begin{aligned}\frac{3}{2}\left(n_A+n_B+n_C\right)k_B\left(\frac{dT_n}{d\tau}\right)=&\left[\frac{3}{2}k_B\begin{pmatrix}\alpha_A n_e n_{iA}+\alpha_B n_e n_{iB}\\+\alpha_C n_e n_{iC}\end{pmatrix}\left(T_e+T_i-T_n\right)\right]\\&+\begin{pmatrix}\alpha_A n_e n_{iA}I_{pA}+\alpha_B n_e n_{iB}I_{pB}+\\\alpha_C n_e n_{iC}I_{pC}\end{pmatrix}\\&+\frac{3}{2}k_B\left[n_e\begin{pmatrix}f_{eA}\delta_{eA}+f_{eB}\delta_{eB}\\+f_{eC}\delta_{eC}\end{pmatrix}\left(T_e-T_n\right)\right.\\&\left.+\begin{bmatrix}\left(f_{iAA}\delta_{iAA}+f_{iAB}\delta_{iAB}+f_{iAC}\delta_{iAC}\right)n_{iA}\\+\left(f_{iBA}\delta_{iBA}+f_{iBB}\delta_{iBB}+f_{iBC}\delta_{iBC}\right)n_{iB}\\+\left(f_{iCC}\delta_{iCC}+f_{iCA}\delta_{iCA}+f_{iCB}\delta_{iCB}\right)n_{iB}\end{bmatrix}\left(T_i-T_n\right)\right]\\&+\left(\frac{3}{2}k_B\right)n_{gn}\begin{bmatrix}\left(1-\gamma_{iA}\right)n_{iAgn}+n_{iBgn}\\+\left(1-\gamma_{iC}\right)n_{iCgn}\end{bmatrix}T_{gn}\\&-\left(\frac{3}{2}k_B\right)n_{gn}\begin{bmatrix}n_{Agn}\left[\gamma_A T_n+\delta_{Agn}\left(1-\gamma_A\right)\left(T_n-T_{gn}\right)\right]\\+n_{Bgn}\delta_{Bgn}\left(T_n-T_{gn}\right)+\\n_{Cgn}\left[\gamma_C T_n+\delta_{Cgn}\left(1-\gamma_C\right)\left(T_n-T_{gn}\right)\right]\end{bmatrix}\\&-\left(\frac{3}{2}k_B\right)\begin{pmatrix}\beta_A n_A+\beta_B n_B\\+\beta_C n_C\end{pmatrix}T_n-E_{diss}.\end{aligned}\quad(2.18)$$

.

2.3.12 Energy balance of graphene sheet

$$\begin{aligned}\frac{d}{d\tau}\left(m_{gn}C_pT_{gn}\right)=&\,n_{egn}\left[\gamma_e\varepsilon^s_{egn}+\left(1-\gamma_e\right)\delta_{egn}\left[\varepsilon^s_{egn}-\left(\frac{3}{2}k_B\right)T_{gn}\right]\right]\\&-\left(\frac{3}{2}k_B\right)\begin{bmatrix}n_{Agn}\left[\gamma_A T_n+\delta_{Agn}\left(1-\gamma_A\right)\left(T_n-T_{gn}\right)\right]\\+n_{Bgn}\delta_{Bgn}\left(T_n-T_{gn}\right)\\+n_{Cgn}\left[\gamma_C T_n+\delta_{Cgn}\left(1-\gamma_C\right)\left(T_n-T_{gn}\right)\right]\end{bmatrix}\\&+\begin{bmatrix}n_{iAgn}\left(\varepsilon^s_{iAgn}+I_{pA}\right)+n_{iBgn}\left(\varepsilon^s_{iBgn}+I_{pB}\right)\\+n_{iCgn}\left(\varepsilon^s_{iCgn}+I_{pC}\right)\end{bmatrix}\end{aligned}$$

Neha Gupta
Delhi Technological University, Delhi, India

$$-\left(\frac{3}{2}k_B\right)\left[\left(1-\gamma_{Ai}\right)n_{iAgn}+n_{iBgn}+\left(1-\gamma_{Ci}\right)n_{iCgn}\right]T_{gn}$$
$$-(lt+ht+lh)\left[\varepsilon\sigma\left({T_{gn}}^4-{T_a}^4\right)\right.$$
$$+\left[\begin{array}{c} n_A\left(\frac{8k_BT_n}{\pi m_A}\right)^{\frac{1}{2}}+n_B\left(\frac{8k_BT_n}{\pi m_B}\right)^{\frac{1}{2}} \\ +n_C\left(\frac{8k_BT_n}{\pi m_C}\right)^{\frac{1}{2}} \end{array}\right]k_B\left(T_{gn}-T_n\right)\Bigg], \quad (2.19)$$

where $\varepsilon_{ijgn}^{s}(Z)=\left(\left(\frac{\left(2-\frac{eV_s}{k_BT_i}\right)}{\left(1-\frac{eV_s}{k_BT_i}\right)}\right)-\frac{eV_s}{k_BT_i}\right)k_BT_i$ is the mean energy collected by ions at the surface of graphene sheet, C_p is the specific heat of the material of the graphene at constant pressure, ε is the emissivity of the material of the graphene, σ is the Stefan –Boltzmann constant.

The first three terms in Eq. (2.19) are the rate of energy transferred to the graphene due to sticking accretion and elastic collision by constituent species of complex plasma. The fourth term is the energy carried away by the neutral species (generated by the recombination of the accreted ions and electrons) from the graphene per unit volume per unit time. The last term is the rate of energy dissipation of the graphene through radiation and conduction to the host gas.

2.4 Results and discussion

Using the analytical equations developed in Sec. 2.3, we investigate the effect of plasma parameters i.e., n_e, T_e, n_{iB}, T_{iB}, n_- and nitrogen doping on the growth characteristics (i.e., thickness) of the graphene sheet with time and subsequently on the field enhancement factor of the graphene sheet. The glow discharge and input parameters used for solving the model equations are listed in Table 2.1, 2.2, 2.3, and 2.4.

Table 2.1. Initial parameters (at τ=0) used in the present model

Parameter	Description	Initial Value
T_{gn}	temperature of graphene	2000 K
T_{n0}	neutral temperature	2000 K
$m_{iA} \approx m_A$	mass of ion and neutral of type A	12 a.m.u.
$m_{iB} \approx m_B$	mass of ion and neutral of type B	1 a.m.u.
ρ_{gn}	density of graphene	4.2 g/cm^3
$\alpha_{A0} \approx \alpha_{B0}$	coefficient of recombination of electrons and ions	1.12×10^{-7}cm^3/sec
γ_e	sticking coefficient of electrons	1
γ_{ij}	sticking coefficient of ions	1
ε	emissivity of graphene	0.6
I_{pA}	ionization energy of type A species	11.26 eV
I_{pB}	ionization energy of type B species	13.60 eV
n_{gn}	number density of graphene sheets	10^4 cm^{-3}
C_p	specific heat of the graphene	7×10^6 ergs/gK
l_0	length of the graphene sheet	100 nm
h_0	height of the graphene sheet	50 nm
t_0	thickness of the graphene sheet	4 nm
ϕ	work function of graphene	5 eV
T_{e0}	electron temperature	0.7 eV
T_{i0}	ion temperature	2400 K
ε_A	mean energy of neutrals of type A	6.2 eV
ε_B	mean energy of neutrals of type B	10.7 eV
ε_{iA}	mean energy of type A positively charged ion	7.3 eV
ε_{iB}	mean energy of type B positively charged ion	12.2 eV
$\varepsilon_{A,disso}$	dissipation energy of type A neutral	42.9 eV
$\varepsilon_{B,disso}$	dissipation energy of type B neutral	19.6 eV

Table 2.2. Additional parameters used for the calculation of undoped graphene sheet

Parameter	Description	Initial Value
n_{e0}	electron number density	10^8 cm^{-3}
n_{iA0}	number density of type A ion	0.8 n_{e0}
n_{iB0}	number density of type B ion	0.2 n_{e0}
n_{A0}	number density of type A neutral	1×10^{10} cm^3/sec
n_{B0}	number density of type B neutral	1×10^{10} cm^3/sec

Table 2.3. Additional parameters used for the calculation of nitrogen doped graphene sheet

Parameter	Description	Initial Value
n_{e0}	electron number density	10^8 cm^{-3}
n_{iA0}	number density of type A ion	0.5 n_{e0}
n_{iB0}	number density of type B ion	0.3 n_{e0}
n_{iC0}	number density of type C ion	0.2 n_{e0}
n_{A0}	number density of type A neutral	1×10^{10} cm^3/sec
n_{B0}	number density of type B neutral	1×10^{10} cm^3/sec
n_{C0}	number density of type C neutral	1×10^{10} cm^3/sec
α_{C0}	coefficient of recombination of electrons and ions	$1.12\times10^{-7}cm^3$/sec
ε_A	mean energy of type A neutral	6.51 eV
ε_B	mean energy of type B neutral	11.07 eV
ε_C	mean energy of type C neutral	8.2 eV
ε_{iA}	mean energy of type A ion	7.8 eV
ε_{iB}	mean energy of type B ion	12.56 eV
ε_{iC}	mean energy of type C ion	7.9 eV
$\varepsilon_{A,disso}$	dissipation energy of type A neutral	53.6 eV
$\varepsilon_{B,disso}$	dissipation energy of type B neutral	46.5 eV
$\varepsilon_{C,disso}$	dissipation energy of type C neutral	21.2 eV
I_{pC}	ionization energy of type C species	14.53 eV
$m_{iC} \approx m_C$	mass of ions and neutrals of type C	14 a.m.u.

Table 2.4. Additional parameters used when negatively charged ions are considered in the plasma

Parameter	Description	Initial Value
n_{p0}	number density of positively charged species	10^8 cm^{-3}
n_{iA0}	number density of type A ion	$n_{p0}/2$
n_{iB0}	number density of type B ion	$n_{p0}/2$
n_{-0}	number density of negatively charged ion	$\varepsilon_r n_{p0}$
n_{e0}	electron number density	$(1-\varepsilon_r)n_{p0}$
n_{A0}	number density of type A neutral	n_{p0}
n_{B0}	number density of type B neutral	n_{p0}
T_{e0}	electron temperature	0.7 eV
T_{-0}	temperature of negatively charged ion	0.6 eV

Figures 2.1 and 2.2 illustrate the variation of normalized thickness (t/t_0) of graphene sheet for different number densities and temperatures of electrons and ions of type B, respectively. From Figs. 2.1 and 2.2, it can be seen that the normalized thickness of graphene sheet first increases with time and then attains a saturation value. Moreover, it can be seen that the normalized thickness of graphene sheet decreases upon increase in number densities and temperatures of electrons and ions of type B. This is because with increase in electron density and temperature ionization of neutral species increases which in turn augments the ion density in the plasma. Thus, presence of large number of ions of type B in the plasma leads to the higher ion bombardment over the graphene sheet surface and results in the more effective etching of the side walls of the graphene sheet. Moreover, neutral species available for accretion also decreases due to more ionization and results in the thinning of the graphene sheet. The results of Fig.2.2 are in compliance with the experimental observations of Kim *et al.*[13] and Chan *et al.*[14].

Figure 2.3 illustrates the variation of thickness of undoped and nitrogen doped graphene sheet with time. It can be seen from Fig. 2.3 that the thickness

of graphene sheet decreases upon nitrogen doping. This can be attributed to the fact that the nitrogen atom, being pentavalent produces an extra electron on the graphene sheet surface which in turn increases the ionization of neutral atoms and thereby increases the ion bombardment and decreases the neutral atoms responsible for effective etching of the graphene sheet and accretion over the graphene sheet surface, respectively. Moreover, the etching effect by nitrogen is additionally considered as the basis for decrease of thickness of nitrogen doped graphene sheet. The results of Fig. 2.3 are in consistence with the experimental observations of Seo *et al* [8].

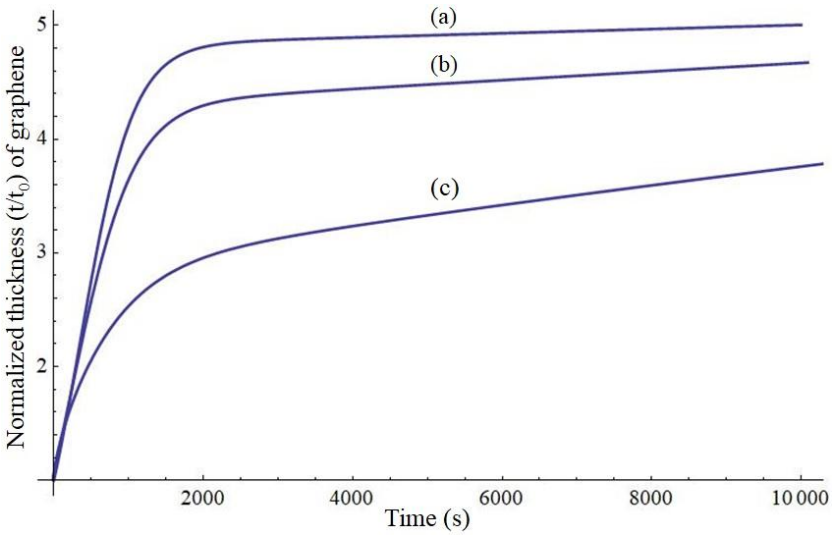

Fig.2.1. Temporal variation of normalized thickness of the graphene sheet for different electron densities and temperatures i.e., (a) $n_{e0} = 10^8\ cm^{-3}$, $T_{e0} = 0.7\ eV$, (b) $n_{e0} = 10^7\ cm^{-3}$, $T_{e0} = 0.6\ eV$, and (c) $n_{e0} = 10^9\ cm^{-3}$, $T_{e0} = 0.8\ eV$.

Figure 2.4 shows the time variation of the thickness of the graphene sheet for different relative number densities of negatively charged ions (ε_r = 0.1, 0.2, 0.3, 0.4). It can be seen from Fig. 2.4 that the thickness of graphene sheet decreases with increase of the relative number densities of negatively charged ions in the plasma. This is because the neutral atoms available for accretion on the graphene sheet surface decrease as the relative number densities of negatively charged ions increase (cf. Fig. 2.5).

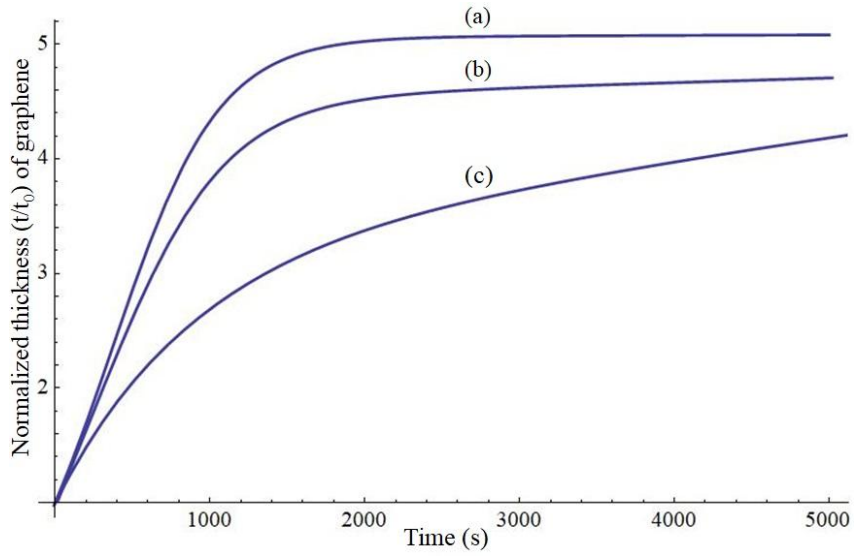

Fig.2.2. Temporal variation of normalized thickness of the graphene sheet for different densities and temperatures of ion of type B, where (a) $n_{iB0} = 10^8\ cm^{-3}$, $T_{i0} = 2100K$, (b) $n_{iB0} = 10^9\ cm^{-3}$, $T_{i0} = 2200K$ and (c) $n_{iB0} = 10^{10}\ cm^{-3}$, $T_{i0} = 2300K$.

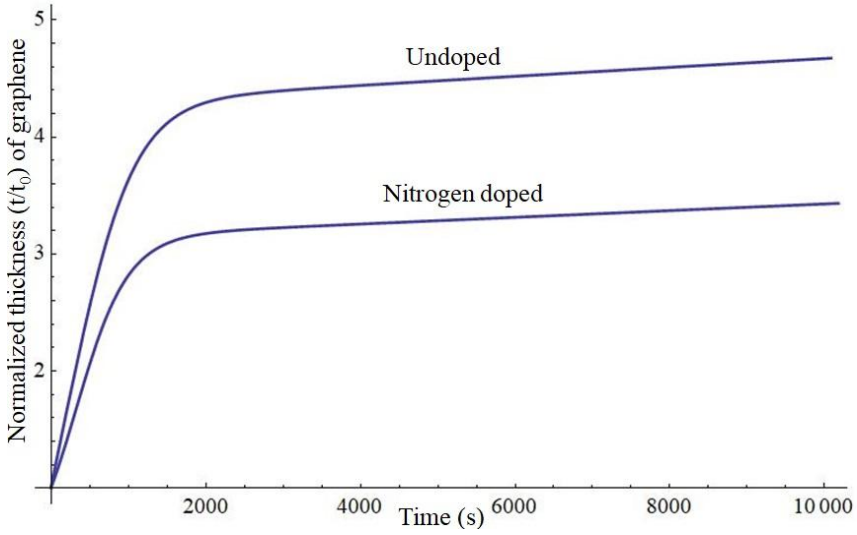

Fig.2.3. Temporal variation of normalized thickness of undoped and nitrogen doped graphene sheet.

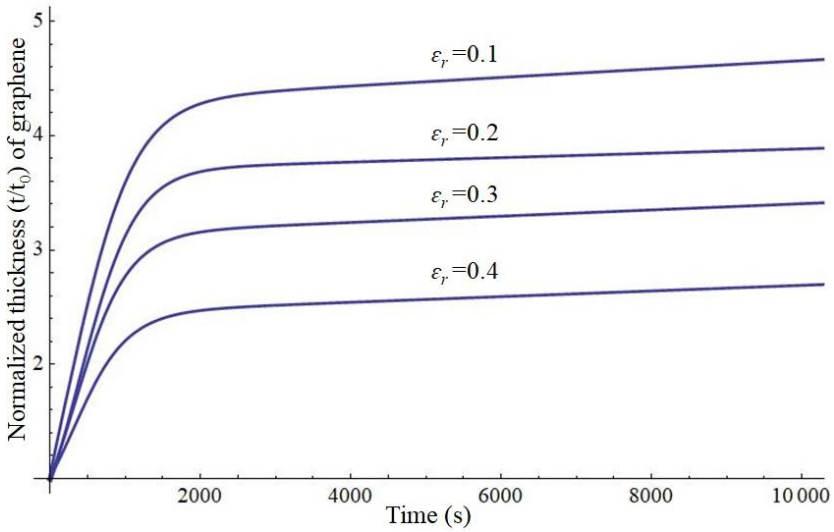

Fig.2.4. Temporal variation of normalized thickness of the graphene sheets for different ε_r .

Figure 2.5 shows the time variation of the number densities of neutral atoms of type A for different relative number densities of negatively charged ions (ε_r = 0.1, 0.2, 0.3, 0.4). It can be seen from Fig. 2.5 that on increasing the relative negatively charged ion density, the neutral density of type A atoms decays faster. This is because, on increasing the negatively charged ion density in plasma, for a fixed value of positive ion density, more and more neutral atoms ionizes to produce ions and electrons. Thus, the neutral atoms available for accretion decreases and as a result the thickness of the graphene sheet decreases.

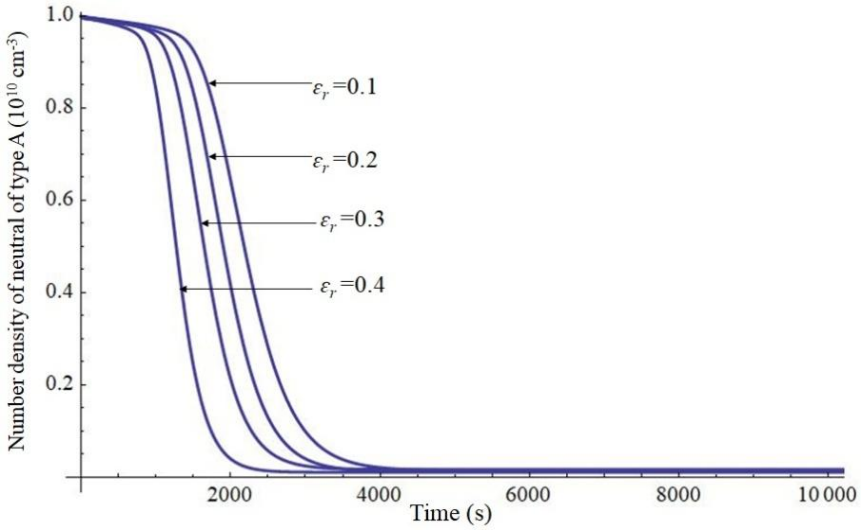

Fig.2.5. Temporal variation of normalized number density of neutrals of type A for different ε_r .

Using the results obtained, the field enhancement factor $\beta(\approx \frac{h}{t}$, where h and t are the height and thickness of the graphene sheet, respectively) [15,16] is calculated for the saturated value of thickness corresponding to the different plasma parameters, undoped and nitrogen doped graphene sheet, and different relative number densities of negatively charged ions in the plasma. Since height (h) has little influence on the field enhancement factor [17], it is assumed to be fixed i.e., 1 μm (estimated from the present investigation for particular set of parameters) for the calculation of β. From the above discussions, it is clear that thickness of the graphene sheet decreases with increase in the plasma parameters (i.e., plasma density and temperatures), nitrogen doping , and on increasing the relative density of negatively charged ions in the plasma, which consequently results in the enhanced field enhancement factor ($\beta \propto \frac{1}{t}$ for a fixed value of h) of the graphene sheet. Therefore, it can be concluded that by increasing the plasma parameters and relative density of negatively charged ions in the plasma and on treating graphene sheet with nitrogen lead to larger β and hence enhanced field emission from the graphene sheet. Soin *et al.*[11] and Palnitkar *et al.*[12] also reported the enhanced field emission characteristics of graphene sheet upon nitrogen doping.

References

[1] K. Yu, P. Wang, G. Lu, K. H. Chen, Z. Bo, J. Chen, Phys. Chem. Lett. **2**, 537 (2011).

[2] A. Malesevic, R. Vitchev, K. Schouteden, A. Volodin, L. Zhang, G. V. Tendeloo, A. Vanhulsel and C. V. Haesendonck, Nanotechnology **19**, 305604 (2008).

[3] N. Soin, S. S. Roy, Christopher O Kane, J. A. D. McLaughlin, T. H. Lim, C. J. D. Hetherington, Cryst Eng Comm **13**, 312 (2011).

[4] Y. S. Kim, J. H. Lee, Y. D. Kim, S.-K. Jerng, K. Joo, E. Kim, J. Jung, E. Yoon, Y. D. Park, S. Seo, S.-H. Chun, Nanoscale **5**, 1221 (2013).

[5] B. L. French, J. J. Wang , M. Y. Zhu, and B. C. Holloway , J. Appl. Phys. **97**, 114317 (2005).

[6] C. D. Wang, M. F. Yuen, T. W. Ng, S. K. Jha, Z. Z. Lu, S. Y. Kwok, T. L. Wong, X. Yang, C. S. Lee, S. T. Lee, and W. J. Zhang, Appl. Phys. Lett. **100**, 253107 (2012).

[7] C. Shen**,** G. Huang**,** Y. Cheng**,** R. Cao**,** F. Ding**,** U. Schwingenschlög and Y. Mei, Nanoscale Res. Lett. **7**, 268 (2012).

[8] D. H. Seo, S. Kumar, A. K. Rider, Z. Han and K. Ostrikov, Opt. Mat. Express **2,** 700 (2012).

[9] M. S. Sodha , S. Misra , S. K. Mishra and S. Srivastava, J. Appl. Phys. **107**, 103307 (2010).

[10] A. Malesevic, R. Kemps, A. Vanhulsel, M. P. Chowdhury, A. Volodin, and C. V. Haesendonck, J. Appl. Phys. **104**, 084301 (2008).

[11] N. Soin, S. S. Roy, S. Roy, K. S. Hazra, D. S. Misra, T. H. Lim, C. J. Hetherington, and J. A. McLaughlin, J. Phys. Chem. C **115**, 5366 (2011).

[12] U. A. Palnitkar, R. V. Kashid, M.A. More, D. S. Joag, L. S. Panchakarla, and C. N. R. Rao, Appl. Phys. Lett. **97**, 063102 (2010).

[13] Y. Kim, W. Song, S. Y. Lee, C. Jeon, W. Jung, M. Kim, and C.-Y. Park, Appl. Phys. Lett. **98**, 263106 (2011).

[14] S. H. Chan, S. H. Chen, W. T. Lin, M. C. Li, Y. C. Lin, and C.-C. Kuo, Nanoscale Res. Lett. **8**, 285 (2013).

[15] S. Watcharotone, R. S. Ruoff, and F. H. Read, Phys. Procedia **1**, 71 (2008).

[16] R. Miller, Y. Y. Lau, and J. H. Booske, Appl. Phys. Lett. **91**, 074105 (2007).

[17] Z. Xu, X. D. Bai and E. G. Wang, App. Phys. Lett. **88,** 133107 (2006).

3

Theoretical modeling of the plasma-assisted catalytic growth and field emission properties of graphene sheet

3.1 Brief outline of the chapter

In the present chapter, a phenomenological model describing the surface deposition kinetics as well as the gas-phase processes of the species responsible for catalyst assisted growth of graphene sheet in the reactive plasma is developed to study the dependence of growth characteristics of graphene sheet on the plasma parameters and henceforth account their effects on the field enhancement factor.

3.2 Introduction

Plasma enhanced chemical vapour deposition (PECVD) technique offers plentiful rewards, for instance, low temperature growth, better control over nanostructure position, size, and shape, high versatility and growth of nanostructures with selected properties [1,2]. Plasma plays a significant role in the nanostructure synthesis [3]. The growth of nanostructures is strongly affected by the ion & electron fluxes from the plasma and may well be effectively controlled by the proper selection of the plasma parameters**.** Extensive studies have been done to study the influence of RF power, feedstock gas ratio, electron-temperature, hydrogen gas, and growth time on the structure, growth rate and dimensions of the graphene sheet [4-8].

Nang and Kim [4] have observed that with the increase of plasma power and growth time, the structural quality of the graphene films is improved and the thickness of graphene is gradually decreased, finally saturating to a single layer graphene (cf. Figs. 2 & 3 of Nang and Kim [4]).

Liu *et al.*[5] have observed that upon increasing the RF power from 500 to 700 W, the deposited carbon material changes from 1-D to 2-D structure and when the RF power increases to above 800 W the growth ratio decreases. The decreasing growth ratio has been attributed to the etching effect of hydrogen radical that overtake the benefit of providing more energetic ions at 800 W RF power.

Jiang *et al.*[6] have studied the effect of gas flow rate on the growth of graphene sheet. They observed that under a certain methane flow rate and ratio of CH_4 to H_2, the size of the graphene flake increases with growth time and then get saturated. They have shown that the synthesized films possess excellent field emission properties with the field enhancement factor of 1.1×10^4.

Kim *et al.*[7] have synthesized graphene film on Ni foil by microwave plasma enhanced chemical vapor deposition (MPECVD) method and found that the number of layers of graphene increases by decreasing the mixing ratio of hydrogen and methane.

Chan *et al.*[8] have shown that high quality graphene films on Cu films are synthesized by increasing the hydrogen concentration by plasma-assisted thermal CVD. Their results indicate that as the H_2 flow rate increases, intensity ratio of 2D peak to G peak, i.e., I_{2D}/I_G increases from 0.98 to 2.29.

To date, several experimental evidences incorporating the effects of catalyst and electric field due to plasma on the vertical growth mechanism of graphene sheet have been given [9-11]. In the catalytic growth, hydrocarbon gas is dissociated on the catalyst surface whereas in the absence of catalyst the free radicals, ions, reactive species are formed by the collision of feedstock gas (hydrocarbons) and electrons in the plasma [12].

Zhu *et al.*[9] reported that initially graphene layers grow parallel to the substrate and then the top carbon layers curl upward due to sufficient level of force at the grain boundaries. They also revealed that the growth direction of the carbon nanosheets is determined by the induced polarization of the graphitic layers associated with the electric field in the plasma sheath.

Terasawa *et al.*[10] have studied and explained the growth mechanism of graphene on Cu by PECVD method. In their findings they have mentioned that the growth of the first layer is due to the catalytic nature of Cu, while the growth of the second and subsequent layers is mainly caused by the radicals generated in plasma.

Ghosh *et al.*[11] have demonstrated the effect of substrate on the growth of graphene nanosheets. They have explained the growth mechanism of vertical graphene nanosheets assisted by electron cyclotron resonance chemical vapor deposition (ECR-CVD) by eliciting the formation of nucleation centers for nanographitic (NG) island formation during surface-plasma interaction, coalescence of islands, and generation of stress at NG grain boundaries.

Moreover, many works on graphene synthesis have reported that the plasma treated graphene sheets have better field emission (FE) properties [6,13-16]. It has been observed that the field enhancement factor of graphene sheet is inversely proportional to the thickness of graphene [17,18]and hence lesser thickness corresponds to higher field emission current densities.

Malesevic *et al.*[13] have found that the few-layer graphene (FLG) synthesized by the MPECVD technique are the good field emitter with low turn-on field of 1V/μm and field amplification factor was observed upto 7500. They have also revealed that the FLG grown with high H_2/CH_2 gas ratio are better field emitters as compared to low H_2/CH_2 gas ratio.

Shih *et al.*[14] have investigated the effect of plasma treatment on the growth, structure and field emission properties of the two-dimensional carbon nanoflakes (CNFs) and revealed that the field emission properties get enhanced on increasing the RF power. They have also illustrated the effect of substrate temperature on the morphology of CNFs.

Wang *et al.*[15] have developed a back gated triode emission device based on field emission characteristic of carbon nanosheets which were synthesized by the RF-PECVD method. The field emission current was stable

for > 200 h at 1.3 mA emission current level. They imputed this result to the high purity and uniform height distribution of the carbon nanosheets.

Srivastava *et al.*[16] have shown that the increase in microwave power strongly affect the structure and morphology of the quasi two-dimensional carbon films. The normal alignment of the films to the substrate, increased density and reduced size are the main contributing factors to the characteristics of field emission from the carbon nanofilms.

3.3 Model

The present chapter enlightens the catalyst-assisted growth of graphene sheet in $Ar+H_2+C_2H_2$ plasma, C_2H_2 acts as a carbon source gas. The plasma consisting of electrons, ions of acetylene ($C_2H_2^+$), hydrogen (H^+) denoted as ions of type 1 and 2, respectively, and neutrals of type 1(acetylene, C_2H_2) and type 2 (hydrogen, H_2) is considered. Copper (Cu) catalyst over the silicon (Si) substrate is considered. The complete d-electron shell of copper resulting in low chemical affinity, minimal solubility of carbon, less precipitation of carbon from copper bulk make copper an effective catalyst for the graphene [19].

The present model considers the following elementary processes for the nucleation and growth of graphene sheet on catalyst-substrate surface in plasma.

(1) Firstly, the applied plasma power fragments the catalyst film to catalyst nanoparticles, subsequently leading to the formation of localized nucleation centres [3].

(2) The hydrocarbon ions formed due to ionization of gas within the chamber, pass through the plasma sheath and then via thermal dissociation, hydrogen induced decomposition (dehydrogenation) and several other processes, they adsorb, diffuse and eventually attach each other to form C-atom clusters [20].

(3) These carbon-clusters diffuse and collide to form graphene islands and thereafter coalescence of these graphene islands lead to the formation of large graphene islands. This leads to the parallel growth of graphene [20].

(4) However, the coalescence of the graphene islands cause stress at the grain boundaries, whose release favors the vertical growth of graphene [11]. The electric field generated by plasma ensures the motion of hydrocarbon ions towards the grain/island boundaries, leading to the formation of vertical graphene sheet.

In a typical PECVD [21-23], plasma sheath (areas with uncompensated surface charge) is formed near the boundaries of plasma-exposed substrate-catalyst surface. The graphene sheet is thus produced in the plasma sheath (rather in the plasma bulk) where the microscopic electric fields near the surface accelerate the ions towards the plasma-exposed surface. In the present model, we consider the sheath electric field (due to space-charge variation) to be directed along the z - axis which accelerates all ions toward the substrate [24]. To investigate the sheath structure, fluxes, and energy of the plasma generated species, the sheath kinetics are considered.

Following Mehdipour *et al.*[24] and Lieberman *et al.*[25]

$$\left(\hat{i}\frac{\partial}{\partial x}+\hat{j}\frac{\partial}{\partial y}+\hat{k}\frac{\partial}{\partial z}\right).(n_p\overrightarrow{v_p}) = f_{iz}n_e \ , \tag{3.1}$$

$$M_p n_p v_p \frac{dv_p}{dz} = en_pE - M_p n_p f_{pn} v_p \ , \tag{3.2}$$

$$\frac{d^2\phi(x)}{dz^2} = -\ 4\pi\sum q_p\xi_p n_p, \tag{3.3}$$

where Eqs. (3.1), (3.2), and (3.3) represents the continuity equation, ion-momentum balance equation, and Poisson equation, respectively, p refers to either electron (e), $C_2H_2^+$, or H^+, n_p, M_p, and v_p are their number density, mass in plasma, and fluid velocity, respectively. f_{iz}, E, f_{pn}, φ, and q_p are the ionization frequency, electric field, collision frequency, electrostatic potential and charge of the species respectively. ξ_p is the p^{th} ion to electron number density ratio, $\sum_p \xi_p = 1,$ and $0 < \xi_p < 1.$

3.3.1 Charging of graphene

The charge developed on the graphene surface is determined by the accretion of electrons and positively charged ions on the surface of graphene sheet.

$$Q'[\tau] = I_{i1gn} + I_{i2gn} - \gamma_e I_{egn}, \tag{3.4}$$

where Q is the charge over the graphene sheet, γ_e is the sticking coefficient of electrons, I_{ijgn} and I_{egn} are the ion and electron collection current at the graphene sheet surface, respectively.

$$I_{ijgn} = n_{ij}(x)\left(lt + ht + lh\right)\left(\frac{k_B T_{ij}}{2\pi^2 m_{ij}}\right)^{\frac{1}{2}}\left\{\frac{2}{\sqrt{\pi}}\left(\frac{eV_S}{k_B T_i}\right)^{\frac{1}{2}} + \exp\left[\frac{eV_S}{k_B T_{ij}}\right] erfc\left[\left(\frac{eV_S}{k_B T_{ij}}\right)^{\frac{1}{2}}\right]\right\} \times \exp\left[-\frac{eU_S}{k_B T_S}\right],$$

$$I_{egn} = \left(\frac{k_B T_e}{2\pi^2 m_e}\right)^{\frac{1}{2}} n_e(x)\left(lt + ht + lh\right)\exp\left[\frac{eV_S}{k_B T_e} + \frac{eU_S}{k_B T_S}\right],$$

where l, t, and h are the length, thickness and height of the graphene sheet, respectively, T_{ij} is the ion temperature, m_{ij} is the ion mass (subscript j refers to either 1 or2 type of positively charged ion as explained earlier), $n_{ij}(x) = n_{ij0}\left(1 - \frac{2e\phi(x)}{m_{ij}v_{i0}^2}\right)^{-1/2}$ is the ion density at any point within the plasma sheath; v_{i0} is the ion velocity, $\phi(x) = \phi_0 \exp\left(-\frac{|x|}{\lambda_d}\right)$ is the electrostatic potential; ϕ_0 is the negative potential at the surface and λ_d is the Debye length, T_s is the substrate or catalyst temperature (assuming catalyst and substrate to be at the same temperature), V_s is the surface potential of the graphene sheet (Refer Eq. (A2) of Appendix A), $n_e(x) = n_{e0}\exp\left[\frac{|e|\phi(x)}{k_B T_e}\right]$ is

Neha Gupta
Delhi Technological University, Delhi, India

the electron density in plasma sheath, T_e is the electron temperature, m_e is the mass of electron, U_s is the substrate bias and k_B is the Boltzmann constant. The negative substrate bias is to attract and accelerate the positive species in plasma to stick into and form the nanostructures [26].

The first and second term on the right hand side of Eq.(3.4) describe the charge developed on the graphene surface due to accretion of positively charged ions of type 1and 2 i.e., ions of acetylene and hydrogen, respectively. The third term represents the decrease in charge due to accretion of electrons at the surface of the graphene sheet.

3.3.2 Kinetic equation of electron density

$$n_e^{'}(\tau) = \left(\beta_1 n_1 + \beta_2 n_2\right) - \left(\alpha_1 n_e n_{i1} + \alpha_2 n_e n_{i2}\right) - \gamma_e n_{gn} I_{egn}, \qquad (3.5)$$

where β_1 & β_2 are the coefficient of ionization of the constituent neutral atoms due to external field, n_e is the electron number density, n_{i1} and n_{i2} are the ion number density of ion type 1 and 2, respectively, n_1 and n_2 are the number density of neutral type 1and 2, respectively. $\alpha_j\left(T_e\right) = \alpha_{j0}\left(\frac{300}{T_e}\right)^k$ cm^3/s is the coefficient of recombination of electrons and positively charged ions [27], $k = -1.2$ is a constant and j refers to either 1 or 2 type of ions.

Equation (3.5) indicates the growth of electron density in the plasma system due to ionization of neutral atoms, recombination of electrons & ions, and electron collection current at the surface of the graphene. The first term on the right hand side of Eq. (3.5) is the gain in electron density per unit time because of ionization of neutral atoms. The second term and third term display the decaying rate of the electron density due to the electron–ion recombination and the electron collection current at the surface of the graphene, respectively.

3.3.3 Kinetic equation of positively charged density

$$n_{i1}^{'}(\tau) = \beta_1 n_1 - \alpha_1 n_e n_{i1} - n_{gn} I_{i1gn} - J_{ai1} + J_{desorp1}, \tag{3.6}$$

$$n_{i2}^{'}(\tau) = \beta_2 n_2 - \alpha_2 n_e n_{i2} - n_{gn} I_{i2gn} - J_{ai2} + J_{desorp2} + J_{th}, \tag{3.7}$$

where $J_{aij} = P_i (2\pi m_{ij} k_B T_{ij})^{-1/2} \times {}^{n_{ij}}\!/_{J_{ij}}$ is the adsorption flux onto the catalyst substrate surface, P_i is the partial pressure of adsorbing species, $J_{desorpij} = j_{ij} \nu \exp\left({}^{-\varepsilon_{ai}}\!/_{k_B T_{ij}}\right)$ is the desorption flux from the catalyst-substrate surface, j refers to either 1 or 2 type of ions, ν is the thermal vibration frequency, ε_{ai} is the adsorption energy, j_{ij} is the ion flux on the catalyst substrate surface, $J_{th} = j_H \nu \exp\left({}^{-\delta\varepsilon_{th}}\!/_{k_B T_s}\right)$ is the flux of type 2 ion (namely hydrogen) on account of thermal dehydrogenation, $\delta\varepsilon_{th}$ is the activation energy of thermal dehydrogenation, j_H is the hydrogen ion flux at catalyst-substrate surface [28].

Eqs. (3.6) and (3.7) refer to the growth rate of positively charged ions in plasma system. The first term on the right hand side describes the gain in ion density per unit time on account of ionization of neutral atoms. The next two terms represent the rate of decrease in positively charged ion density due to electron-ion recombination and ion collection current at the surface of graphene, respectively. The fourth and fifth terms denote adsorption and desorption of ions to/from the catalyst-substrate surface, respectively. The last term in Eq. (3.7) represents the increase of hydrogen ion number density in plasma because of thermal dehydrogenation.

3.3.4 Kinetic equation of neutral species density

$$n_1^{'}(\tau) = \alpha_1 n_e n_{i1} - \beta_1 n_1 + n_{gn}\left(1-\gamma_{i1}\right) I_{i1gn} - n_{gn}\gamma_1 I_{1gn}, \tag{3.8}$$

$$n_2^{'}\left(\tau\right) = \alpha_2 n_e n_{i2} - \beta_2 n_2 + n_{gn}\left(1-\gamma_{i2}\right) I_{i2gn} - n_{gn}\gamma_2 I_{2gn}, \tag{3.9}$$

Neha Gupta
Delhi Technological University, Delhi, India

where $I_{jgn} = n_j(lt + ht + lh)\left(k_B T_n / 2\pi^2 m_j\right)^{1/2}$ is the neutral collection current at the surface of graphene, j refers to either 1 or 2 type of neutral atom, T_n is the neutral temperature, m_j is the mass of neutral atom, n_j is the neutral atom density, γ_j and γ_{ij} is the sticking coefficient of corresponding neutral atoms and ions, respectively.

Eqs. (3.8) & (3.9) describe the growth rate of number density of neutral atoms of type 1 and 2; the first term of the right side denotes the gain in neutral atom density per unit time due to electron–ion recombination. The remaining terms represent the decaying rate of neutral atom density due to ionization, gain in neutral density due to neutralization of ions collected at the surface of the graphene, accretion of neutral atoms of species 1 and 2 on the surface of the graphene, respectively.

3.3.5 Kinetic equation for the growth of graphene nuclei

In the preliminary stage, catalyst (Cu) film fragments into nanoislands of Cu [3].The diameter of islands is known to be function of the thickness of the catalyst film. The island size increases with the thickness of the catalyst film [29]. Since the catalyst activities depend on the size of the catalyst particle, therefore, morphology, growth rate and type of carbon nanostructure formed changes with the catalyst-island size. Small catalyst particles favor the growth of carbon nanotubes while the large catalyst particles promote the growth of graphene [30]. The present model considers the size of the catalyst nanoparticle to be 40 nm [10].

Following Mehdipour and Ostrikov [20], Tewari and Sharma [28]

$$\frac{d}{d\tau}\left(\pi r_g^2\right) = \left[\left\{2n_{CH}\nu\exp\left(\frac{-\delta E_i}{k_B T_s}\right) + 2\theta_{CH} J_{i1} y_d + 2J_{i1} + \frac{J_{i1}\sigma_{ads} J_2}{\nu} + J_c\right\} m_c + \left\{J_{i1}(1-\theta_t) + \frac{J_{i1}\sigma_{ads} J_H}{\nu} + J_{i1}\exp\left(\frac{-\delta E_i}{k_B T_s}\right)\right\} m_{i1}\right]$$

$$\times \frac{2\pi r_{cat}}{\pi r_{cat}^2 \rho_{cat}} \left(D_1 \exp\left(\frac{-E_{sdC}}{k_B T_s} \right) \right) + D_2 \exp\left(\frac{-E_{sdCl}}{k_B T_s} \right) \times \left(\frac{1}{I_{i1g}} \right) + \gamma_{C_2H_2} \pi r_{cat}^2 I_{C_2H_2{}^g}, \quad (3.10)$$

where r_g is the radius of the graphene nuclei, r_{cat} is the radius of the catalyst nanoparticle, ρ_{cat} is the mass density of the catalyst particle. $I_{ijg} = \left(\pi r_g^2 \left(\frac{8k_B T_i}{\pi m_{ij}} \right)^{1/2} n_{ij}(x) \left[1 - Q\gamma_{ji} \right] \exp\left[-\frac{eU_s}{k_B T_s} \right] \right)$ is the ion collection current at the surface of graphene nuclei; where, j refers to either 1 or 2 type of ion, $\gamma_{ji} = e^2 \Big/ \left(r_g k_B T_s \right)$, $I_{jg} \left(= \pi r_g^2 \left(8k_B T_n \Big/ \pi m_j \right)^{1/2} n_j \right)$ is the neutral collection current at the surface of the graphene nuclei, j refers to either 1 or 2 type of neutral atom, $\gamma_{C_2H_2}$ is the neutral atom sticking coefficient, $n_{CH} \left(= \theta_{CH} \nu_0 \right)$ (Denysenko and Ostrikov [31]) is the surface concentration of CH; θ_{CH} is the surface coverage by C_2H_2 radicals [31] and $\nu_0 \left(\approx 10^{15} \text{cm}^{-2} \right)$ is the number of adsorption sites per unit area [31], m_C (= 12 a.m.u) is the mass of the carbon atom and m_{i1} (= 26 a.m.u.) is the mass of type 1 (i.e., $C_2H_2^+$) ions, δE_i ($\approx 1.87\ eV$) is the thermal energy barrier [20], $J_{ij} \left(= n_{ij} \left(k_B T_e \Big/ m_{ij} \right)^{1/2} \right)$ is the flux of type j ion [28], $y_d (\approx 2.49 \times 10^{-2} + 3.29 \times 10^{-2} \times E_i$; where E_i is the ion energy in eV) is the stitching probability[32], $\sigma_{ads} \left(\approx 10^{-16} \text{cm}^2 \right)$ is the cross-section for the reactions of atomic hydrogen [31], $J_\alpha = \left(n_\alpha v_{th\alpha} \Big/ 4 \right)$ is the flux of impinging species α (where $\alpha = C, H$); C and H stands for carbon and hydrogen species, respectively, n_α and $v_{th\alpha}$ are the number density and

Neha Gupta
Delhi Technological University, Delhi, India

thermal velocity of α species, respectively [31], $D_1 \exp\left(\frac{-E_{sdC}}{k_B T_s}\right)$ and $D_2 \exp\left(\frac{-E_{sdCl}}{k_B T_s}\right)$ are the surface diffusion coefficients of carbon monomers and C-atom clusters, respectively with corresponding activation energies E_{sdC} =0.1 eV and E_{sdCl} = 0.82 eV, respectively [20].

Eq. (3.10) traces the development of graphene island on the catalyst nanoparticle. The adsorption, surface diffusion, and accretion of carbon atoms on the surface of the catalyst via thermal dissociation, ion induced dissociation, decomposition of positively charged ions, interaction of adsorbed acetylene ions with atomic hydrogen from plasma, thermal dissociation of carbon source gas of acetylene ions, and other processes lead to the formation of C-atom clusters [20]. The surface diffusion (with energy barrier E_{sdCl}) and agglomeration of these clusters lead to the formation of graphene island (with radius r_g) [20].

In Eq. (3.10), the first term in the first bracket on the right side (see Ref.26) accounts for the carbon yield on the catalyst surface due to thermal dissociation of acetylene ions (with activation energy of thermal dissociation, δE_i); second term (see Ref. 31) denotes the carbon yield due to ion induced dissociation of C_2H_2/ion-induced incorporation of neutrals (see Ref. 32); third term refers the decomposition of acetylene ions, i.e., $C_2H_2^+$; fourth term (see Ref. 31) describes the interaction of ions with atomic hydrogen from the plasma; fifth term (see Ref. 31) is the rate of the incoming flux of carbon atoms onto the catalyst particle. The terms in the second bracket refers to the adsorption flux of type 1 ions to the catalyst surface, interaction of adsorbed type 1 ions with atomic hydrogen from plasma, and thermal dissociation of hydrocarbon source gas C_2H_2, respectively. The term $D_1 \exp\left(\frac{-E_{sdC}}{k_B T_s}\right)$ and D_2

$\exp\left(\frac{-E_{sdCl}}{k_B T_s}\right)$ accounts for the surface diffusion of carbon monomers (with energy barrier $E_{sdC}\left(=0.1\,eV\right)$) and C- clusters (with energy barrier E_{sdCl} $\left(=0.82\,eV\right)$), respectively onto the catalyst surface per unit area mass density. The factor I_{i1g} accounts for the ion collection current on the growing graphene island. The last term denotes the sticking of neutral atoms of type 1 i.e., acetylene to the graphene island.

3.3.6 Growth rate equation for graphene sheet

In the initial stage, formation of graphene islands result in the planar growth of graphene. We believe that the length of graphene advance during the course of the planar growth and we presume its value to be 1.6 μm [6]. However, the parallel growth of graphene eventually switches to the vertical growth due to the stress developed at the graphene island boundaries. Ion bombardment, temperature gradients, and lattice mismatch between catalyst-substrate surface and graphitic material are the main causes of this stress [33]. Under the influence of the electric field due to plasma, carbon atoms diffuse at the graphene island boundaries raising the height and thickness of the graphene sheet in the upward direction. Finally, the etching of carbon due to hydrogen results in the decrease in the thickness of the graphene.

$$l\frac{d\left(h\times t\right)}{d\tau}=\left(\begin{array}{c}\left(\frac{n_1}{\nu}\times D_1\exp\left\{\frac{E_d+E_{inc}}{k_B T_s}\right\}\right)\frac{\pi r_g^2}{2\pi r_g}\times\left(I_{i1gn}\right)\\ +\left(\gamma_{C_2H_2}I_{C_2H_2gn}\right)\end{array}\right)\times\frac{M_{gn}}{\rho_{gn}},\qquad(3.11)$$

$$\left[h\left(\tau\right)+l\right]\frac{d(t)}{d\tau}=\left\{J_{i2}\exp\left(\frac{-\delta E_{sdh}}{k_B T_s}\right)+J_{i2}(1-\theta_t)+J_{i2}+\theta_{CH}\left(J_{i2}\,y_d+\nu_0\nu\right.\right.$$
$$\left.\left.\exp\left(\frac{-\delta E_i}{k_B T_s}\right)\right)\right\}\frac{h(\tau)}{n_{i2}}+\gamma_{C_2H_2}\pi r_g^2 I_{C_2H_2gn},\qquad(3.12)$$

where ρ_{gn} is the graphene sheet density and $M_{gn}\left(\approx 12g\right)$ is the mass of the growing graphene sheet.

Equation (3.11) describes the increase in area of the graphene sheet due to diffusion, of carbon atoms at the graphene island boundaries and ion & neutral collection current at the growing graphene sheet. The first term on the right side of the Eq. (3.11) describes the diffusion (with energy barrier, $E_d \approx 0.13eV$) [9] and attachment of carbon atoms (with energy barrier, $E_{inc} \approx 0.4$ eV) [34] to the border of the growing graphene sheet. The factor I_{i1gn} corresponds to the ion collection on the growing graphene sheet and the last term accounts the sticking of neutral atoms of acetylene on the graphene sheet.

Equation (3.12) describes the decrease in thickness of graphene sheet due to etching of carbon by hydrogen atoms. In Eq.(3.12) the first term on the right hand side refers the incoming flux of type 2 ion, i.e., hydrogen due to thermal dehydrogenation of type 1 ions (with energy barrier $\delta E_{sdh} = 1.7$eV); second term accounts the adsorption of type 2 ions to the surface. The third term is the decomposition of positively charged ions of type 2, fourth term describes ion induced dissociation of acetylene, and fifth term is due to the incorporation of hydrogen ions due to thermal dissociation of acetylene ions [31]. The last term denotes the sticking of neutrals of acetylene on the surface of the graphene sheet.

3.3.7 Energy balance equation for graphene sheet

$$RF\ power = \frac{d}{d\tau}\left(M_{gn}C_pT_S\right) = I_{egn}\left[\gamma_e\varepsilon^s_{egn} + \left(1-\gamma_e\right)\delta_{egn}\left[\varepsilon^s_{egn} - \left(\frac{3}{2}k_B\right)T_S\right]\right]$$
$$-\frac{3}{2}k_B\left[I_{1gn}\left[\gamma_1T_n + \delta_{1gn}\left(1-\gamma_1\right)\left(T_n - T_S\right)\right] + I_{2gn}\delta_{2gn}\left(T_n - T_S\right)\right]$$
$$+\left[I_{i1gn}\left(\varepsilon^s_{i1gn} + I_{z1}\right) + I_{i2gn}\left(\varepsilon^s_{i2gn} + I_{z2}\right) - \left(\frac{3}{2}k_B\right)\left[\left(1-\gamma_{i1}\right)I_{i1gn} + I_{i2gn}\right]T_S\right.$$
$$\left. - A\left[\varepsilon\sigma\left(T_s{}^4 - T_a{}^4\right) + \left[n_1\left(\frac{8k_BT_n}{\pi m_1}\right)^{1/2} + n_2\left(\frac{8k_BT_n}{\pi m_2}\right)^{1/2}\right]k_B\left(T_s - T_n\right)\right], \quad (3.13)$$

where $M_{gn}\left(=(l\times h\times t)\rho_{gn}\right)$ is the mass of the graphene sheet, $A(=lt+lh+th)$ is the surface area of the graphene sheet, C_p is the specific heat capacity of graphene sheet (C_p≈2.1 J $g^{-1}K^{-1}$), $\varepsilon^{s}_{egn}\left(=2k_BT_e\right)$ is the mean energy of electrons collected by graphene [27], $\delta_{egn}\left(\approx 2\frac{m_e}{M_{gn}}\right)$ is the fraction of excess energy of electron lost in a collision with graphene sheet [27], $\delta_{jgn}\left[=\frac{2m_j}{\left(m_j+M_{gn}\right)}\right]$ is the fraction of excess energy of an atom lost in a collision with the graphene sheet [27], T_a is the ambient temperature, T_n is the temperature of the neutral atomic species, $I_{z1}\left(=11.26\,eV\right)$ and $I_{z2}\left(=13.5\,eV\right)$ are the ionization energies of neutral atoms 1 and 2, respectively, $\varepsilon^{s}_{ijgn}(Z)=\left(\left(\frac{\left(2-\frac{eV_s}{k_BT_i}\right)}{\left(1-\frac{eV_s}{k_BT_i}\right)}\right)-\frac{eV_s}{k_BT_i}\right)k_BT_i$ (see Ref.27) is the mean energy collected by ions at the surface of graphene sheet, ε is the emissivity of the material of the graphene sheet and σ is the Stefan –Boltzmann constant.

Equation (3.13) illustrates the effect of RF power on the mass of the graphene sheet. The first two terms in Eq. (3.13) represents the rate of energy transferred to the graphene sheet due to sticking accretion and elastic collision by constituent species of complex plasma. The third term accounts the ionization of neutral species 1 and 2 resulting in the collection of ions on the surface of graphene sheet and fourth term is due to sticking accretion of ions 1 and 2 on the graphene surface. The last term is the rate of energy dissipation of the graphene through radiation and conduction to the host gas.

3.3.8 Field enhancement factor

Following Watcharotone *et al.*[17] and Miller *et al.*[18], the expression for the field enhancement factor of graphene can be written as

$$\beta \approx \frac{h}{t}, \tag{3.4}$$

where h is the height of the graphene sheet and t is the thickness of the graphene sheet.

3.4 Results and discussion

The present chapter serves an analytical model for studying the plasma-sheath-related effects on the graphene growth. In particular, we study the role of different plasma parameters on the growth and field emission properties of graphene sheet with catalyst effects. In the plasma process, substrate-catalyst surface is separated from the plasma by a sheath. The electric field directed from the plasma bulk toward the surface plays a vital role in the growth process of graphene sheet. Due to the variations of the plasma parameters, the sheath thickness changes which in turn affect the electric field strength, thereby, affecting the electron and ion collection current to the graphene surface.

We assume that the applied plasma power ionizes the neutral gas atoms, thereby, creating active species, which fragments the catalyst film into catalyst nanoparticles. Various processes such as thermal & ion-induced dissociation of hydrocarbon gas, decomposition & adsorption of positively charged ions of acetylene, interaction of ions with hydrogen, surface diffusion of species and severalothers have been taken into account to the catalyst surface. In the present example, we have accounted the parallel as well as vertical growth of graphene sheet. At the first stage, the diffusion and attachment of carbon atoms at the catalyst surface results in the formation of C-clusters. These clusters diffuse and stitch together to form graphene islands leading to the parallel growth of graphene.During the second stage, the parallel growth of graphene sheet switches to the vertical growth due to the development of stress at the graphene island boundaries.The nucleation and growth behaviour of vertical graphene

sheet is strongly affected by the in-built electric field associated with plasma, which is responsible for delivery of carbon atoms to the graphene island boundaries and surfaces of the growing vertical graphene sheet. At this stage, graphenesheet grows in height via ion and neutral collection current at the graphene island boundaries and thickens due to diffusion and attachment of carbon atoms at the peripherals of the growing carbon platelets. Further increase in height and thickness occurs due to ion and neutral collection current at the lateral surfaces as well as at the top surface of the growing vertical graphene sheet. This is in accordance with the growth possibilities proposed by Zhao *et al*.[12] for two-dimensional nanostructures. In this case, they proposed that the growth may occur at the contact line between the graphene and substrate, at the active steps/edges on two sides of the graphene sheet, and at the free edges of the graphene sheet [cf. Fig. 2(f) of Zhao *et al*. [12]]. The growing edges are then terminated by the etching effect of hydrogen.

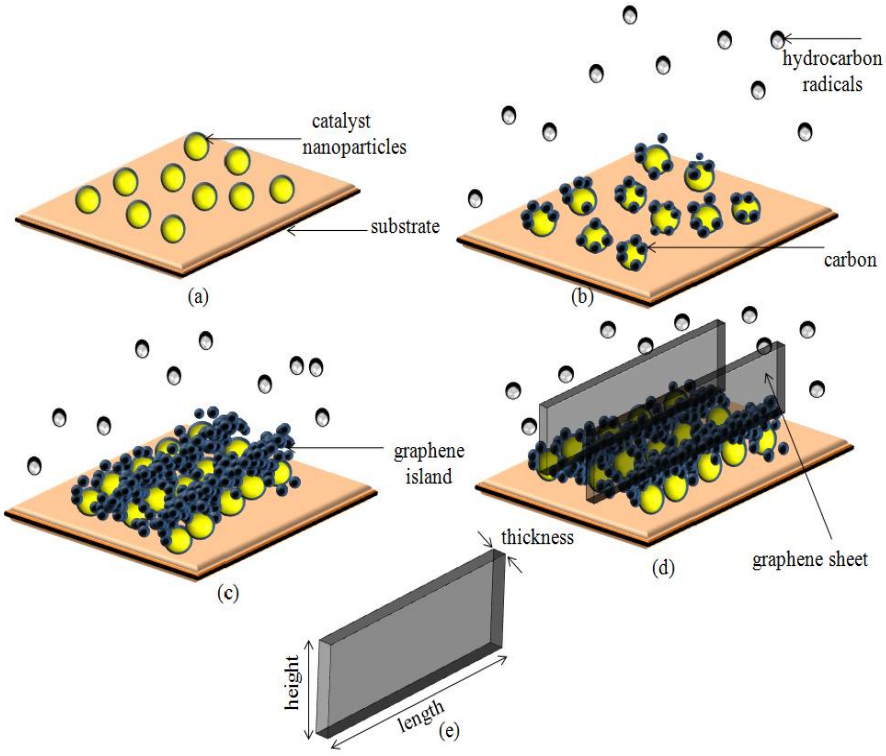

Fig. 3.1. Schematic representation of the formation of graphene sheet on the catalyst-substrate surface under plasma; (a) formation of catalyst nanoparticles on the substrate surface, (b) cluster formation due to the diffusion of carbon atoms on the catalyst nanoparticles, (c) diffusion of clusters leading to the formation of graphene islands,(d) growth of graphene sheet at the bondaries of graphene islands, (e) scheme of the graphene sheet considered.

Figure 3.1 shows the schematic representation of the growth stages of graphene sheet on the catalyst- substrate surface in the presence of plasma. The sketch represents the fragmentation of catalyst film into catalyst nanoparticles, diffusion of carbon monomers to the catalyst particles, diffusion of carbon clusters leading to the formation of graphene island and lastly the vertical growth of graphene sheet due to stress developed at the island boundaries.

Table 3.1. Boundary conditions used in the present model

Parameter	Description	Initial Value
n_{e0}	electron density	10^{11} cm^{-3}
n_{i10}	number density of type 1 ion	$0.7\,n_{e0}$
n_{i20}	number density of type 2 ion	$0.5\,n_{e0}$
n_{j0}	number density of neutral species	10^{12} cm^{-3}
T_{e0}	electron temperature	1.7 eV
T_{i0}	ion temperature	2200 K
T_{n0}	neutral temperature	2000 K
T_s	substrate temperature	600 ^{0}C
Q_0	charge on the graphene sheet surface	-1 stat C
m_{i1}	mass of ion 1	26 a.m.u for $C_2H_2^+$
m_{i2}	mass of ion 2	1 a.m.u for H^+
ρ_{ct}	density of catalyst Cu	8.96g/cm^3
$\alpha_{10} \approx \alpha_{20}$	coefficient of recombination of electrons and ions	$1.12\times10^{-7}$$cm^3$/sec
γ_e	sticking coefficient of electrons	1
γ_{ij}	sticking coefficient of ions	1

Numerical calculations have been carried out to study the dependence of the dimensions (i.e., thickness and height) of the graphene sheet on the plasma parameters (i.e., electron density and temperature, ion density of both type 1 and 2, and temperature) which subsequently influence its field emission properties. We have solved the Eqs. (3.1-3.13) simultaneously with the aid of MATHEMATICA SOFTWARE using all the appropriate boundary conditions

given in Table 3.1 to study the dependence of height and thickness of graphene sheet on plasma parameters.

Figure 3.2 shows the variation of potential of the rectangular graphene sheet along the vertical growth axis i.e., z-axis. From Fig. 3.2, it can be seen that the potential of the rectangular graphene sheet decreases linearly as the distance from the surface is increased.

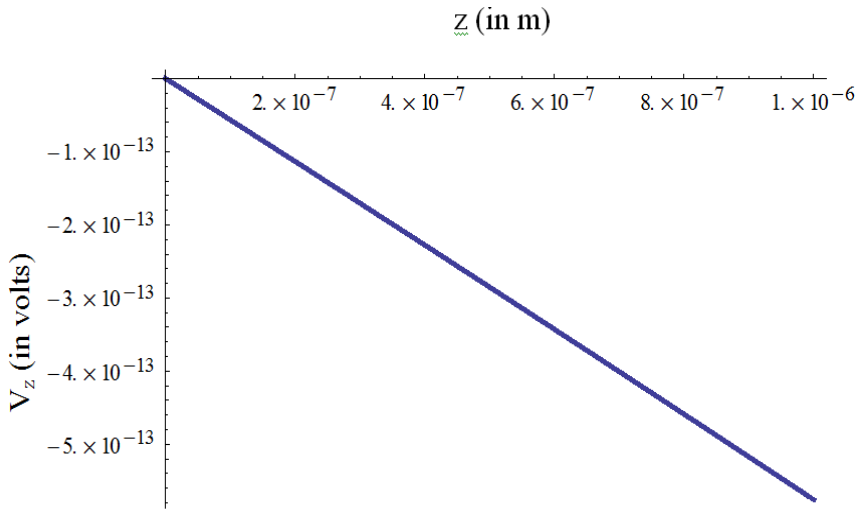

Fig. 3.2. Shows the variation of potential due to the rectangular graphene sheet along the vertical growth axis (z-axis).

Figure 3.3 shows the time-variation of the thickness of the graphene sheet for different electron number densities and electron temperatures (i.e., $n_{e0} = 10^{10}\,\text{cm}^{-3}$ and $T_{e0} = 1.5\,\text{eV}$, $n_{e0} = 10^{11}\,\text{cm}^{-3}$ and $T_{e0} = 1.7\,\text{eV}$, $n_{e0} = 10^{12}\,\text{cm}^{-3}$ and $T_{e0} = 1.9\,\text{eV}$). From Fig. 3.3, it can be seen that the thickness of the graphene sheet increases with time and then attains a saturation value. The figure also shows the decrease of graphene sheet thickness with electron density and temperature. This happens because for larger values of electron density and temperature, rate of ionization of neutral atoms increases due to which number density of positively charged ions and electron increases, therefore, the number of neutral atoms of type 1 available for accretion decreases. Hence, the thickness of the graphene sheet saturates at a lower value.

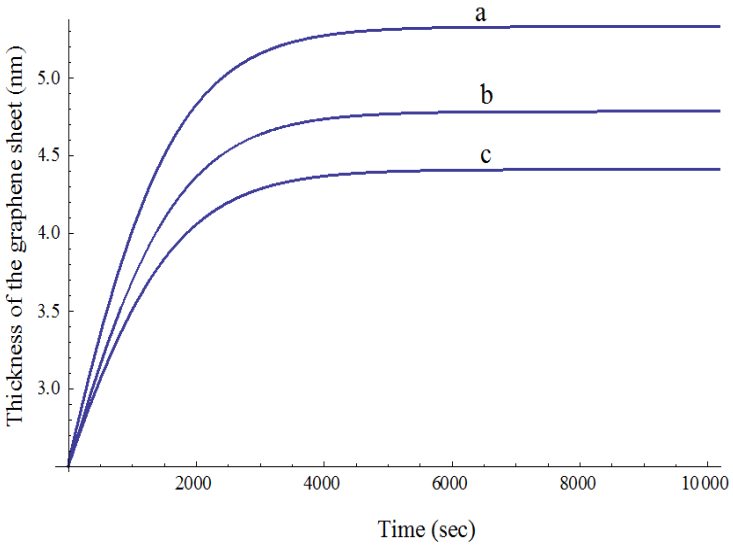

Fig. 3.3. This figure illustrates the time variation of the thickness of the graphene sheet for different electron densities and temperatures (where a, b, and c correspond to $n_{e0} = 10^{10}\,\text{cm}^{-3}$ and $T_{e0} = 1.5$ eV, $n_{e0} = 10^{11}\,\text{cm}^{-3}$ and $T_{e0} = 1.7$ eV, $n_{e0} = 10^{12}\,\text{cm}^{-3}$ and $T_{e0} = 1.9$ eV, respectively). The other parameters are given in the text and Table 3.1.

Figure 3.4 illustrates the variation of thickness of graphene sheet with time for different number density and temperature of ions of type 2 (i.e., $n_{i20} = 10^{10}\,\text{cm}^{-3}$ and $T_{i0} = 2100$ K, $n_{i20} = 10^{11}\,\text{cm}^{-3}$ and $T_{i0} = 2150$ K, $n_{i20} = 10^{12}\,\text{cm}^{-3}$ and $T_{i0} = 2200$ K). From Fig. 3.4, it can be seen that the thickness of graphene sheet decreases with increasing number density of type 2 ions, i.e., of hydrogen ions. This is answerable to the fact that with increasing density of hydrogen ions, the etching of graphene sheet at the edges increases. We assume that two processes occur in our growth mechanism, viz., carbon deposition on the surface and etching of the graphene sheet. On increasing the number density of hydrogen ions, the etching effect becomes more prominent resulting in the decrease of the thickness of the graphene sheet. The theoretical findings of Fig. 3.4 are in compliance with the experimental observations of Kim *et al.*[7]and Chan *et al.*[8].

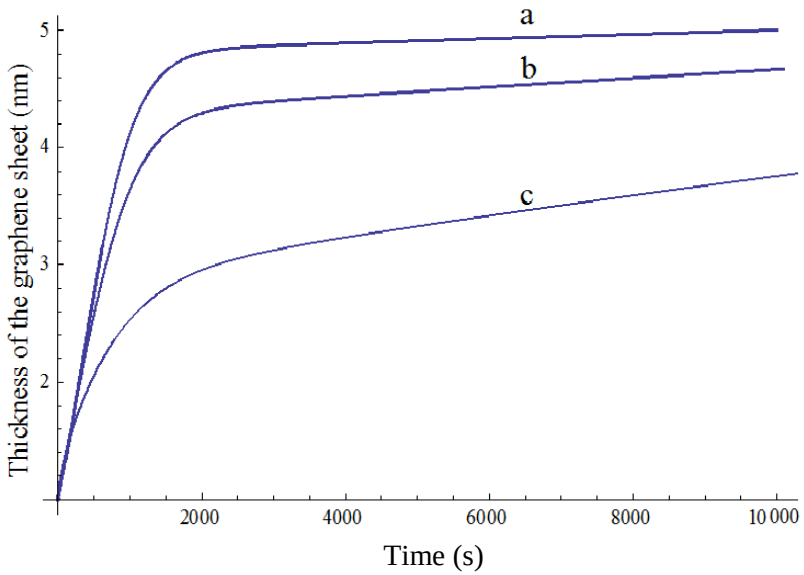

Fig. 3.4. This figure illustrates the time variation of the thickness of the graphene sheet for different ion densities and temperatures of type 2 ion (where a, b, and c correspond to $n_{i20} = 10^{10}\,\text{cm}^{-3}$ and $T_{i0} = 2100$ K, $n_{i20} = 10^{11}\,\text{cm}^{-3}$ and $T_{i0} = 2150$ K, $n_{i20} = 10^{12}\,\text{cm}^{-3}$ and $T_{i0} = 2200$ K, respectively). The other parameters are given in the text and Table 3.1.

Figure 3.5 displays the time evolution of thickness of graphene with RF power (i.e., RF power = 50 W, 100 W, 200 W). From Fig. 3.5, it can be seen that as the RF power is increased the graphene sheet of lesser thickness is observed. This is attributable to the fact that with increasing RF power the electric field in the plasma sheath increases, thereby, increasing the ion bombardment to the vicinity of the graphene sheet which consequently etches up the graphene sheet. The results of Fig. 3.5 comply with the experimental observations of Nang and Kim [4], and Liu *et al.*[5].

Figure 3.6 shows the time-variation of the height of the graphene sheet for different ion density and temperature of type 1 ion (i.e., $n_{i10} = 10^{11}\,\text{cm}^{-3}$ and $T_{i0} = 2150$ K, $n_{i10} = 10^{12}\,\text{cm}^{-3}$ and $T_{i0} = 2200$ K, $n_{i10} = 10^{13}\,\text{cm}^{-3}$ and $T_{i0} = 2250$ K). Fig.3.6 indicates that upon increasing the number density and temperature of type 1 ion, the height of the graphene sheet increases. As the ion density and temperature of type 1 ion increases, the thickness of the plasma sheath increases and faster generation of carbon monomers occurs, consequently, more diffusion

of the carbon ions take place, thereby, increasing the height of the graphene sheet. The results of Fig. 3.6 are in compliance with the experimental findings of Jiang *et al*. [6] (cf. Fig.4 of Jiang *et al.*[6]).

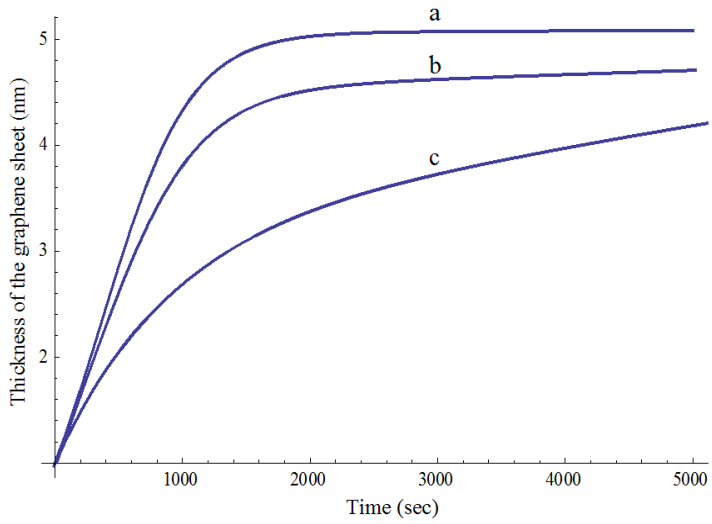

Fig. 3.5. This figure illustrates the time variation of the thickness of the graphene sheet for different RF power. (where a, b, and c correspond to RF power = 50 W, 100W, 200 W, respectively). The other parameters are given in the text and Table 3.1.

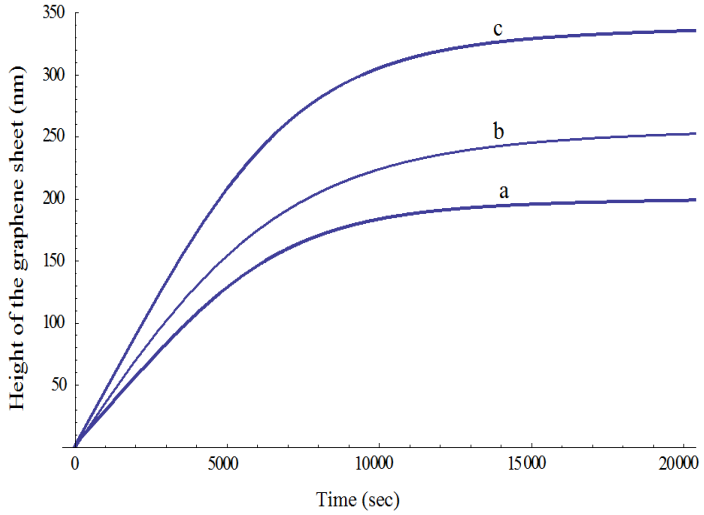

Fig. 3.6. This figure illustrates the time variation of the height of the graphene sheet for different ion density and temperature of type 1 ion (where a, b, and c correspond to $n_{i10} = 10^{11}\,\mathrm{cm}^{-3}$ and $T_{i0} = 2150\ \mathrm{K}$, $n_{i10} = 10^{12}\,\mathrm{cm}^{-3}$ and $T_{i0} = 2200\ \mathrm{K}$, $n_{i10} = 10^{13}\,\mathrm{cm}^{-3}$ and $T_{i0} = 2250\ \mathrm{K}$).The other parameters are given in the text and Table 3.1.

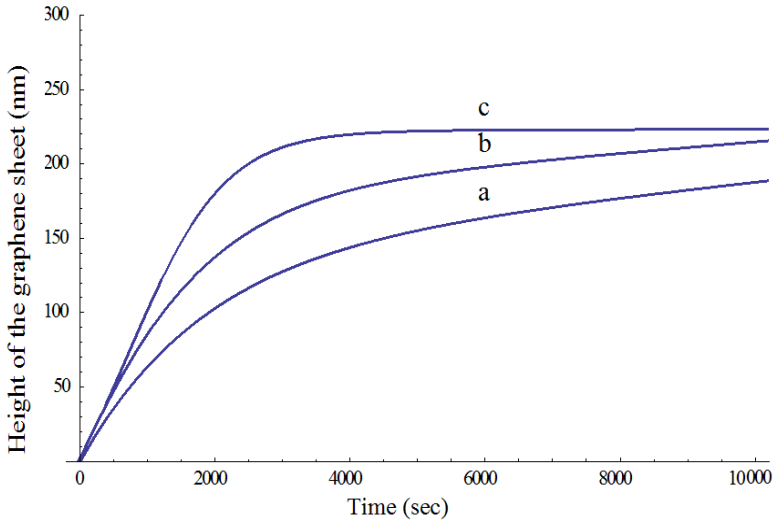

·**Fig. 3.7.**This figure illustrates the time variation of the height of the graphene sheet for different sticking coefficients of atomic species (where a, b, and c correspond to γ_1=0.3, 0.6, 1.0, respectively). The other parameters are given in the text and Table 3.1.

Figure 3.7 shows the time-evolution of the height of the graphene sheet for different values of the sticking coefficients of atomic species of type1(i.e., γ_1=0.3, 0.6, 1.0). The sticking coefficient gives the probability of incorporation of the atomic species into the growing nanostructure [27]. From Fig.3.7, it can be seen that the steady state can be achieved faster as sticking coefficient approaches to unity.

We have hitherto studied the time- evolution of height and thickness of the graphene sheet for a particular set of parameters and further in order to understand the effect of plasma parameters on the field emission factor β ($\approx h/t$, where h is the height and t is the thickness of graphene sheet), we estimated the variation of field enhancement factor with graphene sheet thickness for different electron densities &temperatures and RF powers. It is found that the field enhancement factor increases with increase in the plasma parameters (electron densities & temperatures) and RF powers. (cf. Figs. 3.8 and 3.9, respectively). Figs. 3.8 &3.9 illustrate the variation of field enhancement factor with respect to the saturated value of thickness corresponding to different electron densities &

temperatures, and RF powers, respectively. In this case, β has been calculated for a fixed value of height (i.e., h=160 nm) of the graphene sheet as height has little influence on the field enhancement factor of individual carbon nanostructures [35]. The above result is attributed to the fact that with increase of the plasma parameters (electron densities & temperatures), and RF powers, the thickness of the graphene sheet decreases (cf. Figs. 3.3 and 3.5, respectively) which consequently, enhances the field enhancement factor ($\beta \propto 1/t$ for a fixed value of h) of the graphene sheet.

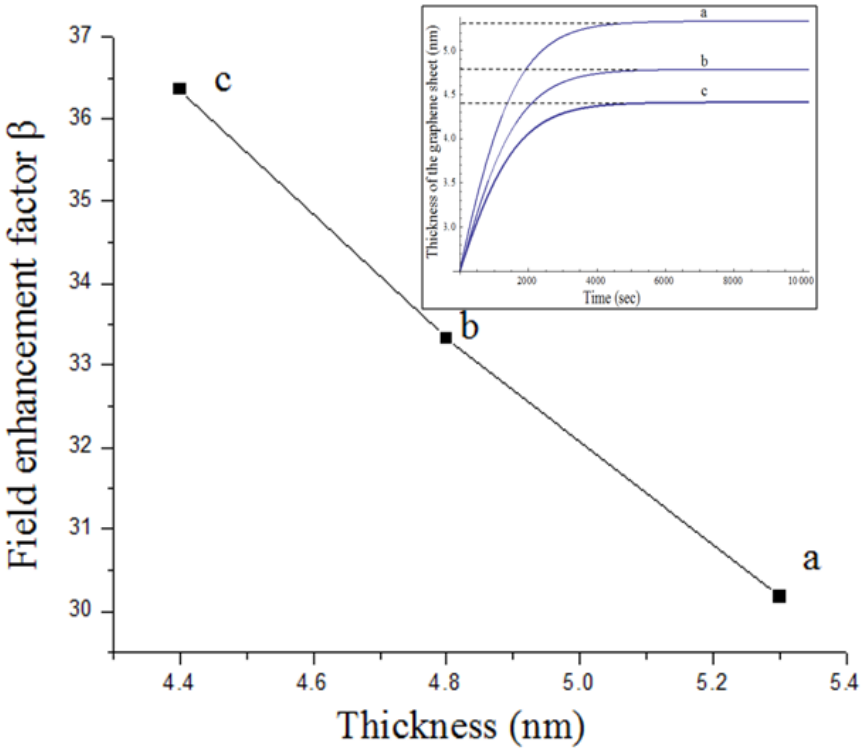

Fig. 3.8. This figure illustrates the variation of field enhancement factor β with the thickness of graphene sheet corresponding to different electron densities and temperatures (where a, b and c corresponds to different values of β at the saturated value of thickness corresponding to different electron densities and temperatures, i.e., a ($=n_{e0}=10^{10}\text{cm}^{-3}$ and $T_{e0}=1.5\text{eV}$), b ($=n_{e0}=10^{11}\text{cm}^{-3}$ and $T_{e0}=1.7\text{eV}$), c ($=n_{e0}=10^{12}\text{cm}^{-3}$ and $T_{e0}=1.9\text{eV}$)). The inset corresponds to the saturated value of thickness at different electron densities and temperatures.

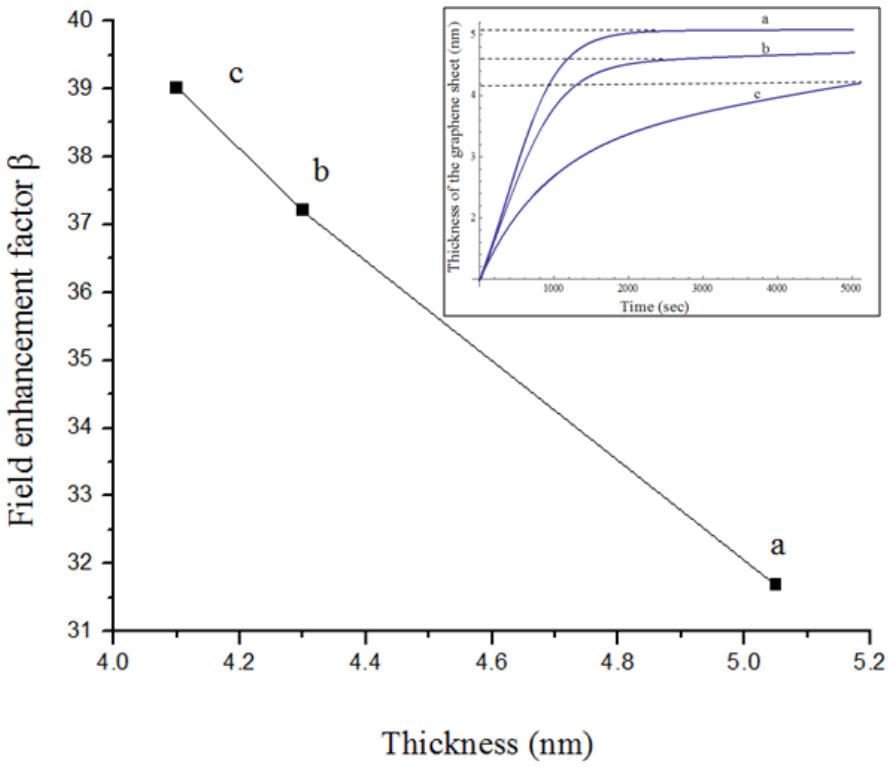

Fig. 3.9. This figure illustrates the variation of field enhancement factor β with the thickness of graphene sheet corresponding to different RF powers (where a, b and c corresponds to different values of β at the saturated value of thickness corresponding to different RF powers, i.e., a (= 50 W), b (= 100 W), and c (= 200 W)). The inset corresponds to the saturated value of thickness at different RF powers.

Using the results obtained, it can be concluded that by suitably varying the plasma parameters, the graphene sheet of large height and lesser thickness can be obtained. The large field enhancement factor $\beta \sim h/t$ can be estimated by manipulating the plasma parameters, and RF power. This result is similar to the experimental observations of Shih *et al.*[14] and Srivastava *et al.*[16]. Therefore, the present work would pave the way for highly efficient graphene-based field emitters.

References

[1] S. Vizireanu, S. D. Stoica, C. Luculescu, L. C. Nistor, B. Mitu, and G. Dinescu, Plasma Sources Sci. Technol. **19**,034016 (2010).

[2] I. Levchenko, M. Keidar, S. Xu, H. Kersten, K. Ostrikov, J. Vac. Sci. Technol. B **31**, 050801 (2013).

[3] K.Ostrikov, Plasma Nanoscience (John Wiley & Sons, 2008).

[4] L.V. Nang and E.-T. Kim, J. Electrochem. Soc. **159**, K93 (2012).

[5] W. Liu, T. Dang, Z. Xiao, X. Li, C. Zhu and X. Wang, Carbon **49,** 884 (2011).

[6] L. Jiang , T. Yang, F. Liu, J. Dong, Z. Yao, C. Shen, S. Deng, N. Xu, Y. Liuand H.-J. Gao, Adv. Mater.**25**, 250 (2013).

[7] Y. Kim, W. Song, S.Y. Lee, C. Jeon, W. Jung, M. Kim, and C.-Y. Park, Appl. Phys. Lett. **98**, 263106 (2011).

[8] S.H. Chan, S.H. Chen, W.T. Lin, M.C. Li, Y.C. Lin and C.-C. Kuo, Nanoscale Res. Lett. **8**, 285 (2013).

[9] M. Zhu, J. Wang, B. C. Holloway, R.A. Outlaw, X. Zhao, K. Hou, V. Shutthanandan, D. M. Manos, Carbon **45,** 2229 (2007).

[10] T-O Terasawa, K. Saiki, Carbon **50,** 869 (2012).

[11] S. Ghosh, K. Ganesan, S.R. Polaki, T. Mathews, S. Dhara, M. Kamruddin, A.K. Tyagi, Appl. Surf. Sci. **349,** 576 (2015).

[12] J. Zhao, M. Shaygan, J. Eckert, M. Meyyappan, and M. H. Rummeli,Nano Lett. **14**, 3064 (2014).

[13] A. Malesevic, R. Kemps, A. Vanhulsel, M.P. Chowdhury, A. Volodin, and C. V. Haesendonck, J. Appl. Phys. **104**, 084301 (2008).

[14] W. -C. Shih, J. -M. Jeng, C. -W. Tsou, J. -T. Lo, H. -C. Chen, and I. -N. Lin, Jpn. J.Appl. Phys. **49,** 08JF11 (2010).

[15] S. Wang, J. Wang, P. Miraldo, M. Zhu, R. Outlaw, K. Hou, X. Zhao, B.C. Holloway, D. Manos, T. Tyler, O. Shenderova, M. Ray, J. Dalton, and G. McGuire, Appl. Phys. Lett. **89**, 183103 (2006).

[16] S.K. Srivastava, A.K. Shukla, V.D. Vankar, V.Kumar, Thin Solid Films **492**, 124(2005).

[17] S. Watcharotone, R. S. Ruoff, and F. H. Read, Physics Procedia **1,** 71 (2008).

[18] R. Miller, Y. Y. Lau, and J.H. Booske,Appl. Phys. Lett. **91**, 074105 (2007).

[19] S. Riikonen, A.V. Krasheninnikov, L. Halonen, and R.M. Nieminen, J. Phys.Chem. C **116**, 5802 (2012).

[20] H. Mehdipour and K. Ostrikov, ACS Nano **6**, 10276 (2012).

[21] Y. Ma, H. Jang, S.J. Kim, C. Pang and H. Chae, Nanoscale Res Lett. **10,** 1 (2015).

[22] Y. Zhang, Q. Zou, H. S. Hsu, S. Raina, Y. Xu, J.B. Kang, J. Chen, S. Deng, N. Xu, and W. P. Kang. ACS Appl. Mater. Interfaces **8**, 7363 (2016).

[23] S. Kumar and K. Ostrikov, Nanoscale **3**, 4296 (2011).

[24] H. Mehdipour, K. Ostrikov, and A. E. Rider, Nanotechnology **21**, 455605 (2010).

[25] M. A. Lieberman and A. J. Lichtenberg, *Principles of Plasma Discharges and Materials Processing* (Wiley Interscience Publication, USA, 1994).

[26] C. H. Lin, H. L. Chang, M. H. Tsai, C. T. Kuo, Diamond Relat. Mater. **11**, 922 (2002).

[27] M. S. Sodha, S. Misra, S. K. Misra, and S. Srivastava, J. Appl. Phys. **107**, 103307 (2010).

[28] A. Tewari and S. C. Sharma, Phys. Plasmas **21**, 063512 (2014).

[29] M. Chhowalla, K. B. K. Teo, C. Ducati, N. L. Rupesinghe, G.A.J. Amaratunga, A.C. Ferrari, D. Roy, J. Robertson, and W. I. Milne, J. Appl. Phys. **90**, 5308 (2001).

[30] J. L. Qi, F. Zhang, X. Wang, L. X. Zhang, J. Cao and J .C. Feng, RSC Adv. **4**, 44434 (2014).

[31] I. Denysenko and K. Ostrikov, J. Phys. D: Appl. Phys. **42,** 015208 (2009).

[32] N. V. Mantzaris, E. Gogolides, A. G. Boudouvis, A. Rhallabi, and G. Turban, J. Appl. Phys. **79**, 3718 (1996).

[33] J. Chen, Z. Bo, G. Lu, *Vertically-Oriented Graphene: PECVD Synthesis and Applications* (Springer International Publishing Switzerland, 2015).

[34] I. Denysenko and N.A. Azarenkov, J. Phys. D: Appl. Phys. **44,** 174031 (2011).

[35] Z. Xu, X. D. Bai, and E. G. Wang, Appl. Phys. Lett. **88**, 133107 (2006).

4

Modeling the effect of doping on the catalyst-assisted growth and field emission properties of plasma-grown graphene sheet

4.1 Brief outline of the chapter

The main focus of the chapter is to understand the better insights of how the nitrogen/boron doping affects the growth profiles of graphene sheet in the reactive plasma environment and estimating the ramifications of doping on the field emission properties from the results obtained.

4.2 Introduction

Plasma treatment offers the advantage of material modification by the introduction of foreign atoms or groups, and thereby altering the material electronic properties [1]. In general, doping with foreign atoms is considered one of the effective methods to intrinsically modify the properties and structure of the graphene sheet (GS), and thus expanding the field emission characteristics. Among the several hetero atoms available for doping, nitrogen and boron are the most frequently used candidates for doping of graphene as they have similar atomic radii size as that of carbon and ability to induce n-type and p-type conduction in graphene. The nitrogen atoms replace the carbon atoms on the carbon nanostructure and function as donors which eventually boost the electron field emission properties whereas the boron atoms reduce the electron concentration due to the formation of electron holes and, therefore the electron field emission decreases [2]. The similar effect of nitrogen and boron doping on the field emission characteristics of carbon nanotubes has been shown theoretically by Sharma *et al.*[3]. Numerous works have been performed to show

that nitrogen and boron doping can effectively change the structure, growth rate, number density and dimensions of graphene [4-7].

Seo *et al.*[4] have investigated the effect of nitrogen concentrations on the dimensions and structure of vertical graphene nanosheets (VGS) using low-temperature plasma-based process. They observed that upon addition of nitrogen to the $CH_4/Ar/H_2$ gas mixture, the VGS length decreases and their number density increases. They also found that the thickness of nanosheets decreases with nitrogen concentration.

Koos *et al.*[5] have synthesized nitrogen doped graphene using methane and ammonia gases and found that the growth rate of graphene decreases by increasing the ammonia gas flow rate. They observed that upon increasing the synthesis temperature and ammonia gas flow rate, the concentration of nitrogen dopants increases.

Tang *et al.*[6] have found that boron doping increases the thickness of graphene (cf. Fig. S2 in the supplementary material of Tang *et al.*[6]). They also revealed that boron content in graphene increases on increasing the ion reaction time of trimethylboron decomposed by microwave plasma.

Jin *et al.*[7] have fabricated nitrogen doped graphene using CVD method with pyridine as both carbon and nitrogen sources. Their results indicate that dopant nitrogen atoms substitute for carbon atoms in the graphene lattice and the synthesized nitrogen doped graphene is monolayer and exhibits n-type behaviour, different from pristine graphene.

Moreover, the influence of nitrogen and boron doping on the field emission characteristics of the graphene has also been studied widely [8-12].

More *et al.* [8] have analyzed the field emission current fluctuations of mulitwalled carbon nanotubes, undoped, nitrogen and boron doped graphene and polyaniline nanotubes. They have shown that amongst these materials, nitrogen doped graphene exhibits low turn-on field and highest field

enhancement factor β. The highest β of nitrogen doped graphene has been attributed to the sharp edges of the graphene.

Takeuchi *et al.*[9] have observed that the electron emission current from the carbon nanowalls (CNWs) increases after the nitrogen plasma treatment. Their findings reveal that incorporation of N atoms increase the nanodomain size, electrical conductivity, and field emission characteristics.

Palnitkar *et al.*[10] used the boron and nitrogen doping to tailor the turn-on voltage and found that the nitrogen doped graphene exhibits the lowest turn on voltage, relative to undoped graphene. They also calculated the field enhancement factor β from the Fowler–Nordheim (FN) plot and found β to be largest for nitrogen-doped graphene followed by undoped and boron doped graphene (cf. Fig.2 of Palnitkar *et al.*[10]). They accredited this observation to the nanometric features and resonance tunnelling.

The low turn-on voltage and increase in the field emission current were also reported by Kashid *et al.*[11] and Soin *et al.*[12]. They explained this behaviour on the basis of change in the structure, improved electrical conductivity, and up-shift of the Fermi level with nitrogen doping.

Using above mentioned motivation, we try to model the effect of different hetero atoms such as nitrogen and boron on the dimensions of GS (i.e., height and thickness) and their repercussion on the GS field enhancement factor. Moreover, despite several experimental evidences, till yet no theoretical model has been developed to study the effect of doping of hetero atoms on the growth and field emission properties of GS. The basic process of catalyst-assisted growth of GS in the presence of plasma remains same as in Chapter 3 but to point up the consequent effects of doping, numerous additional plasma species (i.e., doping species) have been accounted in the plasma and consequently many additional terms and equations have been incorporated in the model of the present chapter.

4.3 Model

Using the model developed in Chapter 3, the catalytic growth of graphene sheet and, typically a PECVD case is examined through a model that accounts acetylene, hydrogen and ammonia/diborane as reaction gases. Fig. 4.1 shows the schematic of graphene sheet growth on the catalyst copper (Cu) over the silicon (Si) substrate surface, subjected to the incoming neutral and ionic species from the reactive plasma of C_2H_2+H_2+NH_3/B_2H_6 gas mixture. In reality, reactive plasma contains a plethora of different ions [13]. However, for simplicity, and following the experimental observations [14] and theoretical works [13,15], the present model considers a plasma consisting of electrons, ions of acetylene ($C_2H_2^+$), hydrogen (H^+), doping ions of NH_3^+/$B_2H_6^+$ denoted as ions of type 1, 2 and 3, respectively and neutrals of type 1, (acetylene, C_2H_2), type 2 (hydrogen, H_2) and type 3 (NH_3/B_2H_6). Among these, ammonia and diborane ions serve the purpose of nitrogen and boron doping, respectively, of the GS.

The stages for the catalyst-assisted growth of doped GS in plasma environment considered in the present model are:

(i) Fragmentation of catalyst film into catalyst nanoparticles.

(ii) Nucleation of graphitic CN_x/CB_x clusters at the catalyst surface on account of reactive acetylene and doping species generated due to ionization of gas within the chamber [16].

(iii) Formation of doped graphene islands due to diffusion and agglomeration of these clusters [16].

(iv) Lateral extension or parallel growth of doped GS due to coalescence of the doped graphene islands [17].

(v) The upward bending of the GS on account of stress generated at the graphene island boundaries.

(vi) The vertical growth of GS via delivery of carbon atoms at the graphene island boundaries.

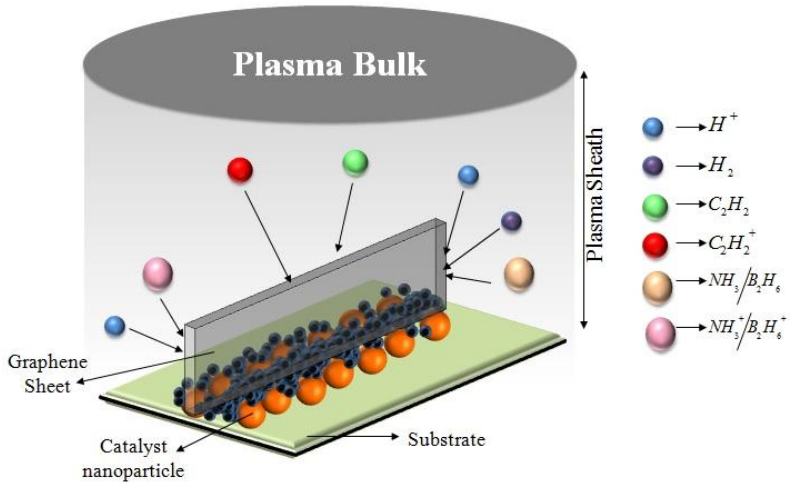

Fig. 4.1. Schematic of particle deposition on the graphene sheet and the catalyst nanoparticles.

Following Mehdipour *et al.*[15], the sheath equations used are described by the continuity equation

$$\frac{d}{dz}\left(n_p v_{pz}\right) = f_{iz} n_e, \tag{4.1}$$

and the ion-momentum balance equation:

$$M_p n_p v_{pz} \frac{dv_{pz}}{dz} = e n_p \frac{d\phi}{dz} - M_p n_p f_{pn} v_{pz}, \tag{4.2}$$

where p denotes either e, $C_2H_2^+$, H_2^+ or $NH_3^+/B_2H_6^+$. M_p, n_p , and v_{pz} are the mass, number density and fluid velocity of the charged species p, respectively. Furthermore, f_{iz} and f_{pn} are the ionization frequency and collision frequency of the electrons and ion species with neutrals, respectively.

The sheath potential ϕ is determined by the Poisson's equation which relates the densities of charge particles to the electrostatic potential.

$$\frac{d^2\phi}{dz^2} = -4\pi e \sum_p \xi_p n_p, \tag{4.3}$$

where ξ_p is the p^{th} ion to electron number density ratio and is supplemented by the condition $\sum_p \xi_p = 1,$ and $0 < \xi_p < 1.$

4.3.1 Charging of graphene

Equation (4.4) describes the charge developed on the GS due to accretion of electrons and positively charged ions on the surface of the GS.

$$Q'[\tau] = \sum_{j=1}^{3} I_{ijgn} - \gamma_e I_{egn} \ , \tag{4.4}$$

where Q is the charge over the GS, j refers to 1, 2 and 3 type of positively charged ions, γ_e is the sticking coefficient of the constituent electrons, I_{ijgn} and I_{egn} are the ion and electron collection current at the GS surface, respectively.

$$I_{ijgn} = n_{ij}(x)\left(lt + ht + lh\right)\left(\frac{k_B T_{ij}}{2\pi^2 m_{ij}}\right)^{\frac{1}{2}}\left\{\frac{2}{\sqrt{\pi}}\left(\frac{eV_S}{k_B T_i}\right)^{\frac{1}{2}} + \exp\left[\frac{eV_S}{k_B T_{ij}}\right] erfc\left[\left(\frac{eV_S}{k_B T_{ij}}\right)^{\frac{1}{2}}\right]\right\} \times \exp\left[-\frac{eU_S}{k_B T_S}\right],$$

$$I_{egn} = \left(\frac{k_B T_e}{2\pi^2 m_e}\right)^{\frac{1}{2}} n_e(x)\left(lt + ht + lh\right)\exp\left[\frac{eV_S}{k_B T_e} + \frac{eU_S}{k_B T_s}\right]$$

where l, t, and h are the length, thickness and height of the GS, respectively, T_{ij} is the ion temperature, m_{ij} is the ion mass (subscript j refers to either 1, 2 or 3 type of positively charged ion as explained earlier), $n_{ij}(x) = n_{ij0}\left(1 - \frac{2e\phi(x)}{m_{ij}v_{i0}^2}\right)^{-1/2}$ is the ion density at any point within the plasma sheath; v_{i0} is the ion velocity, $\phi(x) = \phi_0 \exp\left(-\frac{|x|}{\lambda_d}\right)$ is the electrostatic potential; ϕ_0 is the negative potential at the surface and λ_d is the Debye length, T_S is the substrate or catalyst temperature (assuming catalyst and substrate to be at the same temperature), V_S is the surface potential of the graphene sheet (Refer Eq. (A.2) of Appendix A),

$n_e(x) = n_{e0} \exp\left[\frac{|e|\phi(x)}{k_B T_e}\right]$ is the electron density in plasma sheath, T_e is the electron temperature, m_e is the mass of electron, U_s is the substrate bias and k_B is the Boltzmann constant [18].

In Eq. (4.4), first term on the right hand side describes the charge developed on the GS surface due to accretion of positively charged ions of type 1, 2, and 3. The last term indicates the reduction in charge on account of accretion of electrons at the surface of the GS.

4.3.2 Kinetic equation of electron density

Equation (4.5) describes the growth rate of electron density in plasma

$$n_e'[\tau] = \sum_{j=1}^{3} \beta_j n_j - \sum_{j=1}^{3} \alpha_j n_e n_{ij} - \gamma_e n_{gn} I_{egn}, \qquad (4.5)$$

where β_j is the coefficient of ionization of the constituent neutral atoms due to external field, n_e is the electron number density, $\alpha_j(T_e) = \alpha_{j0}\left(\frac{300}{T_e}\right)^k$ cm^3/sec is the coefficient of recombination of electrons and positively charged ions [19], $k = -1.2$ is a constant and j refers to 1, 2 and 3 types of ions.

In Eq. (4.5), the first term on the right side is the gain in electron density per unit time because of ionization of neutral atoms of type 1, 2, and 3. The second term and third term display the decaying rate of the electron density due to electron–ion recombination and the electron collection current at the surface of the GS, respectively.

4.3.3 Kinetic equation of positively charged density

Equations $(4.6a) - (4.6c)$ refer to the growth rate of positively charged ions of type 1, 2, and 3, respectively in plasma.

$$n_{i1}^{'}(\tau) = \beta_1 n_1 - \alpha_1 n_e n_{i1} - n_{gn} I_{i1gn} - J_{ai1} + J_{desorpi1} + \sum_i k_{i1} n_1 n_{i3}, \quad (4.6a)$$

$$n_{i2}^{'}(\tau) = \beta_2 n_2 - \alpha_2 n_e n_{i2} - n_{gn} I_{i2gn} - J_{ai2} + J_{desorpi2} + J_{th} + \sum_i k_{i2} n_2 n_{i3}, \quad (4.6b)$$

$$n_{i3}^{'}(\tau) = \beta_3 n_3 - \alpha_3 n_e n_{i3} - n_{gn} I_{i3gn} - J_{ai3} + J_{desorpi3} + \sum_i k_{i1} n_1 n_{i3} + \sum_i k_{i2} n_2 n_{i3}, \quad (4.6c)$$

where $J_{aij}\left(= P_i (2\pi m_{ij} k_B T_{ij})^{-1/2} \times {}^{n_{ij}}\!/_{J_{ij}}\right)$ is the adsorption flux onto the catalyst substrate surface [20]; P_i is the partial pressure of adsorbing species, J_{ij} and n_{ij} are the ion flux and ion number density at the catalyst-substrate surface, respectively, j refers to either 1, 2 or 3 type of ions, $J_{desorpij} = n_{ij}\nu \exp\left({}^{-\varepsilon_{ai}}\!/_{k_B T_{ij}}\right)$ is the desorption flux from the catalyst-substrate surface [20]; ν is the thermal vibration frequency, ε_{ai} is the adsorption energy, $J_{th} = n_H \nu \exp\left({}^{-\delta\varepsilon_{th}}\!/_{k_B T_s}\right)$ is the flux of type 2 ion (namely hydrogen) on account of thermal dehydrogenation; $\delta\varepsilon_{th}$ is the activation energy of thermal dehydrogenation, n_H is the hydrogen ion number density at catalyst-substrate surface.

The first term on the right hand side in Eqs. $(4.6a)-(4.6c)$ describes the gain in ion density per unit time on account of ionization of neutral atoms. The second and third term represents the rate of decrease in positively charged ion density due to electron-ion recombination and ion collection current at the surface of the graphene, respectively. The next two terms denote the adsorption and desorption of ions to/from the catalyst-substrate surface, respectively. The term J_{th} in Eq. (4.6b) represents the increase of hydrogen ion number density in plasma because of thermal dehydrogenation [18]. The last term in Eqs. $(4.6a)-(4.6c)$ accounts for the gain of ion density due to ion-neutral reactions [21] and their reaction rate coefficients [22,23] are $k_{i1} = 1.4\times10^{-9}$ cm^3/sec and $k_{i2} = 7.8\times10^{-9}\ T_n^{-0.39}\exp(-14.8/T_n)$ cm^3/sec.

Neha Gupta
Delhi Technological University, Delhi, India

4.3.4 Kinetic equation of neutral species density

Equations $(4.7a)-(4.7c)$ refer to the growth rate of neutrals of type 1, 2, and 3, respectively in plasma.

$$n_1^{'}(\tau) = \alpha_1 n_e n_{i1} - \beta_1 n_1 + n_{gn}\left(1-\gamma_{i1}\right) I_{i1gn} - n_{gn}\gamma_1 I_{1gn} - \sum_i k_{i1} n_1 n_{i3}, \quad (4.7a)$$

$$n_2^{'}(\tau) = \alpha_2 n_e n_{i2} - \beta_2 n_2 + n_{gn}(1-\gamma_{i2}) I_{i2gn} - n_{gn}\gamma_2 I_{2gn} - \sum_i k_{i2} n_2 n_{i3}, \quad (4.7b)$$

$$n_3^{'}(\tau) = \alpha_3 n_e n_{i3} - \beta_3 n_3 + n_{gn}\left(1-\gamma_{i3}\right) I_{i3gn} - n_{gn}\gamma_3 I_{3gn} - \sum_i k_{i1} n_1 n_{i3} - \sum_i k_{i2} n_2 n_{i3}, \quad (4.7c)$$

where $I_{jgn} = n_j (lt + ht + lh)\left(k_B T_n / 2\pi^2 m_j\right)^{1/2}$ is the neutral collection current at the surface of graphene, j refers to either 1, 2 or 3 type of neutral atom, T_n is the neutral temperature, m_j is the mass of neutral atom, n_j is the neutral atom density, γ_j and γ_{ij} are the sticking coefficient of corresponding neutral atoms and ions, respectively.

The first term on the right side in Eqs. $(4.7a)-(4.7c)$ denotes the gain in neutral atom density per unit time due to electron–ion recombination. The next two terms represent the decaying rate of neutral atom density due to ionization, gain in neutral density due to neutralization of ions collected at the graphene surface, respectively. The fourth term is the accretion of neutral atoms of species 1, 2 and 3 on the graphene surface [11] and the last term is the decay in neutral atom density on account of neutral-ion reactions [24].

4.3.5 Kinetic equation for the growth of graphene nuclei

Initially, the applied plasma power fragments the catalyst film into catalyst nanoislands. We consider the size of the catalyst nanoparticle to be 40 nm [25]. Various processes such as thermal and ion-induced dissociation of hydrocarbon gas; adsorption and decomposition of acetylene ions; decomposition, interaction of adsorbed acetylene ions with hydrogen; thermal dissociation of carbon source gas of acetylene ions, surface diffusion;

accretion and other processes leads to the formation of C-atom clusters. The surface diffusion (with energy barrier E_{sdCl}) and agglomeration of these C-clusters lead to the formation of graphene island (with radius R_g) [17].

$$\frac{d}{d\tau}\left(\pi R_g^2\right)=\left[\left\{2n_{CH}\nu\exp\left(\frac{-\delta E_i}{k_BT_s}\right)+2\theta_{CH}J_{i1}y_d+2J_{i1}+\frac{J_{i1}\sigma_{ads}J_{i2}}{\nu}+\right.\right.$$
$$\left.+J_C\right\}\times m_c\left\{J_{i1}(1-\theta_t)+\frac{J_{i1}\sigma_{ads}J_H}{\nu}+J_{i1}\exp\left(\frac{-\delta E_i}{k_BT_s}\right)\right\}m_{i1}\Bigg]$$
$$\times\frac{2\pi R_{cat}}{\pi R_{cat}^2\rho_{cat}}\left(D_1\exp\left(\frac{-E_{sdC}}{k_BT_S}\right)+D_2\exp\left(\frac{-E_{sdCl}}{k_BT_S}\right)\right)\times\left(\frac{1}{I_{i1g}}\right)$$
$$+\gamma_{C_2H_2}\pi R_{cat}^2I_{C_2H_2g}+\gamma_d\pi R_{cat}^2I_{dg}\ , \qquad (4.8)$$

where R_g is the radius of the graphene nuclei, R_{cat} is the radius of the catalyst nanoparticle, ρ_{cat} is the mass density of the catalyst particle, $n_{CH}\left(=\theta_{CH}\nu_0\right)$ is the surface concentration of CH; θ_{CH} is the surface coverage by C_2H_2 species [15] and $\nu_0\left(\approx 10^{15}\,\text{cm}^{-2}\right)$ is the number of adsorption sites per unit area [15], $\delta E_i\,(\approx 1.87\ eV)$ is the thermal energy barrier [16], $y_d\,(\approx 2.49\times10^{-2}+3.29\times10^{-2}\times E_i$; where E_i is the ion energy in eV) is the stitching probability [26], $J_{ij}\left(=n_{ij}\left(k_BT_e/m_{ij}\right)^{1/2}\right)$ is the flux of type *j* ion [18]; where, *j* refers to 1 or 2 type of ion, $\sigma_{ads}\left(\approx 10^{-16}cm^2\right)$ is the cross-section for the reactions of atomic hydrogen [15], $J_\alpha=\left(n_\alpha v_{th\alpha}/4\right)$ is the flux of impinging species α (where $\alpha=C,H$); C and H stands for carbon and hydrogen species, respectively, n_α and $v_{th\alpha}$ are the number density and thermal velocity of α species, respectively [15], $\nu(=10^{13}\text{Hz})$ is the thermal vibration frequency [15], m_C (=12 a.m.u) is carbon atom mass, m_{i1}(= 26 a.m.u

for $C_2H_2^+$) is the mass of type 1 ions, $D_1 \exp\left(\frac{-E_{sdC}}{k_B T_s}\right)$ and $D_2 \exp\left(\frac{-E_{sdCl}}{k_B T_s}\right)$ are the surface diffusion coefficients of carbon monomers and C-atom clusters, respectively with corresponding activation energies, E_{sdC} =0.1 eV and E_{sdCl} = 0.82 eV, respectively [17].

$I_{ijg} = \left(\pi R_g^2 \left(\frac{8k_B T_i}{\pi m_{ij}}\right)^{1/2} n_{ij}(x)\left[1 - Q\gamma_{ji}\right] \exp\left[-\frac{eU_s}{k_B T_s}\right]\right)$ is the ion collection current at the surface of the graphene nuclei, (where, j refers to either 1 or 2 type of ion); $\gamma_{ji} = e^{-2} R_g k_B T_s$, $I_{jg}\left(= \pi R_g^2 \left(8k_B T_n / \pi m_j\right)^{1/2} n_j\right)$ is the neutral collection current at the surface of the graphene nuclei, j refers to neutral atom of type 1, 2 or 3, $I_{C_2H_{2g}}$ and I_{dg} corresponds to the collection current of acetylene and doping neutral atom, respectively and, $\gamma_{C_2H_2}$ and γ_d are the sticking coefficients of neutrals of type 1 and 3, respectively.

Equation (4.8) outlines the growth of graphene island on the catalyst nanoparticle. Here, the first term and second term in the first bracket on the right side [6] indicates the generation of carbon atoms on the catalyst surface due to thermal dissociation of acetylene ions (with activation energy of thermal dissociation, δE_i) and ion induced dissociation of C_2H_2, respectively [15]; third term denotes the decomposition of positively charged hydrocarbon ions, i.e., $C_2H_2^+$; fourth term is the interaction of adsorbed type 1 ions with hydrogen ions [15]; fifth term denotes the rate of the incoming flux of carbon atoms onto the catalyst particle [15]. The terms in the second bracket refers to the adsorption flux of type 1 ions to the catalyst surface, interaction of adsorbed type 1 ions with atomic hydrogen from plasma, and thermal dissociation of hydrocarbon source gas C_2H_2, respectively [15]. The factor I_{i1g} accounts for the collection current of type 1 ion on the growing graphene island. The last two terms denote the accretion of neutral acetylene and doping gas atoms to the graphene island.

4.3.6 Growth rate equation for graphene sheet

$$l\frac{d(h\times t)}{d\tau}=\left(\begin{array}{c}\left(\frac{n_1}{\nu}\times D_1\exp\left\{\frac{E_d+E_{inc}}{k_BT_s}\right\}\right)\frac{\pi R_g^2}{2\pi R_g}\times\left(I_{i1gn}\right)\\+\left(\gamma_{C_2H_2}I_{C_2H_2gn}\right)+\left(\gamma_dI_{dgn}\right)\end{array}\right)\times\frac{M_{gn}}{\rho_{gn}},\qquad(4.9)$$

$$\left[h(\tau)+l\right]\frac{d(t)}{d\tau}=\left\{J_{i2}\exp\left(\frac{-\delta E_{sdh}}{k_BT_s}\right)+J_{i2}(1-\theta_t)+J_{i2}+\theta_{CH}\left(J_{i2}\,y_d+\nu_0\nu\right.\right.$$
$$\left.\exp\left(\frac{-\delta E_i}{k_BT_s}\right)\right)+\theta_{NH}\left(J_{i2}y_d+\nu_0\nu\exp\left(\frac{-\delta E_i}{k_BT_s}\right)\right)\Bigg\}\frac{h(\tau)}{n_{i2}}+$$
$$\gamma_{C_2H_2}\pi R_g^2I_{C_2H_2gn}+\gamma_d\pi R_g^2I_{dgn},\qquad(4.10)$$

where ρ_{gn} is the GS density, M_{gn} is the mass of the growing GS ($M_{gn}\approx 12g$), θ_{CH} and θ_{NH} are the surface coverage by C_2H_2 and NH_3, respectively.

The growth of graphene island results in the formation of planar GS. Due to influence of stress and/or localized electric field due to plasma at the graphene island boundaries, the initial planar growth of GS eventually switches to the vertical growth of GS. At this stage, GS grows due to continuous delivery of dissociated carbon species from the plasma (i.e., due to ion and neutral collection current) at the surface of the growing doped GS [27]. The last two terms in Eq. (4.9) represent the sticking of neutral atoms 1 and 3 at the GS and the factor I_{i1gn} corresponds to the ion collection on the growing doped GS. The diffusion (with energy barrier, $E_d\approx 0.13eV$) and attachment of carbon atoms (with energy barrier, $E_{inc}\approx 0.4$ eV) at the peripherals of the growing graphitic platelets also contribute to the growth of GS [28]. The similar effect has been incorporated in the first term of Eq. (4.9). Moreover, in Eq. (4.9), length (l) of the doped GS has been presumed to be $0.81\,\mu m$ [4] as we believe that the length of the GS progresses during the planar growth of the GS. Finally, the growing edges of the GS are terminated by the etching of carbon atoms [27].This effect has been accounted in Eq.

(4.10) which describes the decrease in thickness of graphene sheet due to etching of carbon atoms. In Eq. (4.10) the first term on the right hand side refers the incoming flux of type 2 ions, i.e., hydrogen due to thermal dehydrogenation of type 1 ions (see Ref.15) and second term accounts the adsorption of type 2 ions to the surface. The third term is the decomposition of positively charged ions of type 2 (see Ref. 15); fourth term describes ion induced dissociation of acetylene (see Ref. 15), and fifth term (see Ref. 15) is due to the incorporation of hydrogen ions due to thermal dissociation of acetylene ions. The next two terms describe the generation of hydrogen due to ion induced dissociation of ammonia [23] and thermal decomposition of ammonia ions [29]. The last two terms denote the sticking of neutrals of type 1 and 3, respectively on the surface of the GS.

4.4 Results and discussion

Using the analytical equations presented in Section 4.3, we investigate the influence of doping on the dimensions (i.e., height and thickness) of GS with time and its repercussions on the field enhancement factor of GS. To elucidate this effect, we have simultaneously solved first order differential Eqs. (4.1)-(4.10) numerically with the aid of MATHEMATICA software using typical glow discharge plasma parameters i.e., at appropriate boundary conditions, viz., at τ =0 given in Table 4.1.

Figure 4.2 shows the variation of thickness of undoped, nitrogen-doped, and boron-doped GS with time. From Fig. 4.2, it can be seen that doping of GS with heteroatoms such as nitrogen decreases the thickness of GS and boron increases the thickness of GS. The decrease in thickness of nitrogen doped GS can be explained in many ways. One such explanation is that the introduction of ammonia in the chamber produces nitrogen and hydrogen species in the plasma which leads to the etching of the GS edges. Moreover, several researchers have reported that addition of ammonia results in the generation of cyanide species (due to reaction of nitrogen species with hydrocarbon species) which further

Table 4.1. Boundary conditions used in the present model

Parameter	Description	Initial Value
n_{e0}	electron density	10^{10} cm^{-3}
n_{i10}	number density of type 1 ion	$0.8\,n_{e0}$
n_{i20}	number density of type 2 ion	$0.7\,n_{e0}$
n_{i30}	number density of type 3 ion	$0.5\,n_{e0}$
n_{j0}	number density of neutral species	5×10^{12} cm^{-3}
T_{e0}	electron temperature	1.6 eV
T_{i0}	ion temperature	2400 K
T_{n0}	neutral temperature	2000 K
T_s	substrate temperature	550 ^{0}C
Q_0	charge on the GS surface	-1 stat C
m_{i1}	mass of ion 1	26 a.m.u for $C_2H_2^+$
m_{i2}	mass of ion 2	1 a.m.u for H^+
m_{i3}	mass of ion 3	17 a.m.u for NH_3^+ and 27.62 a.m.u for $B_2H_6^+$
R_{g0}	radius of graphene nuclei	80 nm (ref.[32])
ρ_{ct}	density of catalyst Cu	8.96g/cm^3
$\alpha_{10} \approx \alpha_{20}$	coefficient of recombination of electrons and ions	1.12×10^{-7}cm^3/sec
γ_{ij}	sticking coefficient of ions	1
γ_e	sticking coefficient of electron	1

augments the etching of the GS and thereby leads to thinning of the GS [14, 7, 30,31]. It has also been reported that NH_3 is more effective source of atomic hydrogen than H_2, therefore the etching effect of hydrogen is more pronounced in nitrogen doped GS as compared to undoped GS [30]. Furthermore, as ammonia ions contain nitrogen which is pentavalent, the presence of nitrogen atom on the GS surface produces an extra electron which increases the ionization of neutral atoms, therefore the number density of neutral atoms available for accretion decreases and eventually lead to GS with reduced thickness. However, in the case of boron doped GS, boron captures an electron

from the GS surface, which decreases the electron density, and hence ionization of neutral atoms reduces. Thus, the thickness of boron doped GS is high due to the reduced ionization and increased number density of neutral atoms available for accretion. The results of Fig. 4.2 are in compliance with the experimental observations of Seo *et al*. [4] and Tang *et al*. [6] (cf. Fig.S2 in supporting information of Tang *et al*. [6]).

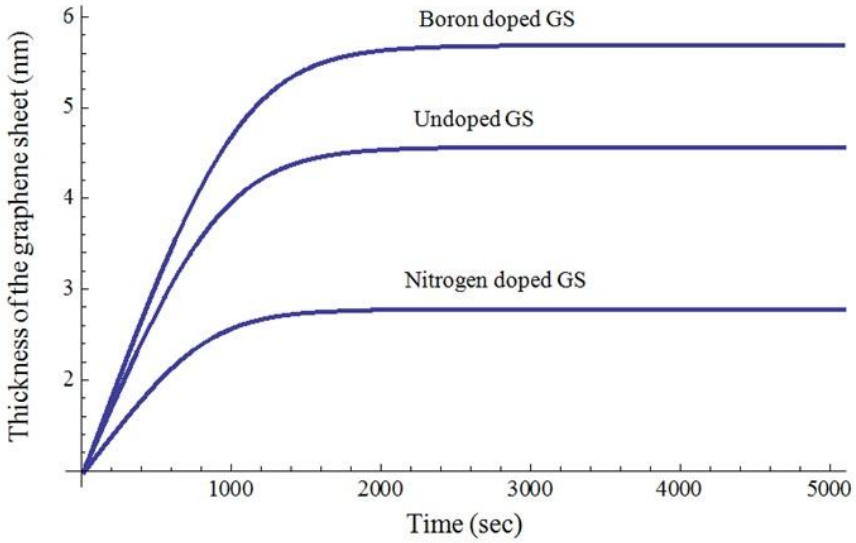

Fig. 4.2. This figure illustrates the time variation of the thickness (in nm) of undoped, nitrogen doped, and boron doped graphene sheet. The other parameters are given in the text and Table 4.1.

Figure 4.3 illustrates the variation of height of undoped, nitrogen doped, and boron doped GS with time. Fig. 4.3 indicates that the height of graphene sheet shortens with nitrogen doping and increases upon doping with boron. This is because the neutral atoms available for accretion is less in the case of nitrogen doping as compared to boron doping, as explained above for Fig. 4.2. The similar effect can be seen from Fig. 4.4 which indicates that the hydrocarbon density decays faster for nitrogen-doped GS followed by undoped and boron-doped GS. In addition, the Fig.4.4 also displays that at a particular time, the hydrocarbon density is least for nitrogen doped GS followed by undoped and boron doped GS. It is believed that upon doping with nitrogen, the generation of cyanide and hydrogen species increases which form a barrier for GS growth. These species act as the sink for carbon that might otherwise participated in the GS growth [26]. The reduction in number density of hydrocarbon species upon addition of ammonia is in compliance with the results

of Bell *et al.*[14], Woo *et al.*[25], and Smith *et al.*[31]. The results of Fig. 4.3 are in accordance with the experimental works of Koos *et al.*[5] (cf. Fig. 4 of Koos *et al.* [5]). The similar effect of nitrogen and boron doping on the height was observed by Sumpter *et al.*[33] and Blase *et al.*[34] in their nitrogen and boron mediated growth of carbon nanotubes, respectively

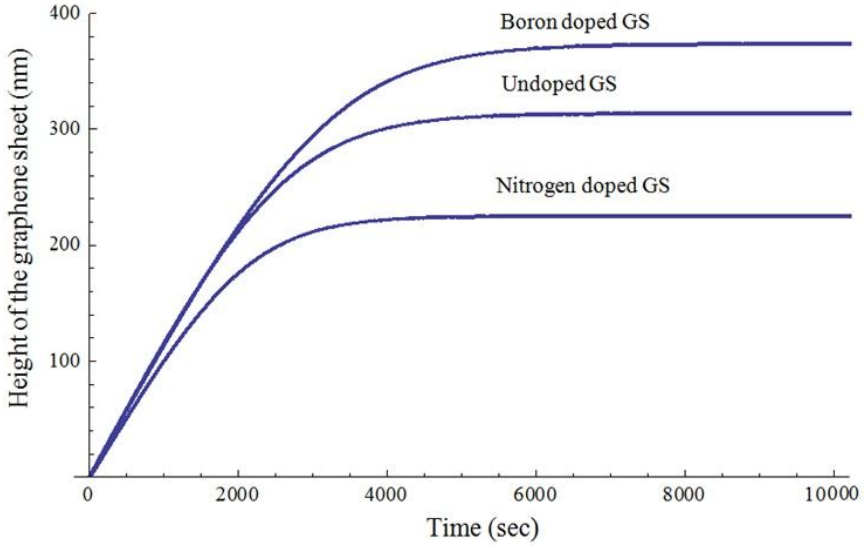

Fig. 4.3. This figure illustrates the time variation of the height (in nm) of undoped, nitrogen doped, and boron doped graphene sheet. The other parameters are given in the text and Table 4.1.

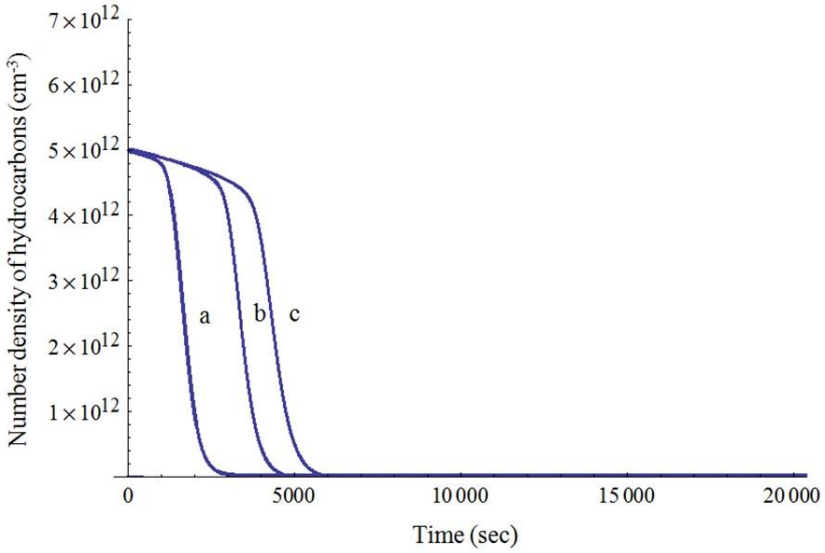

Fig. 4.4. This figure illustrates the time variation of hydrocarbon number density (in cm^{-3}) for undoped (b), nitrogen doped (a) and boron doped (c) graphene sheet. The other parameters are given in the text and Table 4.1.

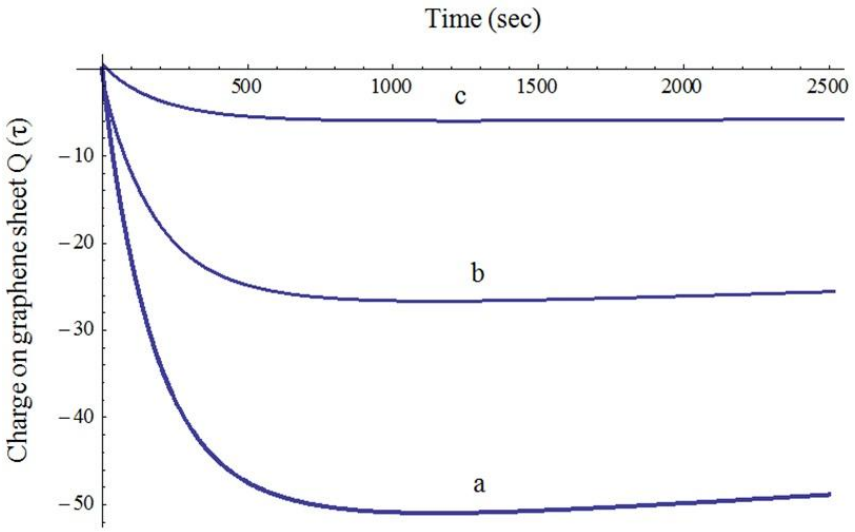

Fig. 4.5. This figure illustrates the time variation of charge for undoped (b), nitrogen doped (a) and boron doped (c) graphene sheet.

Figure 4.5 depicts the time evolution of charge on undoped, nitrogen and boron doped GS. From Fig. 4.5, it can be seen that the charge developed on the nitrogen doped GS is more followed by undoped and boron doped GS. This is ascribed to the fact that upon nitrogen doping the electron number density increases whereas upon doping with boron, the concentration of electron holes increases that engulfs the electron and consequently retards the electron density. The n and p type feature of nitrogen doped and boron doped GS, respectively can be accredited to this observation.

The field emission characteristics are primarily characterized by the field enhancement factor β that specifies the amplification of electric field at the tip of the emitters. The field enhancement factor β ($\approx h/t$, where h is the height and t is the thickness of the GS) [35,36] of GS is mainly dependent on the geometry of the GS. From the above results obtained, we found that the height and thickness of GS changes with the effect of doping. Thus, in order to study the effect of doping on the field emission characteristics of GS, we calculated the field enhancement factor corresponding to saturated value of thickness (i.e., 4.4 nm for undoped GS, 2.65 nm for nitrogen doped GS and 5.6 nm for boron doped GS) and height (i.e., 300 nm for undoped GS, 215 nm for nitrogen doped GS and 360 nm for boron doped GS) for all three types of GS. The variation of field enhancement factor β for the undoped, nitrogen doped and boron doped

GS is illustrated in Fig. 4.6. It is found that nitrogen doped GS has highest field enhancement factor followed by undoped and boron doped GS. This result is attributed to the fact that nitrogen doped GS has least thickness followed by undoped and boron doped GS. Moreover, it can also be seen from Fig. 4.2 and 4.3 that the effect of nitrogen doping is more pronounced on the thickness of GS than on the height of the GS. The results of Fig. 4.6 are similar to the experimental observations of More *et al.*[8], Takeuchi *et al.*[9], Palnitkar *et al.* [10], Kashid *et al.*[11], and Soin *et al.*[12]. Hence, doping of GS with nitrogen improves the field emission characteristics of GS, and boron doping hampers the field emission from GS.

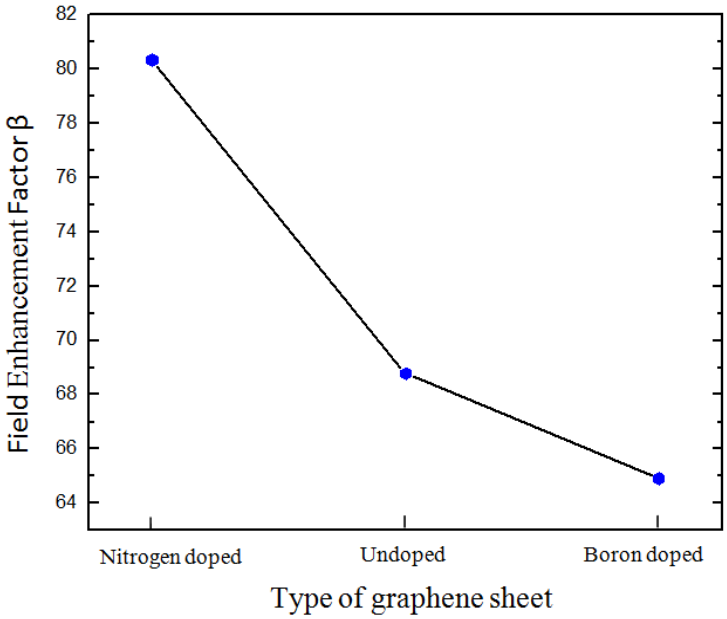

Fig. 4.6. This figure illustrates field enhancement factor β for undoped, nitrogen doped and boron doped graphene sheet.

References

[1] Y. Wang, Y. Shao, D.W. Matson, J. Li, and Y. Lin, ACS Nano **4**, 1790 (2010).

[2] L .H. Chan, K. H. Hong, D. Q. Xiao, W. J. Hsieh, S. H. Lai, H. C. Shih, T. C. Lin, F. S. Shieu, K. J. Chen, and H. C. Cheng, Appl. Phys. Lett. **82,** 4334 (2003).

[3] S. C. Sharma, A. Tewari, and R. Gupta, Journal of Atomic, Molecular, Condensate and Nanophysics **6**, 195 (2015).

[4] D. H. Seo, S. Kumar, A. K. Rider, Z. Han, and K. Ostrikov, Opt. Mat. Express **2**,700 (2012).

[5] A. A. Koos, A. T. Murdock, P. N.-Incze, R. J. Nicholls, A. J. Pollard, S. J. Spencer, A. G. Shard, D. Roy, L. P. Biro, and N. Grobert, Phys. Chem. Chem. Phys.**16**,19446 (2014).

[6] Y. -B. Tang, L .-C.Yin, Y. Yang, X. -H. Bo, Y. -L. Cao, H. -E. Wang, W. -J. Zhang, I. Bello, S. -T. Lee, H. -M. Cheng, and C. -S. Lee, ACS Nano **6**, 1970 (2012).

[7] Z. Jin, J. Yao, C. Kittrell, and J. M. Tour, ACS Nano **5**, 4112 (2011).

[8] M. A. More, R. V. Kashid, S. S. Patil, D. R. Shinde, D.S. Joag, 25th International Vacuum Nanoelectronics Conference, Jeju, pp.1-2, 2012.

[9] W. Takeuchi, H. Kondo, T. Obayashi, M. Hiramatsu, and M. Hori, Appl. Phys. Lett. **98**, 123107 (2011).

[10] U. A. Palnitkar, R. V. Kashid, M. A. More, D. S. Joag, L. S. Panchakarla, and C.N. R. Rao, Appl. Phys. Lett. **97**, 063102 (2010).

[11] R.V. Kashid, M. Z. Yusop, C. Takahashi, G. Kalita, L. S. Panchakarla, D. S. Joag, M. A. More, and M. Tanemura, J. Appl. Phys. **113**, 214311 (2013).

[12] N. Soin, S. S. Roy, S. Roy, K. S. Hazra, D. S. Misra, T. H. Lim, C. J. Hetherington, and J.A. McLaughlin, *J. Phys. Chem. C* **115** (13), 5366 (2011).

[13] I. Denysenko and N. A. Azarenkov, J. Phys. D: Appl. Phys. **44**, 174031 (2011).

[14] M. S. Bell, R. G. Lacerda, K. B. K. Teo, N. L. Rupesinghe, G. A. J. Amaratunga, and W. I. Milne, Appl. Phys. Lett. **85**, 1137 (2004).

[15] H. Mehdipour, K. Ostrikov, and A. E. Rider, Nanotechnology 21, 455605 (2010).

[16] D. Wei, L. Peng, M. Li, H. Mao, T. Niu, C. Han, W. Chen, and A.T.S. Wee, ACS Nano **9**, 164(2015).

[17] H. Mehdipour and K. Ostrikov, ACS Nano **6**, 10276 (2012).

[18] A. Tewari and S. C. Sharma, Phys. Plasmas **21**, 063512 (2014).

[19] M.S. Sodha, S. Misra, S.K. Misra, and S.Srivastava, J. Appl. Phys. **107,** 103307 (2010).

[20] O. A. Louchev, C. Dussarat, and Y. Sato, J. Appl. Phys. **86**, 3 (1999).

[21] I. B. Denysenko, S. Xu, J. D. Long, P. P.Rutkevych, N. A. Azarenkov, and K. Ostrikov, J. Appl. Phys. **95**, 5 (2004).

[22] See http://www.udfa.net/

[23] D.B. Hash, M.S. Bell, K.B.K. Teo, B.A. Cruden, W.I. Milne and M. Meyyappan, Nanotechnology **16**, 925 (2005).

[24] Y. Zhang, Q. Zou, H.S. Hsu, S. Raina, Y. Xu, J.B. Kang, J. Chen, S. Deng, N.Xu, and W.P. Kang. ACS Appl. Mater. Interfaces **8**, 7363, (2016).

[25] J. Li , J. Chen, B. Shen, X. Yan, and Q. Xue, Appl. Phys. Lett. **99**, 163103 (2011).

[26] N.V. Mantzaris, E. Gogolides, A.G. Boudouvis, A. Rhallabi, and G. Turban, J. Appl. Phys. **79**, 3718 (1996).

[27] M. Cai, R.A. Outlaw, S.M. Butler, J.R. Miller, CARBON **50**, 5481 (2012).

[28] Z. Bo, S. Mao, Z.J. Han, K. Cen, J. Chen and K. Ostrikov Chem. Soc. Rev**.44**, 2108(2015).

[29] M. Grunze, C.R. Brundle, D. Tomanek, Surf. Sci. **119,** 133 (1982).

[30] Y.S. Woo, D.Y. Jeon, I.T. Han, N.S. Lee, J.E. Jung, J.M. Kim, Diamond Relat. Mater. **11**, 59 (2002).

[31] J.A. Smith, J.B. Wills, H.S. Moores, A.J.O.-Ewing, and M.N.R. Ashfold, J. Appl. Phys. **92**, 672 (2002).

[32] Z. Bo, K.Yu, G. Lu, P.Wang, S. Mao, J. Chen, CARBON **49,** 1849 (2011).

[33] B .G. Sumpter, V. Meunier, J. M. R. -Herrera, E.C.-Silva, D.A. Cullen, H. Terrones, D. J. Smith, and M. Terrones, ACS Nano **1**, 369 (2007).

[34] X. Blase, J.-C. Charlier, A. De Vita, R. Car, P. Redlich, M. Terrones, W. K. Hsu, H. Terrones, D. L. Carroll, and P. M. Ajayan, Phys Rev Lett **83**, 5078(1999).

[35] S. Watcharotone, R. S. Ruoff, F. H. Read, Physics Procedia **1,** 71 (2008).

[36] R. Miller, Y. Y. Lau, and J.H. Booske, Appl. Phys. Lett. **91**, 074105 (2007).

5

Effect of gas composition on the morphological properties of the graphene nanosheet

5.1 Brief outline of the chapter

The present chapter investigates the effect of different gas mixtures on the catalyst assisted nucleation and growth kinetics of graphene sheet in a reactive low temperature plasma environment. The three different gas mixtures i.e., C_2H_2, CH_4, and CF_4 with hydrogen and argon are considered in the present investigation to examine the variations in the number densities of carbon and hydrogen species generated on the catalyst surface and their consecutive effects on the dimensions (i.e., height and thickness) and number density profiles of the graphene sheet. In addition, the present model describes the key processes involved in catalyst-aided growth of vertical graphene sheet in its entirety, from formation of carbon clusters, nucleation and growth of graphene islands and growth of vertical graphene sheet in the presence of different gas mixtures which have not been presented in the previous chapters.

5.2 Introduction

With a few exceptions of solid or natural precursors (e.g. honey, milk, cheese, butter, and sugar) [1], a variety of carbon containing gases frequently diluted with Ar and/or H_2 are used for graphene sheet growth using PECVD method. Hydrogen plays an essential role of surface passivation i.e., termination of surface dangling bonds and also acts as an effective carbon etching agent to remove the amorphous carbon layer formed during vertical graphene nucleation and growth, thus promoting the crystalline graphitic structure and sharp edges of the growing vertical graphene sheet [2-3]. The addition of Ar to the carbon source gas and hydrogen mixture increases the plasma stability by enhancing the electron energy [4] and in addition, these energetic Ar ions also facilitates the

activation of the initially hydrogen terminated surface bonds [3]. The non-uniformities of the fluxes of hydrogen and argon to the substrate can significantly affect the nanofabrication process. In this regard, Ostrikov *et al.*[4] have shown that by choosing the appropriate process parameters such as working pressure and composition of the reactive gas feedstock, one can prepare a uniform surface for the nanostructures growth from the non-uniform plasmas.

Hydrocarbons (C_2H_4, C_2H_2, or CH_4), fluorocarbons (C_2F_6, CF_4, CHF_3), and carbon dioxide/monoxide are the most common choices of carbon containing precursors for graphene sheet growth via PECVD method. The morphology and growth rate of the graphene sheet is closely related to the type of carbon feedstock gas used for graphene formation. For instance, it was reported that by using C_2H_2 carbon feedstock, vertical graphene sheets synthesized by RF-PECVD get thickened and exhibit higher growth rate than CH_4 grown vertical graphene sheets [5,6]. This observation was accredited to the fact that higher carbon bearing species are accessible in C_2H_2 plasmas due to the low dissociation energies in contrast to CH_4 plasmas [6]. Moreover, the presence of carbon dimers (C_2) in plasma plays a significant role in the vertical graphene sheet growth [7].However, in the plasma aided catalytic growth process of vertical graphene, carbon species are more effectively generated due to dissociation of precursor gases at the catalyst active surface while their dissociation in plasma is not much in principle [8].The reactive C_2 radicals are readily formed in C_2H_2 containing feedstock than in CH_4 due to direct dissociation of $C \equiv C$ bond in C_2H_2 [9]. Shiji *et al.*[10] have compared the morphology, growth rates, thickness, and spacing between the carbon nanowalls (CNWs) grown by RF-PECVD using C_2F_6+H_2, CH_4+H_2, CF_4+H_2, CHF_3+H_2 and C_4F_8+H_2 gas mixtures. It was observed that the CNWs were not grown for plasmas employing C_4F_8+H_2 precursor; however, the growth rates of CNWs for C_2F_6+H_2 is highest and lowest for CF_4+H_2 gas mixtures. Moreover, CNWs grown using CH_4+H_2 gas mixtures were reported to be very thin and wavy in contrast to other fluorocarbon/hydrogen gas mixtures grown CNWs [10]. Furthermore, the trace amount of oxygen addition to C_2F_6+H_2 gas mixture increases the graphitization and control the CNWs nucleation by reducing the amorphous carbon layer under the CNWs [11].

These unique structural variations achieved using different carbon precursors in PECVD process make graphene very attractive candidate for field emission devices. Zhu *et al.*[5] reported that the carbon nanosheets (CNSs) grown using C_2H_2 feedstock are much higher and more vertically oriented than CH_4 synthesized carbon nanosheets; as a result of which C_2H_2 CNSs exhibit low threshold field, high current density and high field enhancement factor than CH_4 CNSs. Likewise, Hiramatsu *et al.*[12] have demonstrated that CNWs synthesized via C_2F_6+H_2 system exhibit lowest onset electric field for emission of electrons among CH_4+H_2, CF_4+H_2, CHF_3+H_2 and C_4F_8+H_2 gas mixtures.

Motivated by the above works [5,6,10-12] of controlling the growth and field emission properties of the graphene sheet by using different carbon feedstocks, we develop a theoretical model to understand the effect of different gas mixtures on the number density profiles of the carbon and hydrogen species generated per unit area on the catalyst surface and further their ramifications on the growth kinetics and number densities of the graphene sheet.

Table 5.1. Plasma species of different gas mixtures considered in the present model

Gas mixture	Neutrals		Ions	
	Type A	Type B	Type A	Type B
CH_4+H_2+Ar	CH_3, CH_4, C_2H_2, C_2H_4	H, H_2	CH_3^+, CH_4^+, C_2H_2+, C_2H_4+	H^+, H_2^+
C_2H_2+H_2+Ar	C_2H_2, C_4H_2, C_4H_3, C_6H_4, C_2H	H, H_2	$C_2H_2^+$, $C_4H_2^+$, $C_4H_3^+$, $C_6H_4^+$, C_2H^+	H^+, H_2^+
CF_4+H_2+Ar	CF, CF_2, CF_3	H, H_2	CF^+, CF_2^+, CF_3^+	H^+, H_2^+

5.3 Model

As considered in chapters 3 and 4, we assume the growth of graphene sheet on the copper catalyst over the silicon substrate surface in an ionized gas mixture of carbon source gas, etchant gas and carrier gas. However, in the present chapter, we investigate the growth of the graphene sheet in three different gas mixtures

i.e., C_2H_2+H_2+Ar, CH_4+H_2+Ar, and CF_4+H_2+Ar. In addition, we consider the growth of graphene sheet in the multi-component plasma consisting of electrons, various ions and neutrals of C_2H_2/CH_4/CF_4+H_2+Ar gas mixtures that have not been accounted in chapters 3 and 4. Table 5.1 shows the plasma composition of these gas mixtures that have been accounted on the basis of literature [13-19] specifying the plasma chemistry of these gas mixtures.

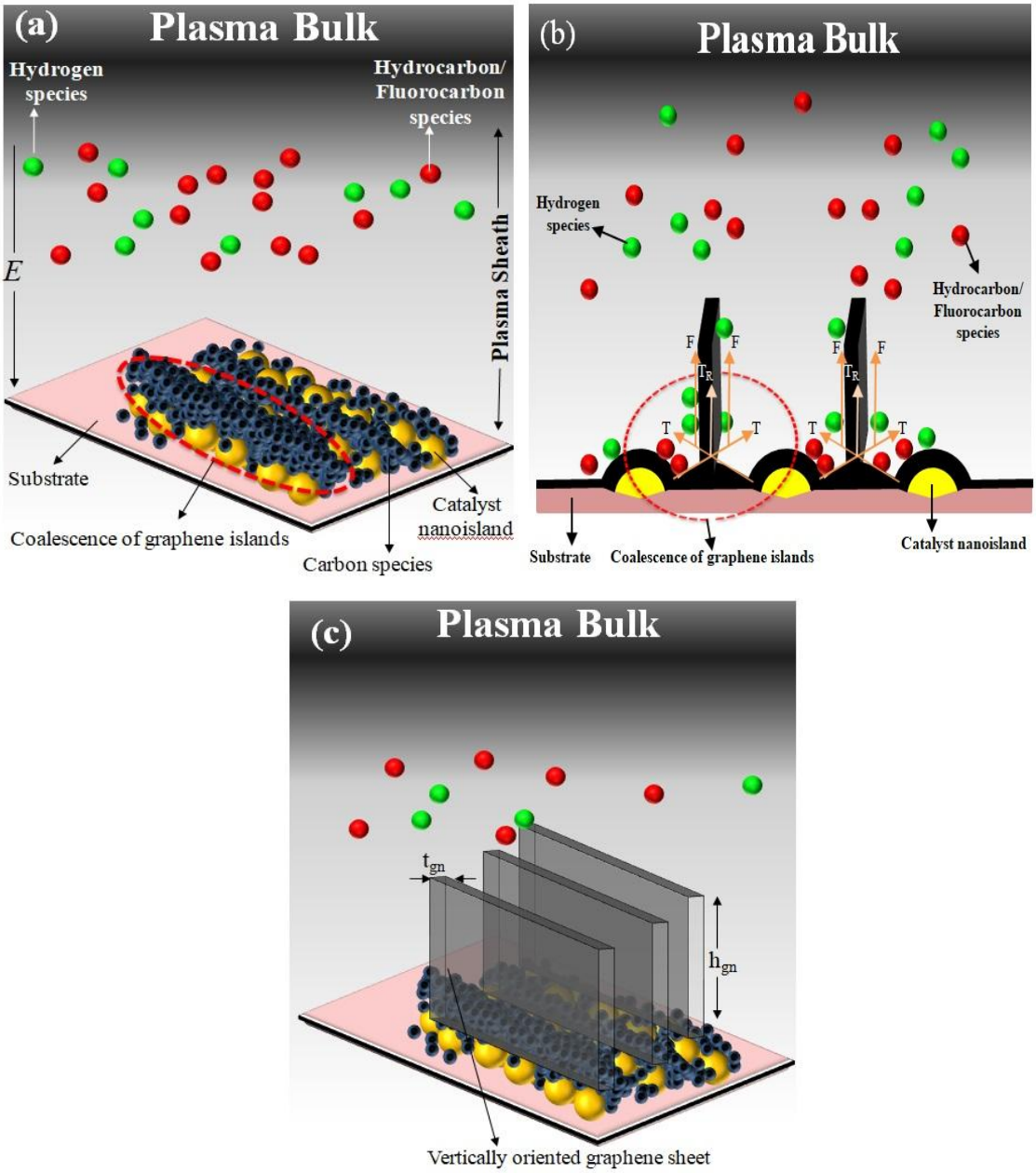

Fig. 5.1. Schematic showing the (a) coalescence of graphene islands and (b) upward growth of the graphene sheet, (c) scheme of the vertical graphene sheet considered in the model.

The catalyst-assisted growth scenario of graphene nanosheet in plasma environment has been presented in Chapter 3. To make it more clear, the schematic of the formation of vertical graphene in the presence of plasma is shown in Fig.5.1. Fig. 5.1(a) shows the initial stage in which the planar growth of 2D graphitic layers takes place due to coalescence of graphene islands formed on account of diffusion and collision of carbon clusters formed on the catalyst surface [20]. However, during the coalescence of graphene islands, internal stress may develop at the graphene island boundaries due to temperature gradients, ion bombardment, and lattice mismatch between the catalyst-substrate surface and the graphitic material [21]. This internal stress is the tensile stress (T) tangential to the planar graphitic layers which tends to bend the free edge of the planar graphitic layers in the upward direction as shown in Fig. 5.1(b) [22]. Further, under the influence of resultant tensile stress (T_R) and electric force (F) due to the plasma sheath at the graphene island boundaries (see Fig. 5.1 (b)), and due to continuous delivery of hydrocarbon species the graphene sheet continues to grow in the vertical direction [22]. Finally, the graphene sheet growth terminates due to the competition between the hydrocarbon deposition and etching effects by hydrogen [21]. The scheme of the graphene sheet considered in the model is shown in Fig. 5.1 (c).

The growth process is strongly affected by the energies and fluxes of hydrocarbon ions and etching gases near the catalyst-substrate surface. These fluxes can be effectively controlled by the plasma parameters and the electric fields induced by the plasma sheath formed near the boundaries of plasma–exposed catalyst-substrate surface which is maintained at a negative potential U_s. It is assumed that the sheath electric field is directed along the z-axis which accelerates all the ions toward the catalyst-substrate surface. In order to investigate the sheath structure formed near the catalyst-substrate surface and the dynamics of the plasma species, the following sheath equations [23,24] are used.

$$\frac{d}{dz}\left(n_r u_{rz}\right) = \upsilon_{iz} n_e, \tag{5.1}$$

$$m_r n_r u_{rz} \frac{du_{rz}}{dz} = en_r \frac{d\phi}{dz} - m_r n_r \upsilon_{rn} u_{rz}, \tag{5.2}$$

$$\frac{d^2\phi}{dz^2} = -4\pi e \sum_r \kappa_r n_r, \tag{5.3}$$

where Eqs. (5.1), (5.2), and (5.3) are the continuity equation, ion-momentum equation, and Poisson's equation, respectively; r indicates either the electron (e), or the positively charged ions considered in the present model; n_r, m_r, and u_{rz} are their number density, mass, and fluid velocity, respectively. υ_{iz} and υ_{rn} are the ionization frequency and collision frequency of electrons and ions with electrons, respectively. ϕ is the sheath potential, κ_r is the r^{th} ion to electron number density ratio, $\sum_r \kappa_r = 1$, and $0 < \kappa_r > 1$.

5.3.1 Kinetic equation of number of carbon species generated on the catalyst surface

Initially, we assume that the applied plasma power segregates the catalyst (Cu) film of thickness 4 nm into N_a (= 6×10^8 cm^{-2}) catalyst nanoislands of size r_c (= 50 nm) each [25]. Carbon and hydrogen species are then generated from the particular composition of plasmas (i.e., $C_2H_2/CH_4/CF_4+H_2+Ar$) on these catalyst nanoislands via several processes which have been incorporated in Eqs. (5.4) and (5.5), respectively. Following Gupta *et al.*[26] and Marvi *et al.*[27]

$$\frac{dN_C}{d\tau} = \sum_A J_A(1-\theta_t) + 2\sum_A n_{sA}\upsilon \exp\left(\frac{-\delta E_i}{k_B T_S}\right) + 2\sum_{iA}\left(\sum_A \frac{n_{sA} y_{di}}{\nu_0}\right) J_{iA} + \sum_{iA} J_{iA} + J_C$$
$$+\sum_{iA}\sum_{iB} \frac{J_{iA}\sigma_{ads} J_{iB}}{\upsilon} - \sum_A n_{sA}\sigma_{ads} J_B - \sum_A n_{sA}\upsilon \exp\left(\frac{-E_{ads}}{k_B T_S}\right) - N_C \upsilon \exp\left(\frac{-E_{ev}}{k_B T_S}\right), \tag{5.4}$$

$$\frac{dN_H}{dt} = \sum_B J_B(1-\theta_t) + \sum_B n_{sB}\nu \exp\left(\frac{-\delta E_i}{k_B T_S}\right) + \sum_{iA}\left(\sum_A \frac{n_{sA} y_{di}}{\upsilon_0}\right) J_{iA} + \sum_{iB} J_{iB}$$
$$- \sum_B n_{sB}\upsilon \exp\left(\frac{-\delta E_{aH}}{k_B T_S}\right) - \sum_B n_{sB}\sigma_{ads} J_B - \sum_B n_{sB}\sigma_{ads} J_{iB}, \tag{5.5}$$

Neha Gupta
Delhi Technological University, Delhi, India

where N_C and N_H are the number densities of carbon and hydrogen species generated per unit area on the catalyst surface, respectively. $J_j = \left(n_j v_{thj} / 4 \right)$ is the flux of impinging neutral species from the plasma (where j stands for species of type A or B; n_j and v_{thj} are the volume number density and thermal velocity of j^{th} type of species in the plasma [23], $n_{sj} \left(= \theta_j \nu_0 \right)$ is the surface concentration of neutral species; θ_j is the surface coverage by species of type j, $\nu_0 \left(\approx 10^{15} \text{cm}^{-2} \right)$ is the number of adsorption sites per unit area [23], $y_d (\approx 2.49 \times 10^{-2} + 3.29 \times 10^{-2} \times E_i$ where E_i is the ion energy in eV) is the stitching probability [28], $\upsilon \left(\approx 10^{13} Hz \right)$ is the thermal vibration frequency [23], $J_{ij} \left(= n_{ij} \left(k_B T_e / m_{ij} \right)^{1/2} \right)$ is the flux of j^{th} type of ion from the plasma (where, j refers to A or B type of ion) [23], $\sigma_{ads} \left(\approx 10^{-16} cm^2 \right)$ is the cross-section for the reactions of atomic hydrogen [23], T_s is the substrate or catalyst temperature (catalyst and substrate temperature are assumed to be same in the absence of heating effect) [27], E_{ads} is the hydrocarbon/fluorocarbon adsorption energy, E_{ev} is the carbon evaporation energy, δE_{aH} is the adsorption energy of etching species, i.e., hydrogen, and δE_i is the thermal energy barrier.

Equation (5.4) describes the rate of generation of carbon species per unit area on the catalyst surface via adsorption of hydrocarbon/fluorocarbon neutral species on the catalyst surface (first term), thermal and ion-induced dissociation of adsorbed hydrocarbon/fluorocarbon neutral species (second and third terms), decomposition of hydrocarbon/fluorocarbon ions (fourth term), direct carbon flux towards the catalyst surface (fifth term), and due to interaction of hydrocarbon/fluorocarbon ions and hydrogen ions i.e., due to ion-ion interaction (sixth term) [27,29]. The last three terms in Eq. (5.4) quantify the loss of carbon from the catalyst surface due to interaction of

adsorbed hydrocarbon species with the neutral hydrogen from the plasma, desorption, and evaporation of carbon atoms, respectively [23,27].

Equation (5.5) describes the rate of generation of hydrogen species per unit area on the catalyst nanoparticle surface. The first four terms account for hydrogen adsorption, hydrogen atom generation due to thermal dissociation of hydrocarbons, ion-induced dissociation of hydrocarbons, and decomposition of ions of type B, respectively. The last three terms account the hydrogen loss due to desorption (fifth term), and interaction of adsorbed hydrogen atoms with incoming hydrogen atoms and ions from the plasma (sixth and seventh terms) [27].

5.3.2 Kinetic equation of number densities of carbon clusters and graphene nuclei/islands

The carbon species created on the catalyst surface diffuse and attach each other to form carbon clusters, which in turn diffuse and collide with each other to form graphene nuclei. These graphene nuclei diffuse and coalesce (or stitch) together to form large graphene islands (with radius r_{Is}) [20]. This leads to the lateral extension or growth of the planar graphene sheet and we assume the length (l_{gn}) of the graphene sheet to be 0.81 μm [30].

$$\frac{dN_{Cl}}{d\tau} = N_a N_C D \exp\left(\frac{-E_{sdC}}{k_B T_s}\right) - N_{Cl} D' \exp\left(\frac{-E_{sdCl}}{k_B T_s}\right) \times \frac{1}{\pi r_c^2} - N_{Cl} N_{Is} D' \exp\left(\frac{-\left(E_{sdCl} + E_{incCl}\right)}{k_B T_s}\right), \quad (5.6)$$

$$\frac{dN_{Is}}{d\tau} = N_{Cl} D' \exp\left(\frac{-E_{sdCl}}{k_B T_s}\right) \times \frac{1}{\pi r_c^2} - \left(N_{Cl} N_{Is} D' \exp\left(\frac{-\left(E_{sdCl} + E_{incCl}\right)}{k_B T_s}\right) + N_c N_{Is} D \exp\left(\frac{-\left(E_{sdC} + E_{incC}\right)}{k_B T_s}\right) + N_{Is} D'' \exp\left(-\frac{E_{sdIs}}{k_B T_s}\right) \times \frac{1}{\pi r_{Is}^2}\right), \quad (5.7)$$

Neha Gupta
Delhi Technological University, Delhi, India

where N_{Cl} and N_{Is} are the surface concentration of carbon clusters and graphene islands, respectively. $D\exp\left(-E_{sdC}/k_BT_s\right)$, $D'\exp\left(-E_{sdCl}/k_BT_s\right)$, and $D''\exp\left(-E_{sdIs}/k_BT_s\right)$ are the surface diffusion coefficients of carbon atoms, carbon clusters, and graphene islands, respectively, with corresponding energy barriers, E_{sdC} ~0.1 eV, E_{sdCl} ~0.82 eV, and E_{sdIs} ~2.6 eV, respectively [20].

Equations (5.6) and (5.7) describe the growth rate of surface concentrations of carbon clusters and graphene islands, respectively. The first term on the right side of Eq. (5.6) specify the generation of carbon clusters on account of surface diffusion of carbon atoms generated on the catalyst surface while the second and last terms account the cluster loss due to diffusion and incorporation of clusters into the graphene nuclei (see supporting information of Mehdipour and Ostrikov [20]). Furthermore, the first, second, third, and last terms of Eq. (5.7) indicate the formation of graphene nuclei due to surface diffusion of clusters, growth of graphene islands due to incorporations of clusters (with energy barrier E_{incCl} ~0.8 eV) and carbon atoms (with energy barrier E_{incC} ~0.85 eV), and coalescence (or ripening) of graphene islands, respectively (see supporting information of Mehdipour and Ostrikov [20]).

5.3.3 Growth rate equation of graphene nuclei/islands

$$\frac{d\left(\pi r_{Is}^2\right)}{d\tau}=\left(\left(N_{Cl}D'\exp\left(\frac{-E_{sdCl}}{k_BT_S}\right)\times\frac{1}{\pi r_c^2}+N_{Cl}N_{Is}D'\exp\left(\frac{-\left(E_{sdCl}+E_{incCl}\right)}{k_BT_S}\right)\right.\right.$$
$$\left.\left.+N_cN_{Is}D\exp\left(\frac{-\left(E_{sdC}+E_{incC}\right)}{k_BT_S}\right)\right)\times 2\pi r_c+N_{Is}D''\exp\left(-\frac{E_{sdIs}}{k_BT_S}\right)\times\frac{1}{2\pi r_{Is}}\right)$$
$$\times\left(\frac{M_c\times j_{iAgIs}}{\rho_c\upsilon}\right)+\gamma_A\pi r_{Is}^2 j_{AgIs}, \qquad (5.8)$$

where M_c (= 63.54 a.m.u.) and $\rho_C \left(= 8.96\ \text{g/cm}^3\right)$ are the mass and density of the catalyst, r_{Is} is the radius of the graphene island. $j_{ijgIs}\left[=\pi r_{Is}^2\left(8k_BT_{ij}/\pi m_{ij}\right)^{1/2} n_{ij}(x)\left[1-Z\gamma_{ij}\right]\left(\exp\left[-\frac{eU_s}{k_BT_s}\right]\right)\right]$ is the ion collection current at the surface of the graphene island [31] (subscript j refers to either A or B type of positively charged ion as explained earlier); Z is the charge over the graphene sheet (can be depicted from Eq. (11)), T_{ij} and m_{ij} are the mass and temperature of ion j, respectively, $\gamma_{ij} = e^{-2} r_{Is} k_B T_s$, $n_{ij}\left(x\right) = n_{ij0}\left(1-\frac{2e\phi(x)}{m_{ij}v_{i0}^2}\right)^{1/2}$ is the ion density at any point within the plasma sheath; v_{i0} is the ion velocity, $\phi(x) = \phi_0 \exp\left(-\frac{|x|}{\lambda_d}\right)$ is the electrostatic potential; ϕ_0 is the negative potential at the surface and λ_d is the Debye length, and $j_{jgIs}\left(=\pi r_{Is}^2\left(8k_BT_n/\pi m_j\right)^{1/2} n_j\right)$ is the neutral collection current at the surface of the graphene island [31]; T_n, m_j and n_j are the temperature, mass and number density of neutral atom j, respectively, and γ_A is the sticking coefficient of neutral of type A.

Equation (5.8) outlines the increase in area of the graphene island due to surface diffusion of clusters (first term), incorporations of clusters and carbon into the graphene island (second and third term), diffusion or coalescence of graphene island to form large graphene island (fourth term), and due to sticking of neutral atoms of type A on the growing graphene island (last term). The factor j_{iAgIs} accounts for the collection currents of ions of type A on the surface of growing graphene island.

5.3.4 Growth rate equation of the graphene sheet

$$l_{gn}\frac{d\left(h_{gn}\times t_{gn}\right)}{d\tau}=\left(\frac{N_C}{\nu}\times D\exp\left(-\left\{\frac{E_{sdC}+E_{incC}}{k_BT_s}\right\}\right)\frac{2\pi r_{Is}}{\pi r_{Is}^2}\times\left(j_{iAgn}\right)+\left(\gamma_A j_{Agn}\right)\right)\frac{M_{gn}}{\rho_{gn}}(1-\xi_s\xi_c), \quad (5.9)$$

$$\left[h_{gn}\left(\tau\right)+l_{gn}\right]\frac{d(t_{gn})}{d\tau}=\left(\gamma_{iB}j_{iBgn}+\gamma_B j_{Bgn}\right)N_H h_{gn}(\tau)\frac{M_{gn}}{\rho_{gn}}, \quad (5.10)$$

where l_{gn}, h_{gn}, and t_{gn} are the length, height and thickness of the graphene sheet, respectively, ρ_{gn} and M_{gn}(~12 g) are the density and mass of the growing graphene sheet, respectively. j_{ijgn} and j_{jgn} are the ion and neutral collection currents at the graphene sheet surface, respectively [30], V_S is the surface potential of the graphene sheet (Refer Eq. (A2) of Appendix A).

$$j_{ijgn}=n_{ij}(x)\left(l_{gn}t_{gn}+h_{gn}t_{gn}+l_{gn}h_{gn}\right)\left(\frac{k_BT_{ij}}{2\pi^2m_{ij}}\right)^{1/2}\left\{\frac{2}{\sqrt{\pi}}\left(\frac{eV_S}{k_BT_{ij}}\right)^{1/2}+\exp\left[\frac{eV_s}{k_BT_{ij}}\right]erfc\left[\left(\frac{eV_s}{k_BT_{ij}}\right)^{1/2}\right]\right\}\times\exp\left[-\frac{eU_s}{k_BT_{ij}}\right],$$

$$j_{jgn}=n_j\left(l_{gn}t_{gn}+h_{gn}t_{gn}+l_{gn}h_{gn}\right)\left(\frac{k_BT_n}{2\pi^2m_j}\right)^{1/2}$$

Once the planar graphitic layers are formed due to coalescence of graphene islands, internal stress or tensile stress is developed at the graphene island boundaries. These internal stresses may cause defects within the initial planar graphitic layer, which trigger the growth of graphene in upward direction [21]. Eq. (5.9) describes the increase in area of the vertical growing graphene sheet. Under the influence of inbuilt electric field associated with the plasma, the graphene sheet grows vertically due to continuous supply of carbon species i.e., due to ion (j_{iAgn}) and neutral collection current (j_{Agn}) at

the graphene island boundaries and the surfaces of the graphene sheet. Moreover, the diffusion and attachment of carbon atoms at the peripherals of the growing graphitic platelets additionally contribute to the vertical graphene sheet growth [first term of Eq. (5.9)]. The factors $\xi_s\left(=J_{iA}y_{sp}\left(1-\theta_t\right)\times\frac{4\pi r_c^2}{\upsilon}\right)$ and $\xi_c\left(=4\pi r_c^2 N_C\right)$ in Eq. (5.9) are the carbon sputtering [28] and amorphous carbon terms, respectively; where y_{sp} is the sputtering yield. Finally, the growth of vertical graphene terminates due to etching of growing graphene sheets by the hydrogen. Eq. (5.10) describes the reduction in thickness of the graphene sheet due to etching of carbon atoms by hydrogen. The first and second terms on the right side of Eq. (5.10) represent the ion and neutral collection currents of species of type B i.e., hydrogen on the surface of the graphene sheet.

5.3.5 Charging of graphene sheet

$$\frac{d\left(Z\right)}{d\tau}=\sum_A j_{iAgn}+\sum_B j_{iBgn}-\gamma_e j_{egn}\ , \tag{5.11}$$

where Z is the charge over the graphene sheet, γ_e is the sticking coefficient of the constituent electrons, and j_{egn} is the electron collection current at the graphene sheet surface.

$$j_{egn}=\left(\frac{k_B T_e}{2\pi^2 m_e}\right)^{1/2} n_e(x)\left(l_{gn}t_{gn}+h_{gn}t_{gn}+l_{gn}h_{gn}\right)\exp\left[\frac{eV_s}{k_B T_e}+\frac{eU_s}{k_B T_s}\right]$$

The first two terms on the right side of Eq. (5.11) describe the charge developed on the graphene sheet surface due to accretion of positively charged ions of type A and B, respectively. The last term specifies the attenuation in charge due to accretion of electrons at the surface of the graphene sheet.

5.3.6 Kinetic balance equations of all the plasma species

$$\frac{dn_e}{d\tau} = \sum_A \beta_A n_A + \sum_B \beta_B n_B - \sum_A \alpha_A n_e n_{iA} - \sum_B \alpha_B n_e n_{iB} - \gamma_e n_{gn} j_{egn}, \quad (512)$$

$$\frac{dn_{iA}}{d\tau} = \beta_A n_A - \alpha_A n_e n_{iA} - n_{gn} j_{iAgn} - \sum_{lAB} k_l n_A n_{iB}, \quad (5.13)$$

$$\frac{dn_{iB}}{d\tau} = \beta_B n_B - \alpha_B n_e n_{iB} - n_{gn} j_{iBgn} - \sum_{lAB} k_l n_A n_{iB}, \quad (5.14)$$

$$\frac{dn_A}{d\tau} = \alpha_A n_e n_{iA} - \beta_A n_A + n_{gn}(1-\gamma_{iA}) j_{iBgn} - n_{gn}\gamma_A j_{Agn} - J_{adA} + J_{desA} - \sum_{lAB} k_l n_A n_{iB}, \quad (5.15)$$

$$\frac{dn_B}{d\tau} = \alpha_B n_e n_{iB} - \beta_B n_B + n_{gn}(1-\gamma_{iB}) j_{iBgn} - n_{gn}\gamma_B j_{Bgn} - J_{adB} + J_{desB} - \sum_{lAB} k_l n_A n_{iB}, \quad (5.16)$$

where β_j is the coefficient of ionization of the constituent neutral atoms due to external field (subscript j refers to either A or B type of neutral atoms), $\alpha_j(T_e) = \alpha_{j0}\left(\frac{300}{T_e}\right)^k$ cm^3/sec is the coefficient of recombination of electrons and positively charged ions; $k(=-1.2)$ is a constant [32] and j refers to A and B types of ions, $J_{adj} = P_j(2\pi m_j k_B T_n)^{-1/2} \times n_j / J_j$ is the adsorption flux onto the catalyst-substrate surface; P_j is the partial pressure of adsorbing species [33], $J_{desj} = n_j \upsilon \exp\left(-\frac{\varepsilon_{ads}}{k_B T_n}\right)$ is the desorption flux from the catalyst-substrate surface [33]; ε_{ads} is the adsorption energy, $J_{th} = n_B \nu \exp\left(-\delta\varepsilon_{th} / k_B T_s\right)$ is the flux of type B neutral species (namely hydrogen) on account of thermal dehydrogenation[33]; $\delta\varepsilon_{th}$ is the activation energy of thermal dehydrogenation.

Equation (5.12) describes the growth rate of electron density in plasma. The first and second terms on the right side in Eq. (5.12) account the gain in

electron density per unit time because of ionization of neutral atoms of type A and B, respectively. The third term and fourth terms symbolize the reduction of electron density per unit time due to recombination of electrons and ions of type A and B, respectively. The last term is the electron collection current at the graphene sheet surface.

Table 5.2. Initial conditions used in the model.

Parameter	Description	Initial Value
n_{e0}	electron density	10^9 cm^{-3}
T_{e0}	electron temperature	2.4 eV
T_{i0}	ion temperature	2400 K
T_{n0}	neutral temperature	2000 K
T_S	substrate temperature	550 ^{0}C
ρ_{ct}	density of catalyst Cu	8.96g/cm^3
$\alpha_{10} \approx \alpha_{20}$	coefficient of recombination of electrons and ions	1.12×10^{-7} cm^3/sec
γ_e	sticking coefficient of electrons	1
γ_{ij}	sticking coefficient of ions	1
δE_{sdh}	energy due to dehydrogenation	1.7 eV
δE_{aH}	hydrogen species adsorption energy	1.8 eV
E_{ev}	carbon evaporation energy	1.8 eV
δE_i	thermal energy barrier on the catalyst surface	1.3 eV for $C_{2n}H_x$, 2.1 eV for CH_x, and 3.3 eV for CF_x species)[ref.43,35]
E_{ads}	adsorption energy	2.9 eV of $C_{2n}H_x$, 1.8 eV for CH_x, and 1.2 eV for CF_x species) [ref.34]

Equations (5.13) & (5.14) are the particle balance equations of positively charged ions of type *A* and *B*, respectively. The first terms on the right hand

side in Eqs. (5.13) & (5.14) describe the growth rate of ion density due to ionization of neutral atoms. The second and third terms represent the decay rate of positively charged ion density due to electron-ion recombination and ion collection current at the graphene sheet surface, respectively. The last term accounts for the gain/loss of ion density due to ion-neutral reactions [14] and their reaction rate coefficients i.e., k_l have been taken from the experimental works of Mao and Bogaerts.[16].

Table 5.3. Experimentally determined initial values of the various species considered in the present model.

CH_4+H_2+Ar gas mixture [ref. 16]			
Neutral species	**Number density (cm^{-3})**	**Ionized species**	**Number density (cm^{-3})**
CH_3	5×10^{12}	**CH_3^+**	6×10^{8}
CH_4	1×10^{14}	**CH_4^+**	6.1×10^{8}
C_2H_2	7×10^{13}	**$C_2H_2^+$**	6×10^{9}
C_2H_4	8×10^{12}	**$C_2H_4^+$**	7×10^{8}
H	9×10^{13}	**H^+**	8×10^{7}
H_2	1×10^{15}	**H_2^+**	9×10^{7}
C_2H_2+H_2+Ar gas mixture [ref. 16]			
Neutral species	**Number density (cm^{-3})**	**Ionized species**	**Number density (cm^{-3})**
C_2H_2	5×10^{13}	**$C_2H_2^+$**	4×10^{9}
C_4H_2	1×10^{12}	**$C_4H_2^+$**	3.8×0^{9}
C_4H_3	1×10^{12}	**$C_4H_3^+$**	3.6×10^{9}
C_6H_4	1.5×10^{12}	**$C_6H_4^+$**	1×10^{9}
C_2H	1.5×10^{10}	**C_2H^+**	3×10^{7}
H	4×10^{13}	**H^+**	2×10^{8}
H_2	1×10^{15}	**H_2^+**	9×10^{8}
CF_4+H_2+Ar			
Neutral species	**Number density (cm^{-3})**	**Ionized species**	**Number density (cm^{-3})**
CF_3	3.5×10^{12}	**CF_3^+**	2.1×10^{8}
CF_2	3×10^{12}	**CF_2^+**	3.1×10^{9}
CF	0.7×10^{10}	**CF^+**	2.6×10^{9}
H	4.1×10^{13}	**H^+**	2.4×10^{8}
H_2	1×10^{15}	**H_2^+**	8.1×10^{8}

Equations (5.15) & (5.16) indicate the balance of neutrals of type A and B in the plasma, respectively. The first terms on the right side in Eqs. (5.15) & (5.16) depict the rate of augmentation of neutral atom density on account of electron–ion recombination. The second and third terms represent the rate

of decrease of neutral atom density due to ionization and increase in neutral atom density due to neutralization of ions collected at the graphene sheet surface, respectively. The fourth term is the accretion of neutral atoms on the graphene sheet surface. The next two terms denote the adsorption and desorption of neutrals to/from the catalyst-substrate surface, respectively. The term J_{th} in Eq. (5.16) represents the increase of hydrogen number density in plasma because of thermal dehydrogenation [33]. The last term is the decay in neutral atom density on account of neutral-ion reactions [14].

5.4 Results and discussion

In this section, the numerical solutions of the model equations developed in the previous section are used to establish the influence of different gas mixtures on the catalyst aided PECVD growth process and field emission characteristics of graphene sheet. In particular, we investigate the consequence of different carbon feedstock gases i.e., C_2H_2, CH_4 and CF_4 on the graphene sheet growth parameters (e.g., graphene sheet dimensions i.e., height and thickness, growth rate of carbon species and etchant species on the catalyst surface, and graphene sheet nucleation density) with time and further its repercussions on the field enhancement factor of the graphene sheet. Using MATHEMATICA software, we have simultaneously solved the first order differential equations (5.1)-(5.16) numerically with the appropriate default set of parameters given in Table 5.2 and Table 5.3. The mass of ion A m_{iA} (= (12×x)+(1×y) a.m.u for $C_xH_y^+$ and 12+(19×x) for CF_x^+), mass of ion B m_{iB} (= (1×x) a.m.u for H_x^+), mass of neutral A m_A(= (12×x)+(1×y) a.m.u for C_xH_y and 12×(19×x) for CF_x), and mass of neutral B m_B (= (1×x) a.m.u for H_x).

Fig. 5.2 shows the time evolution of the height of the graphene sheet for different carbon feedstocks i.e., C_2H_2, CH_4 and CF_4 in the hydrocarbon/fluorocarbon + hydrogen + argon gas mixtures. From Fig. 5.2, it can be seen that the graphene sheet height is maximum for C_2H_2 followed by CH_4 and CF_4. Considering the experimental data on gas composition of CH_4 contained gas mixture for a typically PECVD case [13-15], one may observe that the species (neutrals and ions) mainly present in the plasma are H_x (x=1,2),

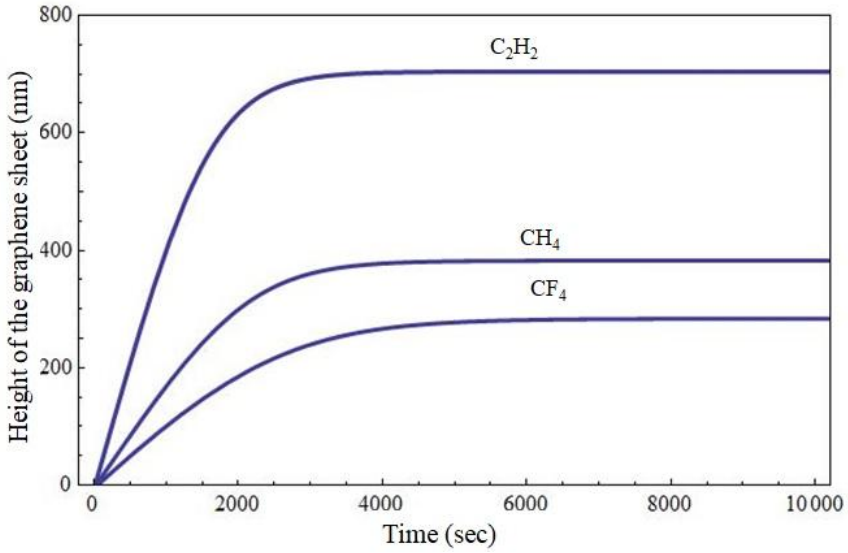

Fig. 5.2. The time evolution of the height (in nm) of the graphene sheet for different carbon precursor gases C_2H_2, CH_4, and CF_4. The other parameters are given in the text and Tables 5.2 and 5.3.

CH_x (x=3, 4), and C_2H_x (x=2, 4) types which have also been accounted in the present model calculations, The CH_x species can hardly dissociate on the catalyst due to high dissociation energies, whereas C_2H_x species are characterized by low dissociation energies [5,16]. Moreover, the adsorption energies for C_2H_x type species is higher than CH_x type species [33], as a result of which the desorption term $\sum_k n_k \upsilon \exp\left(\frac{-E_{ads}}{k_B T_s}\right)$ in Eq. (5.4) becomes dominant for CH_x type species. Thus, C_2H_x type species present in the CH_4/H_2/Ar plasmas are the main contributors of carbon species generation on the catalyst surface [16]. The similar effect can be seen from Fig. 5.3 which indicates that the decay rate of C_2H_x species in plasma is higher than the CH_x species. However, according to the experimental observations [13-18], C_2H_2 contained plasma is predominated by long chain hydrocarbon species (both ions and neutrals) of type $C_{2n}H_x$ (where, n=1, 2 and x=1-4). As can be seen, these species are carbon rich and hydrogen poor as compared to the species (both ions and neutrals) of CH_4+H_2+Ar plasma, as a result they contribute more adequately to the carbon generation on the catalyst surface in contrast to CH_4 contained gas mixture. Additionally, these long chain species enhance the physical sputtering of the amorphous carbon layer formed on the catalyst surface and thus expected to

prevent the poisoning of catalyst surface and maintain the catalytic activity [16]. Furthermore, there is significant lack of carbon generation on the catalyst surface for CF_4 contained gas mixture in contrast to CH_4 and C_2H_2 (cf. Fig. 5.4 (a)) due to their differences in dissociation energies [36]. In addition, in CF_4 growth, the catalytic activity is hampered since most of the H atoms that are responsible for removing the amorphous layer of carbon are significantly lost in the F abstraction from the CF_x species migrating on the growing surfaces and edges of the graphene sheet [12], as a result of which the height of the graphene sheet is significantly lower than CH_4 and C_2H_2 contained gas mixtures.

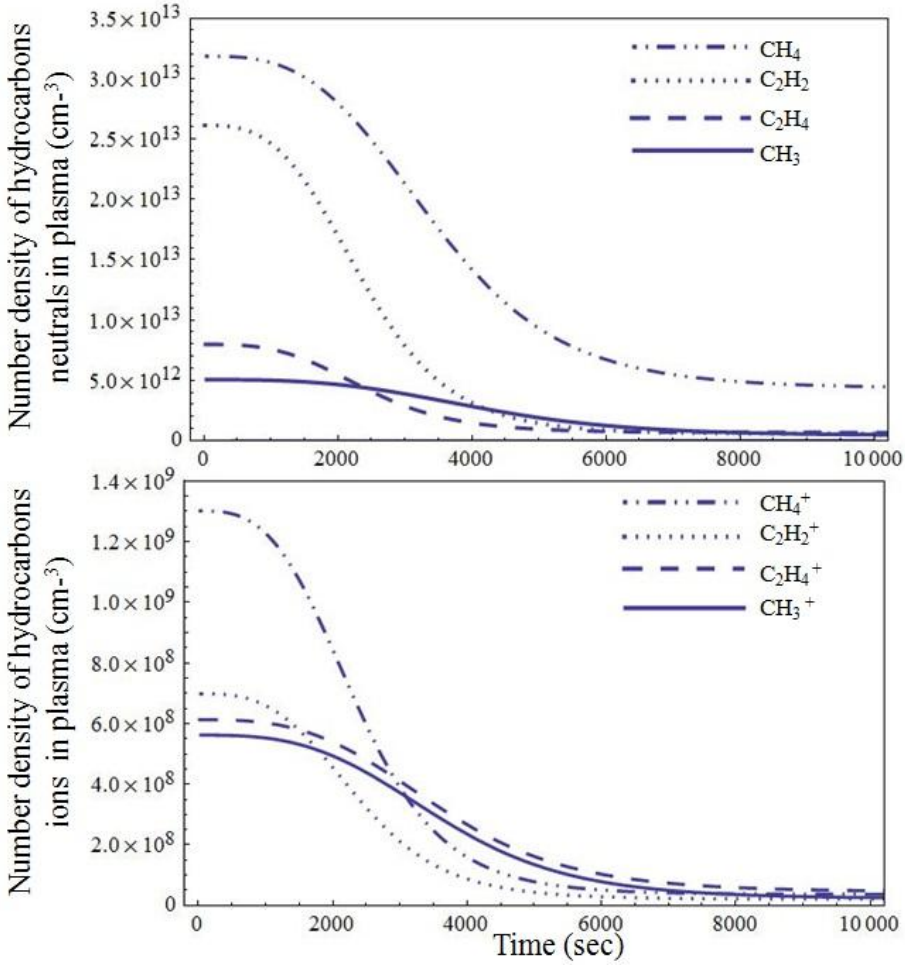

Fig. 5.3. The time evolution of densities of (a) hydrocarbon neutrals and (b) ions in CH_4/H_2/Ar gas mixture. The other parameters are given in the text and Tables 5.2 and 5.3.

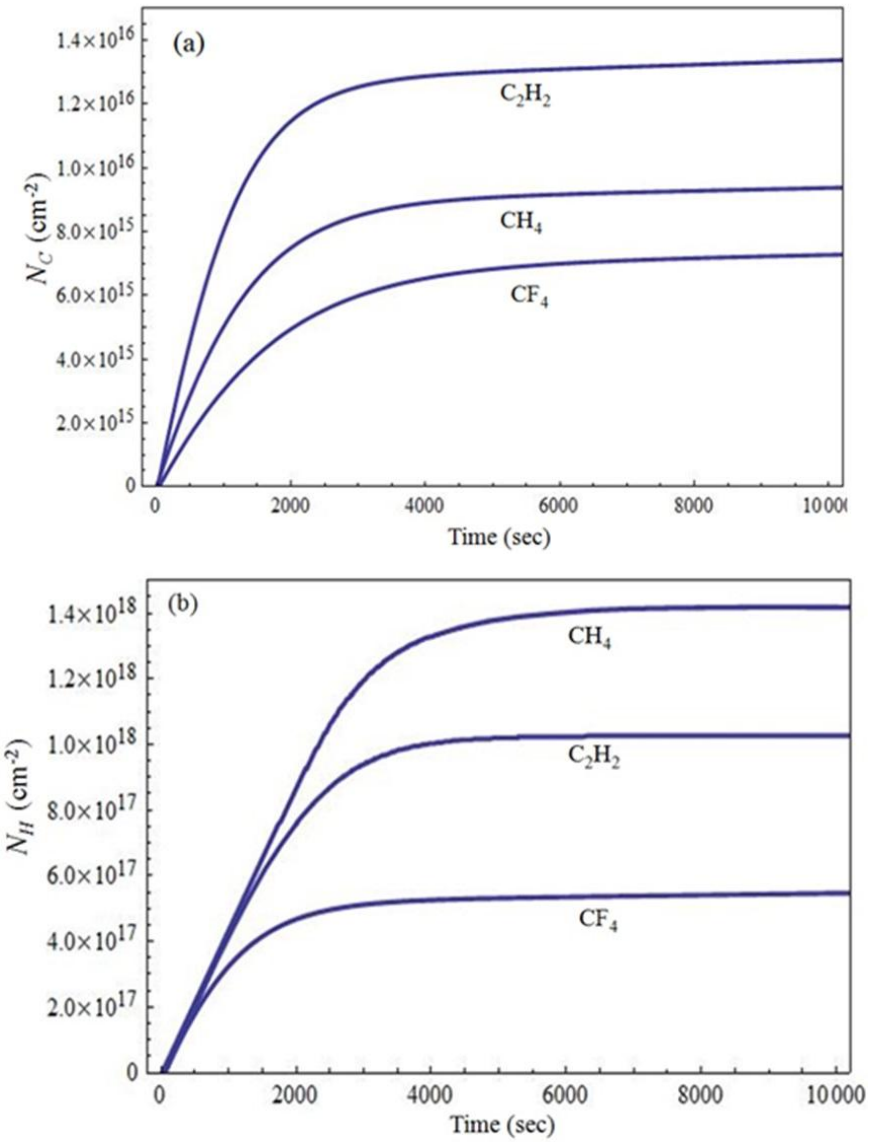

Fig. 5.4. The time evolution of number densities of (a) carbon species (i.e., N_C) and (b) hydrogen species (i.e., N_H) generated per unit area on the catalyst surface for different carbon precursor gases C_2H_2, CH_4, and CF_4. The other parameters are given in the text and Tables 5.2 and 5.3.

Since the graphene sheet grows in height due to diffusion and attachment of carbon atoms generated at the catalyst surface, one can infer that graphene sheet grows higher for C_2H_2 contained gas mixture followed by CH_4 and CF_4 due to plentiful supply of carbon on the catalyst surface in the case of C_2H_2 contained gas mixture followed by CH_4 and CF_4. The results of Fig.5.2 are in compliance with the experimental observations of Zhu *et al.*[5] (cf. Figs. 1(b) and 1(d) of Zhu *et al.*[5]), Cai *et al.*[6], and Shiji *et al.*[10] (cf. Fig. 4 of Shiji *et al.*[10]).

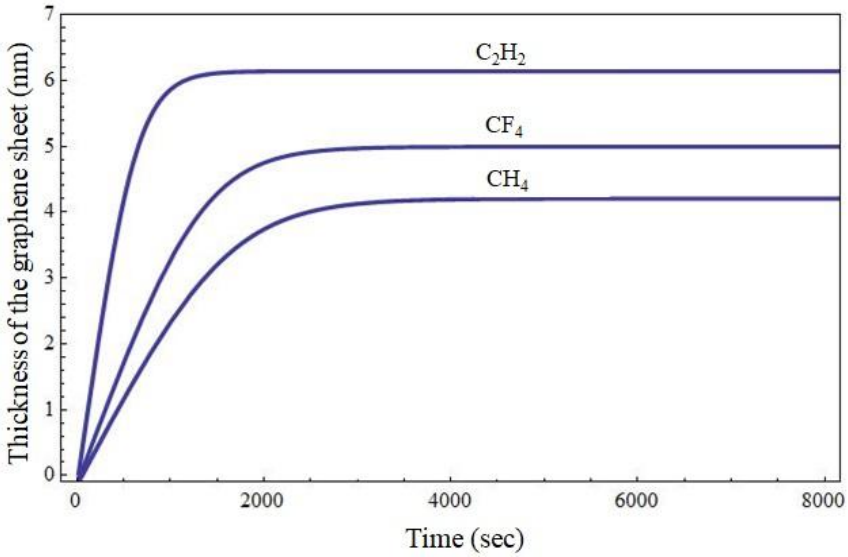

Fig. 5.5. The time evolution of the thickness (in nm) of the graphene sheet for different carbon precursor gases C_2H_2, CH_4, and CF_4. The other parameters are given in the text and Tables 5.2 and 5.3.

Figure 5.5 shows the time evolution of the thickness of the graphene sheet for various carbon gas precursors (i.e., C_2H_2, CH_4 and CF_4). It can be seen from the Fig. 5.5 that the thickness of the graphene sheet is highest for C_2H_2 contained gas mixture followed by CF_4 and CH_4. The reason for the growth of thicker graphene sheets in the case of C_2H_2 contained gas mixture is the plentiful generation of carbon (indicated in Fig. 5.4(a)) and the lesser amount of hydrogen incorporation in the C_2H_2 growth (cf. Fig. 5.4(b)). From Fig. 5.4 (b), it can be seen that the number density of hydrogen species on the catalyst surface (i.e., N_H) is utmost for CH_4 contained gas mixture followed by C_2H_2 and CF_4. This is evidence from the fact that the plasma species of CH_4 contained gas mixture are hydrogen rich and carbon poor in contrast to the plasma species of C_2H_2 and CF_4 contained gas mixtures, therefore, CH_4 contained gas mixture lead to thinner graphene sheets in contrast to C_2H_2 and CF_4. The thinner graphene sheets for CH_4 gas mixture in contrast to C_2H_2 has also been reported experimentally [5,6] (cf. Figs. 1 & 2 of Zhu *et al.* [5] and Figs. 2(b), 2(c) and 4(d) of Cai *et al.*[6]). In CF_4+H_2+Ar plasma, N_H is least (cf. Fig. 5.4(b)) because of its gas composition and due to subtractive reaction of hydrogen species with F from the adsorbed CF_x species. However, the thickness of graphene sheets is intermediate of the thickness of CH_4 and C_2H_2 contained gas

mixtures due to the fact that C_2H_2 contained gas mixture is extremely carbon rich and CH_4 contained gas mixture is exceptionally hydrogen rich in comparison with CF_4 contained gas mixture. Shiji *et al.*[10] have also reported in their experimental work that CF_4 synthesized graphene sheets are much thicker than the graphene sheets grown using CH_4 gas mixture (cf. Fig. 3 of Shiji *et al.*[10]).

Now, we investigate the effect of different gas mixtures on the number density of vertical graphene sheets grown on catalyst-substrate surface via PECVD process. As described earlier in the previous section, the vertical graphene sheet grows due to continuous delivery of carbon atoms, diffusion and attachment of carbon atoms at the graphene nuclei/islands boundaries, therefore, in order to depict the impact of different gas mixtures on the number density of the graphene sheets, we study their consecutive effects on the graphene nuclei number density (i.e., N_{is}). At the early stage of growth, graphene nuclei are formed due to diffusion of carbon clusters and with further increase in growth time, these graphene nuclei diffuse and stitch together to form large graphene islands, and thus the number density of graphene nuclei decreases with growth time as can be seen from Fig. 5.6. This figure illustrates the variation of graphene nuclei density as a function of growth duration for different gas mixtures (i.e., C_2H_2+H_2+Ar, CH_4+H_2+Ar, and CF_4+H_2+Ar). It can be seen from the Fig. 5.6 that C_2H_2 contained gas mixture leads to more effective formation of graphene nuclei i.e., graphene nucleation density is maximum in C_2H_2 in contrast to CH_4 and CF_4. The relative generation of carbon atoms on the catalyst surface (i.e., N_c) plays an imperative role in this regard. This is because, more carbon atoms on the catalyst-substrate surface give rise to faster saturation of the surface with carbon atoms and eventually increases the cluster formation, which in turn, enables faster nucleation of more graphene nuclei on the catalyst surface. Consequently, diffusion and coalescence of graphene nuclei/islands becomes more effective and more graphene islands of large size are formed, therefore, the number density of graphene sheets increases. Accordingly, using Fig. 5.3 it can be concluded that the graphene sheet number density is highest in C_2H_2 contained gas mixture followed by CH_4

and then by CF_4. The similar observation has been reported by Shiji *et al.*[10] (cf. Fig. 3 of Shiji *et al.* [10]).

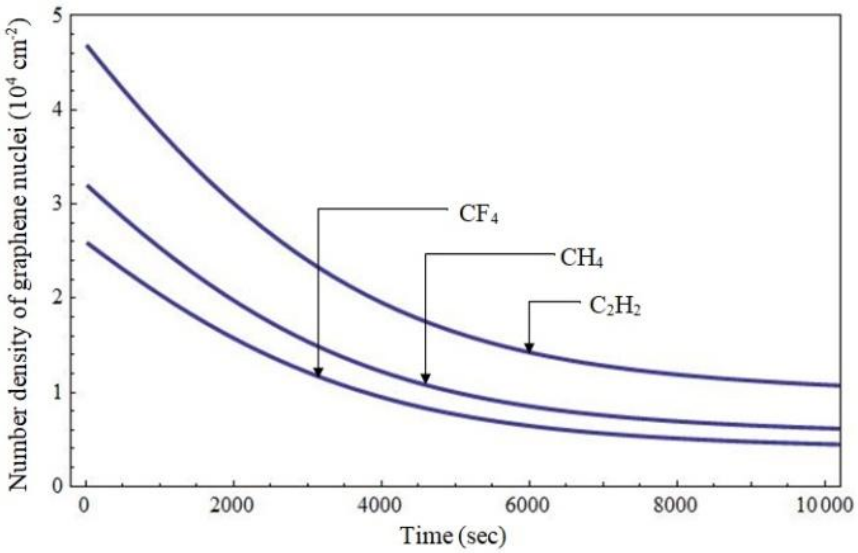

Fig. 5.6. The time evolution of graphene nuclei density for different carbon precursor gases C_2H_2, CH_4, and CF_4. The other parameters are given in the text and Tables 5.2 and 5.3.

Using the above results, we can conclude that geometry (i.e., height and thickness) of the graphene sheet alters considerably upon its PECVD synthesis using different gas mixtures. The field enhancement factor $\beta\left(\approx {}^{h_{gn}}\!/_{t_{gn}}\right.$, where h_{gn} is the height and t_{gn} is the thickness of graphene sheet [37,38]), characteristic of electron field emission from the graphene sheet, is primarily dependent on the geometry of the graphene sheet. Thus, using the above results, we can interpret the field emission characteristics of the graphene sheet grown using different gas mixtures via PECVD process. In order to estimate β, we calculated the saturated value of thickness (i.e., 6.15 nm, 4.2 nm, and 4.95 nm) and height (i.e., 704 nm, 382 nm, and 277.54 nm) of the graphene sheet corresponding to C_2H_2, CH_4 and CF_4 containing gas mixtures, respectively. It can be seen from Fig. 5.7 that graphene sheet grown using C_2H_2 as a carbon source gas has highest field enhancement factor which is followed by CH_4 and then by CF_4. Hence, C_2H_2 containing gas mixture improves the field emission properties in contrast to CH_4 and CF_4. Although the graphene sheets grown using CH_4 and CF_4 are relatively thinner, C_2H_2 grown graphene sheet exhibits

high field emission characteristics due to the fact that graphene sheets grown in this case are relatively much higher in height compared to CH_4 and CF_4. The above observations have been validated by Zhu *et al.*[5] and Saito [39].

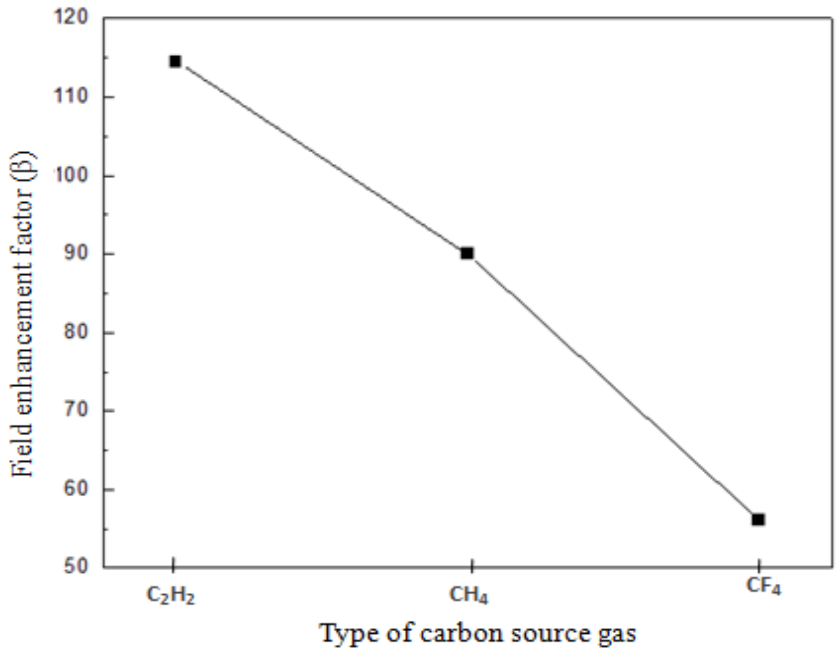

Fig. 5.7. The field enhancement factor of the graphene sheet for different carbon precursor gases C_2H_2, CH_4, and CF_4.

References

[1] D. H. Seo, A. E. Rider, Z. J. Han, S. Kumar and K. Ostrikov, Adv. Mater **25**, 5638 (2013).

[2] Y. Zhu, J. J. Wang, B. C. Holloway, R. A. Outlaw, X. Zhao, K. Hou, V. Shutthanandan, and D. M. Manos, Carbon **45**, 2229 (2007).

[3] Z. Bo, Y. Yang, J. Chen, K. Yu, J. Yan, and K. Cen, Nanoscale**5**, 5180 (2013).

[4] K. Ostrikov, H.-J. Yoona, A. E. Rider, S. V. Vladimirov, Plasma Process. Polym. **4**, 27 (2007).

[5] M. Y. Zhu, R.A. Outlaw, M. B.-Hansen, H. J. Chen, D.M. Manos, Carbon **49**,2526 (2011).

[6] M. Cai, R. A. Outlaw, R. A. Quinlan, D. Premathilake, S. M. Butler, and J. R. Miller, ACS Nano **8**, 5873 (2014).

[7] A. N. Obraztsov, A. A. Zolotukhin, A. O. Ustinov, A. P. Volkov, Y. Svirko, and K. Jefimovs, Diamond Relat. Mater. **12**, 917 (2003).

[8] J. Zhao, M. Shaygan, J. Eckert, M. Meyyappan, and M. H. Rummeli, Nano Lett. **14**, 3064 (2014).

[9] K. Teii, S. Shimada, M. Nakashima, and T. H. Chuang, J. Appl. Phys. **106**, 084303 (2009).

[10] K. Shiji, M. Hiramatsu, A. Enomoto, M. Nakamura, H. Amano, M. Hori, Diamond Relat. Mater. **14**, 831 (2005).

[11] S. Kondo, S. Kawai,W. Takeuchi, K. Yamakawa, S. Den, H. Kano, M. Hiramatsu, and M. Hori, J. Appl. Phys. **106**, 094302 (2009).

[12] M. Hiramatsu and M. Hori, Jpn. J. Appl. Phys. **45**, 5522 (2006).

[13] D. J. Dagel, C. M. Mallouris, and J. R. Doyle, J. Appl. Phys. **79**, 11 (1996).

[14] I. B. Denysenko, S. Xu, J. D. Long, P. P. Rutkevych, N. A. Azarenkov, and K. Ostrikov, J. Appl. Phys. **95**, 2713 (2004).

[15] C. Deschenaux, AAffolter, D Magni, C. Hollenstein, and P.Fayet, J. Phys. D: Appl. Phys. **32**,1876 (1999).

[16] M. Mao and A. Bogaerts, J. Phys. D: Appl. Phys. **43**, 205201 (2010).

[17] J. Benedikt, J. Phys. D: Appl. Phys. **43**, 043001(2010).

[18] J. R. Doyle, J. Appl. Phys. **82**, 4763 (1997).

[19] K. Miyata, M. Hori, and T. Goto, J. Vac. Sci. Technol. A **14**, 2343 (1996).

[20] H. Mehdipour and K. Ostrikov, ACS Nano **6**, 10276 (2012).

[21] Z. Bo, S. Mao, Z. J. Han, K. Cen, J. Chen and K. Ostrikov, Chem. Soc. Rev. **44**,2108 (2015).

[22] B. B. Wang, K. Zheng, Q.J. Cheng, K. Ostrikov, Appl. Surf. Sci. **325**, 251 (2015).

[23] H. Mehdipour, K. Ostrikov, and A.E. Rider, Nanotechnology **21**, 455605 (2010).

[24] M. A. Lieberman and A. J. Lichtenberg, *Principles of Plasma Discharges and Materials Processing* (Wiley Interscience Publication, USA, 1994).

[25] M. Chhowalla, K. B. K. Teo, C. Ducati, N. L. Rupesinghe, G. A. J. Amaratunga, A. C. Ferrari, D. Roy, J. Robertson, and W. I. Milne, J. Appl. Phys. **90**, 5308 (2001).

[26] R. Gupta, S. C. Sharma, and R. Sharma, Plasma Sources Sci. Technol. **26**, 024006 (2017).

[27] Z. Marvi, S. Xu, G. Foroutan, and K. Ostrikov, Phys. Plasmas **22**, 013504 (2015).

[28] N. V. Mantzaris, E. Gogolides, A.G. Boudouvis, A. Rhallabi, and G. Turban, J. Appl. Phys. **79**, 3718 (1996).

[29] B. B. Wang, K. Ostrikov, T. van der Laan, K. Zheng, J. J. Wang, Y. P. Yan and X. J. Quan, J. Mater. Chem. C **1**, 7703 (2013).

[30] D. H. Seo, S. Kumar, A. K. Rider, Z. Han, and K. Ostrikov, Opt. Mat. Express **2**, 700 (2012).

[31] A. Tewari and S. C. Sharma, Phys. Plasmas **21**, 063512 (2014).

[32] M. S. Sodha, S. Misra, S. K. Misra, and S. Srivastava, J. Appl. Phys. **107**, 103307 (2010).

[33] O. A. Louchev, C. Dussarat, and Y. Sato, J. Appl. Phys. **86**, 1736 (1999).

[34] I. Denysenko and N.A. Azarenkov, J. Phys. D: Appl. Phys. **44**, 174031 (2011).

[35] H. Maeda, M. Irie, T. Hino, K. Kusakabe and S. Morooka, Diamond Relat. Mater. **3**, 1072 (1994).

[36] I. Schmidt, F. Hentschel, C. Benndorf, Diamond Relat. Mater. **5**, 1318 (1996).

[37] S. Watcharotone, R. S. Ruoff, and F. H. Read, Phys. Procedia **1**, 71 (2008).

[38] R. Miller, Y. Y. Lau, and J. H. Booske, Appl. Phys. Lett. **91**, 074105(2007).

[39] Y. Saito, Ed. Carbon nanotube and related field emitters: fundamentals and applications (John Wiley & Sons 2010).

6

Multistage modeling to study the PECVD process parameters controlled growth of vertical oriented graphene sheet

6.1 Brief outline of the chapter

The present chapter comprises the plasma kinetics and surface deposition sub-models to study the influence of plasma enhanced chemical vapor deposition (PECVD) process parameters on the plasma composition and characteristics to understand the insights of the evolution of growth characteristics of vertically oriented graphene sheets (VOGS) grown in the $Ar+H_2+C_2H_2$ reactive plasma environment. The spatial distributions of temperature and densities of electrons, positively charged, and neutral species in the plasma reactor are examined using inductively coupled plasma module (ICP) of COMSOL Multiphysics 5.2 modeling suite. The numerical data from the computational plasma model are fed as the input parameters for the surface deposition model to control the growth characteristics of the plasma grown VOGS over the catalyst-substrate surface.

6.2 Introduction

The plane (flat) and rolled form of graphene sheets (carbon nanotubes/nanofibers) have been studied extensively due to their unique properties and potential applications in electronic devices [1-4]. However, in recent years, the graphene sheets oriented vertical to the substrate have gained heightened admiration owing to their additional benefits for many specific applications [5]. Amongst several techniques [6-8] for graphene synthesis, plasma-assisted growth method is exclusively used to fabricate the VOGS perpendicular to the substrate surface [9-11]. The large surface area, non-

agglomerated structure, electrochemical stability, and sharp edges render VOGS to be promising candidates for the field emission devices [5, 11-13]. It has also been reported that the field emission properties of the field emitters are strongly associated with their structural characteristics [14, 15]. Thus, in order to obtain highly enhanced field emission properties from the VOGS, it is crucially important to deterministically control their growth characteristics which can be done by suitably optimizing the PECVD process parameters such as total gas pressure, input plasma power, substrate temperature, and biasing applied to the substrate. These PECVD process parameters ultimately affect the plasma characteristics such as number density and temperature of neutral and charged species (electrons and positively charged ions) in the plasma [16-19] which consequently, affect the fluxes of neutral and charged species towards the substrate surface and significantly affect the structural and growth characteristics of the VOGS [20-23].

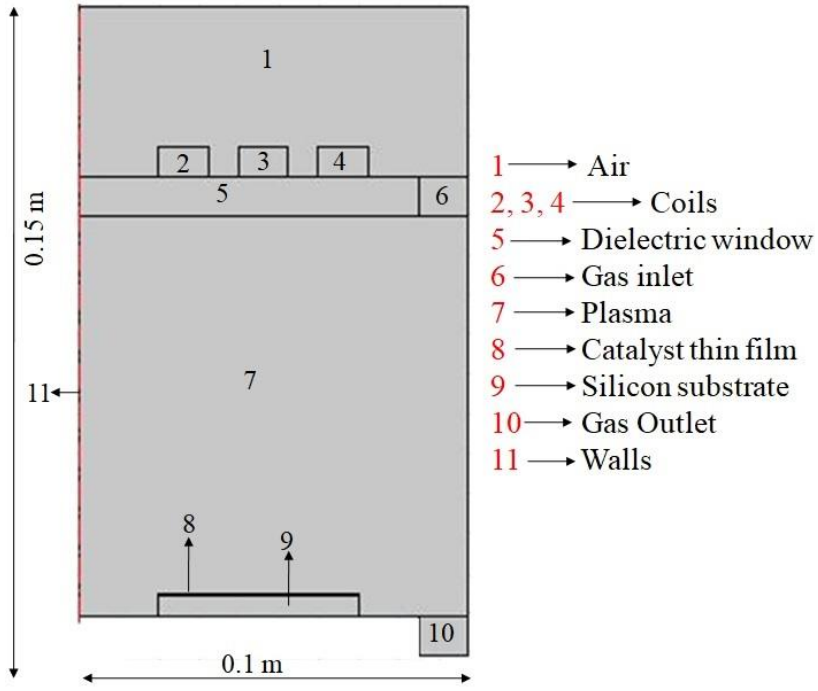

Fig. 6.1. Geometry constructed in the computational model using COMSOL Multiphysics 5.2 modelling suite. All the domains are assigned numbers, and their descriptions are given adjacent to the geometry.

6.3 Methodology and model

The methodology adopted in the present chapter includes the computational and analytical approach to elucidate the effects of PECVD process parameters namely, total gas pressure and input plasma power on the plasma characteristics which further affect the growth characteristics of VOGS in the PECVD system composed of the $Ar+H_2+C_2H_2$ reactive gas mixture. The Fig. 6.1 represents the model geometry constructed within the 2D axis-symmetric workspace in COMSOL Multiphysics 5.2 simulation software. 5 turn inductive coil connected to 13.56 MHz generator is taken as the source of inductively coupled plasma. The power applied to the coils passes to the plasma reactor through the dielectric material situated at the bottom of the coils and generates the plasma inside the reactor which is fed with the mixture of argon, hydrogen, and acetylene.

Table 6.1. Parameters used in the computational model.

Parameter	Value
Gas temperature	0.18 eV
Reduced electron mobility	$4\times10^{24}V^{-1}m^{-1}s^{-1}$
Relative permittivity of vacuum	1
Relative permittivity of silicon substrate	12
Negatively bias to substrate	-300 V
Relative permittivity of dielectric material	4.2
Relative permeability of vacuum	1
Electrical conductivity of coil	6×10^{7} S/m
Electrical conductivity of vacuum	0
Electrical conductivity of dielectric material	0

The ICP module is computed in COMSOL Multiphysics 5.2 modelling suite to evaluate the distribution of the number densities, energies, and transport of the electrons and heavy species (ions and neutral species). The number density, mean energy, and temperature of electrons are computed using the drift-diffusion interface; number densities and energies of the heavy species are computed using heavy species transport interface; and electric field, electric potential, and charge in the plasma are computed using the electrostatic

interface in the ICP module in frequency transient domain with appropriate parameters provided in Table 6.1. The volumetric species and reactions in the plasma considered in the present computation are listed in Table 6.2 and Table 6.3, respectively. The outcomes of the computations are linked to the input parameters for the surface deposition model to study the growth characteristics of VOGS over the catalyst (copper) nanoislands placed over the silicon substrate surface.

Table 6.2. Neutrals and positively charged species considered in the present model

Type	Neutrals	Positively charged species
X	C_2H, C_2H_2, C_2H_3, C_4H, C_4H_2, C_4H_3 C_6H, C_6H_2	C_2H^+, $C_2H_2^+$, $C_2H_3^+$, C_4H^+, $C_4H_2^+$, $C_4H_3^+$ C_6H^+, $C_6H_2^+$,
Y	H_2, H	H_2^+, H^+

Table 6.3. Volumetric reactions considered in the computational model and their corresponding rate coefficients/ionization energies, and the references where the value of rate coefficients/ionization energies are adopted from

Reactions	Rate coefficient (cm^3/s) or ionization energy (eV)	Reference
$e^- + Ar \rightarrow Ar^+ + 2e^-$	15.8	35
$e^- + C_2H_2 \rightarrow C_2H_2^+ + 2e^-$	11.4	35
$e^- + C_2H_2 \rightarrow C_2H^+ + H + 2e^-$	16.5	35
$e^- + C_2H_2 \rightarrow CH^+ + CH + 2e^-$	20.6	35
$e^- + C_2H_2 \rightarrow C_2H + H^+ + 2e^-$	18.4	35
$e^- + C_2H_2 \rightarrow C_2H + H + 2e^-$	7.5	35
$e^- + H_2 \rightarrow H_2^+ + 2e^-$	15.4	35
$e^- + H \rightarrow H^+ + 2e^-$	15.4	35
$e^- + H_2 \rightarrow H + H + e^-$	8.87	35
$e^- + C_4H_2 \rightarrow C_4H + H + e^-$	7.5	35
$e^- + C_6H_2 \rightarrow C_6H + H + e^-$	7.5	35
$e^- + C_4H_2 \rightarrow C_4H_2^+ + 2e^-$	10.19	35
$e^- + C_6H_2 \rightarrow C_6H_2^+ + 2e^-$	9.55	35
$e^- + C_6H \rightarrow C_6H^+ + 2e^-$	9.55	35
$e^- + C_4H_3 \rightarrow C_4H_3^+ + 2e^-$	10.19	35

$e^- + C_4H \rightarrow C_4H^+ + 2e^-$	10.19	35
$e^- + C_2H \rightarrow C_2H^+ + 2e^-$	11.4	35
$H^+ + C_4H \rightarrow C_4H^+ + H$	2×10^{-9}	35
$H^+ + C_6H \rightarrow C_6H^+ + H$	2×10^{-9}	35
$H^+ + C_2H_2 \rightarrow C_2H^+ + H_2$	4.30×10^{-9}	35
$H^+ + C_4H_2 \rightarrow C_4H^+ + H_2$	2×10^{-9}	35
$H_2^+ + H \rightarrow H_2 + H^+$	6.40×10^{-10}	35
$H_2^+ + C_2H_2 \rightarrow C_2H_2^+ + H_2$	5.30×10^{-9}	35
$H_2^+ + C_4H \rightarrow C_4H_2^+ + H$	1.70×10^{-10}	35
$C_2H + C_4H^+ \rightarrow C_6H^+ + H$	6.00×10^{-10}	35
$C_2H + C_4H_2^+ \rightarrow C_6H_2^+ + H$	1.30×10^{-9}	35
$C_2H_2 + C_2H^+ \rightarrow C_4H_2^+ + H$	1.20×10^{-9}	35
$C_2H_2 + C_2H_3^+ \rightarrow C_4H_3^+ + H_2$	2.40×10^{-10}	35
$C_2H_2 + C_4H^+ \rightarrow C_6H_2^+ + H$	1.50×10^{-9}	35
$C_2H_2 + C_2H_2^+ \rightarrow C_4H_3^+ + H$	9.50×10^{-10}	35
$C_2H_2 + C_2H_2^+ \rightarrow C_4H_2^+ + H$	1.20×10^{-9}	35
$C_2H_2^+ + H_2 \rightarrow C_2H_3^+ + H$	1.00×10^{-11}	35
$C_2H_2^+ + C_6H_2 \rightarrow C_6H_6^+ + C_2H_2$	5.00×10^{-10}	35
$C_2H_3 + C_2H_2^+ \rightarrow C_4H_3^+ + H_2$	3.30×10^{-10}	35
$C_2H_3 + C_4H_2^+ \rightarrow C_6H_4^+ + H$	1.20×10^{-9}	35
$C_2H_3^+ + H \rightarrow C_2H_2^+ + H_2$	6.80×10^{-11}	35
$C_2H_3^+ + C_4H \rightarrow C_6H_2^+ + H_2$	4.00×10^{-10}	35
$C_2H_3^+ + C_6H \rightarrow C_6H_2^+ + C_2H_2$	5.0010^{-10}	35
$H^+ + Ar \rightarrow H + Ar^+$	$3.9\times10^{-15}T_g^{1/2}(1+7.9\times10^{-5}T_g)\times\exp(-2.5\times10^4/T_g)$	36
$H_2^+ + Ar \rightarrow H_2 + Ar^+$	3.3×10^{-10}	37
$H_2^+ + Ar \rightarrow ArH^+ + H$	1.2×10^{-9}	36
$Ar^+ + H_2 \rightarrow H_2^+ + Ar$	$0.02\times8.9\times10^{-10}$	38
$Ar^+ + H_2 \rightarrow ArH^+ + H$	$0.98\times8.9\times10^{-10}$	38
$Ar^+ + C_2H_2 \rightarrow C_2H_2^+ + Ar$	0.42×10^{-9}	39

The catalyst nanoislands have peculiar ability to dissociate the hydrocarbon and hydrogen species on their active surface to generate building units (carbon species) of the graphene sheet and hydrogen radicals which etch

and sharpen the edges of the graphene sheet via various complex processes [24, 25] discussed in Eqs. (6.1) & (6.2), respectively.

$$\partial_\tau(\bar{n}_C) = \sum_X J_X(1-\theta_t) + \sum_X \bar{n}_X\, \upsilon \exp\left(-\frac{\Delta\varepsilon_{X\_diss}}{k_B T_S}\right) + \sum_{iX}\left(\sum_X \bar{n}_X\right)\frac{J_{iX}\, y_d}{\upsilon_0} + \sum_{iX} J_{iX}$$
$$+\sum_{iY}\left(\sum_{iX} J_{iX}\right)\frac{J_{iY}\sigma_{ads}}{\upsilon} - \sum_Y\left(\sum_X \bar{n}_X\right) J_Y \sigma_{ads}$$
$$-\bar{n}_C\, \upsilon \exp\left(-\frac{\Delta\varepsilon_{Evp}}{k_B T_S}\right) - \sum_X \bar{n}_X\, \upsilon \exp\left(-\frac{\Delta\varepsilon_{X\_ads}}{k_B T_S}\right) - \bar{n}_C\, \sigma_{ads}\, \bar{n}_H\, \upsilon, \qquad (6.1)$$

$$\partial_\tau(\bar{n}_H) = \sum_Y J_Y(1-\theta_t) + \sum_{iX}\left(\sum_X \bar{n}_X\right)\frac{J_{iX}\, y_d}{\upsilon_0} + \sum_X \bar{n}_X\, \upsilon \exp\left(-\frac{\Delta\varepsilon_{X\_diss}}{k_B T_S}\right) + \sum_{iY} J_{iY}$$
$$-\sum_Y \bar{n}_Y\, \upsilon \exp\left(-\frac{\Delta\varepsilon_{Y\_ads}}{k_B T_S}\right) - \bar{n}_C\, \sigma_{ads}\upsilon\, \bar{n}_H - \sum_Y \bar{n}_Y\, \sigma_{ads} J_Y - \sum_Y \bar{n}_Y\, \sigma_{ads} J_{iY}, \qquad (6.2)$$

where $\bar{n}_C$ and $\bar{n}_H$ are the concentration of building units (carbon species) and hydrogen radicals on the surface of catalyst nanoislands, respectively, $J_j\left(=n_j v_{th}/4\right)$ is the flux of impinging neutral species (j=X and Y for hydrocarbons and hydrogen species, respectively) [26] , $\bar{n}_j\ (=\theta_j \upsilon_0)$represents the surface concentration of neutrals on the catalyst nanoislands active surface; θ_j is the j^{th} species surface coverage, $\nu_0\left(\approx 10^{15}\,\mathrm{cm}^{-2}\right)$is the number of adsorption sites per unit area [26], $y_d(\approx 2.49\times10^{-2} + 3.29\times10^{-2}\times E_i$ is the stitching probability; $E_i$is the electron energy[27], $J_{ij}\left(=n_{ij}\left(k_B T_e/m_{ij}\right)^{1/2}\right)$ is the flux of positively charged species [26], $\sigma_{ads}\left(\approx 10^{-16} cm^2\right)$ is the cross-section for the interaction of hydrogen radicals with hydrocarbon species on the surface of catalyst nanoislands [26], $\Delta\varepsilon_{X\_diss}(=2.1\,eV)$ is the dissociation energy of species of type X, $\Delta\varepsilon_{Evp}(=1.8\,eV)$ is the evaporation energy of carbon species from the surface of nanoislands, $\Delta\varepsilon_{X_ads}(=1.8\ \mathrm{eV})$and $\Delta\varepsilon_{Y\_ads}(=1.8\ \mathrm{eV})$ are the adsorption energies of species of type X and Y, respectively [25]. The LHS of

Neha Gupta
Delhi Technological University, Delhi, India

Eqs. (6.1) & (6.2) are the functions of growth time and descriptions of each and every term on RHS are given in the Table 6.4 and 6.5, respectively.

Table 6.4. Descriptions of all the functional terms used in the Eq. (6.1) and their corresponding reactions involved [15, 25-27, 40], where 'as' stands for adsorption, 'pl' stands for plasma and 'dsp' stands for desorption.

Term	Reaction involved	Description
$J_X(1-\theta_t)$	$C_aH_{b(pl)} \rightarrow C_aH_{b(ad)}$	adsorption of hydrocarbon neutral species on the catalyst nanoislands active surface
$\bar{n}_X \upsilon \exp\left(\frac{-\Delta\varepsilon_{X\_diss}}{k_B T_S}\right)$	$C_aH_{b(ad)} \rightarrow aC_{(ad)} + bH_{(ad)}$	thermal dissociation of hydrocarbon neutral species
$\bar{n}_X \frac{J_{iX} y_d}{\upsilon_0}$	$C_aH_b^+ + C_aH_{b(ad)} \rightarrow a\,C_{(ad)} + H_{Y(pl)} + C_aH_b^+$	ion-induced dissociation of hydrocarbon neutral species
J_{iX}	$C_aH_b^+ \rightarrow aC_{(ad)} + H_{b(pl)}$	decomposition of positively charged species
$J_{iX}\frac{J_{iY}\sigma_{ads}}{\upsilon}$	$C_aH_b^+ + H^+ \rightarrow aC_{(ad)} + 2H_{b(pl)}$	generation of carbon species due to interaction between hydrocarbons and hydrogen ions
$\sum_Y \left(\sum_X \bar{n}_X\right) J_Y \sigma_{ads}$	$C_aH_{b(ad)} + H_{(pl)} \rightarrow C_aH_{b'(pl)}$	loss of adsorbed hydrocarbons from catalyst nanoislands surface due to interaction with hydrogen radicals
$\bar{n}_C \upsilon \exp\left(\frac{-\Delta\varepsilon_{Evp}}{k_B T_S}\right)$	$C_{(ad)} \rightarrow C_{(evaporation)}$	evaporation of carbon species generated on the nanoislands surface
$n_X \upsilon \exp\left(\frac{-\Delta\varepsilon_{X\_dsop}}{k_B T_S}\right)$	$C_aH_{b(ad)} \rightarrow C_aH_{b(dsp)}$	desorption of the adsorbed hydrocarbons on the nanoislands surface
$\bar{n}_C \sigma_{ads} \bar{n}_H \upsilon$	$aC_{(ad)} + bH_{(ad)} \rightarrow C_aH_{b(pl)}$	loss of carbon species due to the interaction with hydrogen species

Table 6.5. Descriptions of all the functional terms used in the Eq. (6.2) and their corresponding reactions involved [15, 25-27, 40], where 'as' stands for adsorption, 'pl' stands for plasma and 'dsp' stands for desorption.

Term	Reaction involved	Description
$J_Y(1-\theta_t)$	$H_{(pl)} \rightarrow H_{(ad)}$ $H_{2(pl)} \rightarrow H_{2(ad)}$	adsorption of hydrogen neutral species on the catalyst nanoislands active surface
$\bar{n}_Y \upsilon \exp\left(\frac{-\Delta\varepsilon_{dH}}{k_B T_S}\right)$	$H_{(ad)} \rightarrow H_{(dsp)}$	desorption of hydrogen species from catalyst nanoislands surface
$\bar{n}_Y \sigma_{ads} J_Y$	$H_{(ad)} + H_{(pl)} \rightarrow H_{2(pl)}$	loss of hydrogen species due to interaction with incoming hydrogen neutral species
$\bar{n}_Y \sigma_{ads} J_{iY}$	$bH_{(ad)} + H^+_{(pl)} \rightarrow b'H_{2(pl)} + H^+$	loss of hydrogen species due to interaction with incoming hydrogen ions

These building units diffuse over the catalyst nanoislands surface and attach with each other to from clusters (a bunch of few carbon species around the nanoislands). Due to the continuous dissociation of hydrocarbons and generation of carbon species, these clusters tend to diffuse and agglomerate to nucleate graphene nuclei. The surface concentration of these clusters with respect to growth time can be evaluated using the Eq. (6.3) that incorporates the surface diffusion of carbon species over the catalyst nanoislands surface (first term), the decrease in the numbers of clusters due to their diffusion and attachment to the graphene nuclei/island (second and third term) [28].

$$\partial_t(\bar{n}_{CL}) = D\bar{n}_{ct}\,\bar{n}_C - D'\bar{n}_{CL}\frac{4}{\pi D_{ct}^2} - \bar{n}_{CL}\,\bar{n}_{GN}\,D_0\exp\left(-\frac{(\Delta\varepsilon_{sd\_CL} + \Delta\varepsilon_{inc\_CL})}{k_B T_s}\right), \quad (6.3)$$

where D_{ct} is the diameter of the catalyst nanoisland, $\bar{n}_{CL}$, $\bar{n}_{ct}$, and $\bar{n}_{GN}$ are the surface concentrations of carbon clusters, catalyst nanoislands, and graphene nuclei, respectively. $D\left[=D_0\exp\left(-\Delta\varepsilon_{sd\_C}/k_B T_s\right)\right]$ is the coefficient of surface diffusion for carbon species, $D'\left[=D_0\exp\left(-\Delta\varepsilon_{sd\_CL}/k_B T_s\right)\right]$ is the coefficient of surface diffusion for clusters, $\Delta\varepsilon_{sd\_C}$ $(=0.1\text{ eV})$ and $\Delta\varepsilon_{sd\_CL}$ $(=0.82\text{ eV})$ are the

surface diffusion energies of carbon species and clusters, respectively. $\Delta\varepsilon_{inc\_CL}$ is the incorporation energy of clusters into graphene nuclei [28]. Moreover, the surface concentration of graphene nuclei over the substrate surface can be evaluated using the Eq. (6.4) that incorporates the surface diffusion of the clusters to form graphene nuclei (first term), attachment of clusters and building units to the existing nuclei (second& third terms). These graphene nuclei agglomerate and form graphene islands which in turn lead to the decrease in the surface concentration of the nuclei (fourth term) [28].

$$\begin{aligned}\partial_\tau(\bar{n}_{GN}) = \bar{n}_{CL}\, D' \times \frac{4}{\pi D_{ct}^2} - \bar{n}_{CL}\, \bar{n}_{GN}\, D_0 \exp\left(-\frac{\left(\Delta\varepsilon_{sd\_CL} + \Delta\varepsilon_{inc\_CL}\right)}{k_B T_s}\right) \\ + \bar{n}_C\, \bar{n}_{GN}\, D_0 \exp\left(-\frac{\left(\Delta\varepsilon_{sd\_C} + \Delta\varepsilon_{inc\_C}\right)}{k_B T_s}\right) \\ - \bar{n}_{GN}\, D_0 \exp\left(-\frac{\Delta\varepsilon_{sdGI}}{k_B T_s}\right) \times \frac{4}{\pi D_{GI}^2},\end{aligned} \tag{6.4}$$

where $\Delta\varepsilon_{inc\_CL}\left(\approx 0.8\ \text{eV}\right)$ and $\Delta\varepsilon_{inc\_C}\left(\approx 0.85\ \text{eV}\right)$ are the incorporation energies with which clusters and carbon species, respectively diffuse into the graphene nuclei. D_{GI} is the diameter of the graphene island and $\Delta\varepsilon_{sdGI}\ \left(\approx 2.6\ \text{eV}\right)$ is the energy with which graphene nuclei diffuse into the graphene islands [28]. The continuous diffusion of the graphene nuclei into the graphene islands leads to the growth of the graphene islands which can also be regarded as the growth of planar/flat graphene sheet with respect to substrate surface [28]. The factors responsible for the growth of planar graphene (graphene island) are discussed in the Eq. (6.5) that accounts the diffusion of carbon clusters (first term), attachment of carbon clusters and building units to the graphene island (second and third term), amalgamation of graphene islands (fourth term), and the accretion of hydrocarbon neutrals on the growing graphene island surface (last term).

$$\partial_\tau (A_{GI}) = \left[\left\{ \frac{\bar{n}_{CL}}{A_{ct}} D_0 \exp\left(-\frac{\Delta\varepsilon_{sd\_CL}}{k_B T_s} \right) + \bar{n}_{CL}\ \bar{n}_{GN}\ D_0 \right. \right.$$
$$\times \exp\left(-\frac{\left(\Delta\varepsilon_{sd\_CL} + \Delta\varepsilon_{inc\_CL}\right)}{k_B T_s} \right) + \bar{n}_C\ \bar{n}_{GN} D_0$$
$$\left. \left. \exp\left(-\frac{\left(\Delta\varepsilon_{sd\_C} + \Delta\varepsilon_{inc\_C}\right)}{k_B T_s} \right) \right\} \times \pi D_{ct} + \bar{n}_{GN}\ D_0 \right.$$
$$\left. \exp\left(\frac{\Delta\varepsilon_{sdGI}}{k_B T_s} \right) \times \frac{1}{\pi D_{GI}} \right] \times \left(\frac{M_{ct} \times I_{iAGI}}{\rho_{ct} \upsilon} \right) + \frac{\gamma_X \pi D_{GI}^2 I_{AGI}}{4}, \qquad (6.5)$$

where $A_{GI}\left(=\frac{\pi D_{GI}^2}{4}\right)$ and $A_{ct}\left(=\frac{\pi D_{ct}^2}{4}\right)$ are the area of the graphene islands and catalyst nanoislands, respectively. M_{ct} (=63.54 a.m.u.) and ρ_{ct} are the mass and density of the copper catalyst, respectively. $I_{ijGI} = \frac{\pi D_{GI}^2}{4}\left(\frac{8k_B T_{ij}}{\pi m_{ij}}\right)^{\frac{1}{2}}$ $n_{ij}\left[1 - Z\gamma_{ij}\right]\left(\exp\left[-\frac{eU_s}{k_B T_s}\right]\right)$ is the current accumulated at the graphene island surface due to positively charged species [29]; n_{ij} is the number density of positively charged species near the substrate surface, z is the charge number developed over the graphene sheet, T_{ij} and m_{ij} are the temperature and mass of positively charged species, respectively; T_s is the substrate temperature, $I_{jGI}\left[=\pi\frac{D_{GI}^2}{4}\left(\frac{8k_B T_n}{\pi m_j}\right)^{\frac{1}{2}} n_j\right]$ is the current accumulated at the graphene island surface due to neutral species [29]; n_j is the number density of neutrals near the substrate surface, T_n, m_j, and γ_j are the temperature, mass, and sticking coefficient of neutral species, respectively.

When the growth of planar graphene is initiated, an internal stress (tangential stress) is induced at the graphene islands boundaries which cause the defects on the graphene islands [5]. Under the combined effect of the electric force exerted by the electric field induced in the plasma sheath and resultant of

the tangential stress, graphene sheet eventually begins to grow in vertical upward direction (perpendicular to the substrate surface). The Eq. (6.6) describes the rate with which area of growing VOGS changes.

$$l\partial_\tau(h\times t)=\left[\frac{4\bar{n}_C\,\pi D_{GI}}{\nu}D_0\exp\left(-\frac{\left(\Delta\varepsilon_{sd\_C}+\Delta\varepsilon_{inc\_C}\right)}{k_BT_s}\right)\frac{I_{iAGN}}{\pi D_{GI}^2}+\right.$$
$$\left.\gamma_X I_{XGN}\right]\times\frac{M_{GN}}{\rho_{GN}}(1-\alpha_S\alpha_C), \qquad (6.6)$$

where l, t, and h are the lateral length (dimension of the graphene sheet parallel to the substrate surface), thickness and vertical height (dimension of the graphene sheet normal to the substrate surface) of the VOGS, respectively. ρ_{GN} and $M_{GN}(\approx 12g)$ are the density and mass of the growing VOGS, respectively. I_{ijGN} and I_{jGN} are the collection currents due to positively charged and neutral species on the growing VOGS, respectively. V_s is the surface potential of the VOGS [see Eq. (A.2) of Appendix A].

$$I_{ijGN}=n_{ij}(lt+ht+lh)\left(\frac{k_BT_{ij}}{2\pi^2m_{ij}}\right)^{\frac{1}{2}}\left\{\frac{2}{\sqrt{\pi}}\left(\frac{eV_s}{k_BT_i}\right)^{\frac{1}{2}}\right.$$
$$\left.+\exp\left[\frac{eV_s}{k_BT_{ij}}\right]erfc\left[\left(\frac{eV_s}{k_BT_{ij}}\right)^{\frac{1}{2}}\right]\right\}\times\exp\left[-\frac{eU_s}{k_BT_s}\right], \qquad (6.7)$$

$$I_{jGN}=n_j(lt+ht+lh)\left(\frac{k_BT_n}{2\pi^2m_j}\right)^{\frac{1}{2}} \qquad (6.8)$$

The Eq. (6.6) incorporates the vertical growth of graphene sheet due to diffusion and incorporation of building units at the growing edges of the graphene layers and accretion of the hydrocarbon neutral species contribute to the VOGS growth (first & the second term, respectively). Moreover, the formation and sputtering of the amorphous carbon layer on the catalyst active surface is one of the major growth rate-determining steps. Therefore, the multiplication term $(1-\alpha_S\alpha_C)$ indicative to the poisoning of the catalyst is also

taken into account in the VOGS growth in Eq. (6.6) [27]; where $\alpha_S = J_{iX} y_{sp} (1-\theta_t) \times \frac{\pi D_{ct}^2}{\upsilon}$, $\alpha_C = \pi D_{ct}^2 \bar{n}_C$, and y_{sp} is the sputtering yield. The growth of VOGS saturates/ceases due to etching of terminal carbons by the hydrogen and leads to the reduction in the thickness of the VOGS as discussed in Eq. (6.9) that incorporates the collection of positively charged and neutral species of hydrogen on the surface of the VOGS (first & second term, respectively).

$$\left[h(\tau)+l\right]\partial_\tau(t) = \left[\gamma_{iY} I_{iYGN} + \gamma_Y I_{YGN}\right]\bar{n}_H \frac{M_{GN}}{\rho_{GN}} h(\tau), \tag{6.9}$$

During the growth, the charge developed over the graphene sheet surface can be evaluated using the Eq. (6.10) that accounts the accumulation of positively charged species (first & second term) and electrons.

$$\partial_\tau Z = \sum_X I_{iXGN} + \sum_Y I_{iYGN} - \gamma_e I_{eGN}, \tag{6.10}$$

where I_{eGN} is the current accumulated at the graphene sheet surface due to the electrons.

$$I_{eGN} = \left(\frac{k_B T_e}{2\pi^2 m_e}\right)^{\frac{1}{2}} n_e (lt + ht + lh) \exp\left[\frac{eV_s}{k_B T_e} + \frac{eU_s}{k_B T_s}\right] \tag{6.11}$$

where n_e is the number density of electrons near the substrate surface.

6.4 Results and discussion

In the present work, the effects of process parameters on the plasma characteristics using 2D axis-symmetric ICP module in COMSOL Multiphysics 5.2 are studied. The numerical data of number densities and temperatures of the various plasma species on varying the total gas pressure and input plasma power obtained from the computational model (see Tables 6.6-6.10) are fed as the input parameters in the surface deposition model to study the growth characteristics

(height, thickness, and surface density) of the VOGS during PECVD process along with the other experimentally determined initial conditions [30] and glow discharge parameters [16,25] given in the Table 6.11.

Table 6.6. Spatial distribution of electron density and temperature for different gas pressures and input power obtained from the computational Figs. 6.2- 6.6

Parameters		Gas Pressure			Input plasma power		
		50 mTorr	100 mTorr	150 mTorr	100 W	200 W	300 W
Electron density (m^{-3})	Bulk plasma	2.77×10^{17}	9.49×10^{16}	9.09×10^{15}	2.77×10^{17}	3.81×10^{17}	8.88×10^{17}
	Near the substrate	0.66×10^{17}	1.34×10^{16}	2.72×10^{15}	0.66×10^{17}	1.49×10^{17}	5.15×10^{17}
Electron Temperature (eV)	Bulk plasma	2.76	1.97	1.54	2.76	3.06	3.33
	Near the substrate	2.51	1.78	1.05	2.51	2.74	3.20

Table 6.7. Spatial distribution of the number densities of neutral species for different gas pressures obtained from the computational model at input plasma power of 100W

Neutral species	50 mTorr		100 mTorr		150 mTorr	
	Bulk plasma	Near the substrate	Bulk plasma	Near the substrate	Bulk plasma	Near the substrate
C_2H	8.74×10^{15}	4.39×10^{15}	6.97×10^{17}	0.14×10^{17}	7.13×10^{18}	0.56×10^{18}
C_2H_2	7.56×10^{18}	5.05×10^{18}	7.77×10^{21}	3.89×10^{21}	6.47×10^{23}	1.24×10^{23}
C_2H_3	9.28×10^{17}	3.90×10^{17}	6.67×10^{18}	2.39×10^{18}	8.42×10^{19}	3.78×10^{19}
C_4H	5.29×10^{13}	0.23×10^{13}	8.42×10^{13}	3.45×10^{13}	9.23×10^{14}	3.57×10^{14}
C_4H_2	9.91×10^{17}	3.35×10^{17}	5.12×10^{19}	1.11×10^{19}	7.79×10^{21}	4.27×10^{21}
C_4H_3	9.23×10^{16}	5.49×10^{16}	1.89×10^{18}	0.42×10^{18}	6.88×10^{19}	2.19×10^{19}
C_6H	4.77×10^{13}	3.05×10^{13}	6.99×10^{12}	2.42×10^{12}	4.32×10^{12}	1.21×10^{12}
C_6H_2	8.38×10^{16}	2.42×10^{16}	7.27×10^{18}	2.12×10^{18}	5.28×10^{20}	2.09×10^{20}
H_2	4.46×10^{23}	1.02×10^{23}	9.20×10^{22}	6.50×10^{22}	3.45×10^{22}	1.19×10^{22}
H	7.17×10^{18}	2.19×10^{18}	7.33×10^{20}	2.27×10^{20}	8.34×10^{21}	3.37×10^{21}

Table 6.8. Spatial distribution of the number densities of positively charged species (ions) for different gas pressures obtained from the computational model at input plasma power of 100W

Charged species	100 mTorr		150 mTorr	
	Bulk plasma	Near the substrate	Bulk plasma	Near the substrate
C_2H^+	8.07×10^{12}	3.15×10^{13}	7.89×10^{12}	2.59×10^{12}
$C_2H_2^+$	9.46×10^{13}	5.48×10^{13}	5.59×10^{12}	1.26×10^{12}
$C_2H_3^+$	6.56×10^{13}	2.15×10^{13}	9.48×10^{14}	5.15×10^{14}
C_4H^+	8.47×10^{10}	3.47×10^{10}	1.56×10^{10}	0.15×10^{10}
$C_4H_2^+$	4.52×10^{13}	1.09×10^{13}	8.48×10^{12}	3.44×10^{12}
$C_4H_3^+$	9.15×10^{14}	5.65×10^{14}	4.27×10^{14}	0.18×10^{14}
C_6H^+	7.28×10^{8}	4.24×10^{8}	6.45×10^{7}	2.15×10^{7}
$C_6H_2^+$	8.48×10^{9}	5.24×10^{9}	1.45×10^{9}	7.10×10^{8}
H_2^+	1.05×10^{14}	7.45×10^{13}	1.34×10^{13}	6.64×10^{12}
H^+	5.48×10^{19}	9.21×10^{18}	9.45×10^{19}	2.14×10^{19}

Table 6.9. Spatial distribution of the number densities of neutral species for different input power obtained from the computational model at total gas pressure of 50mTorr

Neutral species	200 W		300 W	
	Bulk plasma	Near the substrate	Bulk plasma	Near the substrate
C_2H	7.12×10^{14}	3.15×10^{14}	6.15×10^{13}	1.26×10^{13}
C_2H_2	4.56×10^{17}	0.56×10^{17}	5.51×10^{16}	0.84×10^{16}
C_2H_3	8.71×10^{16}	2.41×10^{16}	7.72×10^{15}	3.48×10^{15}
C_4H	9.45×10^{12}	4.12×10^{12}	0.94×10^{12}	5.16×10^{12}
C_4H_2	5.56×10^{16}	2.51×10^{16}	8.15×10^{15}	2.02×10^{15}
C_4H_3	1.23×10^{16}	0.56×10^{16}	9.45×10^{14}	4.85×10^{14}
C_6H	4.07×10^{12}	0.15×10^{12}	7.15×10^{11}	0.94×10^{11}
C_6H_2	4.12×10^{15}	0.48×10^{15}	9.45×10^{13}	4.48×10^{13}
H_2	7.48×10^{21}	2.05×10^{21}	2.16×10^{20}	0.11×10^{20}
H	8.45×10^{16}	1.56×10^{16}	4.12×10^{15}	0.45×10^{15}

Table 6.10. Spatial distribution of the number densities of positively charged species (ions) for different input power obtained from the computational model at total gas pressure of 50mTorr

Neutral species	100 W		200 W		300 W	
	Bulk plasma	Near the substrate	Bulk plasma	Near the substrate	Bulk plasma	Near the substrate
C_2H^+	6.45×10^{13}	3.33×10^{13}	7.54×10^{14}	4.12×10^{14}	8.18×10^{15}	3.76×10^{15}
$C_2H_2^+$	8.67×10^{15}	5.44×10^{15}	4.67×10^{16}	1.78×10^{16}	2.34×10^{17}	0.32×10^{17}
$C_2H_3^+$	5.55×10^{14}	3.34×10^{14}	4.12×10^{15}	2.39×10^{15}	8.59×10^{15}	5.67×10^{15}
C_4H^+	3.73×10^{11}	1.02×10^{11}	8.73×10^{11}	4.83×10^{11}	6.02×10^{12}	4.08×10^{12}
$C_4H_2^+$	8.17×10^{14}	3.15×10^{14}	6.37×10^{15}	1.71×10^{15}	5.25×10^{16}	1.58×10^{16}
$C_4H_3^+$	7.79×10^{14}	3.84×10^{14}	4.45×10^{15}	2.04×10^{15}	6.43×10^{16}	2.17×10^{16}
C_6H^+	5.81×10^{9}	2.29×10^{9}	9.28×10^{10}	3.26×10^{10}	7.53×10^{11}	4.99×10^{11}
$C_6H_2^+$	5.51×10^{10}	1.62×10^{10}	8.26×10^{10}	4.71×10^{10}	6.29×10^{11}	3.18×10^{11}
H_2^+	9.27×10^{14}	4.35×10^{14}	7.18×10^{15}	2.45×10^{15}	9.63×10^{16}	3.61×10^{16}
H^+	7.92×10^{18}	3.29×10^{18}	7.39×10^{20}	3.81×10^{20}	7.72×10^{21}	4.13×10^{21}

Table 6.11. Initial conditions fed into the surface deposition model (analytical model)

Parameter	Value
T_i (ion temperature)	0.05 eV
T_n (neutral atom temperature)	0.05 eV
ρ_{ct} (Density of catalyst)	8.96 g/cm^3
$\alpha_{10} \approx \alpha_{20}$ (electron-ion recombination coefficient)	1.12×10^{-7} cm^3/sec
T_s (substrate temperature)	550 ^{0}C
γ_e (electron sticking coefficient)	1
γ_{ij} (ion sticking coefficient)	1
γ_j (neutral atom sticking coefficient)	1
θ_t (total surface coverage)	0.01
D_{ct} (Diameter of the catalyst nanoislands)	100 nm
$\bar{n}_{ct}$ (number density of catalyst nanoislands)	6×10^{8}cm^{-2}

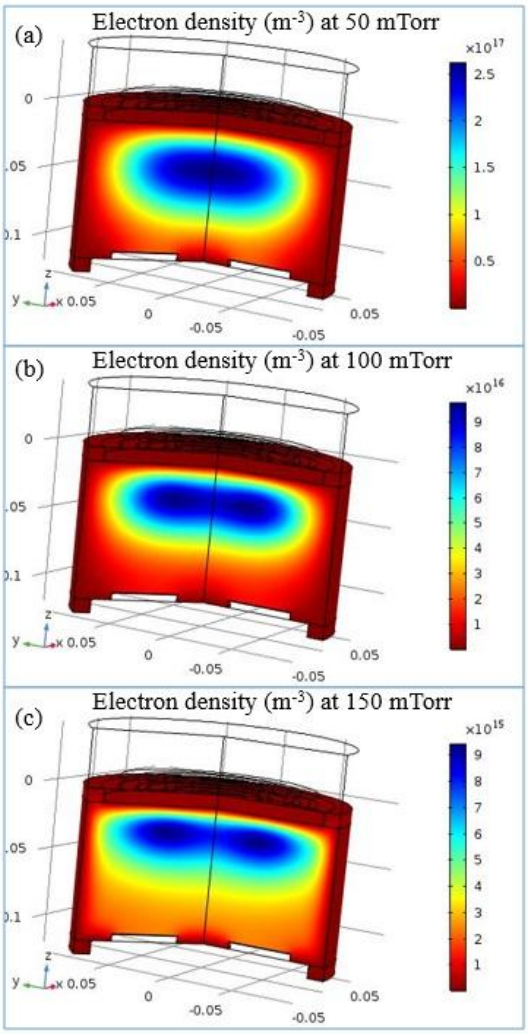

Fig. 6.2. 2D axis-symmetric computational plots showing the variation of electron number density with gas pressure, i.e., (a) 50 mTorr, (b) 100 mTorr, and (c) 150 mTorr at constant input plasma power of 100 W. All other parameters are given in the text.

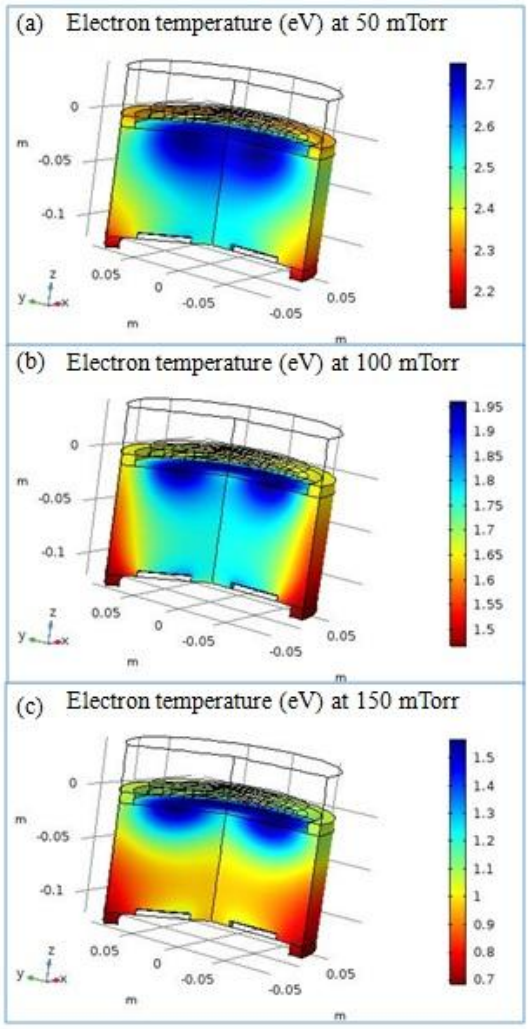

Fig. 6.3. 2D axis-symmetric computational plots showing the variation of electron temperature with gas pressure, i.e., (a) 50 mTorr, (b) 100 mTorr, and (c) 150 mTorr at constant input plasma power of 100 W. All other parameters are given in the text.

Figures 6.2 & 6.3 show the computational plots of electron number density and temperature at different total gas pressures, respectively. The numerical data obtained from these computational plots (Figs. 6.2 & 6.3) is summarized in Table 6.6 which shows that electron number density and temperature decreases from bulk plasma region to substrate surface. This is because significant numbers of electrons are consumed in the collisions with other plasma species and in the ionization/dissociation of other plasma species in the bulk plasma region.

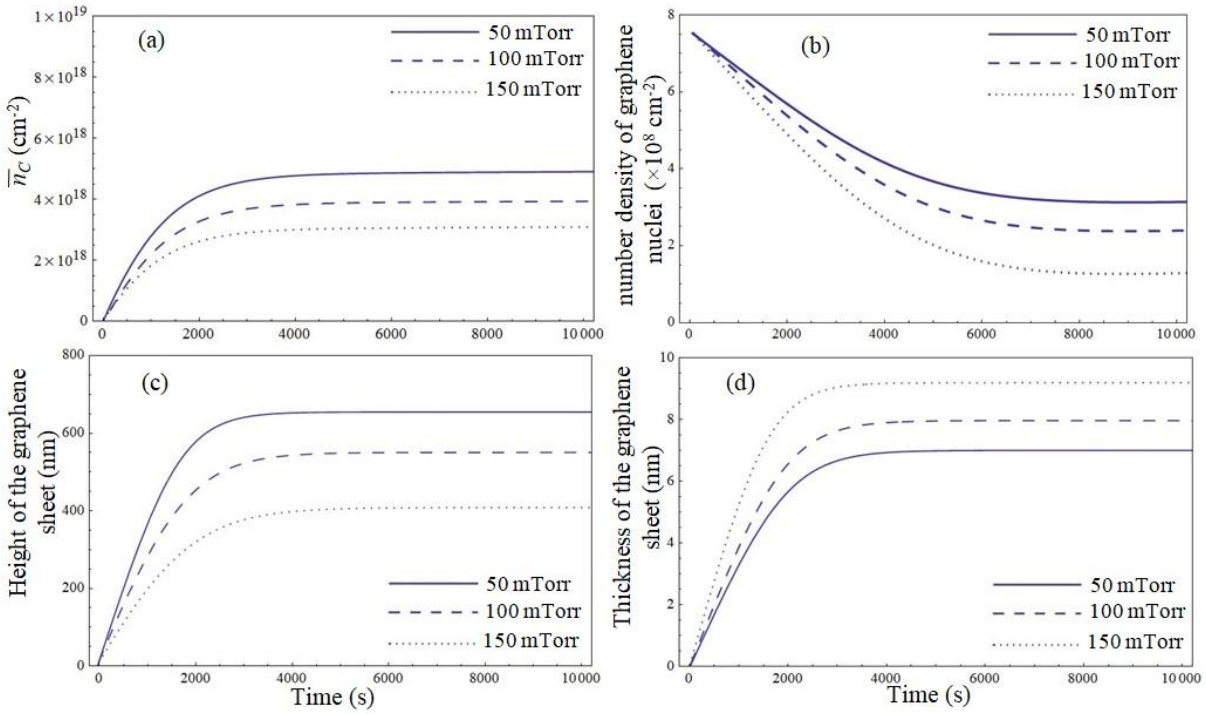

Fig. 6.4. Temporal variations of (a) number density of carbon species generated per unit area on the catalyst nanoislands surface (i.e., $\overline{n}_C$), (b) number density of graphene nuclei (i.e., $\overline{n}_{GN}$), (c) height of the graphene sheet, and (d) thickness of the graphene sheet as a function of the gas pressure at constant input plasma power of 100 W. All other parameters are given in the text.

From Figs. 6.2 & 6.3 and Table 6.6, one can also see the appreciable reduction in the number density and temperature of electrons when total gas pressure is raised. With an increase in the gas pressure from 50 mTorr to 150 mTorr, the plasma concentrated region decreases. Therefore, the mean free path is expected to decrease considerably which in turn increase the collisions between electrons and other plasma species due to which one can expect the significant loss in the number density and energy of the electrons. The effect of variation of electron density and electron temperature with pressure are in agreement with the works of Mao and Bogaerts [16], Shivkumar *et al.*[17], and Collison *et al.* [19]. At high gas pressure, the presence of less energetic electrons in the plasma directly affects the density of neutral species. The numerical data of spatial distributions of number densities of neutral species (hydrocarbons and hydrogen) in the plasma for different gas pressures obtained from the computational model are given in Table 6.7. The numerical data reveals that number densities of hydrocarbon neutral species in the plasma chamber get enhanced when the gas pressure is increased. This is because of the low rate of dissociation and

ionization of the hydrocarbon neutral species due to the absence of the energetic electrons. However, the number density of hydrogen radicals in the plasma chamber increases with increase in gas pressure. At high pressure, the number density and energy of electrons is low, but plasma has sufficient power to dissociate hydrogen molecules [31] which in turn increase the number density of hydrogen radicals and thereby, the density of hydrogen molecules decreases. Therefore, one can expect the much high flux of hydrogen radicals towards the substrate surface as compared to the flux of hydrocarbon species. Takeuchi *et al.*[20] investigated the impact of operating pressure on the densities of carbon and hydrogen species in the plasma consisting C_2F_6/H_2 gas mixture and found that hydrogen to carbon densities ratio in the plasma increases with increase in gas pressure. At low gas pressure, the plasma concentrated region expands, and therefore, a strong electric field is setup in the plasma chamber (between the coil's bottom surface and substrate top surface) which considerably drives the energetic positively charged species towards the catalyst-substrate surface which is maintained at low temperature (T_s< 800K). Thus, the rate of dissociation of positively charged species and ion-induced decomposition rate of hydrocarbon species on the catalyst nanoislands surface increases, and consequently, the large number of building units ($\bar{n}_C$) are generated on the catalyst active surface as shown in figure 4(a). Also, the interaction of adsorbed hydrocarbon species with hydrogen atoms from the sheath is reduced because the hydrogen density in plasma is substantially low at low gas pressures. Therefore, the continuous supply of carbon species directs the carbon cluster formation rate in the forward direction which in turn accelerates the diffusion of clusters to form a large number of graphene nuclei. Thus, one can think of the augmentation in the surface density of VOGS at low gas pressure [cf. Fig. 6.4(b)]. The results shown in Fig. 6.4(b) are compatible with experimental studies of Takeuchi *et al.*[20] and Cho *et al.*[21] (cf. Fig. 2(a) of Cho *et al.*[21]).

At low gas pressure, the Bohm velocity of ions and thereby the kinetic energy of ions impinging on the substrate surface increases. Therefore, on reducing the gas pressure, the interaction of the highly energetic hydrocarbon ions with adsorbed hydrocarbon neutrals increases which ultimately leads to the rapid generation of the carbon species and their faster diffusion towards the growing edges of the VOGS [22]. This results in the growth of VOGS at the higher rate

(height of the graphene sheet per unit growth time) when the gas pressure is reduced as can be seen from Fig. 6.4(c). However, the reduction in the thickness of the graphene sheet is found at low gas pressure which can be seen from Fig. 6.4(d). This is because of the higher etching of the graphene sheets due to the presence of a large number of energetic ions in the plasma. Such thickness reduction on reducing gas pressure is also reported by Wang *et al.* [22] and is similar to the ion-enhanced etching of carbon nanofibers at low gas pressure reported by Wei *et al.* [32]. Moreover, the numerical plots obtained in Fig. 6.4(c) are in good agreement with the experimental observations of Takeuchi *et al.*[20] [cf. Fig. 7(a)] and Cho *et al*.[21] [cf. Fig. 2(b)].

Apart from gas pressure, input plasma power is also an important PECVD process parameter to control the characteristics of the plasma. When input plasma power is raised, the plasma concentrated region expands, and a strong electric field is set up in the plasma, as a result of which number density and temperature of electrons in the plasma increases (cf. computational Figs. 6.5 and 6.6). Collison *et al.* [19] experimentally observed the increase in the electron density and temperature with plasma power. The numerical data obtained from these figures is listed in Table 6.6. The presence of large number of electrons with high energy in the plasma leads to the more ionization of the neutral species. The spatial distribution of the densities of the positively charged species (ions) obtained from the computational model is given in Table 6.10 which clearly shows the increase in ion number density with increase in input plasma power. The higher amount of charged species in the plasma dominates the ion dissociation and ion-induced dissociation of hydrocarbon species over the catalyst surface as a result carbon species (building units) generation rate increases rapidly [see Fig. 6.7(a)]. The quick and large supply of building units raises the concentration of clusters due to which the effective number of graphene nuclei increases [see Fig. 6.7(b)] which ultimately increase the surface concentration of VOGS. The continuous delivery of the carbon species due to the accessibility of a large number of charged species enhance the diffusion and incorporation of the carbon species over the growing edges of the VOGS, and consequently, accelerate the growth rate of VOGS [see Fig. 6.7(c)].

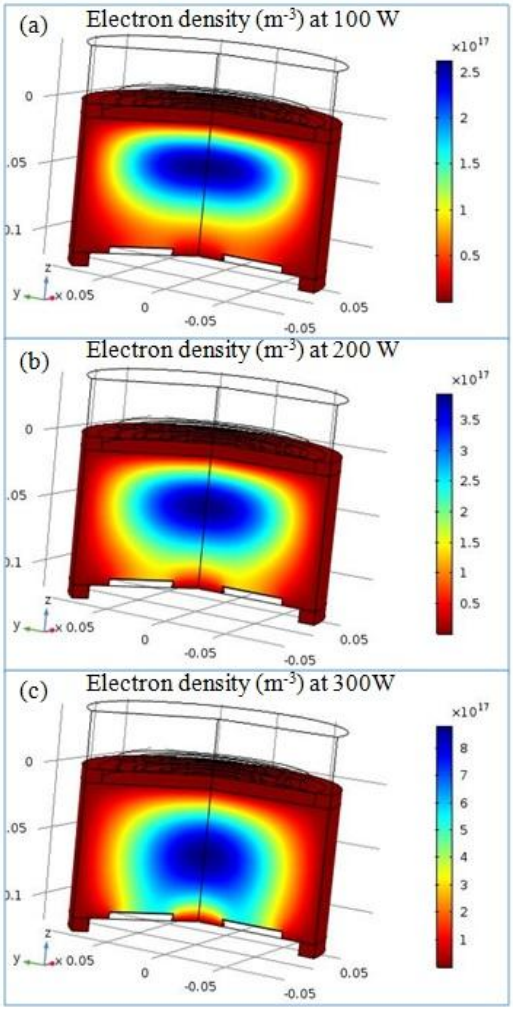

Fig. 6.5. 2D axis-symmetric computational plots showing the variation of electron number density with input plasma power, i.e., (a) 100 W, (b) 200 W, and (c) 300 W at constant gas pressure of 50 mTorr. All other parameters are given in the text.

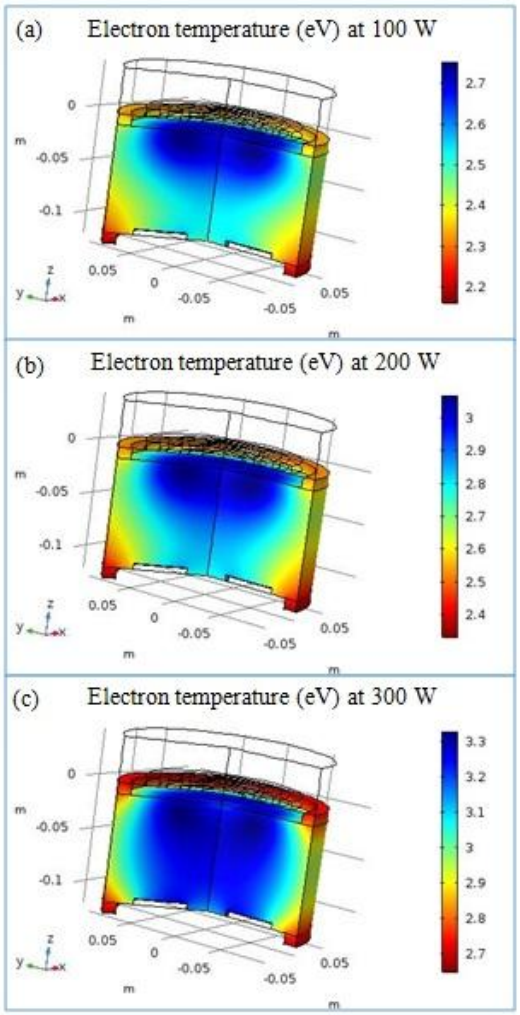

Fig. 6.6. 2D axis-symmetric computational plots showing the variation of electron temperature with input plasma power, i.e., (a) 100 W, (b) 200 W, and (c) 300 W at constant gas pressure of 50 mTorr. All other parameters are given in the text.

However, at high input plasma power, i.e., around 400 Watt, the significant drop in the growth rate of the VOGS is observed. This is because when input plasma power is increased above the certain optimum value (300 Watt), the rate at which carbon species generated over the catalyst surface increases rapidly [see Fig. 6.7(b)]. The excessive supply of the carbon species suppress the carbon diffusion due to the formation of amorphous carbon layer over the catalyst surface and blocks the further dissociation of hydrocarbon species and thus, reduce the height of the VOGS. Moreover, the presence of a large number of highly energetic ions in the plasma at high input plasma power

etches the graphene sheet at the higher rate, thereby, decreasing the thickness of the VOGS [see Fig. 6.7(d)]. A comparison of theoretical plots obtained in Fig. 6.7 with experimental observations of the Srivastava *et al.*[14], Cho *et al.*[21] (cf. Fig. 2 (b) of Cho *et al.*[21]), Nang and Kim [33] (cf. Fig. 4 (b) of Nang and Kim [33]), Zhu *et al.* [23], and Ghosh *et al.* [34] (cf. Fig. 7 (g) of Ghosh *et al.* [34]) confirms the adequacy of the present model.

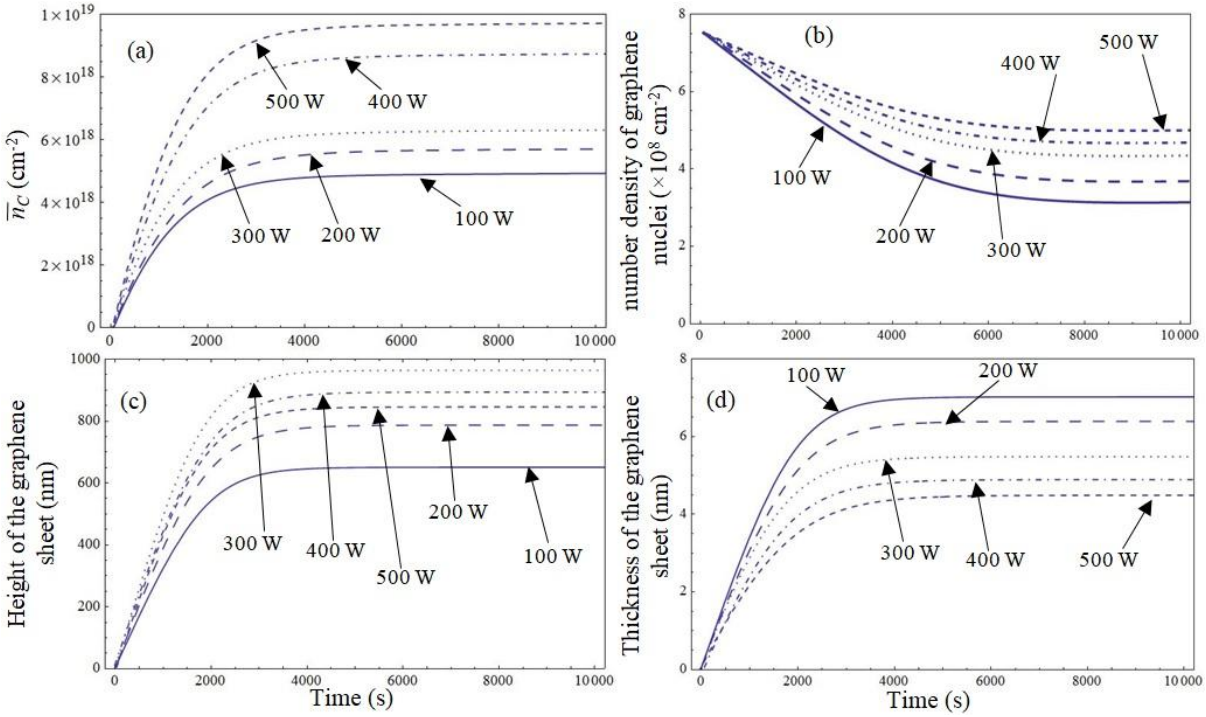

Fig. 6.7. Temporal variations of (a)number density of carbon species generated per unit area on the catalyst nanoislands surface (i.e., $\bar{n}_C$), (b) number density of graphene nuclei (i.e., $\bar{n}_{GN}$), (c) height of the graphene sheet, and (d) thickness of the graphene sheet as a function of the input plasma power at constant input gas pressure of 50 mTorr. All other parameters are given in the text.

References

[1] C. N. R. Rao, A. K. Sood, K. S. Subrahmanyam, and A. Govindaraj, Angew. Chem. Int. Ed.**48**, 7752 (2009).

[2] W. Choi, I. Lahiri, R. Seelaboyina, and Y. S. Kang, Crit. Rev. Solid State Mater. Sci.35, 52 (2010).

[3] L. Hu, D. S. Hecht, and G. Grüner, Chem. Rev.110, 5790 (2010).

[4] M. Terrones, Int. Mater. Rev.49, 325 (2004).

[5] Z. Bo, S. Mao, Z. J. Han, K. Cen, J.Chen, and K. Ostrikov, Chem. Soc. Rev.44, 2108(2015).

[6] I. Levchenko, O. Volotskova, A. Shashurin, Y. Raitses, K. Ostrikov, and M. Keidar, Carbon48, 4570 (2010).

[7] L. G. De Arco, Y. Zhang, A. Kumar, and C. Zhou, IEEE Trans. Nanotechnol. 8, 135 (2009).

[8] S. Stankovich, D. A. Dikin, R. D. Piner, K. A. Kohlhaas, A. Kleinhammes, Y. Jia, Y. Wu, S. B. T. Nguyen, and R. S. Ruoff, Carbon 45, 1558 (2007).

[9] C. Yang, H. Bi, D. Wan, F. Huang, X. Xie, and M. Jiang, J. Mater. Chem. A1, 770(2013).

[10] K. Shiji, M. Hiramatsu, A. Enomotu, M. Nakamura, H. Amano, and M. Hori, Diamond Relat. Mater. 14, 831 (2005)

[11] A. Malesevic, R. Kemps, A. Vanhulsel, M. P. Chowdhury, A. Volodin, and C. V. Haesendonck, J. Appl. Phys. 104, 084301 (2008).

[12] L. Jiang , T. Yang , F. Liu , J. Dong , Z. Yao , C. Shen, S. Deng , N. Xu , Y. Liu, and H. -J. Gao, Adv. Mater.25, 250 (2013).

[13] M. Y. Zhu, R. A. Outlaw, M. B. -Hansen, H. J. Chen, D.M. Manos, Carbon 49, 2526 (2011).

[14] S. K. Srivastava, A. K. Shukla, V. D. Vankar, V. Kumar, Thin Solid Films **492**, 124 (2005).

[15] B. B. Wang, K. Ostrikov, T. van der Laan, K. Zheng, J. J. Wang, Y. P. Yan and X. J. Quan, J. Mater. Chem. C**1**, 7703(2013).

[16] M. Mao, and A. Bogaerts, J. Phys. D: Appl. Phys.**43**, 205201 (2010).

[17] G. Shivkumar, S. S. Tholeti, M. A. Alrefae, T.S. Fisher, and A.A. Alexeenko, J. Appl. Phys.**119**, 113301 (2016).

[18] M. A. Lieberman, A. J. Lichtenberg, *Principles of Plasma Discharges and Materials Processing* (Wiley, NY 1994).

[19] W. Z. Collison, T. Q. Ni, and M. S. Barnes, J. Vac. Sci. Technol. A **16**, 100(1998).

[20] W. Takeuchi, H. Sasaki, S. Kato, S. Takashima, M. Hiramatsu, and M. Hori, J. Appl. Phys.**105**, 113305 (2009).

[21] H. J. Cho, H. Kondo, K. Ishikawa, M. Sekine, M. Hiramatsu, and M. Hori, Carbon **68**, 380 (2014).

[22] Y. Wang, L. Li, Q. Cheng, C. He, Journal of Luminescence **161**, 7 (2015).

[23] M. Zhu, J. Wang, B. C. Holloway, RA. Outlaw, X. Zhao, K. Hou, V. Shutthanandan, D. M. Manos, Carbon **45**, 2229(2007).

[24] R. Gupta and S. C. Sharma, Phys. Plasmas **24**, 073504 (2017).

[25] Z. Marvi, S. Xu, G. Foroutan, and K. Ostrikov, Phys. Plasmas **22**, 013504 (2015).

[26] H. Mehdipour, K. Ostrikov, and A.E. Rider, Nanotechnology**21**, 455605(2010).

[27] N. V. Mantzaris, E. Gogolides, A.G. Boudouvis, A. Rhallabi, and G. Turban, J. Appl. Phys. **79**, 3718(1996).

[28] H. Mehdipour and K. Ostrikov, ACS Nano **6**, 10276 (2012).

[29] A. Tewari and S. C. Sharma, Phys. Plasmas 21, 063512 (2014).

[30] M. Chhowalla, K. B. K. Teo, C. Ducati, N. L. Rupesinghe, G. A. J. Amaratunga, A. C. Ferrari, D. Roy, J. Robertson, and W. I. Milne, J. Appl. Phys. **90**, 5308 (2001).

[31] Z. Bo, Y. Yang, J. Chen, K. Yu, J. Yan, and K. Cen, Nanoscale **5**, 5180(2013).

[32] H. W. Wei, K. C. Leou, M. T. Wei, Y. Y. Lin, C. H. Tsai, J Appl Phys. **98**, 044313, (2005).

[33] L. V. Nang and E.-T. Kim, J. Electrochem. Soc.**159**, K93 (2012).

[34] S. Ghosh, S. R. Polaki, N. Kumar, S. Amirthapandian, M. Kamruddin, and K. Ostrikov, Beilstein J Nanotechnol **8**, 1658 (2017).

[35] UMIST http://www.udfa.net/

[36] T. G. Beuthe, J. S. Chang, Jpn. J. Appl. Phys. **38**, 4576 (1999).

[37] M. Sode, T. S.-Selinger, and W. Jacob, J. Appl. Phys. **114**, 063302(2013).

[38] M. J. Redondo, M. Cueto, J. L. Doménech, I. Tanarro, and V. J. Herrero, RSC advances **4**, 62030(2014).

[39] F. J. G.-Vázquez and J. M. Albella, Plasma Sources Sci. Technol. **11**, 498 (2002).

[40] I. Denysenko, N. A. Azarenkov, J. Phys, D: Appl. Phys.**44**, 174031 (2011).

7

Investigations on the plasma enabled growth of vertical graphene sheets on CNT surface

7.1 Brief outline of the chapter

In the present chapter, a theoretical model is developed to describe the plasma-assisted nucleation and growth kinetics of vertical graphene (VG) sheet on the carbon nanotube (CNT) surface. Using the model, we demonstrated that variations in the plasma enhanced chemical vapor deposition (PECVD) process control parameters such as the total gas pressure, input power, and substrate bias can be used for significant variation in the plasma composition and characteristics that in turn control the ion bombardment and generation of carbon species on the CNT surface, and consequently tune the VG sheet growth characteristics such as, height, thickness and number density profiles of VG sheet on the CNT surface.

7.2 Introduction

The growth of VG has been realized on various substrates such as dielectrics [1,2], semi-conductive Si [3], metals [4,5], carbon cloth [6], silicon nanowires and nanocones [7,8], diamond-like carbon films [9], and carbon nanotubes (CNTs) [9-15]. The growth of VG on CNT surface (graphenated CNT) has attracted substantial interest since this hybrid structure is reported to have potential applications in high-performance field emitters than individual CNT or VG. The graphene layer protrusions or foliates growing from the CNT surface enables significantly higher charge storage capacity and field emission stability than either of the two materials can achieve on their own. The exemplary field emission from this VG-CNT hybrid is expected owing to the adorable properties of CNT (incomparable high aspect ratio and excellent electrical conductivity) and increased surface area due to the exposed sharp edges of graphene protruded

from the CNT surface [9-13]. This unique hybrid structure is also reported to be widely used for making photoconductors [16], supercapacitors [17], fuel cells [18], gas sensors [14], and transparent conductors [19]. For the first time, the graphene sheets growing radial to the tube axis of nitrogenated CNTs were synthesized by Kurt and Karimi [20] via hot filament chemical vapor deposition (HF-CVD) technique in nitrogen–methane–ammonia environment.

PECVD method has been widely used for the production of graphene foliates on CNT [9-14]. According to previous reports [9-12], the VG nucleation on CNT is defect guided i.e., VG growth starts with the induced defects of CNT by intensive bombardment of ions in PECVD. Parker *et al.*[15] proposed a model of nucleation of graphitic foliates from external CNT walls resulting by the buckling of large diameter CNTs walls due to build-up of residual stress at the outer CNT walls. PECVD is a complex process, owing to the existence of energetic electrons, various ions, radicals and other neutral species in the plasma, and thus possible to attain the controllable structure and growth characteristics of as-grown VG by adequately altering the plasma parameters, input power, gas type and proportion, and gas pressure for specific applications [21].

In previous chapters, we developed an analytical model to unveil the catalyst-aided growth mechanism of VG sheet in the complex plasma environment and also studied the influence of growth time, plasma parameters, different gas mixtures, and doping on the growth characteristics of VG sheet. However, in order to augment the relevance of typical PECVD synthesis experiments of graphenated CNTs [9-14], we endeavour to develop a phenomenological model to describe the major processes responsible for the VG sheet growth on CNT template in plasma environment, such as creation of defects on the CNT surface, formation of clusters, growth of graphene nuclei and VG sheet on CNT. This model considers the multi-fluid plasma sheath related effects linked to the surface deposition processes along with the kinetics of neutrals, positively charged species, and electrons, and rate of charge accumulation on the VG sheet surface. In addition, we report the effects of controlling the total gas pressure, input power, growth time, and substrate bias

on the amount and size of VG sheet grown on the CNT surface. Specifically, we exhibit that variations in gas pressure, input power, and substrate bias affect the plasma characteristics (i.e., number density, temperature, and energy of plasma species), which subsequently alter the carbon generation on CNT surface and defect sites, and influence the density as well as dimensions of VG sheets grown over the CNT surface.

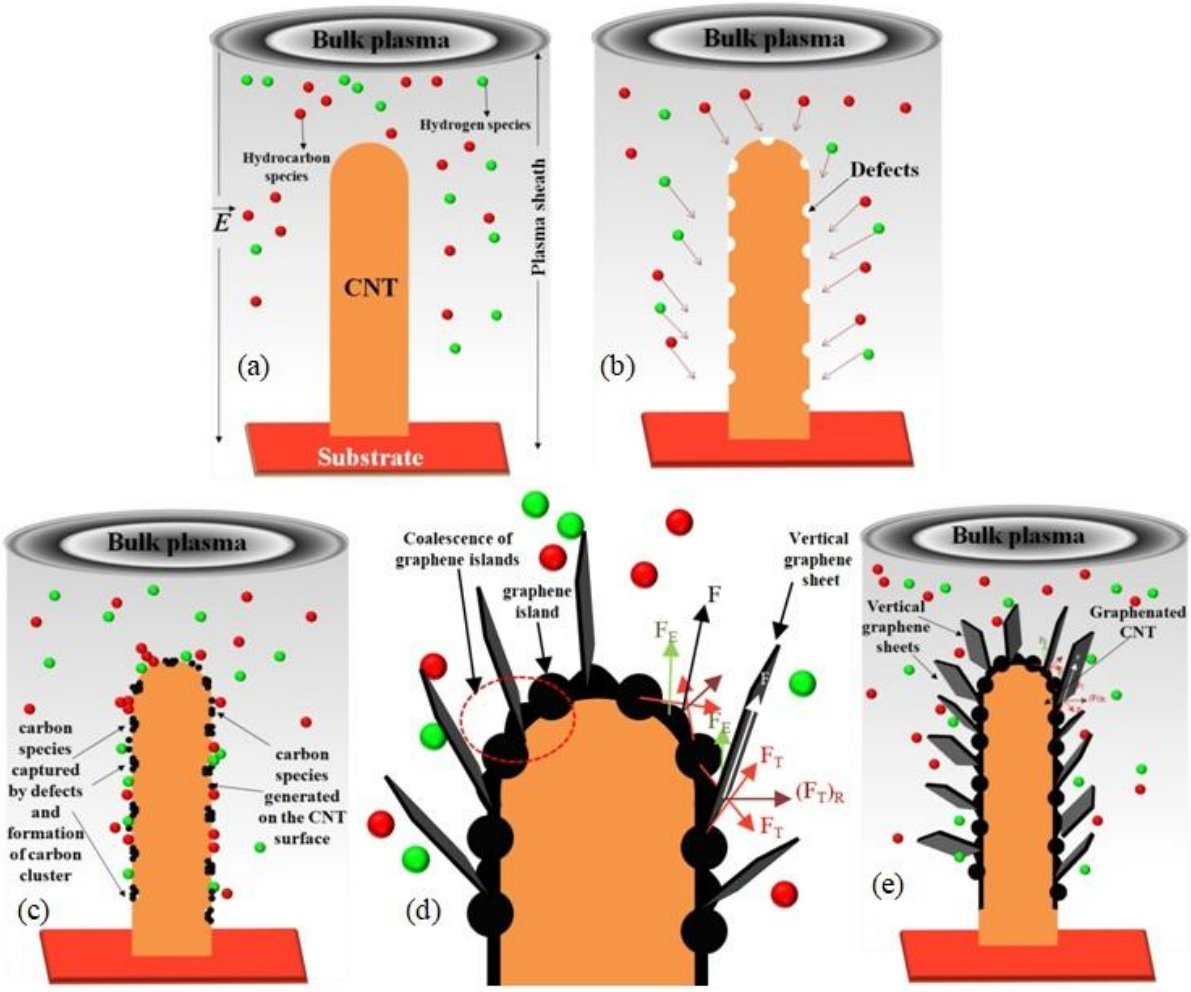

Fig.7.1. Schematic showing the (a) charged and neutral species impinging on the CNT surface (b) formation of defects on the CNT surface (c) carbon species generation on the CNT surface and formation of C- clusters at the defective sites (d) amalgamation of GIs and vertical growth of the graphene sheet, and (e) VG sheets growing like plant leaves on CNT surface.

Table 7.1. Ions and neutral species considered in the model.

Neutrals		Ions	
Type 1	**Type 2**	**Type 1**	**Type 2**
CH_3, CH_4, C_2H_2, C_2H_4	H, H_2	CH_3^+, CH_4^+, C_2H_2+, C_2H_4+	H^+, H_2^+

7.3 Analytical model

In this section, we present the basic assumptions and equations to describe the nucleation and growth dynamics of VG sheet on CNT surface via PECVD route. We consider the hemispherical tip CNT of diameter ($2a_C$ = 60nm) and length (l_C = 1.5µm) as a template for the growth of graphene sheet in the plasma constituting the ionized gas mixture of CH_4/H_2[12]. Fig. 7.1(a) shows the sketch of CNT erected on a conductive silicon substrate (maintained at negative potential U_s) subjected to plasma of CH_4/H_2 gas mixture. The present model considers the plasma comprising of electrons, various positively charged and neutral species of CH_4 and H_2. Table 7.1 details the neutral and positively charged species accounted in the model which is representative of experiments on plasma chemistry of CH_4/H_2 gas mixture [22]. We consider the induced sheath electric field to be in the vertically downward direction i.e., along the z-axis. The density and speed of the charged species, neutrals number density, and sheath structure are investigated using the following plasma sheath equations [23,24].

$$\frac{d}{dz}\left(n_{ij}u_{ijz}\right) = f_{ij}n_e, \tag{7.1}$$

$$\frac{d}{dz}(n_e u_{ez}) = \sum_j f_{ij}n_e, \tag{7.2}$$

$$m_{ij}n_{ij}u_{ijz}\frac{du_{ijz}}{dz} = -en_{ij}\frac{d\phi}{dz} - T_{ij}\frac{dn_{ij}}{dz} - m_{ij}n_{ij}f_{ijn}u_{ijz}, \tag{7.3}$$

$$0 = en_e\frac{d\phi}{dz} - T_e\frac{dn_e}{dz} - m_e n_e f_{en}u_{ez}, \tag{7.4}$$

Neha Gupta
Delhi Technological University, Delhi, India

where m_{ij}, n_{ij}, T_{ij}, and u_{ijz} are the masses, number densities, temperature, and fluid velocities of the positively charged species, respectively (j corresponds to the positively charged ions of type 1 and 2 [see Table 7.1)]. m_e, n_e, T_e, and u_{ez} are the masses, number densities, temperature, and fluid velocities of electrons, respectively.

Equations (7.1) and (7.2) are the continuity equations for ions and electrons, respectively and account the electron-impact ionization of neutrals with ionization frequency $f_{ij} = \xi_{ij}\eta_{ij}N_n$, where ξ_{ij} is the ionization potential, $\eta_{ij} = {}^{n_{ij}}\!/_{n_e}$ or ${}^{p_j}\!/_{p_0}$ (here p_j and $p_0 (= N_n T_i)$ are the pressure of the j^{th} gas and total gas pressure, respectively), and $N_n = \sum_j \eta_j n_j$ corresponds to the total number density of neutral species, where n_j is the number density of j^{th} neutral. Thus, the ionization rate (i.e., $f_{ij} \propto n_j \exp(-E_{ij}/T_e)$, where E_{ij} is the first ionization potential energy of j^{th} neutral) rises with both the neutral density temperature of electrons. Furthermore, the collisions of ions and electrons with neutrals with collision frequency, $f_{\alpha n} = \sigma_\alpha N_n U_\alpha$ (where α refers to electrons and j ions; σ_α is the collision cross section and U_α is the mean speed of the charged species α) have been taken into account in momentum balance equations, i.e., Eqs. (7.3) and (7.4), respectively [23].

Finally, the sheath equations to be solved are completed by the Poisson's equation that correlates the number densities of ions and electrons to the electric sheath potential ϕ as follows:

$$\frac{d^2\phi}{dz^2} = -4\pi e\left(n_e - \sum_j \eta_{ij} n_{ij}\right). \tag{7.5}$$

The ion energies and fluxes of the ionic and neutral species at the CNT surface are determined by solving the above set of Eqs. (7.1)-(7.5) with the following boundary conditions [23]:

$\phi = 0$, $\frac{d\phi}{dz} = -\frac{T_e}{e\lambda_i}$, where $\lambda_i \left(= T_n / \sigma p_0\right)$ is the ion mean free path and $u_{ez} = 0$, $u_{ijz} = v_{ij0}$, where $v_{ij0} = \sqrt{T_e / m_{ij}}$.

The main processes accounted in the present model for the nucleation and growth of graphene sheets on CNT surface (considering CNT as a starting material) in the plasma environment, are shown in Fig. 7.1. The Fig. 7.1 (b) shows the preliminary stage in which the defects sites are created on the CNT surface when exposed to the plasma. The applied plasma power dissociates the source gases in the chamber and a range of hydrocarbon and hydrogen ions are created which subsequently results in the formation of an electric field near the CNT surface [25]. Under the electric field and applied substrate bias, ions with high enough energy keep bombarding the CNT surface to break some C-C bonds; some get replaced by C-H bonds and thereby creates local defects that act as nucleation sites for the growth of two-dimensional graphene sheets on the CNT surface [13,26]. Further, we consider the growth of graphene sheets on these defective sites proceeds in the same manner as discussed previously in many studies [27-29]. The carbon atoms generated on the CNT surface on account of several surface processes get captured by defects present on the CNT surface, which then diffuse and agglomerate to form C (carbon)- clusters [cf. Fig. 7.1(c)] [28,29]. Furthermore, these C- clusters at the defective sites diffuse and collide with each other forming the graphene islands (GIs) and subsequently these GIs amalgamate or stitch with each other to form large GIs or flat graphene sheet with respect to CNT surface (see Fig. 7.1(d)) [28,30]. During the amalgamation of these GIs internal tensile force F_T may build-up at the GIs boundaries, which may tend to align the upper edge of these graphitic layers in the direction normal to the CNT surface as shown in Fig. 7.1(d) [29]. The ion bombardment, temperature gradients, and difference in structure and expansion coefficients of amorphous CNT and flat graphene nanosheet are the main sources of internal stress [27,28]. Furthermore, the in-built electric field induced by the plasma sheath also exerts a force (F_E) on these graphitic layers in the direction parallel to the CNT surface (see Fig. 7.1(d)) [29]. Under the action of the resultant (F) of these two forces (i.e., $(F_T)_R$ and F_E) and continuous

dissociation and diffusion of hydrocarbon and carbon species, respectively, graphene sheets grow like plant leaves erected on the stem (CNT) [cf. Fig. 7.1(e)] [14].

7.3.1 Formation of defects on the CNT surface

Equation (7.6) describes the rate of energy balance at the surface of CNT placed over Si-substrate during its interaction with plasma of CH_4 gas diluted in H_2. The power transferred to the CNT surface [i.e., tip and curved surface of CNT) (R.H.S of Eq. (7.6)] by incident plasma species i.e., positively charged ions, neutrals, and electrons (first term), due to formation of neutrals at the CNT surface (second term), etching of the CNT surface by hydrogen (third term) and ion sputtering (fourth term) leads to the CNT surface modification and the formation of defects on the CNT surface. The LHS of Eq. (7.6) accounts the rate of formation of defects per micron length of the CNT surface. Hydrogen and ion irradiation induced defects on the CNT surface and the introduction of micro-defects on the Si-substrate in the presence of H_2/CH_4 plasma have been reported earlier [31-33].

$$
\begin{aligned}
P_{in} = \frac{\partial}{\partial t}(m_C C_C T_s) = \rho_C A_C l_C C_C T_S \frac{1}{n_D}\frac{\partial}{\partial t}(n_D) \\
= \left[\sum_{j}^{1,2}\left\{\left(j_{ij}^{C_{tip}} + j_{ij}^{C_{cur}}\right)\varepsilon_{ij}^{C} + \left(j_{j}^{C_{tip}} + j_{j}^{C_{cur}}\right)\varepsilon_{j}^{C}\right\}\right. \\
+\left(j_{e}^{C_{tip}} + j_{e}^{C_{cur}}\right)\varepsilon_{e}^{C} + \left[\frac{3}{2}k_B T_S \sum_{j}^{1,2}(1-\gamma_{ij})\left(j_{ij}^{C_{tip}} + j_{ij}^{C_{cur}}\right)\right] \\
\left.+\left[\left(\upsilon_0 \sigma_{ads} J_B U_b\right) A_C\right] + \left[\left(\sum_{j}^{1,2} J_{ij} y_s(E_i)(1-\theta_t)\right) A_C\right], \qquad (7.6)
\end{aligned}
$$

where m_C, $A_C\left(=2\pi a_C^2 + 2\pi a_C l_C\right)$, C_C, and ρ_C are the mass, area, specific heat, and density of CNT, respectively. n_D is the number of defects produced per micron length of the CNT surface and T_S is the CNT surface temperature (T_s is assumed to be uniform along the CNT). During the plasma- surface interaction, the CNT surface gets heated up and attains a constant temperature T_s [34].

$J_j\left(=\frac{n_j v_{thj}}{4}\right)$ and $J_{ij}\left(=n_{ij}\sqrt{\frac{k_B T_e}{m_{ij}}}\right)$ are the fluxes of impinging neutral and positively charged species of type *j*, respectively (subscript *j* refers to species of type 1or 2) [35,23]. $\varepsilon_\alpha^C\left[=\left(\frac{2-Z\xi_\alpha}{1-Z\xi_\alpha}-Z\xi_\alpha\right)k_B T_\alpha\right]$ refers to the mean energies collected by the CNT surface due to α species (subscript α refers to electrons, ions and neutrals of type *j; j* refers to species of type 1or 2), where $\xi_\alpha=\frac{E_b}{k_B T_\alpha}$ and E_b is the energy barrier at the CNT surface [36]. $j_{ij}^{C_{tip}}$ and $j_{ij}^{C_{cur}}$ are the collection currents at the CNT tip and curved surface, respectively due to positively charged species of type *j* [37].

$$j_{ij}^{C_{tip}}\left[=\pi a_C^2\left(\frac{8k_B T_{ij}}{\pi m_{ij}}\right)^{\frac{1}{2}} n_{ij}(x)\left[1-Z\gamma_i\right]\left(\exp\left[-\frac{eU_s}{k_B T_s}\right]\right)\right]$$

$$j_{ij}^{C_{cur}}==n_{ij}(x)a_C l_C\left(\frac{2\pi k_B T_{ij}}{m_{ij}}\right)^{\frac{1}{2}}\left\{\frac{2}{\sqrt{\pi}}\left(\frac{eV_s}{k_B T_{ij}}\right)^{\frac{1}{2}} erfc\left(\frac{eV_s}{k_B T_{ij}}\right)^{\frac{1}{2}}\right\}+\exp\left[\frac{eV_s}{k_B T_{ij}}\right]\exp\left[-\frac{eU_s}{k_B T_s}\right]$$

where Z is the charge number over the CNT surface [38], $n_{ij}(x)=n_{ij0}\left(1-\frac{2e\phi(x)}{m_{ij}v_{ij0}^2}\right)^{1/2}$ is the density of positively charged species as a function of spatial coordinate within the plasma sheath; v_{ij0} is the velocity of positively charged species, $\phi(x)=\phi_0\exp\left(-\frac{|x|}{\lambda_d}\right)$ is the plasma sheath potential as a function of spatial coordinate; ϕ_0 is the negative bias applied at the substrate surface and $\lambda_d\left(=\sqrt{\frac{k_B T_e}{n_e e^2}}\right)$ is the Debye length, $\gamma_i=eV_{tip}(z)$; $V_{tip}(z)\left(=\frac{e}{2\sqrt{2}\pi\varepsilon_0 a_C}\right)$ is the potential at the hemispherical tip of the CNT (evaluated using Ref. 37), T_{ij} and m_{ij} are the temperature and mass of the

positively charged species of type *j*, respectively, and V_s is the potential at the CNT curved surface. $\gamma_{ij}\,(\simeq 1)$ is the sticking coefficient of positively charged species, $j_e^{C_{tip}}$ and $j_e^{C_{cur}}$ are the electron collection current at the CNT tip and curved surface, respectively.

$$j_e^{C_{tip}}\left[=\pi a_C^2\left(\frac{8k_BT_e}{\pi m_e}\right)^{\frac{1}{2}} n_e(x)\exp\left[\frac{Z\gamma_i}{k_BT_e}+\frac{eU_s}{k_BT_s}\right]\right],$$

$$j_e^{C_{cur}}\left[=n_e(x)a_C l_C\left(\frac{2\pi k_BT_e}{m_e}\right)^{\frac{1}{2}}\exp\left[\frac{eV_s}{k_BT_e}+\frac{eU_s}{k_BT_s}\right]\right]$$

where $n_e(x)=n_{e0}\exp\left[\frac{|e|\phi(x)}{k_BT_e}\right]$ is the electron density as a function of spatial coordinate within plasma sheath, $j_j^{C_{tip}}=n_j(x)\pi a_c^2\left(\frac{8k_BT_j}{\pi m_j}\right)^{\frac{1}{2}}$ and $j_j^{C_{cur}}=n_j(x)\pi a_c l_c\left(\frac{2\pi k_BT_j}{m_j}\right)^{\frac{1}{2}}$ are the collection currents at the tip and curved surface of CNT, respectively due to neutral species of type *j* [38], $\upsilon_0\left(\approx 10^{15}\,\mathrm{cm}^{-2}\right)$ is the number of adsorption sites per unit area, $\sigma_{ads}\left(\approx 10^{-16}\,\mathrm{cm}^2\right)$ is the cross-section of the reactions with atomic hydrogen [39], y_s is the sputtering yield which is dependent on ion energy [40], U_b is the surface binding energy of carbon in CNT, and θ_t is the total surface coverage [39]. Using Eq. (7.6) we estimated the linear density of defects generated on the CNT surface upon interaction with CH_4/H_2 plasma and using mass conservation, the size of the resulting defects is estimated to be $r_D=\left.a_C\left(1+\frac{a_C}{l_C}\right)\right/2n_D$.

7.3.2 Generation of hydrogen radicals and carbon species

The incoming fluxes of neutrals and ions of type 1 and 2 interact with the CNT surface and contribute to the generation of hydrogen radicals and carbon species

on the CNT surface via various surface processes, which have been accounted in the underneath equations.

$$\dot{N_H} = \sum_2 J_2(1-\theta_t) + \sum_1 n_{S1}\upsilon \exp\left(\frac{-\delta E_{td}}{k_B T_S}\right) + \sum_{i1}\left(\sum_1 \frac{n_{S1} y_d}{\upsilon_0}\right) J_{i1} + \sum_{i1} J_{i1} - \sum_2 n_{S2}\upsilon \exp\left(\frac{-\delta E_{aH}}{k_B T_S}\right) - \sum_2 n_{S2}\sigma_{ads} J_2 - \sum_{i2}\left(\sum_2 n_{S2}\sigma_{ads}\right) J_{i2}, \quad (7.7)$$

$$\dot{N_c} = \sum_1 J_1(1-\theta_t) + \sum_1 n_{s1}\upsilon \exp\left(\frac{-\delta E_{td}}{k_B T_S}\right) + \sum_{i1}\left(\sum_1 \frac{n_{S1} y_d}{\upsilon_0}\right) J_{i1} + \sum_{i1} J_{i1} + \sum_{i2}\left(\sum_{i1} \frac{J_{i1}\sigma_{ads}}{\upsilon}\right) J_{i2} - \sum_1 n_{S1}\upsilon \exp\left(\frac{-E_{ads}}{k_B T_S}\right) - \sum_2\left(\sum_1 n_{S1}\sigma_{ads}\right) J_2 - N_c \upsilon \exp\left(\frac{-E_{ev}}{k_B T_S}\right), \quad (7.8)$$

where N_H and N_C are the surface concentrations of hydrogen radicals and carbon species generated on the CNT surface, respectively. The other symbols and terms used in Eqs. (7.7) and (7.8) are explained in Table 7.2 and 7.3, respectively.

Table 7.2. Explanation for the symbols used in Eqs. (7.7) and (7.8).

Symbols	Explanation
$n_{Sj}\left(=\theta_j \upsilon_0\right)$	surface concentration of neutral species of type *j*[39]
θ_j	surface coverage by species of type *j*[39]
$\upsilon\left(\approx 10^{13} Hz\right)$	thermal vibration frequency[39]
$y_d\,(\approx 2.49\times10^{-2} + 3.29\times10^{-2}\times E_i)$	stitching probability[40]
E_i	ion energy in eV
$\delta E_{td}\left(=2.1\text{ eV}\right)$	thermal dissociation energy of hydrocarbons [24]
$E_{ads}\left(=1.8\text{ eV}\right)$	adsorption energy of hydrocarbons [24]
$\delta E_{aH}\left(=1.8\text{ eV}\right)$	adsorption energy of hydrogen species [24]
$E_{ev}\left(=1.8\text{ eV}\right)$	carbon evaporation energy [24]

Table 7.3. Explanation for the functional terms used in Eqs. (7.7) and (7.8).

Functional Terms	Explanation
$J_2(1-\theta_t)$	adsorption of neutral hydrogen
$n_{S1}\upsilon\exp\left(\frac{-\delta E_{td}}{k_B T_S}\right)$	thermal dissociation of adsorbed hydrocarbon species
$\frac{n_{S1}y_d}{\upsilon_0}J_{i1}$	ion-induced dissociation of adsorbed hydrocarbon species
J_{i1}	decomposition of hydrocarbon ions
$n_{S2}\upsilon\exp\left(\frac{-\delta E_{aH}}{k_B T_S}\right)$	desorption of hydrogen radicals
$n_{S2}\sigma_{ads}J_2$	loss of adsorbed hydrogen species due to interaction with hydrogen atom from the plasma
$n_{S2}\sigma_{ads}J_{i2}$	loss of adsorbed hydrogen species due to interaction with hydrogen ions from the plasma
$\frac{J_{i1}\sigma_{ads}}{\upsilon}J_{i2}$	carbon generation due to reaction between hydrocarbon and hydrogen ion
$n_{S1}\upsilon\exp\left(\frac{-E_{ads}}{k_B T_S}\right)$	desorption of hydrocarbon species
$n_{S1}\sigma_{ads}J_2$	loss of adsorbed hydrocarbon species due to interaction with hydrogen atom from the plasma
$N_c\upsilon\exp\left(\frac{-E_{ev}}{k_B T_S}\right)$	evaporation of carbon

7.3.3 Growth rate equation of graphene nuclei/island

The carbon species generated on CNT surface get captured by defects, which then diffuse and agglomerate to form C-clusters and further these C-clusters diffuse and collide, forming the graphene nuclei/island. These GIs then grows in size due to diffusion and coalescence among them [28,30]. The growth rate of graphene nuclei/island is expressed in velocity units (nm/sec) in Eq. (7.9).

$$\dot{r}_{gn}=\left[N_c\left\{D\exp\left(\frac{-\left(E_{sdc}+E_{inc}\right)}{k_B T_s}\right)+D'\exp\left(\frac{-\left(E_{sdcl}+E_{incl}\right)}{k_B T_s}\right)+D''\exp\left(\frac{-\left(E_{sdgn}\right)}{k_B T_s}\right)\right\}\right]\times\frac{A_d}{A_{gn}}\times\frac{2\pi r_d\times j_{i1}^{gn}}{\upsilon}+\gamma_1\left(2\pi r_{gn}\right)j_1^{gn}, \quad (7.9)$$

where r_{gn} and $A_{gn}\left(=\pi r_{gn}^2\right)$ are the radius and area of the graphene nuclei/island, respectively. $A_d\,(=\pi r_D^2)$ is the area of the defect at the CNT surface. j_{i1}^{gn} and j_1^{gn} are the collection currents due to ions and neutrals of type 1 at the growing GI, respectively [35]. $\gamma_1(\approx 1)$ is the sticking coefficient of neutral hydrocarbon species. $E_{sdC} \approx 0.1$ eV, $E_{inc} \approx 0.85$ eV, $E_{sdCl} \approx 0.82$ eV, $E_{incl} \approx 0.85$, and $E_{sdIs} \approx 2.6$ eV are the energy barriers for surface diffusion and incorporation of carbon atoms, surface diffusion and incorporation of C- clusters, and diffusion of GIs, respectively [30].

Equation (7.9) traces the growth of GI owing to the surface diffusion and incorporation of carbon monomers and C-clusters into the defective sites at the CNT surface (first and second terms), and due to diffusion or amalgamation of GIs (third term) [30]. Furthermore, the factors j_1^{gn} and j_{i1}^{gn} account the accretion of neutral atoms and ion collection current of type *1* species at the surface of the growing GIs.

7.3.4 Growth of vertical graphene sheet over CNT

The amalgamation or stitching of GIs lead to the formation of planar graphitic layers or flat graphene on the CNT surface, and consequently, tensile force is build-up at the GIs boundaries due to the difference in the structure and expansion coefficients of amorphous CNT and flat graphene sheets, which then trigger the growth of VG sheet [28].

$$l_g \frac{d}{d\tau}\left(t_g \times h_g\right) = \left[\frac{N_c}{\upsilon} \times D \exp\left(-\frac{\left(E_{sdc} + E_{inc}\right)}{k_B T_s}\right) \times A_{gn} \times 2\pi r_d \times j_{i1}^g + \left(\gamma_1 j_1^g\right) + \left(\gamma_{i2} j_{i2}^g + \gamma_2 j_2^g\right) N_H h_g(\tau)\right] \times \frac{m_g}{\rho_g} \quad , \qquad (7.10)$$

where l_g, h_g, t_g, $m_g(\approx 12g)$, and ρ_g are the length, height, thickness, mass, and density of the graphene sheet, respectively. j_j^g and j_{ij}^g are the collection currents at the surface of graphene sheet due to neutral and positively charged

species, respectively, V_{gs} is the potential at the graphene sheet surface [[refer Eq. (A.2) of Appendix A]].

$$j_j^g = n_j\left(l_g t_g + h_g t_g + l_g h_g\right)\left(\frac{k_B T_n}{2\pi^2 m_j}\right)^{\frac{1}{2}}$$

$$j_{ij}^g = n_{ij}(x)\left(l_g t_g + h_g t_g + l_g h_g\right)\left(\frac{k_B T_{ij}}{2\pi^2 m_{ij}}\right)^{\frac{1}{2}}\left\{\frac{2}{\sqrt{\pi}}\left(\frac{eV_{gs}}{k_B T_i}\right)^{\frac{1}{2}} + \exp\left[\frac{eV_{gs}}{k_B T_{ij}}\right] erfc\left[\left(\frac{eV_{gs}}{k_B T_{ij}}\right)^{\frac{1}{2}}\right]\right\} \times \exp\left[-\frac{eU_s}{k_B T_s}\right]$$

Equation (7.10) accounts the processes responsible for the VG sheet growth over the CNT surface. The first term on the R.H.S of Eq. (7.10) represents the increase in the area of the VG sheet due to diffusion and attachment of carbon atoms at the borders of the growing VG sheet. In addition, under the influence of the in-built electric field and substrate bias VG sheet grows due to ion collection current and sticking of neutrals at the GIs boundaries and VG sheet surface. Lastly, the VG sheet growth terminates due to etching of terminal carbons present at the edges of VG sheet by hydrogen. The last term on the R.H.S of Eq. (7.10) represents the accumulation of positively charged and neutral species of type 2 on the VG sheet surface.

7.3.5 Charge developed over the graphene sheet surface

$$\dot{Q} = \sum_1 j_{i1}^g + \sum_2 j_{i2}^g - \gamma_e j_e^g \ , \qquad (7.11)$$

where Q is the charge number over the graphene sheet surface, j_e^g is the collection current at the graphene sheet surface due to electrons, and $\gamma_e(=1)$ is the electron sticking coefficient.

$$j_e^g = n_e\left(l_g t_g + h_g t_g + l_g h_g\right)\left(\frac{k_B T_e}{2\pi^2 m_e}\right)^{\frac{1}{2}} \exp\left[\frac{eV_{gs}}{k_B T_e} + \frac{eU_s}{k_B T_s}\right]$$

Equation (7.11) accounts the charge build-up over the graphene sheet surface due to accretion of positively charged species (first and second terms). The last term signifies the decay rate of charge because of accumulation of electrons at the graphene sheet surface.

7.3.6 Number density balance equations of plasma species

$$\dot{n_e} = \sum_{j=1}^{2} \beta_j n_j - \sum_{j=1}^{2} \alpha_j n_e n_{ij} - \frac{\gamma_e}{\lambda_d}\left(\eta_g j_e^g + \eta_C\left(j_e^{C_{tip}} + j_e^{C_{cur}}\right)\right), \tag{7.12}$$

$$\dot{n_{i1}} = \beta_1 n_1 - \alpha_1 n_e n_{i1} - \frac{1}{\lambda_d}\left(\eta_g j_{i1}^g + \eta_C\left(j_{i1}^{C_{tip}} + j_{i1}^{C_{cur}}\right)\right) + \sum_{l12} k_l n_1 n_{i2} + \frac{P_{in}}{E_{dis1} V}, \tag{7.13}$$

$$\dot{n_{i2}} = \beta_2 n_2 - \alpha_2 n_e n_{i2} - \frac{1}{\lambda_d}\left(\eta_g j_{i2}^g + \eta_C\left(j_{i2}^{C_{tip}} + j_{i2}^{C_{cur}}\right)\right) + \sum_{l12} k_l n_1 n_{i2} + \frac{P_{in}}{E_{dis2} V}, \tag{7.14}$$

$$\begin{aligned}\dot{n_1} = {} & \alpha_1 n_e n_{i1} - \beta_1 n_1 - \frac{1-\gamma_{i1}}{\lambda_d}\left(\eta_g j_{i1}^g + \eta_C\left(j_{i1}^{C_{tip}} + j_{i1}^{C_{cur}}\right)\right) \\ & - \frac{\gamma_1}{\lambda_d}\left(\eta_g j_1^g + \eta_C\left(j_1^{C_{tip}} + j_1^{C_{cur}}\right)\right) - J_{ad1} + J_{des1} - \sum_{l12} k_l n_1 n_{i2},\end{aligned} \tag{7.15}$$

$$\begin{aligned}\dot{n_2} = {} & \alpha_2 n_e n_{i2} - \beta_2 n_2 - \frac{1-\gamma_{i2}}{\lambda_d}\left(\eta_g j_{i2}^g + \eta_C\left(j_{i2}^{C_{tip}} + j_{i2}^{C_{cur}}\right)\right) \\ & - \frac{\gamma_2}{\lambda_d}\left(\eta_g j_2^g + \eta_C\left(j_2^{C_{tip}} + j_2^{C_{cur}}\right)\right) - J_{ad2} + J_{des2} - \sum_{l12} k_l n_1 n_{i2},\end{aligned} \tag{7.16}$$

where β_j is the ionization coefficient of the neutral species, $\alpha_j(T_e) = \alpha_{j0}\left(\frac{300}{T_e}\right)^k$ cm^3/sec is the coefficient of recombination of electrons and positively charged species; $\alpha_{10} \approx \alpha_{20}$ (= 1.12×10^{-7} cm^3/sec), $k(=-1.2)$ is a constant [36], J_{adj} and J_{desj} are the adsorption and desorption flux of type j species onto/from the CNT surface, J_{th} is the flux of etching species (i.e., hydrogen) due to thermal dehydrogenation [35], E_{disj} is the dissociation energy of j^{th} neutral, V is the volume of the plasma chamber, and k_l is the rate coefficient of ion-neutral reaction which have been accounted from Ref. 22.

Equation (7.12) indicates the growth of electron density per unit time in plasma. The first term on the R.H.S of Eq. (7.12) signifies the rate of increase in electron density due to ionization of neutral species. The last two terms indicate the rate of decay in electron density on account of recombination of electrons and positively charged species, and electron collection current at the graphenated CNT surface, respectively.

Equations (7.13) & (7.14) describe the balance of positively charged species of type 1 and 2, respectively in the plasma because of the ionization of neutral species (first term), recombination of the electrons and positively charged species (second term), collection current at the graphenated CNT surface due to positively charged species (third term), ion-neutral reactions (fourth term), and due to the dissociation by applied input power.

Equations (7.15) & (7.16) describe the balance of neutral atoms of type 1 and 2, respectively in the plasma on account of the recombination of electrons and positively charged species (first term), ionization of neutral species (second term), neutralization of ions collected at the graphenated CNT surface (third term), accumulation and adsorption of neutral species at the graphenated CNT surface (fourth and fifth term), desorption of neutrals from the graphenated CNT surface (sixth term), and reactions between neutral and positively charged species (last term).

7.4 Results and discussion

The analytical model Eqs. (7.1)-(7.16) presented in Sec. II are solved simultaneously using MATHEMATICA software and their numerical solutions are used to investigate the effect of variation in total gas pressure, input power, and substrate bias on the plasma composition and characteristics that in turn control the amount and size of VG on pre-grown CNT surface. The default set of parameters used for the calculation are given in Table 7.4. Mass of neutral atom of type 1 i.e., m_1 $(=(12\times x)+(1\times y)$ a.m.u for C_xH_y), mass of neutral atom of type 2 m_2 $(=(1\times x)$ a.m.u for H_x), mass of ion of type 1 m_{i1} $(=(12\times x)+(1\times y)$ a.m.u for

$C_xH_y^+$, and mass of ion $2m_{i2}$ $(=(1\times x)$ a.m.u for $H_x^+)$, chamber volume V=1.05×10^4 cm^{-3}.

Table 7.4. Parameters used in the present model

Parameter	Value
n_{e0} (electron number density)	0.5×10^{10}cm^{-3}
T_{e0} (electron temperature)	1.5 eV
T_{i0} (ion temperature)	0.05 eV
T_n (neutral temperature)	0.05 eV
T_s (substrate temperature)	630 K
CH_4(neutral density)	1×10^{14} cm^{-3}[Ref. 22]
CH_3(neutral density)	5×10^{12} cm^{-3}[Ref. 22]
C_2H_2(neutral density)	5×10^{13} cm^{-3}[Ref. 22]
C_2H_4(neutral density)	1.5×10^{12} cm^{-3}[Ref. 22]
H(neutral density)	7×10^{13} cm^{-3}[Ref. 22]
H_2(neutral density)	1×10^{15} cm^{-3}[Ref. 22]
CH_4^+(ion density)	5×10^8 cm^{-3}[Ref. 22]
CH_3^+(ion density)	4×10^8 cm^{-3}[Ref. 22]
$C_2H_2^+$(ion density)	5×10^9 cm^{-3}[Ref. 22]
$C_2H_4^+$(ion density)	6×10^8 cm^{-3}[Ref. 22]
H^+(ion density)	7×10^7 cm^{-3}[Ref. 22]
H_2^+(ion density)	8×10^7 cm^{-3}[Ref. 22]

In order to study the effects of variation of total gas pressure on the VG sheet growth characteristics (e.g., nucleation density of VG sheet on CNT surface, height, and thickness of VG sheet protruded from the CNT surface), we first explore the influence of variation of p_0 (at fixed input power and substrate bias) on plasma parameters and composition, such as electron density, electron temperature, number densities of neutrals, and energy of ions.

Figures 7.2(a) and 7.2(b) show the temporal variations of electron density and electron temperature for different total gas pressures (i.e., p_0= 50mTorr, 100mTorr, and 150mTorr). It can be seen from Figs. 7.2(a) and 7.2(b) that electron density and electron temperature decreases with time and get significantly reduced with increasing p_0 at fixed input power of 300W and

substrate bias of -50 V, respectively. These results can be explained on the fact that pressure increase is accompanied by the decrease in the mean free path due to which there are more collisions between electrons and other neutral species in the chamber which subsequently, makes the electrons to lose their energy faster and results in reduced electron temperature and electron density. The effect of variation of electron density and electron temperature with pressure are in agreement with the works of Mao and Bogaerts [22] and Shivkumar *et al.*[41] for CH_4/H_2 and H_2plasma, respectively. The variations of electron density and electron temperature with time are in agreement with the observations of Harilal *et al.*[42]. In addition, the reduction in electron temperature and sheath width with p_0 results in the decrease of velocity (i.e., Bohm velocity) and kinetic energy of ions (i.e., E_i) impinging on the CNT surface [43]. The effect of increasing p_0 on the energy of ions is shown in Fig. 7.2(c).

Since electrons lose their energy faster at high pressures; the dissociation rate of neutrals in plasma is low. However, with increasing pressure at fixed rf power and substrate bias, the decreasing plasma energy was sufficient to dissociate hydrogen molecules but unable to dissociate increasing hydrocarbon molecules [21]. The comparable effect can be seen from Fig. 7.3, which specifies that the decay rate of hydrogen species in plasma is higher than the hydrocarbon species accounted in the model. Therefore, on increasing pressure, the density ratio of hydrogen to carbon atoms in plasma increases, which in turn leads to augmentation in the hydrogen radicals flux onto the CNT surface. This result is in accordance with the study conducted by Takeuchi *et al.*[44] to measure the influence of operating pressure on hydrogen and carbon atom densities in plasmas employing C_2F_6/H_2 gas mixture. They reported that the hydrogen to carbon atom densities in plasma increases on increasing gas pressure.

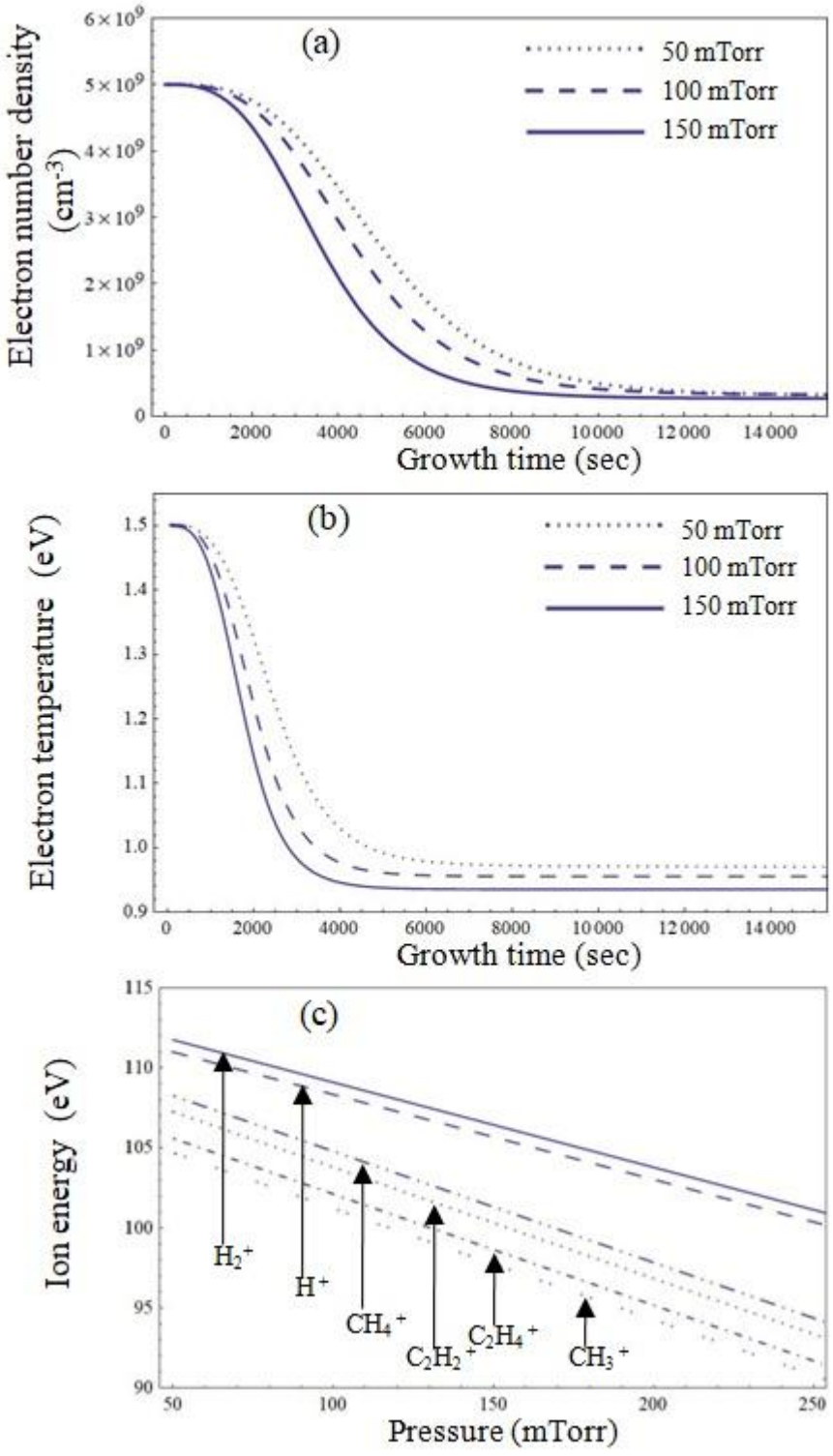

Fig.7.2. Variations of (a) electron density as a function of time, (b) electron temperature as function of time, and (c) ion energy for different values of the total gas pressure at fixed P_{in}= 300W and U_s= -50 V. The other parameters are given in the text.

Neha Gupta
Delhi Technological University, Delhi, India

Moreover, at low pressures, the plasma sheath becomes wider; as a result of which a very strong electric field is generated which quickly drives the energetic ions towards the substrate. These energetic ions enhance the ion-induced dissociation and ion decomposition processes on the CNT surface (at low substrate temperature, i.e., T_s< 800K) [39], which results in the enhancement of N_c (i.e., number of carbon species generated per unit area on the CNT surface). This effect can be seen from Fig. 7.4(a) which illustrates that the surface concentration of carbon species on the CNT surface increases upon reducing the total gas pressure. Also, the interaction of adsorbed hydrocarbon species with hydrogen atoms from the sheath is reduced at relatively low pressures because the hydrogen atom density in plasma is substantially low at reduced gas pressures (cf. Fig. 7.3). All these changes result in the excessive supply of carbon on the CNT surface. Thus, we estimate that increased ion energy at relatively low pressures results in amorphous carbon deposition on the CNT surface with increased defect density.

Figure 7.4(b) shows the time-evolution of the defects number density on CNT surface for different total gas pressures (i.e., p_0=50mTorr, 100mTorr, and 150mTorr). It can be seen from Fig. 7.2 that at relatively low pressure, i.e., atp_0= 50mTorr, the defect generation on the CNT surface is highest. This is evidence of the fact that the energy of ions impinging on the CNT surface is high at low pressures [cf. Fig. 7.2(c)] and thus dislocates C-atoms from their original positions. As discussed previously in Sec. II, the graphene sheet nucleation on CNT surface is defect guided; we conjecture that the availability of more carbon atoms on CNT surface at relatively low pressures increases the cluster formation on the increased defect sites generated on the CNT surface. Subsequently, the diffusion and agglomeration of these clusters lead to the formation of large GIs with increased number density, and therefore we depict that the number density of VG sheets increases on reducing the gas pressure. The increased densities of defects, as well as VG sheet density on CNT surface on decreasing the total gas pressure, have also been reported by Qi *et al.*[12] (cf. Figs. 2(c)-(f) of Qi *et al.*[12]). In addition, Cho *et al.*[45] (cf. Fig. 2(a) of Cho *et*

al.[45]) and Takeuchi *et al.*[44]have also observed that the number density of carbon nanowalls grown on Si substrate decreases with increasing pressure.

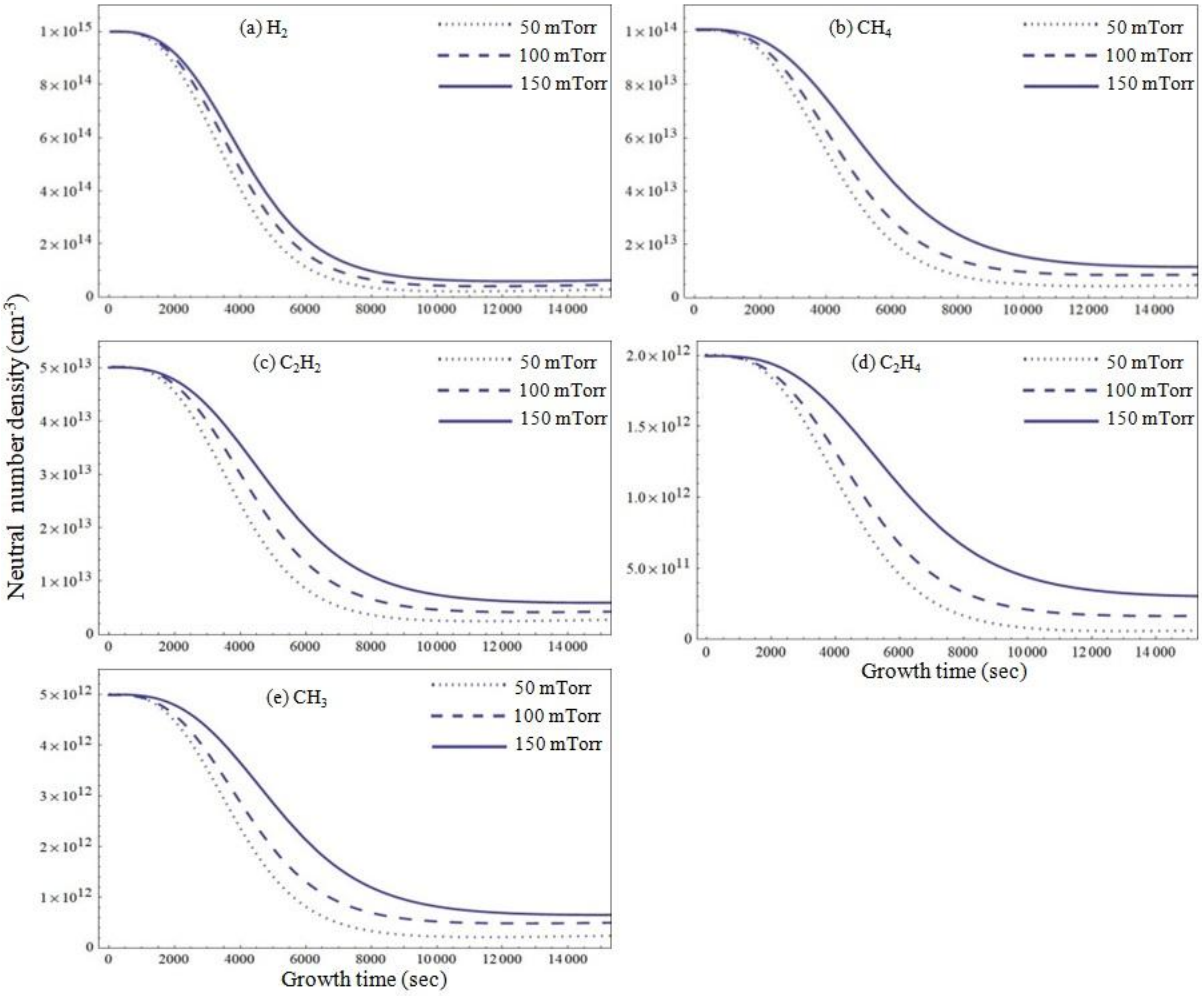

Fig.7.3. Time variations of different neutral species in plasma for different gas pressures at fixed P_{in}= 300W and U_s= -50 V. The other parameters are given in the text.

Furthermore, on decreasing the gas pressure, the diffusion of high energy carbon radicals generated due to the interaction of high energy hydrocarbon ions and adsorbed hydrocarbon radicals occurs rapidly [46]. Due to the availability of high N_c and their faster diffusion and attachment at the growing VG sheet edges, the height of the VG sheet increases at reduced gas pressures. The effect of variation of pressure on height (h_g) of the VG sheet grown on CNT is shown in Fig. 7.4(c). Moreover, the Fig. 7.4(d) shows that the thickness (t_g) of the VG sheet is low at reduced gas pressures. This is because the etching effect due to high energy ion bombardment is prominent at low

pressures. The similar effect of pressure on thickness of VG sheet has also been reported by Wang *et al.*[46]. The results illustrated in Fig. 7.4 (c) are in compliance with the experimental works of Cho *et al.*[45] (cf. Fig. 2(a) of Cho *et al.*[45]) and Takeuchi *et al.*[44] (cf. Fig. 7(a) of Takeuchi *et al.*[44]).

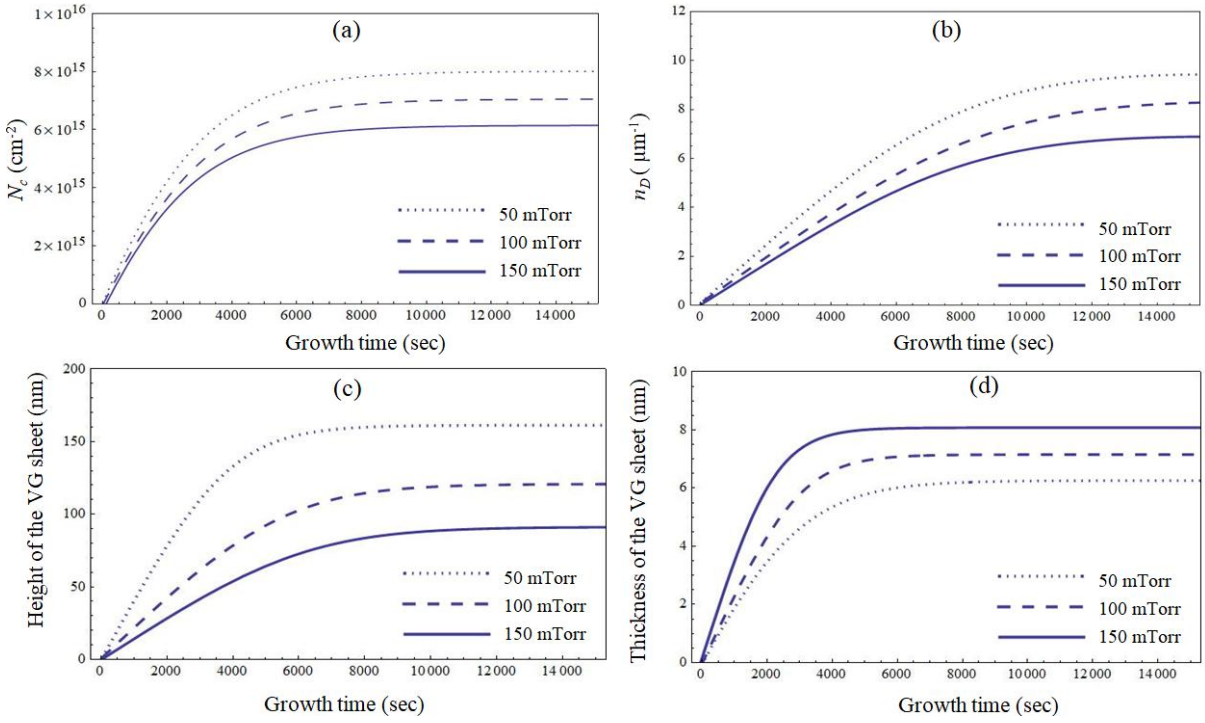

Fig.7.4. Time variations of the (a) number of carbon species generated per unit area on the CNT surface, (b) number density of defects generated per unit micron length of the CNT surface, (c) height of the VG sheet, and (d) thickness of the VG sheet for different gas pressures at fixed P_{in}= 300W and U_s= -50 V. The other parameters are given in the text.

Fig. 7.5 shows temporal evolution of the linear defect density, height, and thickness of VG sheet on the CNT surface for different input power (i.e., P_{in}=300W, 600W, and 900W) at constant gas pressure, p_0=50mTorr and substrate bias, U_s= -50V. It can be seen from Fig. 7.5 that n_D, i.e., the linear density of defects (number of defects produced per unit micron length of the CNT) on the CNT surface and height (h_g) of the VG sheet protruded from the CNT increases with P_{in}, while the thickness of the VG sheet is reduced with P_{in}.

When the input power is raised at constant pressure and substrate bias, the electric field as well as ionization of gases inside the chamber increases, as a

result, the electron density, electron temperature, and energy of ions in the plasma sheath increases [cf. Figs. 7.6(a)-7.6(c)], and consequently, the ion

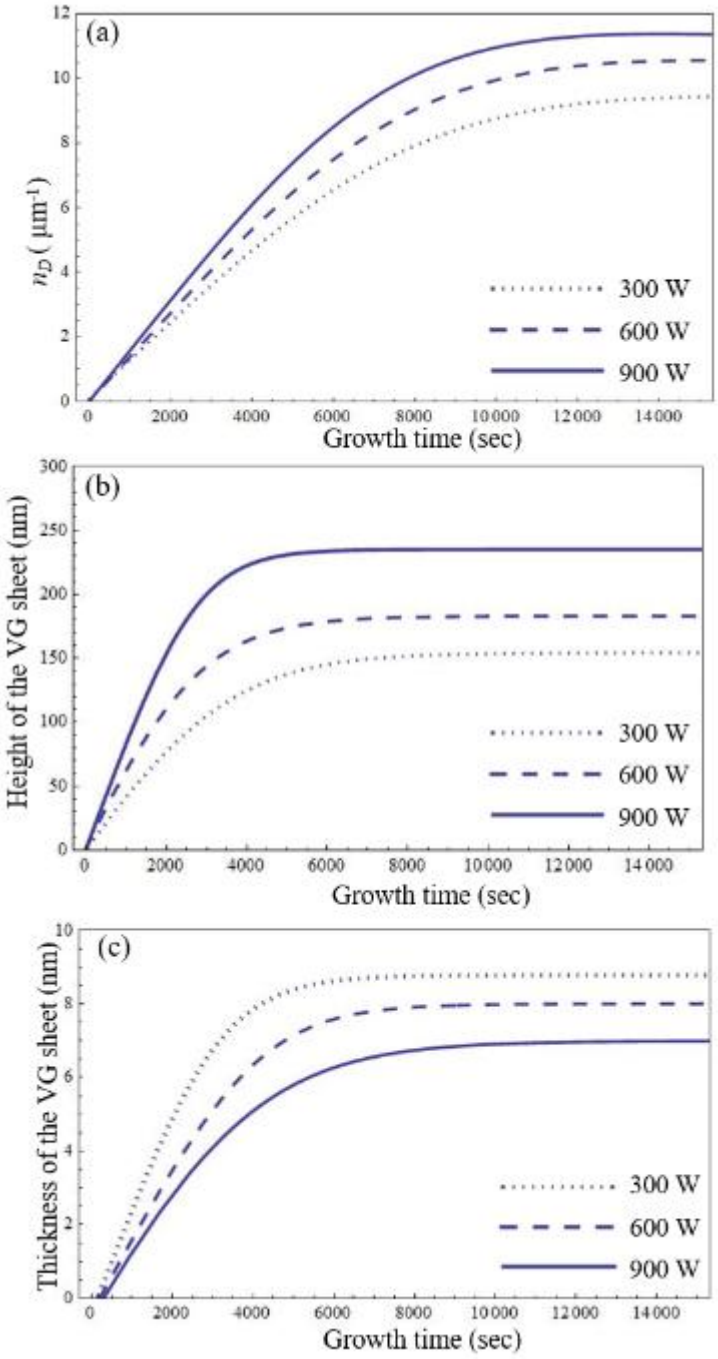

Fig.7.5. Time variations of the (a) linear density of defects generated on the CNT surface, (b) height of the VG sheet, and (c) thickness of the VG sheet for different input power at fixed p_0=50mTorr and U_s= -50 V. The other parameters are given in the text.

decomposition and ion-induced decomposition processes on the CNT surface (at low substrate temperature) are expected to get enhanced, which in turn lead to plentiful generation of carbon on the CNT surface (cf. Fig. 7.6 (d)). Thus, at high input power, the high energy ion bombardment on the CNT surface results in amorphous carbon deposition with increased defect density. The high N_c on the CNT surface at high input power enables the faster generation of graphitic clusters at the defect sites, and consequently, the diffusion and amalgamation of GIs become more effective leading to the formation of large size GIs with increased number density, and therefore, we can infer that the number density of VG sheets increases on raising the input power. Moreover, the high energy hydrocarbon ions on colliding with hydrocarbon radicals on the CNT surface generate carbon radicals that effectively diffuse to the edges of the growing VG sheet on the CNT surface due to high energy owing to the collision reaction, and thereby, increase the height of the VG sheet at high input power [cf. Fig. 7.5(b)] [Ref. 46]. On the other hand, at high plasma power, the highly energetic hydrogen species etch the VG sheets at a higher rate, due to which the thickness of the VG sheet decreases [cf. Fig. 7.5 (c)].

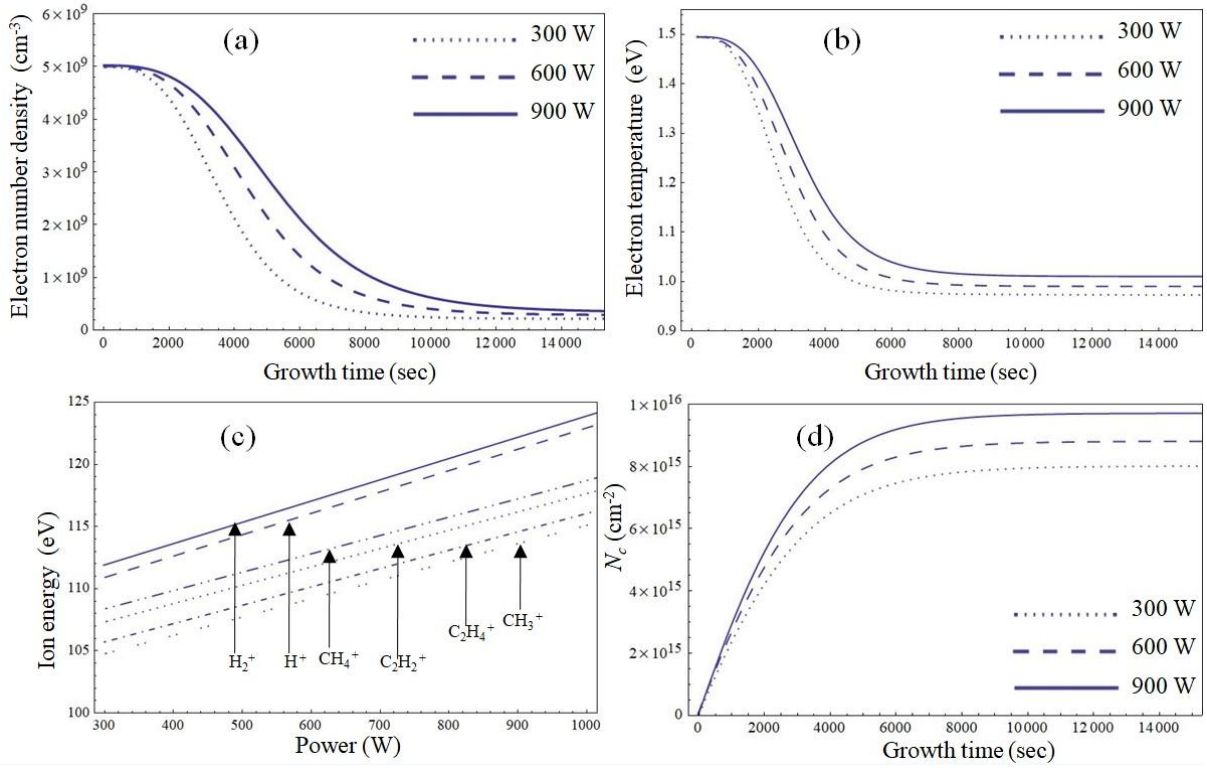

Fig.7.6. Variations of (a) electron density as a function of time, (b) electron temperature as function of time, (c) ion energy, and (d) number of carbon species generated per unit area on the CNT surface as a function of time for different values of input power at fixed p_0=50mTorr and U_s= -50 V. The other parameters are given in the text.

The similar effect of augmentation in the densities of defects and VG sheets on the CNT surface upon the increasing the input power has been reported by Liu *et al.*[11]. Moreover, the similar variations of height and thickness of VG sheets with input power have been observed by Cho *et al.*[45] and Nang and Kim [47] for VG sheets grown on the Si and Cu substrate, respectively.

Now, we investigate the effect of variation of applied substrate bias on the growth characteristics of the VG sheet protruded from the surface of pre-grown CNT. The applied substrate bias plays an important role in controlling the sheath width, electric field, direction and kinetic energy of ions focusing on the CNT surface [8,24]. On increasing the applied bias at the conductive substrate, the sheath width increases, as a result of which the electric field and energy of ions in the plasma sheath get enhanced, which in turn augments the ion bombardment induced sputtering process leading to the increase in linear defect density on the CNT surface with U_s. The effects of variation of substrate bias on the energy of ions and defect density on the CNT surface is depicted in Figs. 7(a) and 7(b), respectively.

Moreover, the high energy ions at high applied bias boost the ion-decomposition and ion-induced dissociation processes, which results in high carbon generation on the CNT surface [cf. Fig. 7.8(a)]. Therefore, the height and graphene sheet density on the CNT increases with applied bias due to the generation of high N_c and n_D, respectively. The time variation of the height of the VG sheet with substrate bias is shown in Fig. 7.8 (b).The increase in height and density of VG sheet on CNT due to high N_c and n_D has been discussed in the previous results. The behaviour of number density of VG sheets compares favourably with the experimental observations of Kumar and Ostrikov [8]. Moreover, the thickness of VG sheet decreases due to enhanced etching of graphene sheet edges by high energy hydrogen species. The temporal evolution

of the thickness of the VG sheet for different bias conditions is shown in Fig. 7.8(c).

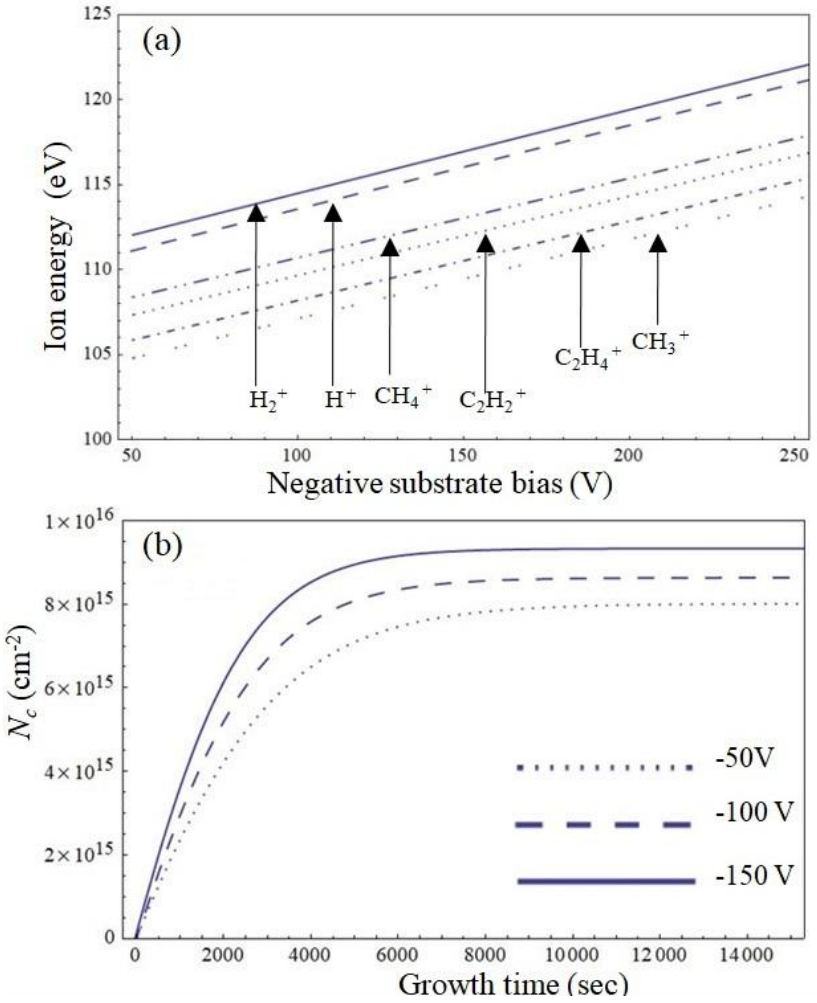

Fig.7.7. Variations of (a) ion energy and (b) number of carbon species generated per unit area on the CNT surface as a function of time for different values of substrate bias at fixed p_0=50mTorr and P_{in}= 300W. The other parameters are given in the text.

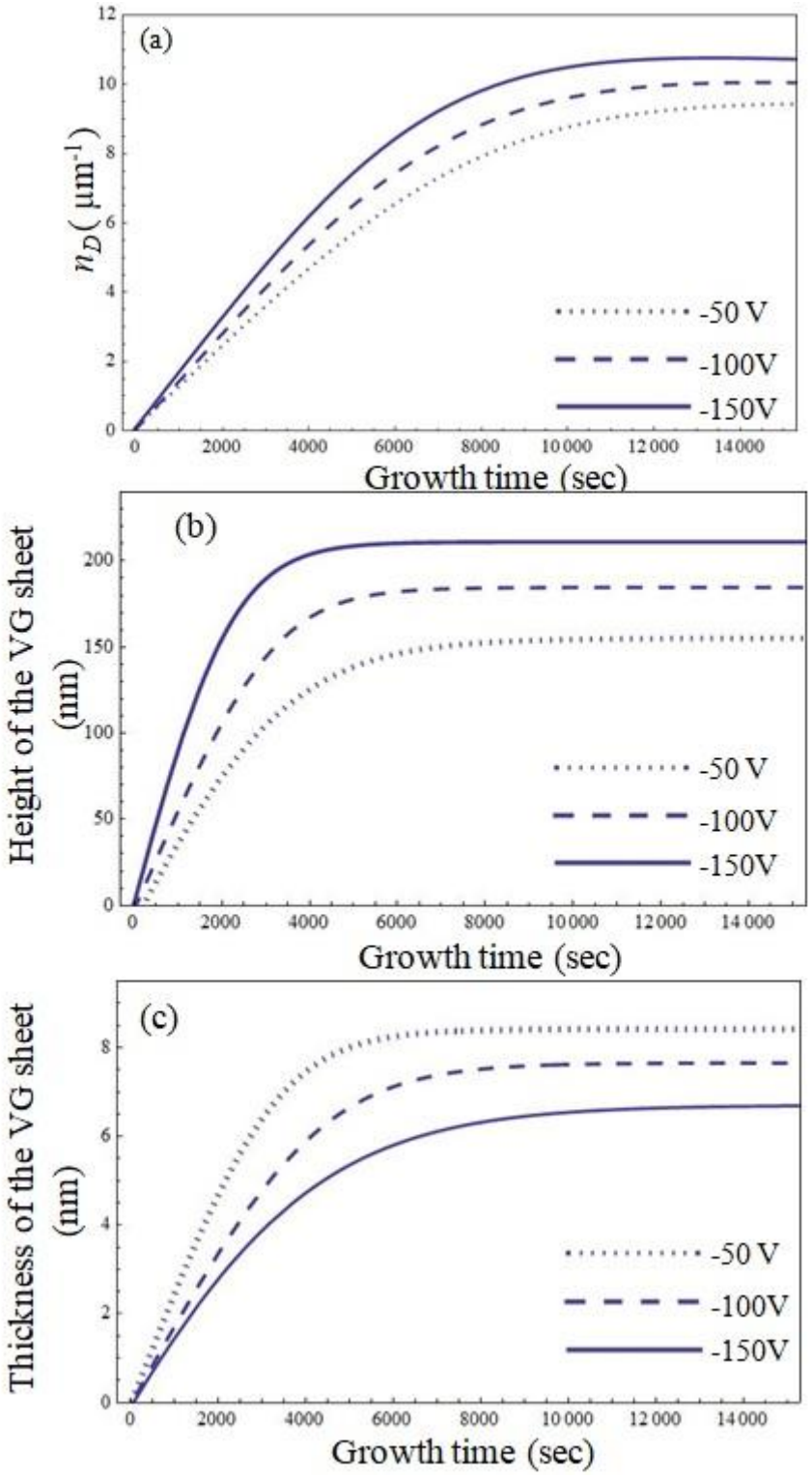

Fig.7.8. Time variations of the (a) linear density of defects generated on the CNT surface, (b) height of the VG sheet, and (c) thickness of the VG sheet for different values of substrate bias at fixed p_0=50mTorr and P_{in}= 300W. The other parameters are given in the text.

References

[1] M. Hiramatsu, K. Shiji, H. Amano, and M. Hori, Appl. Phys. Lett. **84**, 4708 (2004).

[2] J. J. Wang, M. Y. Zhu, R. A. Outlaw, X. Zhao, D. M. Manos, B. C. Holloway, and V. P. Mammana, Appl. Phys. Lett. **85**, 1265 (2004).

[3] S. Wang, J. Wang, P. Miraldo, M. Zhu, R. Outlaw, K. Hou, X. Zhao, B. C. Holloway, D. Manos, T. Tyler, O. Shenderova, M. Ray, J. Dalton, and G. McGuire, Appl. Phys. Lett. **89**, 183103 (2006).

[4] K. H. Yu, P. X. Wang, G. H. Lu, K. H. Chen, Z. Bo, and J. H. Chen, J. Phys. Chem. Lett. **2**, 537 (2011).

[5] K. Yu, Z. Bo, G. Lu, S. Mao, S. Cui, Y. Zhu, X. Chen, R. S. Ruoff, and J. Chen, Nanoscale Res. Lett. **6**, 202 (2011).

[6] H.-C. Chang, H.-Y. Chang, W.-J. Su, K.-Y. Lee, and W.-C. Shih, Appl. Surf. Sci. **258**, 8599 (2012).

[7] R.R.Devarapalli, R.V. Kashid, A.B. Deshmukh, P. Sharma, M.R. Das, M.A. More, and M.V. Shelke, J. Mater. Chem. C **1**, 5040 (2013).

[8] S. Kumar and K. Ostrikov, Nanoscale **3**, 4296 (2011).

[9] J.-H. Deng, G.-A. Cheng, R.-T. Zheng, B. Yu, G.-Z. Li, X.-G. Hou, M.-L. Zhao, and D.-J. Li, Carbon **67,** 525 (2014).

[10] J.-H. Deng, R.-N. Liu, Y. Zhang, W.-X. Zhu, A.-L. Han, G.-A.Cheng, Journal of Alloys and Compounds **723**, 75(2017).

[11] J. Liu, B. Zeng, X. Wang, W. Wang, and H. Shi, Appl. Phys. Lett. **103**, 053105 (2013).

[12] J.L. Qi, F. Zhang, L.X. Zhang, J. Cao and J.C. Feng, Mater. Res. Express **1,** 025601 (2014).

[13] L.-A. Gautier, V. Le Borgne, M. A. El Khakani, Carbon **98**, 259(2016).

[14] K. Yu, G. Lu, Z. Bo, S. Mao, and J. Chen, J. Phys. Chem. Lett. **2**, 1556 (2011).

[15] C.B. Parker, A.S. Raut, and B. Brown, J. Mater. Res. **27**, 1046 (2012).

[16] Y. Liu, F. Wang, X. Wang, X. Wang, E. Flahaut, X. Liu , Yao Li , X. Wang , Y. Xu , Y. Shi, and R. Zhang, Nat. Commun. **6**, 8589 (2015).

[17] H. -C. Hsu, C. -H. Wang, S. K. Nataraj, H. -C. Huang, H. -Y. Du, S.-T. Chang, L. -C. Chen, K. -H. Chen, Diamond & Related Materials **25**, 176 (2012).

[18] H. -Y. Du, C. -H. Wang, H. -C. Hsu, S. -T. Chang, H. -C. Huang, L. -C. Chen, K. -H. Chen, Int. J. Hydrogen Energy **37**, 18989 (2012).

[19] C. Li, Z. Li, H. Zhu, K. Wang, J. Wei, X. Li, P. Sun, H. Zhang and D. Wu, J. Phys. Chem. C **114**,14008 (2010).

[20] R. Kurt and A. Karimi, Chem. Phys. Chem. **2**, 388 (2001).

[21] Z. Bo, Y. Yang, J. Chen, K. Yu, J. Yan, and K. Cen, Nanoscale **5**, 5180 (2013).

[22] M. Mao and A. Bogaerts, J. Phys. D: Appl. Phys. **43,** 315203 (2010).

[23] H. Mehdipour, K. Ostrikov, A. E. Rider, and Z. Han, Plasma Process. Polym. **8**, 386 (2011).

[24] Z. Marvi, S. Xu, G. Foroutan, and K. Ostrikov, Phys. Plasmas 22, 013504 (2015).

[25] Y.P. Raizer, Gas Discharge Physics, Springer-Verlag, Berlin, 1991.

[26] L. Zeng, D. Lei, W. Wang, J. Liang, Z. Wang, N. Yao , and B. Zhang , Appl. Surf. Sci. **254**, 1700 (2008).

[27] Z. Bo, S. Mao, Z. J. Han, K. Cen, J. Chen, and K. Ostrikov, Chem. Soc. Rev. **44**, 2108 (2015).

[28] B. B. Wang, K. Zhu, K. Ostrikov, R. W. Shao, and K. Zheng, J. Appl. Phys. **119**, 024302 (2016).

[29] B. B. Wang, K. Zeng, Q. J. Cheng, and K. Ostrikov, Appl. Surf. Sci. **325**, 251 (2015).

[30] H. Mehdipour and K. Ostrikov, ACS Nano **6**, 10276 (2012).

[31] A. S. Barnard, M. L. Terranova, and M. Rossi, Chem. Mater.**17**, 527(2005).

[32] A. V. Krasheninnikov, K. Nordlund, M. Sirvio, E. Salonen, and J. Keinonen, Phys. Rev. B **63,** 245405 (2001).

[33] B. B. Wang, W. L. Wang, and K. J. Liao, Thin Solid Films **401**, 77 (2001).

[34] S. K. Srivastava, A.K. Shukla, V.D. Vankar, and V. Kumar, Thin Solid Films **492**, 124 (2005).

[35] A. Tewari and S. C. Sharma, Phys. Plasmas **21**, 063512 (2014).

[36] M.S. Sodha, S. Misra, S.K. Misra, and S. Srivastava, J. Appl. Phys. **107**, 103307 (2010).

[37] See http://www.its.caltech.edu/~teinav/Lectures/Ph%201b/Lecture%2010%20-%2002-09-2017.pdf for potential of a hemisphere.

[38] R. Gupta, S.C. Sharma, and R. Sharma, Plasma Sources Sci. Technol. **26**, 024006 (2017).

[39] H. Mehdipour, K. Ostrikov, and A.E. Rider, Nanotechnology **21**, 455605 (2010).

[40] N. V. Mantzaris, E. Gogolides, A. G. Boudouvis, A. Rhallabi, and G. Turban, J. Appl. Phys. **79**, 3718(1996).

[41] G. Shivkumar, S. S. Tholeti, M. A. Alrefae, T.S. Fisher, and A.A. Alexeenko, J. Appl. Phys. **119**, 113301 (2016).

[42] S. S. Harilal, C.V. Bindhu, R. C. Issac, V. P. N. Nampoori, and C. P. G. Vallabhan, J. Appl. Phys. **82**, 2140 (1997).

[43] ‘‘Principles of Plasma Discharges and Materials Processing’’, M. A. Lieberman, A. J. Lichtenberg, Wiley, NY 1994.

[44] W. Takeuchi, H. Sasaki, S. Kato, S. Takashima, M. Hiramatsu, and M. Hori, J. Appl. Phys. **105**, 113305 (2009).

[45] H. J. Cho, H. Kondo, K. Ishikawa, M. Sekine, M. Hiramatsu, M. Hori, Carbon **68,** 380 (2014)

[46] Y. Wang, L. Li, Q. Cheng, C. He, Journal of Luminescence **161,** 7(2015).

[47] L. V. Nang and E.-T. Kim, J. Electrochem. Soc. **159**, K93 (2012).

8
Conclusion and Future Scope

8.1 Conclusion

The work carried out in the present thesis aims to develop the analytical model to elucidate the mechanisms of the growth of graphene sheet in the reactive plasma environment. A theoretical model comprising the charge neutrality, energy and particle balance equations of all the plasma species (neutrals and charged species) is developed to understand the effect of plasma parameters, nitrogen doping and negative ions on the growth (without catalyst) of embryonic graphene by condensation in the plasma environment. However, to explicate the catalyzed growth of vertical graphene sheet in reactive plasma environment, an analytical model is developed that incorporates the plasma sheath equations to investigate the energy and fluxes of the plasma species, (electrons, positively charged and neutrals species); kinetics of the plasma species, dissociation of the plasma species over the catalyst nanoislands to generates building units (carbon species) surface via various complex surface processes, diffusion of building units, formation of carbon clusters, formation of graphene nuclei, formation of graphene island, and planar growth of graphene island which eventually grown in vertical direction under the inclusion of electric field induced in the plasma sheath. The present work of the thesis may help to understand the better insights of the plasma parameters, operating parameters, and gaseous sources on the growth characteristics of the vertical graphene sheet. From the results obtained in the present work, the field emission characteristics of the graphene sheet are estimated. In brief, the work done in the present thesis can be summarized as follows:

- The plasma parameters strongly influence the growth profile of the graphene sheet. The thickness of the graphene sheet decreases with the plasma parameters, number density of hydrogen ions and RF power, and consequently the field emission of electrons from the graphene sheet surface increases. The introduction of negative ions in plasma leads to the growth of graphene sheet with lesser thickness and the height of the graphene sheet is found to increase with ion density and sticking coefficient of carbon species.

- Nitrogen doping results in reduced thickness and shortened height of the graphene sheet. However, boron doping increases the thickness and height of the graphene sheet. The field emission properties of the graphene sheet have been proposed on the basis of the results obtained. It is concluded that nitrogen doped graphene sheet exhibits better field emission characteristics as compared to undoped and boron doped graphene sheet.

- The growth and field emission properties of the graphene sheet also depend on the type of carbon source gas or carbon feedstock gas. The three different gas mixtures i.e., C_2H_2, CH_4, and CF_4 with hydrogen and argon are considered in the present investigation to examine the variations in the number densities of carbon and hydrogen species generated on the catalyst surface and their consecutive effects on the dimensions (i.e., height and thickness) and number density profiles of the graphene nanosheet. The thickness and height of the graphene sheet are maximum for C_2H_2 gas mixtures and least for CH_4 and CF_4, respectively. Moreover, it is estimated that C_2H_2 contained gas mixture enhances the field emission characteristics of the graphene sheet followed by CH_4 and CF_4.

- The computational model in COMSOL Multiphysics 5.2 Simulation software is developed to analyze the spatial distributions of number density and temperature of plasma species in the PECVD reactor. The outcomes of the computational model are linked as the input parameters of the surface deposition model to investigate the growth

characteristics of the vertically oriented graphene sheet (VOGS) in the reactive PECVD system. It is found that the density and temperature of each plasma species decreases from bulk plasma surface to substrate surface. It is also observed that the PECVD process parameters i.e., gas pressure and plasma power affect the density distribution of plasma species. The energetic electrons get lost in the plasma region at high pressure (constant input power) and low input power (constant gas pressure) due to the weak electric field in the plasma and large number of collisions between electrons and other plasma species. At low pressure, the building units (carbon species) generate at higher rates on the catalyst nanoislands active surface and thus, enhance the growth and surface density of VOGS on the substrate surface. However, it is found that VOGS growth rate increases when input plasma power is raised from 100 W to 300 W and decreases with further increase in the plasma power; whereas, the surface density of VOGS increases with plasma power. Moreover, the presence of energetic hydrogen radicals and other positively charged species at low pressure and high power etch the VOGS more effectively and reduce the thickness of the VOGS.

- An analytical model is developed to understand the better insights of the growth mechanism of the graphene over CNT surface (CNT-graphene hybrid) in the PECVD system. The PECVD operating parameters (total gas pressure, input plasma power, and substrate bias) affects the surface density of the defects formed over the CNT surface and growth profile of the graphene sheet. When the total gas pressure is lowered and the input power and substrate bias are enhanced, the number densities and height of the VG sheet on the CNT surface are increased; however, the thickness of the VG sheet is reduced.

8.2 Future scope of the present work

The present work of the thesis can be extended to fabricate the thin and long VOGS for their potential applications in the field emitters as the field emission characteristics of the VOGS depend on its geometrical characteristics, i.e., height and thickness.

The present work covers most of the important aspects for the deterministically controlled synthesis of the vertical graphene sheet in plasma. However, there are some aspects which can be deepen further for the future development of the synthesis of the VOGS.

- The role of plasma on the lateral size of the graphene sheet can be investigated deeply.
- Experimentally, it is reported that the tapered graphene sheet is formed in reality. What are the essential factors responsible for it?
- During the PECVD growth, the vertically oriented graphene sheets are not exactly normal to the substrate surface. The alignment mechanism of the graphene sheet during PECVD growth can be investigated to enhance the field emission properties.

APPENDIX A

Potential due to rectangular graphene sheet

Following Ref. [1] we consider a charged rectangular graphene sheet in 3-D space. The geometry of the problem is given in Fig. A.1. l, h, and t are the length, height and thickness of the graphene sheet, respectively.

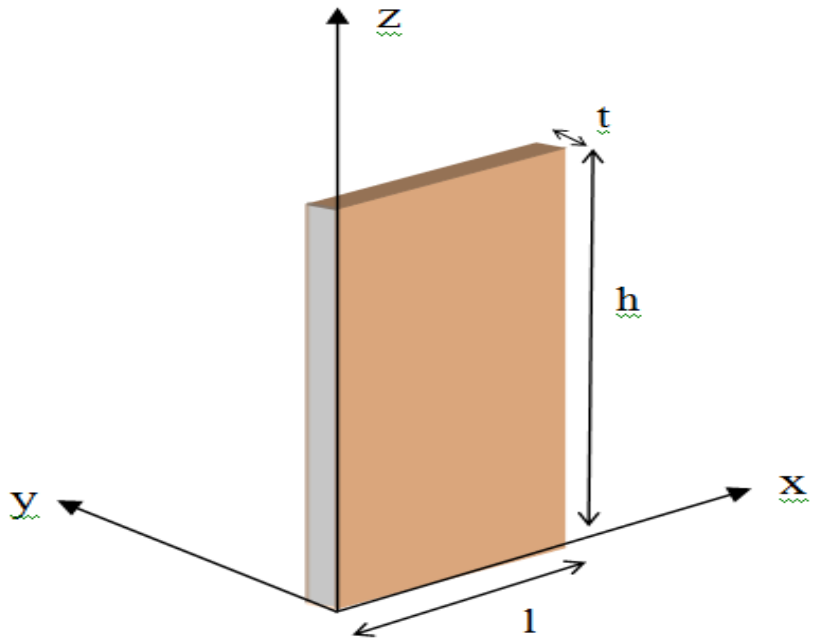

Fig. A.1. The 3-D view of rectangular graphene sheet.

Potential due to the sheet in 3-D space is given by:

$$V = \frac{1}{2}\times\frac{1}{4\pi\varepsilon_0}\times\frac{e}{l\times t}\Bigg[-2z\left(\tan^{-1}\left(\frac{J}{2t\sqrt{N}}\right)+\tan^{-1}\left(\frac{K}{2t\sqrt{P}}\right)+\tan^{-1}\left(\frac{L}{2t\sqrt{Q}}\right)\right.$$
$$\left.+\tan^{-1}\left(\frac{M}{2t\sqrt{R}}\right)\right)+(t-2y)\log(l-2x+\sqrt{N})+(l-2x)\log(t-2y+\sqrt{N})$$
$$-(t-2y)\log(-l-2x+\sqrt{P})+(l+2x)\log(t-2y+\sqrt{P})$$
$$-(l-2x)\log(-t-2y+\sqrt{Q})+(t+2y)(\log(l-2x+\sqrt{Q})$$
$$-\log(-l-2x+\sqrt{R}))-(l+2x)\log(-t-2y+\sqrt{R})\Bigg], \qquad \text{(A.1)}$$

where

$$J = (l-2x)(t-2y),$$
$$K = (l+2x)(t-2y),$$

$$L = (l-2x)(t+2y),$$
$$M = (l+2x)(t+2y),$$
$$N = \sqrt{(l-2x)^2 + (t-2y)^2 + 4z^2},$$

$$P = \sqrt{(l+2x)^2 + (t-2y)^2 + 4z^2},$$

$$Q = \sqrt{(l-2x)^2 + (t+2y)^2 + 4z^2},$$

$$R = \sqrt{(l+2x)^2 + (t+2y)^2 + 4z^2}$$

Now, the potential due to sheet along z-axis

$$V_z = \frac{1}{(l \times t)} \times 7.2 \times 10^{-10} \left(-8z \tan^{-1}\left(\frac{l \times t}{2z\sqrt{S}}\right) - 2l \log\left(-t + \sqrt{S}\right)\right.$$
$$\left. + 2l \log\left(t + \sqrt{S}\right) - 2t \log\left(-l + \sqrt{S}\right) + 2t \log\left(l + \sqrt{S}\right),\right. \qquad \text{(A.2)}$$

where $S = l^2 + t^2 + 4z^2$.

Neha Gupta
Delhi Technological University, Delhi, India

Reference:

[1] See http://blog.wolfram.com/2012/09/27/3d-charges-and-configurations-with-sharp-edges/for potential due to the rectangular graphene sheet in 3-D space.